COMPETITION EFFECTS IN CHARGED PARTICLE INDUCED REACTIONS

Thesis by

John Lehrer Zyskind

In Partial Fulfillment of the Requirements

for the Degree of

Doctor of Philosophy

California Institute of Technology

Pasadena, California

1979

(Submitted May 21, 1979)

ACKNOWLEDGMENTS

I should begin by thanking Professor William A. Fowler, who inspired this work, guided my understanding of it, and constantly impressed me with its urgency, and Professor Charles A. Barnes, my advisor, whose wise counsel and experimental skepticism were of great help. This thesis owes a great deal to close collaboration with a number of colleagues: Dr. John M. Davidson, Dr. M. Tezer Esat, Dr. Roscoe E. Marrs, Dr. D. Graham Sargood, Dr. Mark H. Shapiro, and Dr. Ray H. Spear. Working with all of them was a pleasure, a privilege, and an education. I would especially like to thank my mother's compatriot, Ray Spear. During his visit at Caltech his energetic participation was crucial in giving this project the overall form it assumed, and I am still benefiting from his lessons in writing in the scientific dialect of the English language.

Many members of the Kellogg staff were very helpful in phases of this work, among them: Evaline Gibbs, Marty Watson, Jan Rasmussen, Gloria Laird, Will Schick, Don Woshnak, Bud Warrick, and Otto Orient.

It is perhaps premature at this point, but I believe I already have convincing evidence that the preparation of this thesis is benefiting greatly from the careful and expeditious work of Ruth Stratton (typing, X1826) and Heather Marr (illustration, 794-9008).

I gratefully acknowledge the generous support of the Fannie and John Hertz Foundation from September 1973 until December 1977. This research was supported in part by the National Science Foundation [PHY76-83685].

This thesis might never have been finished if I had done nothing else. Fortunately, wonderful recreational activities have enabled me to attack it with renewed vigor. I would like to mention some of those involved. For sharpening my ear and deepening my perception of the beauty of music I thank James Boyk and Johann Sebastian Bach. I also thank all those with whom I have swum at Caltech but with special mention for two people in particular: my long time work-out partner and friend, Fred Gelbard, with whom swimming first became a social activity for me; and my coach, Scot MacFarland, who strives to instill high standards of excellence in his swimmers without killing the fun and is sufficiently open-minded to work earnestly with swimmers of all shapes, sizes, and ages (and almost all speeds) if they are willing to pay the price in one currency or another, all of them hard in one way or another.

Above all others I would like to thank my mother and father for the many great benefits I have derived from them during our long association, which dates back as far as I can remember. As a result of their love and teaching I wanted to pursue these studies and was able to pursue them successfully. But, perhaps the most valuable gift I have received at their hands is the shining example provided by the admirable tenacity with which they are facing difficult circumstances, surmounting formidable obstacles, and showing that in this too there can be joy.

If gratitude is appropriate, then so is celebration. I hope that events will prove the following words, which I borrow from Sir Winston Churchill, to be as fitting here as they were for the more momentous occasion on which he first uttered them:

"Now this is not the end.
It is not even the beginning of the end.
But it is, perhaps, the end of the beginning."

W. S. Churchill
11/10/42 at the Lord Mayor's London
Mansion House, London.

ABSTRACT

Absolute cross sections have been measured for 14 reactions: $^{54}Cr(p,\gamma)^{55}Mn$ for 0.83 MeV $\leq E_p \leq$ 3.61 MeV, $^{54}Cr(p,n)^{54}M_n$ for 2.23 MeV $< E_p <$ 3.61 MeV, $^{51}V(p,\gamma)^{52}Cr$ for 0.93 MeV $< E_p <$ 4.47 MeV, $^{51}V(p,n)^{51}Cr$ for 1.58 MeV $< E_p <$ 4.47 MeV, $^{68}Zn(p,\gamma)^{69}Ga$ for 1.67 MeV $\leq E_p \leq$ 4.97 MeV, $^{68}Zn(p,n)^{68}Ga$ for 3.77 MeV $\leq E_p \leq$ 5.03 MeV, $^{68}Zn(p,\alpha)^{65}Cu$ for 3.36 MeV $\leq E_p \leq$ 5.48 MeV, $^{48}Ca(p,\gamma)^{44}Sc$ for 0.58 MeV $\leq E_p \leq$ 2.67 MeV, $^{48}Ca(p,n)^{48}Sc$ for 0.96 $\leq E_p \leq$ 2.67 MeV, $^{37}Cl(\alpha,\gamma)^{41}K$ for 2.90 MeV $\leq E_\alpha \leq$ 5.23 MeV, $^{62}Ni(\alpha,\gamma)^{66}Zn$ for 5.07 MeV $\leq E_\alpha \leq$ 8.64 MeV, $^{62}Ni(\alpha,n)^{65}Zn$ for 6.95 MeV $\leq E_\alpha \leq$ 8.76 MeV, $^{64}Ni(\alpha,\gamma)^{68}Zn$ for 4.50 MeV $\leq E_\alpha \leq$ 7.45 MeV, and $^{64}Ni(\alpha,n)^{67}Zn$ for 5.29 $\leq E_\alpha \leq$ 7.44 MeV. Substantial drops in cross section, by factors from three to five, were observed above the neutron thresholds for all of the radiative capture reactions except $^{48}Ca(p,\gamma)^{49}Sc$. These "competition cusps" are caused by competition from the neutron channel. In the $^{48}Ca(p,\gamma)^{49}Sc$ and $^{68}Zn(p,\alpha)^{65}Cu$ reactions, significant though smaller neutron competition effects were observed. The measured cross sections have been compared with cross sections calculated using global Hauser-Feshbach models. It was thus established that: (i) isospin mixing should be assumed to be complete in these nuclear reaction models, (ii) width fluctuation corrections should be included in the treatment of the competition effects, and (iii) black nucleus strength functions for the neutron channels lead to inadequate neutron transmission functions, and should be replaced by more realistic strength functions which include the

effects of size resonances. Cross sections calculated with current versions of global Hauser-Feshbach models, which incorporate these modifications, agree with those measured for the fourteen reactions studied to within a factor of two in almost all cases, and to within a factor of three in all cases.

CONTENTS

Chapter I	Introduction	1
Chapter II	Experimental Procedures, Data Analysis, and Results	8
A.	Reactions Studied and Target Chambers	8
B.	Target Fabrication	9
C.	Determination of Target Thicknesses	11
D.	Gamma-Ray Detection	15
E.	Analysis of γ-Ray Data	17
F.	Neutron Detection	22
G.	Analysis of Neutron Data	27
H.	Detection of α-Particles and Data Analysis for $^{68}Zn(p,\alpha)^{65}Cu$ Measurements	29
Chapter III	Theory and Discussion	31
A.	Summary of the Data	31
B.	Theory	34
(i)	Competition and Global Hauser-Feshbach Models	34
(ii)	Transmission Functions	37
(iii)	Width Fluctuation Corrections	42
(iv)	Size Resonances	46
(v)	Isospin Mixing	49
C.	Summary and Conclusions	53
Appendix A	A Cusp in the $^{54}Cr(p,\gamma)^{55}Mn$ Reaction	57
Appendix B	Cross Section Measurements and Thermonuclear Reaction rates for $^{48}Ca(p,\gamma)^{49}Sc$ and $^{48}Ca(p,n)^{48}Sc$	68
References		84
Tables		91
Figures		158

CHAPTER I

INTRODUCTION

The chemical elements as we now find them are believed to result from nuclear transmutations in various astronomical environments prior to the formation of the solar system. The quasi-static carbon, neon, oxygen, and silicon burning which occur during the later stages of the evolution of massive stars, and the short-lived but vigorous explosive nucleosynthesis accompanying the supernova explosion which ends the star's life are especially important settings for nucleosynthesis. Charged particle- and neutron-induced reactions build up heavier nuclei during these stages of stellar evolution, and are thought to be the sources of many of the nuclear species from neon to iron (see, for example, Trimble 1975).

For hydrostatic burning the temperatures and densities are too low, and for explosive nucleosynthesis the time too short, to reach nuclear statistical equilibrium in all nuclear reactions; consequently, calculations of the composition of the products must be carried out by following complete networks of nuclear reactions. Provided the thermodynamic history and initial composition are known, the results of such calculations depend primarily on the cross sections used in the calculation of the thermonuclear reaction rates. Reaction rates have been experimentally determined for many reactions of interest both by numerical integration of measured cross sections (e.g., Howard 1974 and Solomon 1978), and by measuring yields in targets sufficiently thick to

stop the beam (Roughton 1976). But because of the high temperatures and densities involved, rates are needed for a very large number of reactions; many of the targets are radioactive or thermally raised into excited states. Thus, for many reactions, the rates cannot at present be calculated from experimental data because the cross sections have not yet been measured, and for many more, prospects of measurements being carried out in the near future are slim, or altogether out of the question.

The need for these reaction rates has led to the development of semi-empirical models based on the Hauser-Feshbach expression for energy-averaged cross sections, with the required transmission functions based on the optical model for particle channels and on giant resonance and single particle forms for the γ-ray channels (Michaud 1970b, Woosley 1975, Mann 1976 , Zimmerman 1977). The models are global in the sense that, given the charges, numbers of neutrons, mass excesses and level schemes for the nuclei involved, all cross sections are calculated from one set of parameters with a smooth functional dependence on the energy and masses. In principle, such a model should provide a good description of cross sections for reactions in which the compound nucleus mechanism is dominant and the density of compound states is sufficient to justify the statistical assumptions underlying the model for energy intervals of interest. Because the cross sections are averaged with a weighting factor representing the Maxwell-Boltzmann velocity distribution in calculating thermonuclear rates, the energy-averaged cross sections calculated from the Hauser-Feshbach models should be appropriate for most of

the charged-particle and neutron-induced reactions on medium mass nuclei occurring during hydrostatic and explosive carbon, oxygen, neon, and silicon burning, and for the neutron-induced reactions on intermediate and heavy nuclei occurring during the r- and s-processes.

Calculations performed with an earlier version of one of these global models (Woosley 1975) predicted that, above the thresholds for the emission of s-wave neutrons in a number of proton- and α-particle-induced reactions, the cross sections for the competing radiative capture and charged particle emitting reactions would decrease precipitously by a factor as large as one hundred. Similar but smaller threshold effects in energy-averaged cross sections have been observed in elastic neutron scattering, and were shown by Meyerhof (1962) to result from the unitarity of the collision matrix. Because s-wave neutrons experience no Coulomb or angular momentum barriers, their emission is favored over that of charged particles; their emission is favored over that of γ-rays because of the weakness of electromagnetic interactions compared to strong interactions in the nucleus. Unitarity requires that flux be conserved; as the cross section for neutron emission increases, there must be compensating decreases in the cross sections for other products. This situation is illustrated schematically in Figure 1. These threshold effects in energy-averaged cross sections are different from the cusps first predicted by Wigner (1948) and discussed at greater length by Baz (1958) and Newton (1959). The "Wigner cusps" arise from a square root singularity in the derivative of the collision matrix which results from combining the requirement of unitarity with the proper analytic continuation

of the collision matrix across the threshold. From an R-matrix analysis, Meyerhof (1963) has shown that when the cusp is averaged over many levels, the competition threshold effect observed in energy-averaged cross sections results. Such competition threshold effects may be termed level-averaged cusps or competition cusps, although they are not cusps in the strict mathematical sense of the word as are the Wigner cusps; all further references to cusps in this thesis will refer to the competition cusps.

In comparisons with a wide range of experimental data, the global Hauser-Feshbach models have been quite successful in reproducing the observed cross sections, usually to within a factor of two (Mann 1975a and 1975b, Holmes 1976a and 1976b, and Fowler 1975). For many of these reactions the cross sections have little energy dependence other than that arising from barrier penetration effects, and are sensitive primarily to the transmission functions for one channel. Thus radiative thermal neutron capture reactions usually provide a measure of γ-ray transmission functions, and (p,n) and (α,n) reactions measure proton and α-particle transmission functions except just above the neutron threshold. However, it is also crucial for nucleosynthesis calculations that the models be able to predict accurately the effects of competition between different outgoing channels. For example, in explosive nucleosynthesis, (p,γ) reactions contribute to the build-up of heavier species, whereas (p,n) reactions do not. The emitted neutron will be captured, of course, but probably by a different species of nucleus, quite possibly one which does not participate in the main stream of

nucleosynthesis. The study of reactions for which competition effects play a major role is also important because the strong energy dependence of the cross sections, reflecting the interplay of transmission functions in the competing channels, provides a sensitive probe of aspects of the nuclear reaction models not stringently tested by the earlier experimental work.

As a result of these considerations, and stimulated by the successful observation of the first of the predicted competition cusps in the excitation function of $^{64}Ni(p,\gamma)^{65}Cu$ by Mann, Dayras, and Switkowski (1975c), a program was undertaken to measure absolute cross sections for a number of reactions for which prominent competition effects were predicted, and for the associated neutron producing reactions.

The magnitude of the drop at the $^{64}Ni(p,n)^{64}Cu$ threshold was found to be a factor of ten smaller than the first predictions (Woosley 1975), and also smaller than that predicted by Mann's program HAUSER*4 (Mann 1976a). Mann et al. (1975c) showed that an adequate fit to the observed excitation function could be obtained if width fluctuation corrections were included in the calculations performed with the HAUSER*4 program. Fowler (1976) pointed out that, if isospin mixing were not complete, the depth of the cusp would be strongly dependent on the degree of mixing. With the partial isospin mixing formalism of Grimes et al. (1972), Fowler showed that KGHFP calculations performed with an isospin mixing parameter equal to 0.4 reproduced the observed excitation function quite well.

Because of the ambiguities in the causes of reduced competition cusps, several proton-induced reactions predicted to show substantial

competition effects and the associated (p,n) reactions were studied: $^{51}V(p,\gamma)^{52}Cr$, $^{51}V(p,n)^{51}Cr$ (Zyskind 1977 and 1979a), $^{54}Cr(p,\gamma)^{55}Mn$, $^{54}Cr(p,n)^{54}Mn$ (Zyskind 1978), $^{68}Zn(p,\gamma)^{69}Ga$, $^{68}Zn(p,\alpha)^{65}Cu$, and $^{68}Zn(p,n)^{68}Ga$ (Esat 1977 and 1979). These reactions and studies of $^{65}Cu(p,\gamma)^{66}Zn$ and $^{65}Cu(p,\alpha)^{62}Ni$ (Switkowski 1978a and 1978b) confirmed that while the early calculations (Woosley 1975) were quite successful in predicting where threshold effects would be found, they consistently predicted the magnitudes of the drops in the cross sections at thresholds to be larger than those actually observed by factors ranging from three to ten. As noted above, it was found to be possible to reproduce the observed threshold effects in proton capture reactions either by using a value of 0.4 for the isospin mixing parameter (Zyskind 1977), or by modifying the KGHFP by including width fluctuation corrections in the Tepel approximation, and correcting the black nucleus strength function for the effects of size resonances (Zyskind 1978). Since threshold effects in (α,γ) reactions are insensitive to isospin effects, and to decide between these alternatives, we studied the $^{37}Cl(\alpha,\gamma)^{41}K$, $^{62}Ni(\alpha,\gamma)^{66}Zn$ and $^{64}Ni(\alpha,\gamma)^{68}Zn$ reactions for which prominent competition effects were predicted (Woosley 1975), and the associated $^{62}Ni(\alpha,n)^{65}Zn$ and $^{64}Ni(\alpha,n)^{67}Zn$ reactions (Davidson 1977 and Zyskind 1979b). Again, the threshold effects were found to be smaller than those predicted by at least a factor of three, and to be much better reproduced by calculations employing width fluctuation corrections and, in the case of the KGHFP, empirical neutron strength functions reflecting the effects of size resonances. Similar results were found for the $^{68}Zn(p,\alpha)^{65}Cu$ reaction, for which the

magnitude of the competition effects is also relatively insensitive to isospin effects. These results and other considerations have led to the conclusion that the isospin mixing is effectively complete and isospin effects can therefore be ignored in the excitation region of the present work. In contrast, width fluctuation corrections and realistic neutron strength functions have been shown to be important, and these are included in current versions of the nuclear reaction models.

The $^{48}Ca(p,\gamma)^{49}Sc$ reaction, which was predicted to have a prominent competition cusp, plays a role in the nucleosynthesis of neutron-rich, intermediate mass nuclei during explosive carbon burning (Clayton 1974). To determine the reaction rates for this reaction and the competing $^{48}Ca(p,n)^{48}Sc$ reaction, and to test the reaction models for a very neutron-rich, doubly magic target with a very low neutron threshold, cross sections were measured for these reactions (Zyskind 1979c).

CHAPTER II

EXPERIMENTAL PROCEDURES, DATA ANALYSIS, AND RESULTS

A. Reactions Studied and Target Chambers

Absolute cross sections were measured for the fourteen reactions involving competition effects listed in Table I. Also given in the table are the Q-values, neutron thresholds, and energy ranges studied for each reaction. Proton and helium ion beams produced by the ONR-CIT tandem Van de Graaff accelerator were delivered to the all-metal target chamber mounted on the "south 20°" beam line, as shown in Figure 2, for most reactions. The stainless steel chamber with copper gaskets was pumped by an ion pump and isolated from the accelerator vacuum system by an in-line, liquid-nitrogen cold trap (Dyer 1974). This set-up minimized the deposition of carbon during bombardment, an especially serious source of contamination for α-particle-induced reactions because of the positive Q-value and large cross section of the $^{13}C(\alpha,n)^{16}O$ reaction. Secondary electron emission from the target was suppressed by applying a bias of +300V to the target, which was electrically isolated from the chamber. For the measurements of the $^{51}V(p,\gamma)^{52}Cr$, $^{51}V(p,n)^{51}Cr$, $^{68}Zn(p,\gamma)^{69}Ga$, $^{68}Zn(p,n)^{68}Ga$, and $^{37}Cl(\alpha,\gamma)^{41}K$ cross sections, the experimental configuration was similar except that the target chamber consisted of a glass tee mounted on the center beam line. For the last three reactions the targets were water cooled because of their low melting points, and secondary electrons were suppressed by placing a -300 V bias on an aluminum ring surrounding the stem of the glass tee 2 cm upstream of the target. The configuration for the $^{68}Zn(p,\alpha)^{65}Cu$ measurements, which were carried out in the scattering chamber on the center beam line, is shown

in Figure 3.

The ^{54}Cr target was mounted with its surface at an angle of 51° to the beam direction. The ^{68}Zn target used in the (p,γ) and (p,n) measurements and the ^{37}Cl target were mounted with their surfaces at an angle of 45° to the beam direction. Targets for the other measurements were oriented with their surfaces normal to the beam.

B. Target Fabrication

Most of the targets consisted of layers deposited by vacuum evaporation on either tantalum or tungsten backings of thicknesses ranging from 5 to 20 thousandths of an inch. The ^{68}Zn transmission target used in the measurements of the $^{68}Zn(p,\alpha)^{65}Cu$ reaction was deposited on a thin carbon foil. To facilitate comparison of the measured cross sections with Hauser-Feshbach calculations, the target layer should be sufficiently thick that the beam energy loss in traversing the layer is great enough to average over many compound nuclear resonances. Where possible, the thicknesses of the targets for proton induced reactions were about 1 mg/cm^2, and for α-particle induced reactions about 0.25 mg/cm^2. In some cases this was not possible because of difficulties in target manufacture. For the transmission target used in the study of the $^{68}Zn(p,\alpha)^{65}Cu$ reaction, the thickness was limited by the requirement that the outgoing α-groups be resolved.

Enriched isotopes were used for all except the vanadium (natural vanadium is 99.75% ^{51}V) targets. The isotopic enrichments of the target materials are given in Table II. The natural vanadium and isotopically enriched nickel isotopes (obtained from ORNL Separated Isotopes Division) were available in metallic form, and were evaporated from standard open

tungsten and tantalum boats to make the targets. The enriched ^{54}Cr and ^{68}Zn were obtained in the chemical form of oxides and the ^{48}Ca in the form of calcium carbonate (all from the same source). When heated, the calcium carbonate decomposes into volatile CO_2 and CaO, so the calcium is also in the form of an oxide. These oxides are generally not convenient materials to evaporate because of their very high melting points. The elimination of the oxygen can be accomplished by heating the oxide in the presence of a suitable reducing agent; however, such reactions often proceed at very high temperatures and occur with such violence that unless performed in a closed vessel, the materials are spewed all over. This problem was solved by carrying out the reduction and evaporation in a baffled tantalum boat of the type shown in Figure 4. The load placed in the boat consisted of the oxide of the material to be evaporated (or the carbonate in the case of the calcium) mixed with a powder of the reducing agent (tantalum filings for the reduction of the CaO, and carbon for the ZnO and Cr_2O_3). The boat was then heated resistively. When the boat attained a white heat the reduction proceeded and left TaO in the boat or emitted volatile CO_2 as the reduced, metallic target material was evaporated onto the target backing placed over the chimney. Even with the protection provided by the boat's baffles, if the temperature was held at too high a level and the reduction and evaporation carried out too quickly, chunks were emitted from the chimney. The directionality of the emission from the chimney had the advantage of conserving target material, but the disadvantage of increasing the variation in target thickness over the surface of the target.

The enriched chlorine was obtained in the form of NaCl. Because of its low atomic number, the sodium would have constituted a most serious contaminant. Consequently the targets were made from $PbCl_2$. This was produced by combining the NaCl in an aqueous solution with $PbNO_3$, from which the $PbCl_2$ precipitated. The precipitate was rinsed six times in distilled water, chilled to minimize the $PbCl_2$ solubility. Each rinse was centrifuged and the supernatant liquid poured off to eliminate the $NaNO_3$. The $PbCl_2$ was finally dried, and the target was made by evaporating this material from a conventional open boat.

C. Determinations of Target Thicknesses

Thicknesses were measured for a number of targets by weighing. However, this method was not deemed satisfactory for targets made using enclosed boats because of the variation in thickness across their surfaces. The use of backscattering techniques (Snyder 1950, Brown 1951, Chu 1978) permitted the target thickness profile to be determined. The configuration for these measurements was similar to that shown in Figure 3 for the $^{68}Zn(p,\alpha)^{65}Cu$ measurements, except that, for the backscattering on the targets with thick backings, the beam current was collected from the target rod. Figures 5 and 6 show spectra obtained for the backscattering of 3 MeV protons on a ^{54}Cr target, and of 3.7 MeV α-particles on a vanadium target, respectively. These spectra are dominated by the steps arising from particles Rutherford scattered from the high atomic number backing materials. Superposed on this is the bump arising from elastic scattering from the target layer material.

The target thicknesses were extracted from such data in two ways. For the earlier backscattering measurements, the thickness was obtained

from the shift in the location of the thick target step of particles backscattered by the backing material caused by beam energy loss in the target layer. The process of scattering from the bare backing is shown schematically in Figure 7a. The energy of the scattered particles, E_E, is given by

$$E_E = kE_A \tag{II.1}$$

where k is a constant of proportionality, sometimes called the scattering factor, depending on the scattering angle $\theta_S = \theta_A + \theta_E$ and target and projectile masses, but independent of energy (Chu 1978). The scattering from the backing when a target layer is present is shown in Figure 7b. In this case, the measured energy of particles scattered from the backing material is

$$E_E = k\left(E_A - \int_A^C \frac{dE}{dx}\, dx\right) - \int_C^E \frac{dE}{dx}\, dx \tag{II.2}$$

where dE/dx is evaluated at each point for the appropriate energy resulting from previous energy losses due to passage through the target layer and, for the scattered particles, scattering from the surface of the backing. For the targets used in the present work it was sufficiently accurate to evaluate the energy losses using two values of dE/dx which were constant for the paths ABC and CDE evaluated at the target centered energies E_B and E_D. With this approximation, the target thickness T can be obtained from the observed shift in the scattering edge, S , using the relation

$$S = kE_A - E_E = T\left[\frac{k}{\cos\theta_A}\left(\frac{dE}{dx}\right)_B + \frac{1}{\cos\theta_E}\left(\frac{dE}{dx}\right)_D\right] \qquad \text{(II.3)}$$

The above method is not satisfactory in cases where a significant but unknown fraction of the mass in the target layer may consist of substances other than the target material. There was reason to believe this might be the case for the ^{48}Ca target. Its thickness was therefore determined by comparing the yield of α-particles scattered from the Ca to the height of the step resulting from α-particles scattered from the surface of the backing. This is illustrated in Figure 7c. The thickness of the target layer, T_t, in units of mass, is given by

$$T_t = \frac{N_t}{H_b}\frac{A_t}{A_b}\frac{\sigma_b(E_C)}{\sigma_t(E_{eff})}\Delta T_b \qquad \text{(II.4)}$$

In this expression N_t is the area of the α-particle group arising from particles scattered from the target layer; H_b is the height of the step corresponding to α-particles scattered from the surface of the backing; A_t and A_b are the atomic masses of the target and backing materials, respectively; $\sigma_b(E_C)$ and $\sigma_t(E_{eff})$ are the laboratory differential cross sections for Rutherford scattering of α-particles on the backing and target materials, respectively, evaluated at the appropriate energies; and ΔT_b is defined as shown in Figure 7c as the thickness of a layer of backing material such that α-particles scattered from its surface (point C) and its back (point C') after traversing the overlying target layer differ in energy upon their reemergence from the target layer by an energy dE/dn, the energy per channel in the backscattering spectrum. The cross section $\sigma_t(E_{eff})$ is given by the approximation of Chu et al. (1978) for the

average of the Rutherford cross section over a finite interval

$$\sigma(E_{eff}) = \sigma(E_A) \frac{1}{1 - \frac{\Delta E_{AC}}{E_A}} \qquad \text{(II.5)}$$

where $\Delta E_{AC} = E_A - E_C$. The energy E_C is evaluated using methods similar to those used to determine the target thickness from the shift in the backscattering edge. The method of comparing the Rutherford yields from the target layer and the backing has the advantage that it is not sensitive to contaminants in the target layer which give rise to α-particle groups which are resolved from that arising from scattering on the target material. In comparing the two yields, the solid angle and the integrated beam cancel out. Where this method was used to determine the target thickness, it was established that the elastic scattering was essentially Rutherford by checking that its excitation curve was proportional to the inverse square of the effective bombarding energy.

The target thicknesses adopted and the methods by which they were determined are given in Table 2. The ^{54}Cr, ^{62}Ni, ^{68}Zn, and ^{48}Ca targets were also weighed. Because of the large variations of target thickness over the surfaces of these targets, it was necessary to use the information obtained from the backscattering profiles of target thickness to determine the value at the beam spot. This nonuniformity also complicates comparison of the results from weighing and backscattering, but, except for the Ca target discussed below, the two methods appeared to be in good agreement. The vanadium target used in the cross section measurements was weighed, but was too thick for backscattering measurements. To insure that

there was no large amount of oxygen present in the target, cross sections were measured for the $^{51}V(p,\gamma)^{52}Cr$ reaction for $1.76 \leq E_p \leq 2.00$ MeV using a thinner target. The thickness of this target was measured to be 190 $\mu gm/cm^2$ of vanadium by comparison of Rutherford yields from the backing and target layer. These cross sections agreed with those determined using the thicker target to within 6%. The normalization found with the thinner target was adopted.

The thickness of the ^{48}Ca target was also measured at various times by weighing and by measuring the shift of the backscattering edge. The latter measurements include contributions from whatever oxygen and carbon is on the target as well as the calcium. The monotonic increase with time of the thicknesses measured in these two ways, and the values of these thicknesses indicate that, in spite of storing and transporting the targets under argon, the calcium became oxidized and eventually turned to $CaCO_3$. The various thickness measurements indicate that it is an excellent approximation to assume that the composition of the target was CaO during the experiment. Uncertainty in this assumption about the target composition introduces no uncertainty in the measured cross sections, and only a very small uncertainty in the effective bombarding energies.

D. Gamma-Ray Detection

Gamma-rays were detected with a 73 cc Ge(Li) detector placed either at 55° or at 125° to the beam direction, generally at distances between 2 and 10 cm from the target. In some cases a few mm of lead shielding was placed over the detector face to attenuate prolific, low energy γ-rays. Details of the detection geometries for the individual experiments are

given in Table 3. The detector efficiencies were calibrated for each experiment by using radioactive sources placed in the target position and resonances in the $^{27}Al(p,\gamma)^{28}Si$ reaction. Absolute calibrations were performed with ^{22}Na source number 7956, the activity of which was 4.56 ± 0.05 μCi on 2 February 1969. The calibration of this source was checked against other absolutely calibrated ^{22}Na and ^{60}Co sources from Amersham and Isotopes Products Laboratory, and the various calibrations were found to be in agreement to within a few percent. Except for the $^{68}Zn(p,\gamma)^{69}Ga$ measurements, the relative efficiency of the Ge(Li) detector as a function of γ-ray energy was determined by using a ^{56}Co source, and the 2.046 and 1.800 MeV resonances in the $^{27}Al(p,\gamma)^{28}Si$ reaction, for which the γ-ray energies and relative intensities are given in Table 4. A typical efficiency curve is shown in Figure 9. For the $^{68}Zn(p,\gamma)^{69}Ga$ measurements, there were γ-rays of interest with energies of 319 and 574 keV; in addition to the above sources and reactions, the relative efficiency was extended to lower energies by using ^{182}Ta, ^{207}Bi, and ^{226}Ra sources, and checked with an absolutely calibrated ^{133}Ba source. A relative efficiency curve for such low energy γ-rays is shown in Figure 8. The γ-ray energies and relative intensities used in compiling this curve are given in Table 4.

At bombarding energies below neutron thresholds, the γ-ray spectra were typically dominated by lines originating from the decay of low-lying excited states in the compound nucleus. For example, the $^{51}V(p,\gamma)^{52}Cr$ spectrum for $E_p = 1.9$ MeV, shown in Figure 10, is dominated by the 1.43 MeV line from the decay of the first excited state of ^{52}Cr. As the

bombarding energy is increased the quality of the spectrum deteriorates slowly as the yields increase for γ-rays from inelastic scattering and decay of excited states populated by neutron emission. This is illustrated in the spectrum shown in Figure 11 for a bombarding energy of 3.75 MeV, which is dominated by lines from decay of excited states of ^{51}Cr and ^{51}V. These problems were most severe for low energy γ-rays and extended to γ-rays of higher and higher energy as the bombarding energy was increased. For most reactions the highest energy at which γ-ray cross sections could be measured was determined by the point at which these background problems prevented extraction of reliable areas for the peaks of interest.

Dead-time corrections typically ranged from less than 1% below the neutron threshold to a maximum of about 20% at the highest bombarding energies.

To check the accuracy of the γ-ray cross section measurements, the absolute strength of the 2.046 MeV resonance in ^{27}Al(p,γ)^{28}Si was measured to be 22 ± 4 eV, in good agreement with other reported values (Kennedy 1977).

E. Analysis of Gamma-Ray Data

Cross sections for producing individual γ-rays were determined from the areas extracted from the Ge(Li) spectra by assuming an angular distribution of the form $a_0+a_2P_2(\cos\theta)$. To check this assumption, angular distributions for the 1.43 MeV γ-ray produced in the ^{51}V(p,γ)^{52}Cr reaction were measured at bombarding energies of 1.5, 2.25, and 3.0 MeV. No deviations from the form $a_0+a_2P_2(\cos\theta)$ greater than the precision of the measurements (∿ 2%) was observed. To obtain the total cross sections for (p,γ) or (α,γ) reactions, it is necessary to add the cross sections for

the production of individual γ-rays in such a way that each cascade is counted once, and only once. The method developed to accomplish this is illustrated in the following discussion for the $^{54}Cr(p,\gamma)^{55}Mn$ reaction, which includes essentially all of the complications which were encountered in other cases.

For $E_p < 3.2$ MeV it was possible to extract areas for individual γ-rays resulting from the decay of excited states in ^{55}Mn to either the ground state or the 126 keV first excited state. Their energies are given in the two columns of Table 5 headed "excitation function." The two most prolific γ-rays were the 1529 and 2565 keV lines, the excitation functions of which are shown in Figures 19 and 20. At no bombarding energy was it possible to observe the 126 keV γ-ray arising from the decay of the first excited state. A preliminary total (p,γ) cross section was determined by adding up the cross sections for producing the individual γ-rays. In this sum the cross sections for the 858 and 1885 keV γ-rays were multiplied by weighting factors of 1.05 and 1.56, respectively, to allow for the known branching ratios for unobserved transitions from the 984 keV state to the ground state and from the 1885 keV state to the first excited state. For $E_p > 3.2$ MeV, reliable peak area extractions were only possible for the seven γ-rays whose energies are given in Table 6 for that range of bombarding energies. The cross sections for these γ-rays were then added, with a weighting factor of 1.56 for the 1885 keV line. This sum was then multiplied by 1.14 to normalize to the sum of the thirteen cross sections used for $E_p < 3.2$ MeV, to obtain the preliminary total (p,γ) cross sections for $E_p > 3.2$ MeV. The normalization factor was determined by taking the average of the ratios of the two sums for proton energies running from

2.646 to 3.152 MeV; the small standard deviation of 0.01 reflects the fact that the ratio remained relatively constant over this range; this is not surprising since many different cascades are included in each sum and averages are taken over many compound nuclear resonances.

The preliminary cross section determination described above considers only decays which pass through the twelve excited states for which γ-decays are shown in Table 5 under the heading "excitation functions." Other decays may be treated in two groups: (i) γ_0 and γ_1 decays, those proceeding via primary γ-transitions from the capture state in the compound nucleus directly to the ground and first excited states, respectively, and (ii) other cascades not passing through the 12 states, the decays of which give rise to the 13 γ-rays used in determining the preliminary cross sections. For all other reactions studied, the group (i) decays included only γ_0 decays. From several long runs of the $^{54}Cr(p,\gamma)^{55}Mn$ reaction, γ-ray spectra were obtained over the proton energy range from 1.4 to 2.8 MeV with sufficiently good statistical precision to permit the observation of primary transitions. From these we found it necessary to increase the preliminary $^{54}Cr(p,\gamma)^{55}Mn$ cross sections by an average of 10% to allow for group (i) decays.

The group (ii) γ-rays arise from decays directly to the ground state (and to the 126 keV first excited state as well, in the case of the $^{54}Cr(p,\gamma)^{55}Mn$ reaction) of excited states in the compound nucleus (other than the capture state) which are not populated sufficiently strongly to give statistically significant peaks in the individual run spectra. An average relative intensity of group (ii) transitions was determined by analyzing sums of spectra from large numbers of runs, which improves the

statistical significance of the peak areas. The major γ-rays observed in this manner are shown in Table 5 in the columns headed "cross section." It was found necessary to increase the preliminary cross sections by 18% to allow for the average intensity of group (ii) transitions. No strong systematic variations of these corrections with bombarding energy were present.

The preliminary cross sections were therefore multiplied by a factor of 1.27 to include the effects of group (i) and group (ii) transitions. Because of the many compound nuclear resonances averaged over for each data point, the many decay modes included in these corrections, the absence of pronounced systematic variations with energy, and the small size of the correction compared with the uncorrected preliminary cross sections, the above procedure should provide a satisfactory determination of the total $^{54}Cr(p,\gamma)^{55}Mn$ cross sections. The resulting cross sections are shown in Figure 21.

Similar methods were used in the determination of the total cross sections for the other (p,γ) and (α,γ) reactions studied. Figures 12-18 provide information on decays in the compound nuclei involved. In Table 6, the relevant facts for the cross section determinations for each reaction are summarized. For the $^{68}Zn(p,\gamma)^{69}Ga$ reaction the primary γ_0 lines could be seen for many bombarding energies, and the necessary correction was found to decrease systematically from 8% of the preliminary cross section to 1% as the bombarding energy was increased. For the $^{62}Ni(\alpha,\gamma)^{66}Zn$ reaction, the γ_0 line was also observed at many bombarding energies but no systematic trends were apparent. The cross sections resulting from such

analyses are shown in Figures 21 through 27 and listed in Tables 7 through 13. The error bars shown represent counting statistics only and, except for the $^{48}Ca(p,\gamma)^{49}Sc$ excitation function, are indicated whenever larger than the data points. For all experiments, the reproducibility of the measurements was checked at many energies and found to be within the statistical precision of the number of counts. It is estimated that uncertainties in the overall normalization of the cross sections do not exceed 21%; this is the sum in quadrature of uncertainties in relative detector efficiency (5%), absolute Ge(Li) efficiency due primarily to geometrical effects (10%), charge collection (5%), target thickness (10%), angular distribution effects (10%), target composition (3%), and correction to the preliminary cross sections for weak branches (10%).

For low bombarding energies, and in the region of the neutron thresholds, the cross sections depend very strongly (and nonlinearly) on the bombarding energy; therefore, the shift of the effective energy from the target-centered value was evaluated by a method suggested by Barnes and described in Mak, Ashery, and Barnes (1974). The corrected effective energies typically differed from the target-centered energies by no more than 5 or 10 keV at the lowest energies, and at the higher energies when this difference became less than 1 or 2 keV the target-centered energies were used. It is estimated that the combined uncertainties in the effective incident energy, arising from all causes do not exceed 8 keV for the (α,γ) reactions, 6 keV for the $^{68}Zn(p,\gamma)^{69}Ga$ data, and 4 keV for the other (p,γ) reactions studied. In the energy region studied for these reactions, the cross sections vary sufficiently slowly with energy that these uncertainties

in effective bombarding energies are not serious. For example, it is in the energy range between 0.8 and 2.1 MeV that $^{48}Ca(p,\gamma)^{49}Sc$ and $^{48}Ca(p,n)^{48}Sc$ cross sections are needed for calculation of thermonuclear reaction rates at astrophysically interesting temperatures of about 2×10^9 °K (see Appendix B). A shift of 4 keV in the energy scale for the $^{48}Ca(p,\gamma)^{49}Sc$ and $^{48}Ca(p,n)^{48}Sc$ data would have very little effect on the thermonuclear reaction rates. It is also often of interest to extrapolate cross sections to lower energies. The strongest energy dependences of the low-energy cross sections are factored out of the astrophysical S-factor

$$S = E\sigma(E)\ \exp(E_G^{1/2}/E^{1/2}) \qquad \text{(II.6)}$$

where

$$E_G^{1/2} = 0.98948\ Z_0 Z_1 A^{1/2}\ \text{MeV}^{1/2} \quad , \qquad \text{(II.7)}$$

E is the center-of-mass energy and A is the reduced mass in the incident channel. The uncertainties in the determination of the S-factor at the lowest bombarding energy provide a good indication of the uncertainties in extrapolating the experimental cross sections to lower energies. For the $^{48}Ca(p,\gamma)^{49}Sc$ reaction at $E_p^{lab} = 580$ keV, the 42% uncertainty in cross section gives rise to a 42% uncertainty in the S-factor, but the 4 keV uncertainty in the energy results in only a 7.5% uncertainty in the S-factor.

F. Neutron Detection

The neutrons were detected with a BF_3 "long counter." The geometries for the various experiments are given in Table 14. A schematic diagram of the BF_3 long counter is shown in Figure 28. The paraffin moderates the

neutrons so they may be detected by the BF_3 tube, which is mainly sensitive to thermal neutrons. The efficiency for a counter based on the same design as that used in this experiment, at 1 m from the neutron source, has been found to rise by about 15% from the efficiency for 23 keV neutrons to a plateau response level by the time neutron energies have attained 2.2 MeV, and to fall by about 5% as the neutron energy rises further to 5 MeV (Allen 1960). Because of their short thermalization distance, low energy neutrons have a greater probability to diffuse out of the front face of the paraffin and this is one reason for the lower efficiency for detection of low energy neutrons. The holes in the front face of the paraffin improve the low energy response. The fall-off for high neutron energies arises in large part from a decrease in the effective solid angle of the detector as neutron energy is increased. This occurs because the BF_3 long counter behaves as a detector with a solid angle proportional to the inverse square of its effective distance from the source, $r+r_0$,

$$\Omega \propto \frac{1}{(r+r_0)^2} \qquad \text{(II.8)}$$

where r is the distance from the source to the detector face, and r_0 is a mean thermalization distance for the neutrons, which does not depend on r. It does, however, increase with increasing neutron energy because higher energy neutrons require a greater distance to become thermalized. Values for r_0 found by different investigators vary, but generally rise from about 0.8 cm for 25 keV neutrons up to about 6 cm for neutrons of 5 MeV (Allen 1960). For the experiments reported here, as bombarding energies are raised, the neutron energies rise and new neutron groups

appear as neutron thresholds are crossed. For counting neutrons with such a complex, unknown spectrum, which changes from one bombarding energy to another, the flat response of the long counter is very attractive.

The efficiency of the BF_3 long counter used in these experiments was measured by comparing the number of neutrons counted from several (p,n) reactions with the absolute intensities of γ-rays arising from the decays of the radioactive residual nuclei. In these measurements, the γ-rays from the activity of interest remaining from earlier bombardments were counted with the beam off from time t_{ri} to time t_{rf} (the result is the residual activity, n_r); then the targets were bombarded from time t_{bi} to time t_{bf}, and neutrons were counted by the BF_3 long counter (the result is n_n). Finally, with the beam off, the γ-rays from the activity produced were counted from time t_{ai} to time t_{af} (with result n_a). This procedure is illustrated in Figure 29. The efficiency for detecting neutrons is then given by

$$\varepsilon_n = \varepsilon_\gamma \frac{n_n}{KB_\gamma(n_a - n_b)} \qquad \text{(II.9)}$$

where n_b is the number of γ-rays detected during the time interval (t_{ai},t_{af}) arising from the activity already present before the bombardment began at t_{bi};

$$n_b = n_r\, e^{-\lambda_d(t_{ai}-t_{ri})} \frac{1 - e^{-\lambda_d(t_{af}-t_{ai})}}{1 - e^{-\lambda_d(t_{rf}-t_{ri})}} \quad ;$$

and $\frac{1}{K}$ is the fraction of all (p,n) residual nuclei formed during the bombardment interval (t_{bi},t_{bf}) which decay during the activation counting interval (t_{ai},t_{af}):

$$K = \frac{\lambda_d(t_{bf}-t_{bi})}{[1-e^{-\lambda_d(t_{bf}-t_{bi})}]} \quad \frac{1}{e^{+\lambda_d(t_{ai}-t_{bf})}[1-e^{-\lambda_d(t_{af}-t_{ai})}]}; \qquad \text{(II.11)}$$

B_γ is the fraction of the decays which result in production of the γ-ray which is counted; λ_d is the decay rate of the radioactive (p,n) residual nucleus:

$$\lambda_d = 1/\tau_d \qquad \text{(II.12)}$$

where τ_d is its mean life; and ε_γ is the efficiency for the Ge(Li) detector to detect γ-rays of interest in the detection geometry. Three reactions, $^{48}Ca(p,n)^{48}Sc$, $^{68}Zn(p,n)^{68}Ga$, and $^{51}V(p,n)^{51}Cr$, were used to insure that no errors were likely to arise from mistakes in the branching ratios. The decay rates, λ_d, from the resulting activities, the energies of the γ-rays detected, and their branching ratios, B_γ, are given in Table 14. The efficiency of the 100 cc Ge(Li) detector used to detect the γ-rays was calibrated by using radioactive sources as described in Section D of this chapter.

The results of the various efficiency measurements are listed in Table 14. That for $^{68}Zn(p,n)^{68}Ga$ is the average of results found for the three bombarding energies listed. The efficiency was measured in several geometries distinguished by different distances from the neutron source to the long counter. The measurements for the three different reactions using the activation technique are all in good agreement with one another. Measurements of the efficiency with an Am-Be source yielded about 40% lower efficiencies, but this is probably explained by the smaller effective solid angle which the long counter presents for the neutrons from the Am-Be

source, these neutrons having an average energy of about 5 MeV. An effect of this kind of about 10% has been reported previously for measurements made with a neutron source 1 m from a similar long counter. For the present geometry, with the source 27 cm from the long counter, the difference in efficiency for detecting low energy neutrons produced from the (p,n) reactions and the higher energy neutrons produced by the Am-Be source is estimated to be about 40% as observed. The efficiency for detecting neutrons for experiments where the target-to-long-counter distance did not coincide with any of the calibration geometries was determined by interpolating between the geometries for which the efficiency was measured by the activation technique by using the relation

$$\varepsilon_n(r) = \varepsilon(r_m)\left(\frac{r_m+r_0}{r+r_0}\right)^2 \qquad \text{(II.13)}$$

where r_m is a source to detector distance for which the efficiency was measured by the activation technique; $\varepsilon(r_m)$ is the efficiency measured in that geometry; and the value of r_0 is taken to be 2 cm, the value appropriate for neutrons of several hundred keV energy (Allen 1960).

Efficiency measurements were made with the $^{48}Ca(p,n)^{48}Sc$ and $^{68}Zn(p,n)^{68}Ga$ reactions at a number of different bombarding energies, to test the flatness of the long counter response as the neutron spectrum changed. The results of these measurements are shown in Figure 30. The energy scale is the amount by which the center of mass energy of the beam at the target surface exceeds the neutron threshold for population of the ^{68}Ga ground state in the case of the $^{68}Zn(p,n)^{68}$ data, and the threshold for population of the 622 keV (3^+) third excited state of ^{48}Sc (which is

the effective threshold for neutron production because of the high spins of the lower lying states) in the case of the $^{48}Ca(p,n)^{48}Sc$ data. The error bars are statistical only. The various neutron thresholds in the relevant energy ranges are indicated to give an idea of the complexity of the spectra. The $^{68}Zn(p,n)^{68}Ga$ data show that, for the range of neutron spectra resulting from the first MeV above threshold, the long counter response is quite flat. The $^{48}Ca(p,n)^{48}Sc$ data shown in Figure 29 indicate that the response continues to be quite flat, perhaps decreasing from 5 to 10% by 2.7 MeV above the effective threshold. Based on these measurements, it was assumed that the long counter efficiency is essentially independent of the amount by which the bombarding energy exceeds the neutron threshold over the limited range of the present experiments. The greater flatness of the low energy response and the faster falloff of the response at higher neutron energies, than reported in Allen's article (1960), may arise from differences in the long counters used. But the differences may also arise from the greater influence of the energy dependence of r_0 on the effective solid angle in the geometries used in our work, with the long counter 27 cm or 42 cm from the neutron source. In the work reported by Allen (1960) the long counter was 100 cm from the neutron source.

G. Analysis of Neutron Data

The measured excitation functions for the reactions studied are shown in Figures 31 through 36. In determining the angle-integrated absolute cross sections, any departures from isotropy in the angular distributions, which were expected to be small, were ignored. In

measurements of angular distributions for $^{51}V(p,n)^{51}Cr$ at proton energies of 2.25 and 3.00 MeV, deviations at other angles from the neutron yield at 90° were less than 10%. These results are consistent with the work of Schiffer and Lee (1958), who found that for (p,n) reactions on targets in the mass range with which we are dealing, anisotropies are less than 20%. To eliminate counts arising from sources other than neutrons produced by the reaction of interest, a background was subtracted. In most cases it was sufficient to make a linear extrapolation of the cross sections measured below the neutron threshold. This background generally had little effect except at energies immediately above threshold. For example, the extrapolated background for $^{54}Cr(p,n)^{54}Mn$ (E_{th} = 2.199 MeV) amounted to 40% of the detected neutrons at an effective bombarding energy of 2.225 MeV, 9% at 2.253 MeV, 4% at 2.293 MeV, and decreased rapidly in importance thereafter. For the $^{48}Ca(p,n)^{48}Sc$ data, contributions from contaminants were severe below the 1.157 MeV threshold for the 3^+ ^{48}Sc state. At E_p = 1.1 MeV, the background comprises 40% of the counts, and the data for this and lower energies are very uncertain because of this background subtraction. At E_p = 1.183 MeV the background comprises only 9% of the counts and decreases rapidly in importance for higher energies. For the $^{62}Ni(\alpha,n)^{65}Zn$ data (E_{th} = 6.901 MeV) the background corrections amounted to 32% at 7.00 MeV, 15% at 7.15 MeV, 11% at 7.30 MeV, and decreased in importance at higher energies. Yields were measured for bombardments of a bare backing at several energies to confirm that the contributions to the background arising from sources other than contaminants in the evaporated target layer could be adequately approximated by assuming a linear energy dependence. For the $^{64}Ni(\alpha,n)^{67}Zn$ data (E_{th} = 5.169 MeV), the background was somewhat larger, and was determined by comparing excitation functions measured for bombardments of a ^{64}Ni target and of a backing which was prepared

simultaneously and in the same manner but did not have a ^{64}Ni layer evaporated onto it. The resulting corrections amount to 86% at an effective bombarding energy of 5.46 MeV, 14% at 5.66 MeV, and 9% at 5.86 MeV.

As for the γ-ray data, the effective energies given are those found from the e-folding technique of Mak, Ashery, and Barnes (1974), where the resultant effective energies differ from the target-centered energy by more than a few keV, and by the target-centered energy when they do not.

When the energy of the beam before striking the target, E_b, exceeds the lowest neutron threshold energy, E_{th}, but by an amount less than the amount of energy the beam loses in traversing the target layer, ΔE, both the effective energy and the cross section determination must reflect this fact. For such runs, the effective energy is calculated assuming a target thickness which is only the fraction $(E_b-E_{th})/\Delta E$ as great as its actual value. Similarly, this effective target thickness has also been used in the cross section determination for such near-threshold runs. The error bars for such points reflect the additional uncertainty in target thickness arising from the assumed 5 keV uncertainty in the bombarding energy, E_b, as well as the statistical counting errors.

The uncertainties in the overall normalization of the absolute cross sections for the neutron data are estimated to be about 21%, the sources of error being similar to those for the γ-ray data.

H. Detection of α-Particles and Data Analysis for $^{68}Zn(p,\alpha)^{65}Cu$ Measurements

Alpha-particles were detected with two silicon surface barrier detectors, both at 160°, with Ta apertures defining a solid angle of

16.8 mster for each detector. The spectrum in Figure 37 shows the α_0 group and the elastic proton group. The cross sections were normalized to the elastic proton yield at 3.36 MeV, which was determined to arise from Rutherford scattering by checking the predicted $1/E^2$ dependence of the elastic scattering excitation function. Angular distributions of the α_0 groups were measured at 4.030 MeV, 4.48 MeV, and 4.975 MeV, and were found to show no anisotropies greater than 15%. Departures from anisotropy were therefore ignored in determining the absolute angle integrated cross sections. These are given in Figure 38 and Table 22.

The energy steps taken in this excitation function were either 40 keV or 20 keV. The smaller energy steps were taken from 3.8 to 4.3 MeV, the region encompassing the major features of the excitation function, i.e., the threshold effects and the isobaric analog resonance at 4.1 MeV. The beam energy loss in the target ranged from 7 keV down to 5 keV, depending on the bombarding energy. Although it was necessary to use energy steps larger than the beam energy loss in the target for reasons of time, the widths of the major interesting features of the excitation function were greater than the energy steps. Because the beam energy loss in the target layer was so small, the bombarding energies were not corrected for target thickness.

For all runs the dead time corrections amounted to less than 10%, and for most runs did not exceed 5%. The uncertainties in the overall normalization of the absolute cross sections do not exceed 20%, the sum in quadrature of uncertainties in the solid angle (5%), charge integration (5%), target thickness (5%), and angular distribution effects (15%).

CHAPTER III

THEORY AND DISCUSSION

A. Summary of the Data

Cross sections were measured for fourteen charged particle induced reactions: seven radiative capture reactions, one (p,α) reaction, and six neutron producing reactions. These are listed in Table 1. For all reactions studied, the energy ranges over which the cross sections were measured were restricted to energies below the Coulomb barriers, and the excitation functions characteristically rise with energy as the barrier penetration becomes greater. For the capture and (p,α) reactions the energy ranges included the lowest threshold for neutron production as well as a number of the subsequent thresholds. The excitation functions shown in Figures 19-27 and 38 show that, at these neutron thresholds, the increase in cross section with bombarding energy is interrupted, in most cases by a drop in cross section by a factor of three to five as the energy increases above the first neutron threshold ($^{51}V(p,\gamma)^{52}Cr$, $^{54}Cr(p,\gamma)^{55}Mn$, $^{37}Cl(\alpha,\gamma)^{41}K$, $^{62}Ni(\alpha,\gamma)^{66}Zn$, and $^{64}Ni(\alpha,\gamma)^{68}Zn$).

In some cases the effects are not as straightforward: for $^{48}Ca(p,\gamma)^{49}Sc$ the cross sections appear unaffected by the first three neutron thresholds and only cease to increase, but still do not drop significantly above the fourth threshold; for $^{68}Zn(p,\gamma)^{69}Ga$ the drop occurs mainly after the second threshold and, for $^{68}Zn(p,\alpha)^{65}Cu$, the drop is smaller and also occurs mainly after the second threshold. The case of $^{48}Ca(p,\gamma)^{49}Sc$ will be dealt with in some detail in Appendix B, where it is shown how such threshold effects can be understood.

For some of the reactions for which the excitation functions do show large drops above the first neutron threshold, there are additional features in the excitation functions which appear to correspond to higher neutron thresholds. For example, in the $^{51}V(p,\gamma)^{52}Cr$ excitation function, after the drop occasioned by the first (p,n) threshold at E_p = 1.56 MeV, the cross section rises again as the energy increases from 1.8 to 2.5 MeV. At 2.5 MeV the excitation function ceases to rise with increasing energy; then, at 2.9 MeV, the cross sections begin to fall again with increasing energy. These features at 2.5 and 2.9 MeV are attributed to competition effects at thresholds for populating excited states in ^{51}Cr by neutron emission, and will be discussed later.

While, in most cases, the target thicknesses and energy steps were too large to see the resonances corresponding to individual compound nucleus states, narrow resonances are visible in many of the excitation functions for proton induced reactions. These are isobaric analog resonances ($T^>$ states) and are so indicated in the figures.

In similar studies of competition effects, the Melbourne group have measured absolute cross sections for the production of the 1529 and 2565 keV γ-rays in $^{54}Cr(p,\gamma)^{55}Mn$ (Wilkinson 1978) and for the $^{48}Ca(p,\gamma)^{49}Sc$ and $^{48}Ca(p,n)^{48}Sc$ reactions (Kennett 1979). Their $^{54}Cr(p,\gamma)^{55}Mn$ results agree with the data presented in this thesis to within 10%. For the proton-induced reactions on ^{48}Ca the comparison is complicated by the fluctuations in the cross sections and the difference in target thicknesses (their target was about one-fifth as thick as ours). However, a careful comparison indicates that their cross sections are in good agreement with the Caltech data, although the Melbourne data tend to be greater than our data

by about 15% for both the $^{48}Ca(p,\gamma)^{49}Sc$ and $^{48}Ca(p,n)^{48}Sc$ reactions. This is well within the combined uncertainties of the cross section determinations of the two sets of measurements.

The $^{48}Ca(p,n)^{48}Sc$ cross sections measured by de Waal et al. (1971) are a factor of two lower than the Caltech data. The measurements by the Bhabha group of the $^{54}Cr(p,n)^{54}Mn$ (Kailas 1975) and $^{51}V(p,n)^{51}Cr$ (Mehta 1977) cross sections are generally 25 to 30% higher than our data, which is within the estimated uncertainties, for proton energies below 3 MeV, but rise faster above 3 MeV. By E_p = 3.5 MeV their data are approximately 60% higher than our data. The $^{51}V(p,n)^{51}Cr$ cross sections of Mehta et al. (1977) are twice as great by the time the bombarding energy reaches 4 MeV.

There have also been a number of experimental studies of isobaric analog resonances in the reaction $^{51}V(p,\gamma)^{52}Cr$ (Teranishi 1966, Price 1972, Roy 1974, Faini 1973), $^{54}Cr(p,\gamma)^{55}Mn$ (Peters 1973), $^{54}Cr(p,n)^{54}Mn$ (Moses 1971a and 1971b), $^{68}Zn(p,n)^{68}Ga$ (Vourvopoulos 1966 and Egan 1970), and $^{48}Ca(p,\gamma)^{49}Sc$ (Chasman 1967, Vingiani 1968, Struve 1973, and Adachi 1973). These studies were concerned mainly with studying the location and decay properties of the analog resonances, and are of interest in the present work mainly for identifying the analog resonances appearing in our excitation functions. Dubois et al. (1966) have also measured the $^{48}Ca(p,\gamma)^{49}Sc$ excitation function for $800 < E_p < 1400$ keV, but did not measure absolute cross sections.

In summary, the data presented in this thesis are in good agreement with the Melbourne data for the $^{54}Cr(p,\gamma)^{55}Mn$, $^{48}Ca(p,\gamma)^{49}Sc$, and

$^{48}Ca(p,n)^{48}Sc$ reactions, but are in disagreement with data published by other groups for the $^{48}Ca(p,n)^{48}Sc$, $^{51}V(p,n)^{51}Cr$, and $^{54}Cr(p,n)^{54}Mn$ reactions. From the information presented in these papers it is not possible to determine the origin of the discrepancies; however, in the work presented here considerable care was taken to insure that the absolute cross sections were correctly determined, and in what follows it will be assumed that this was done successfully.

B. Theory

(i) Competition and Global Hauser-Feshbach Models

In Figures 21-27, 31-36, and 38 the experimental data are compared with theoretical curves representing calculations for current versions of two global Hauser-Feshbach models: the Kellogg global Hauser-Feshbach program (called KGHFP) (Zimmerman 1977) and the HAUSER*4 code (Mann 1976).

To permit comparison with the experimental data, we have in some cases plotted $\langle\sigma(E_{eff})\rangle_{\Delta E}$ instead of plotting the theoretical cross sections, $\sigma(E)$. $\langle\sigma(E_{eff})\rangle_{\Delta E}$ is the cross section averaged over an energy interval ΔE, corresponding to the beam energy loss in the target, centered at E_c and weighted by the reciprocal of the stopping cross section, $\varepsilon(E)$:

$$\langle\sigma(E_{eff})\rangle_{\Delta E} = \frac{\int_{E_c-\frac{\Delta E}{2}}^{E_c+\frac{\Delta E}{2}} \frac{\sigma(E)}{\varepsilon(E)}\, dE}{\int_{E_c-\frac{\Delta E}{2}}^{E_c+\frac{\Delta E}{2}} \frac{dE}{\varepsilon(E)}}$$

As for the experimental data, the effective energy to which this cross section is assigned is obtained from ΔE, E_c, and the theoretical excitation function from the e-folding criterion of Mak, Ashery, and Barnes. The latter procedure was carried out only for the $^{51}V(p,\gamma)^{52}Cr$ reaction and the three (α,γ) reactions. For other reactions it had no significant effect.

The calculated curves are generally in good agreement with the data and, in particular, they reproduce quite accurately the features of the excitation functions attributed to competition effects. Such competition effects can be understood in terms of the Hauser-Feshbach reaction model, and they provide stringent tests of the models. The studies reported in this thesis and by others (Mann 1975c, Switkowski 1978a and 1978b) concerned with competition effects have led to several refinements in the global Hauser-Feshbach models. To elucidate how the competition effects are predicted by and serve as tests of the global Hauser-Feshbach models, we shall discuss the models and the competition-related refinements with special attention to their treatment of the competition effects for the $^{51}V(p,\gamma)^{52}Cr$ reaction.

The Hauser-Feshbach formula for the energy-averaged cross section for the reaction A(a,b)B is (Hauser 1952)

$$\langle\sigma_{ab}\rangle = \sigma_{ab}^{HF}(E_a) = \frac{\pi\lambda\!\!\!^{-2}_a}{(2S_a+1)(2S_A+1)} \sum_{J,\Pi} (2J+1) \frac{T_a(J,\Pi)T_b(J,\Pi)}{\sum_c T_c(J,\Pi)} \qquad \text{(III.1)}$$

In this expression, E_a is the center of mass energy for the incident channel, a; $\lambda\!\!\!^{-}_a$ is the corresponding reduced wavelength; S_a is the

projectile spin, and S_A is the target spin for channel a. The transmission functions, $T_c(J,\Pi)$, are the total transmission functions for the decay of the compound states of spin J and parity Π into the pair c+C; these will be discussed in the next subsection (ii). Excited states of C must be included.

For compound nuclear states which can emit s-wave neutrons, the neutron transmission function generally will quickly dominate the other terms in the denominator of equation (III.1) above the neutron threshold. Thus the cross sections for the weaker competing channels will decrease above the neutron threshold. The effects can be quite dramatic as in the case of the $^{51}V(p,\gamma)^{52}Cr$ data of the present work. Because the ^{51}V target and the ^{51}Cr ground state both have the same spin and parity ($7/2^-$), compound states which are formed by s-wave protons can decay by emission of s-wave neutrons above the first neutron threshold (E_p^{lab} = 1.56 MeV), and a substantial competition cusp results. The features at 2.7 and 3.0 MeV result from neutron competition when the neutron thresholds are crossed for populating the 1165 keV $9/2^-$ and 1480 keV $11/2^-$ excited states of ^{51}Cr, respectively. These states can be formed by s-wave neutron decay of the compound states formed by d-wave protons. Such considerations are discussed in detail for the reaction $^{48}Ca(p,\gamma)^{49}Sc$ in Appendix B.

Although the calculations of Woosley et al. (1975) using an earlier version of the KGHFP successfully predicted where these competition effects could be found, the magnitude of the drop in the cross section above the neutron threshold was consistently overpredicted by a factor of three to five for the proton-induced reactions studied (Mann 1975c, Switkowski 1978a and 1978b, Zyskind 1978, and Esat 1977). The basic HAUSER*4 model

also overpredicted the depth of the competition cusps, though not as severely.

Several effects, which were not originally included in the models, have been suggested to explain this discrepancy: (i) width fluctuation corrections (Mann 1975c), (ii) size resonances (which are not included in the black nucleus strength functions used in the equivalent square well models of KGHFP), and (iii) partial isospin mixing in the compound nuclear states (Fowler 1976). After presenting the basic models in subsection (ii) we will discuss in subsections (iii) to (v) the role of each of these effects in the global Hauser-Feshbach models and their treatment of the competition.

(ii) Transmission Functions

Transmission functions for each partial wave, in each particle channel, T_{ℓ_c}, are calculated from the optical potential as a function of channel energy. These are combined to obtain the transmission function for the decay of the compound nucleus states of spin J and parity Π into the pair $c+C^{\lambda}$, where the residual nucleus, C, is left in the excited state, λ, of excitation energy E_C^{λ}, spin S_C^{λ}, and parity $^{\lambda}_{C}$. The result is

$$T_c^{\lambda}(J,\Pi;E_{\lambda c}) = \sum_{\ell_c, s_c} T_{\ell_c}(E_{\lambda c}) \qquad \text{(III.2)}$$

The sum runs over all combinations of ℓ_c and s_c which can couple with $(S_C^{\lambda},\Pi_C^{\lambda})$ to form a compound state of spin J and parity Π, where s_c is the channel spin resulting from coupling S_C and s_c. The appropriate channel energy is

$$E_{\lambda c} = E_a + Q_{ac} - E_C^{\lambda} \qquad \text{(III.3)}$$

where E_a is the channel energy in the incident channel, a+A, and Q_{ac} is the Q-value for the reaction A(a,c)C. To obtain $T_c(J,\Pi)$, the total transmission function for the decay of (J,Π) compound states into the pair c+C, the transmission functions for each final state in channel c must be added:

$$T_c(J,\Pi) = \sum_{\lambda=1}^{N} T_c^{\lambda}(J,\Pi;E_{\lambda c}) + \int_{S_C^{\lambda},\Pi_C^{\lambda}} \int_{E_C^N}^{\infty} \rho(E_C^{\lambda},S_C^{\lambda},\Pi_C^{\lambda})\ T_c(J,\Pi,E_{\lambda c})\ dE_C^{\lambda}\, dS_C^{\lambda}\, d\Pi_C^{\lambda} \qquad \text{(III.4)}$$

The level density formula $\rho(E_C^{\lambda};S_C^{\lambda},\Pi_C^{\lambda})$ estimates the number of states at excitation energies above the energy E_C^N of the highest discrete state known. The level density term has been omitted in the calculations discussed here. Because discrete-level information is included for ^{51}Cr states up to an excitation energy of 2256 keV, the omission of the level density term is not significant.

In all cases, discrete level information for residual nuclei in charged particle channels was included for energies high enough that transmission functions for populating higher states will be negligibly small. For the neutron channel, discrete level information was included for most states which could be populated at the highest bombarding energies. For example, discrete level information for the ^{51}Cr nucleus produced in the $^{51}V(p,n)^{51}Cr$ reaction is included up to an excitation energy of 2256 keV. The threshold for this state occurs at a proton bombarding energy of 3.86 MeV, and the effects of higher ^{51}Cr levels are expected to be unimportant even at the highest bombarding energy

(4.47 MeV).

The major difference in approach between the two global models with which we are concerned lies in the method of calculating the particle transmission functions from the optical model. The HAUSER*4 program of Mann (1976) starts from an optical potential, the form of which is determined from optical model analyses of broad ranges of elastic scattering data. The general form of the potential is

$$V(r) = Uf(r,R_U,a_U) + i\,W_v f(r,R_v,a_v) + i\,W_s g(r,R_s,a_s)\ , \qquad \text{(III.5)}$$

where

$$f(r,R,a) = \frac{1}{1+\exp[(r-R)/a]} \quad \Rightarrow \tfrac{1}{2} \text{ when } r = R \qquad \text{(III.6)}$$

is the Woods-Saxon form factor with radius R and surface diffuseness parameter a, and

$$g(r,R,a) = 4a\frac{d}{dr} f(r,R,a) = \frac{4\exp(\frac{r-R}{a})}{[1+\exp(\frac{r-R}{a})]^2} \qquad \text{(III.7)}$$

$$\Rightarrow 1 \text{ when } r = R$$

is the derivative Woods-Saxon form factor representing surface absorption. The coefficients of, and the radius and diffuseness parameters for the various terms in the neutron optical potential are those found in the global optical model analyses of elastic scattering differential cross sections and total reaction cross sections carried out by Wilmore and Hodgson (1964). For protons, the optical model parameters of Bechetti and Greenlees (1969) were used. The α-particle optical model parameters are those adopted by Mann (1975a) based on the work of McFadden and Satchler (1966). The neutron, proton and α-particle optical model

parameters are shown in Table 23.

The transmission functions are calculated from the scattering solutions to the radial Schrödinger equations of the appropriate orbital angular momentum, with the centrifugal and Coulomb potentials added to the optical potential, either from the complex phase shifts, δ_ℓ,

$$T_\ell = 1 - |\exp 2i\delta_\ell|^2 \qquad \text{(III.8)}$$

for $T_\ell > 10^{-4}$, or by integrating the square of the wave function weighted by the imaginary part of the potential

$$T_\ell = \int_0^\infty |\psi|^2 [W_v f(r,R_v,a_v) + W_s\, g(r,R_s,a_s)]\, r^2\, dr \qquad \text{(III.9)}$$

for $T_\ell < 10^{-4}$ (Mann 1975b).

The KGHFP model, on the other hand, is based on calculating transmission functions from the equivalent square well representation of the optical potential (Vogt 1962 and 1968, Michaud, Scherk, and Vogt 1970a, and Michaud and Fowler 1970b), which has the advantage that the transmission functions are given by analytic expressions. This is a very important feature in a global model for which computing economy is necessary in order that it be feasible to carry out the large number of cross section calculations necessary. Michaud, Scherk, and Vogt (1970) formulated a prescription by which an "equivalent" square well potential of the form

$$V(r) = \begin{cases} V_o + iW_o & r < R \\ 0 & r > R \end{cases} \qquad \text{(III.10)}$$

can be constructed for any diffuse-edged Woods-Saxon potential. The transmission functions of the square well are identical to those of the

diffuse well with respect to the absorption, barrier penetration and their resonant properties. The difference is that, because of the sharp interface at r=R in the square well, waves are reflected much more strongly than by a diffuse well. It has been found, however, that the greater reflectivity of square wells is almost energy-independent, and can be corrected for by an energy-independent reflection factor, f. When the square well transmission function is multiplied by f, the result is equal to the diffuse well transmission functions. In an equivalent square well potential with a diffuseness parameter a = 0.5 fm, the reflection factor is f = 2.7 for nucleons and f = 4.8 for alpha particles (Michaud 1970b).

The square well transmission functions are given by (Moldauer 1969)

$$T_\ell = 1 - \exp\ (-\tau_\ell), \qquad \text{(III.11)}$$

where

$$\tau_\ell = 4\pi f P_\ell s_\ell \quad . \qquad \text{(III.12)}$$

P_ℓ is the barrier penetrability, and s_ℓ is the strength function

$$s_\ell = \frac{1}{\pi} \sum_p \frac{\gamma_{\ell p}^2 W_o}{(E_{\ell p}-E)^2 + W_o^2} \quad , \qquad \text{(III.13)}$$

which is a sum of contributions from single particle states (Michaud 1970a) (also termed size resonances) at energy $E_{\ell p}$ and reduced width $\gamma_{\ell p}^2$. The s_ℓ may be evaluated analytically using the properties of spherical Bessel functions without the extensive computation necessary for numerical solution of the Schrodinger equation.

For the KGHFP model, the calculations were further simplified, for computing economy, by replacing the square well strength functions by

the black nucleus strength functions. The black nucleus functions have no dependence on energy or nuclear mass, and average over the size resonances. The choice of radius and depth of the equivalent square well are unaffected by the use of black nucleus strength functions, and the reflection factors are also unaffected (Michaud 1970a).

The well depth, V_0, and the radius, R_0, for the Woods-Saxon well to which the constructed square well is made equivalent, are a well-depth of 50 MeV for nucleons and 60 MeV for α-particles, and a radius of $1.25A^{1/3}$ fm for nucleons and $1.09A^{1/3}+ 1.6$ fm for α-particles, where A is the target mass. The radius of the equivalent square well, R_1, equals $R_0 + 0.1$ fm for nucleons and $R_0 + 0.7$ fm for α-particles. The depth of the equivalent square well is $V_0(R_0/R_1)^2$.

For both Hauser-Feshbach models, the γ-ray transmission functions are calculated by employing a giant dipole form for the E1 strength function, and a single-particle estimate for the M1 transitions, following the prescription of Holmes et al. (1976a).

(iii) Width Fluctuation Corrections

With the aid of computer experiments, considerable progress has been made recently in confirming that, for a random matrix model of the S-matrix, the energy-averaged compound nucleus cross sections can be accurately calculated from the Hauser-Feshbach expression if it is modified to include the so-called width fluctuation corrections (Tepel 1974, Moldauer 1975, and Hoffmann 1975a and 1975b). These correct primarily for the effects of channel-channel correlations. The corrected cross section takes the form

$$\langle \sigma_{ab} \rangle = \sigma_{ab}^{HF} W_{ab} = \frac{T_a T_b}{\sum_c T_c} W_{ab} \ , \qquad \text{(III.14)}$$

where σ_{ab}^{HF} is the usual Hauser-Feshbach cross section formula; and W_{ab} is the width fluctuation correction factor for channels a and b, having the form (Moldauer 1976)

$$W_{ab} = \left\langle \frac{\Gamma_{\lambda a} \Gamma_{\lambda b}}{\sum_c \Gamma_{\lambda c}} \right\rangle \frac{\langle \sum_c \Gamma_{\lambda c} \rangle_\lambda}{\langle \Gamma_{\lambda a} \rangle_\lambda \langle \Gamma_{\lambda b} \rangle_\lambda} \qquad \text{(III.15)}$$

The $\Gamma_{\lambda c}$ are the widths of compound states λ for the channels c, the brackets represent energy averages over the enclosed quantities, and the brackets with subscript λ are averages over the compound states. Moldauer (1975) has given a prescription for calculating W_{ab} based on averaging over the expected statistical distributions of the widths. Tepel et al. (1974) have found an approximation for W_{ab} which is much easier to use. They argued that the main effect of the width fluctuation correction is an enhancement of the elastic scattering which occurs because the amplitudes for incident and outgoing channels are then identical and hence fully correlated. They assume that the Bohr independence hypothesis is valid for inelastic channels, for which the cross section then resembles the normal Hauser-Feshbach expression, while for true elastic scattering in which all quantum numbers for the incident and outgoing channels are the same, the cross section is multiplied by the enhancement factor W_a (not to be confused with W_{ab}). Thus

$$\langle \sigma_{ab} \rangle = \frac{V_a V_b}{\sum_c V_c} \left[1 + \delta_{ab} (W_a - 1) \right] . \qquad \text{(III.16)}$$

The width-fluctuation-corrected transmission functions, V_a, are related to the usual optical model transmission functions, T_a, by the unitarity requirement,

$$T_a = \langle \sigma_a \rangle \equiv \sum_b \langle \sigma_{ab} \rangle \ . \qquad \text{(III.17)}$$

These equations may be solved for the V_a in terms of the T_a. One finds

$$V_a = T_a[1 + V_a(\sum_c V_c)^{-1} (W_a - 1)]^{-1} \ , \qquad \text{(III.18)}$$

which has a unique solution for the V_a's. If $W_a = 1$, $V_a = T_a$, and the normal Hauser-Feshbach expression results. Equation (III.18) can be solved by iteration, or approximated by substituting $T_a(\sum_c T_c)^{-1}$ for $V_a(\sum_c V_c)$, to obtain an expression for V_a in terms of the optical model transmission functions,

$$V_a = T_a[1 + T_a(\sum_c T_c)^{-1} (W_a - 1)]^{-1} \ . \qquad \text{(III.19)}$$

In numerical computer experiments W_a was found to be fitted by the expression (Tepel 1974)

$$W_a = 1 + 2 \ (1 + \sqrt{T_a})^{-1} \ . \qquad \text{(III.20)}$$

The width-fluctuation-corrected cross sections are obtained by substituting these width-fluctuation-corrected transmission functions into equation (III.16).

The width fluctuation corrections have a significant effect on the magnitude of the competition cusps. In order that flux be conserved, the

cross sections for inelastic channels are decreased to compensate for the enhancement in the elastic channel. The effect is greater for dominant channels (see eq. III.18), ranging from no effect when $T_a << \sum_c T_c$ up to a factor of two to three depletion as $T_a/\sum_c T_c$ approaches unity. Below the neutron threshold, where the proton and gamma ray channels are dominant, the calculation with width fluctuation corrections (curve S in Fig. 39) is lower than that without (curve A in Fig. 39) by as much as 30%. Above the neutron threshold, the neutron channel quickly becomes dominant, and the width fluctuation correction has the greatest effect on V_n and a small effect on V_p and V_γ. The magnitude of the drop in the $^{51}V(p,\gamma)^{52}Cr$ cross section above the threshold is approximately proportional to $(V_n + V_p + V_\gamma)/(V_p + V_\gamma) \simeq V_n/(V_p + V_\gamma)$ (see eq. III.16) and thus is smaller for the calculation with width fluctuation corrections. At higher energies, as more neutron channels open up, the width fluctuation corrections become less important.

Thus the inclusion of the width fluctuation corrections improves the fit of the calculations to the data significantly, and is therefore necessary for the accurate treatment of competition effects. Similar results have been observed in other proton-induced reactions in which competition effects are important (Mann 1975c, Switkowski 1978a and 1978b, Zyskind 1978 and 1979c). The width fluctuation correction has the greatest effect on the neutron transmission functions because the neutron channel is dominant, but, just because of this dominance, the (p,n) cross section is insensitive to the neutron transmission functions and thus to the effects of the width fluctuation corrections.

Moldauer (1976) has recently suggested that the Tepel approxima-

tion may be in error by as much as 10% for reactions in which both incident and exit channels have much smaller transmission functions than one or more dominant channels. In more recent work (Hoffmann 1975a and 1975b), it has been found that the Tepel approximation can be made more accurate by using an improved enhancement factor which has a weak dependence on $\sum_c T_c$, in addition to its dependence on T_a, and by iterating equation (III.18) once. The KGHFP has been modified recently to carry out the first iteration of equation (III.18). The resulting $^{51}V(p,\gamma)^{52}Cr$ cross sections do not differ from those obtained by applying equation (III.19) by more than 7% anywhere, and for most energies the difference is less than 1%.

(iv) Size Resonances

The black nucleus strength functions used in the equivalent square well models (Woosley 1975, Zimmerman 1977, and Holmes 1976a) are independent of nuclear mass, A, and channel energy, E. However, size resonances, with peaks at values of A for which single particle states occur at zero energy (Hodgson 1971), give rise to a strong dependence of the strength functions on A and E. Because the widths of the size resonances are about 10 MeV and the strength functions are most important at low energies where the transmission function is proportional to τ_ℓ (see eq. III.11 and III.12), the effect of the size resonances can be incorporated by using the values of the strength functions at low energy. Measured low energy neutron strength functions have been compiled for a large number of targets by Musgrove (1973). The ratio of the measured strength functions tabulated by Musgrove to the black nucleus values can

be determined by dividing the tabulated values by 2.4×10^{-4}.

The conversion factor is so much smaller than one because the compilation gives $\langle \Gamma/D \rangle_\ell$ evaluated at 1 eV; this is twice the penetrability evaluated at 1 eV times the true strength functions s_ℓ,

$$\left\langle \frac{\Gamma}{D} \right\rangle_\ell = 2P(1 \text{ eV})\ s_\ell \ . \qquad \text{(III.21)}$$

For cases where the strength functions have not been measured, they may be interpolated from the cases which have been measured. The strength functions for the ^{51}Cr+n system interpolated from those in Musgrove's table are 1.85 times the black nucleus strength functions for s-waves, and 0.09 times the black nucleus value for p-waves. This ratio is given for the other reactions studied in Table 24. The s-wave value is used for all even partial waves and the p-wave value for all odd partial waves. It should be noted that the ratio r of the neutron strength function to the black nucleus value is not a direct input to the KGHFP. Instead, this information is inserted into the calculation by adjusting the neutron reflection factor f_n. The ratios r may be deduced from values of f_n, where these are reported, by dividing f_n by 2.7. Thus the values of f_n employed are given by 0.9×10^4 times the strength function reported by Musgrove (1973).

The effect of employing realistic neutron strength functions on the treatment of the competition can be seen by comparing curves S and C in Figure 39. The drop in cross section at the (p,n) threshold is about a factor of two greater for curve C, which was calculated from the black nucleus strength functions, than for curve S because the p-wave transmission functions calculated from the realistic strength functions are about a

factor of 10 less than those calculated from the black nucleus strength functions. In this case, the competitition from p-wave neutrons is greatly reduced as compared with the predictions of the black nucleus strength function. As was the case for the width fluctuation corrections, the $^{51}V(p,n)^{51}Cr$ cross sections are much less sensitive to the neutron strength functions than the $^{51}V(p,\gamma)^{52}Cr$ cross sections because the neutron channel is dominant.

Much less is known about the proton strength functions. Figure 40 shows the effect of varying the proton strength functions. The effects are not great below the neutron threshold where the contrary variations of the odd-ℓ and even-ℓ strength functions tend to cancel. Above the neutron threshold the effects are more pronounced because of the competition. Because ^{51}Cr is about 20 to 25 mass units from the maximum at $A \simeq 75$ in the proton s-wave strength function (Schiffer 1958 and Elwyn 1966) at $A \simeq 75$, the appropriate curve is probably either curve S or F. Thus for the case of ^{51}V+p black nucleus strength functions for the protons are quite adequate; Figure 40 does show, however, that, especially where competitition effects are important, the difference between using black nucleus and realistic strength functions can be quite large. It may prove possible, with further analysis, to calculate more reliable proton strength functions from the available (very limited) experimental data on the locations of the size resonances, and by employing an optical model calculation to determine the variation of the strength functions with mass number.

Because of the closer size resonance spacing for the heavier alpha particle and the wider resonances resulting from the stronger

absorption, the size resonances overlap for α-particle induced reactions and the black nucleus strength functions should be a good approximation.

For the HAUSER*4 code, the correct strength functions result automatically from the optical model calculation of the transmission functions, if the optical model parameters are correct.

(v) Isospin Mixing

The basic global Hauser-Feshbach models described in subsections (i) and (ii) do not include isospin effects. There have been several treatments of partial isospin mixing between ground state isospin ($T^<$) states and analog ($T^>$) states in nuclear reactions occurring at sufficiently high excitation energy so that both overlap (e.g., Grimes 1972, Harney 1977, and other references in Lane 1978). By comparing these studies with one another and with the case where neither $T^<$ or $T^>$ states overlap, Lane (1978) has found a prescription which is applicable to the intermediate regime as well. The resulting cross section expression for the assumption of equal strength functions for both isospin channels is

$$\sigma_{ab} = \sigma^<_{ab} + \sigma^>_{ab} = \frac{(\beta^<_a + \mu\beta^>_a)(\beta^<_b + \mu\beta^>_b) T_a T_b}{\sum_c (\beta^<_c + \mu\beta^>_c) T_c} + (1-\mu) \frac{\beta^>_a \beta^>_b T_a T_b}{\sum_c \beta^>_c T_c} \quad . \qquad \text{(III.22)}$$

In this expression, T_c is the usual isospin-independent transmission function calculated from the optical model; $\beta^<_c$ and $\beta^>_c$ are the squares of the Clebsch-Gordan coefficients representing the appropriate isospin couplings and listed in Table 25; and μ is termed the isospin mixing parameter. The isospin mixing parameter satisfies the condition $0 \leq \mu \leq 1$, and is given by

$$\mu = \left\langle \frac{\Gamma_{>}^{\downarrow}}{\Gamma_{>}^{\uparrow} + \Gamma_{>}^{\downarrow}} \right\rangle \qquad \text{(III.23)}$$

where $\Gamma_{>}^{\downarrow}$ is the mixing width of a typical $T^{>}$ state into the surrounding $T^{<}$ states, and $\Gamma_{>}^{\uparrow}$ is the sum of the partial widths of the $T^{>}$ state for decay into particle and gamma-ray channels before being mixed into the $T^{<}$ states. Note that for every channel, c, $\beta_c^{<} + \beta_c^{>} = 1$, and for $\mu = 1$, $\sigma_{ab}^{>}$ vanishes and $\sigma_{ab}^{<}$ reduces to the usual Hauser-Feshbach expression, equation (III.1).

Values of μ ranging from 0.2 to 0.7, typically near 0.4, have been found at higher excitation energy from the value of the ratio $\sigma_{pp'}\sigma_{\alpha\alpha'}/\sigma_{p\alpha}\sigma_{\alpha p}$ (Harney 1977 and Lux 1977). If isospin mixing is not complete, the presence of $T^{>}$ states could have profound effects on the competition between (p,γ) and (p,n) reactions. The incoming proton can populate both $T^{>}$ and $T^{<}$ states, and states of both isospins may decay by γ-ray emission (see Table 25 and eq. III.22). But $\beta_n^{>} = 0$ and only the $T^{<}$ states may emit neutrons. So $\sigma_{p\gamma}^{<}$ is decreased by competition from the neutrons and $\sigma_{p\gamma}^{>}$ is not. For values of μ less than unity, the competition cusp is then less deep than if isospin is completely mixed ($\mu = 1$), and the depth of the drop after the cusp provides a measure of the degree of isospin mixing, as illustrated by the KGHFP calculations for several values of μ shown in Figure 41.

Because of the low analogue threshold (E_p = 0.763 MeV) and the relatively high density of analogue states (> 10/MeV) (Teranishi 1966), the effects on the competition of taking $\mu < 1$ should be very marked for the $^{51}V(p,\gamma)^{52}Cr$ reaction. Comparison of the calculated curves with the

experimental data (see Fig. 41) suggests that isospin is essentially completely mixed ($\mu = 1$). Similar conclusions can be drawn for other proton-induced reactions for which competition effects are important (Mann 1975c, Switkowski 1978a and 1978b, and Zyskind 1978 and 1979c). Findings that $\mu = 0.4$ for the reactions $^{64}Ni(p,\gamma)^{65}Cu$ (Fowler 1976) and $^{51}V(p,\gamma)^{52}Cr$ (Zyskind 1977) resulted from comparison of the experimental data with calculations performed before width fluctuation corrections and realistic neutron strength functions had been incorporated in the KGHFP.

The $^{37}Cl(\alpha,\gamma)^{41}K$, $^{62}Ni(\alpha,\gamma)^{66}Zn$ and $^{64}Ni(\alpha,\gamma)^{68}Zn$ reactions were studied to resolve this problem of the relative importance of isospin mixing, on the one hand, and width fluctuation corrections and realistic neutron strength functions, on the other. In α-induced reactions, $T^>$ states are not populated because $T = 0$ for ^4He, and it follows that $\sigma^>_{\alpha\gamma} = 0$ (see Table 25 and eq. III.22) and the value of μ has little effect on the shape of the excitation function. Thus the size of the drop in the cross sections at neutron thresholds for α-induced reactions can only be significantly affected by the treatment of width fluctuation corrections and the neutron strength functions. As for the (p,γ) reactions, the drop in cross section above the neutron threshold is generally predicted by the earlier calculations (Woosley 1975) to be a factor of three greater than observed experimentally. The calculations including width fluctuation corrections and realistic neutron strength functions are in much better agreement with the data than those made without these corrections. This indicates that it is necessary that the models include width fluctuation corrections and realistic neutron strength functions. With this

established, comparison of the calculations with experimental (p,γ) data indicates that isospin mixing is complete.

Our finding that μ = 1 is consistent with high resolution measurements of isobaric analogue resonances in intermediate mass nuclei. The mixing widths, $\Gamma_{>}^{\downarrow}$, deduced from these studies are typically of order 10 keV or greater (Bilpuch 1976 and Mekjian 1973), while the decay widths, $\Gamma_{>}^{\uparrow}$, are typically not more than about 1 keV.

The lower values of μ found from measurements of the ratio $\sigma_{pp'}\sigma_{\alpha\alpha'}/\sigma_{p\alpha}\sigma_{\alpha p}$ are valid for much higher excitation energies (Harney 1977 and Lux 1977). The particle decay widths for the analogue states are much greater at such high excitation energies, since many channel energies are well above the Coulomb and angular momentum barriers, and $\Gamma_{>}^{\uparrow}$ may become comparable to $\Gamma_{>}^{\downarrow}$.

If external mixing is neglected, $\sigma_{ab}^{<}$ with μ = 0 should be used below the analogue threshold, σ_{ab} with μ = 1 should be used for energies for which the analogue states are dense enough to be treated statistically, and a smooth transition from one prescription to the other should be made for intermediate energies. However, in cases where competition cusps are expected at low bombarding energies, i.e., cases with significant neutron excess, the ground state isospin, $T^{<}$, is usually greater than two. As a result $\beta^{>} < \beta^{<}$, and the difference between σ_{ab} and $\sigma_{ab}^{<}$ is small. For KGHFP calculations reported here, unless otherwise stated, σ_{ab} with μ = 1 was used, except for the ^{48}Ca+ p reactions for which $\sigma_{ab}^{<}$ with μ = 0 was used.

C. Summary and Conclusions

The preceding comparison of theory and experiment shows that studies of the competition effects at neutron thresholds, such as those reported in this thesis, are a powerful technique for testing global Hauser-Feshbach models. The competition effects were studied under a variety of circumstances: e.g., for a light target (^{37}Cl), for a doubly magic and extremely neutron-rich target (^{48}Ca), for a compound nucleus with a high density of analogue states near the neutron threshold (^{52}Cr produced by ^{51}V+p), and for both proton and α-particle projectiles. Several conclusions can be drawn from these studies: isospin mixing should be assumed to be essentially complete in the excitation region near the lower neutron thresholds; width fluctuation corrections should be included; and the KGHFP, which is based on an equivalent square well representation of the optical model with black nucleus strength functions, must be corrected with more realistic neutron strength functions such as those interpolated from the compilation of Musgrove (1973). Results of calculations carried out with such models are shown in Figures 21-27, 31-36, and 38. These calculations in general give very good representations of the experimental data. In particular, the predictions of the magnitude of the drop in cross sections resulting from competition effects are quite accurate and are much better than those of the earlier calculations of Woosley (1975). The comparison with experiment indicates that cross sections predicted by the newer global Hauser-Feshbach models are appropriate for calculating astrophysical reaction rates for use in nucleosynthesis calculations. This is illustrated by the ^{48}Ca(p,γ)^{49}Sc and ^{48}Ca(p,n)^{48}Sc reactions discussed in Appendix B, for

which the thermonuclear rates calculated from the KGHFP cross sections are in much better agreement with those calculated from the experimental cross sections than are the theoretical rates which were used in earlier studies of nucleosynthesis (Howard 1972). Thermonuclear reaction rates calculated from the earlier cross section calculations of Woosley et al. (1975) are in press (Woosley 1979). These cross section calculations have generally been found to be in error by a factor of three or more for exit channels competing with neutron emission. Errors in the thermonuclear reaction rates needed for astrophysical calculations will often not be as serious because of contributions to the rates from the region of energies below the neutron threshold. The magnitude of the drop in the $^{51}V(p,\gamma)^{52}Cr$ cross sections above the $^{51}V(p,n)^{51}Cr$ is correctly predicted by the current KGHFP calculations, but is predicted by the calculations of Woosley et al. (1975) to be more than a factor of three larger than experimentally observed. Nevertheless, the thermonuclear reaction rates calculated from these two sets of cross section calculations agree to within 20% for temperatures below 5×10^9°K. For extremely neutron rich species with low neutron thresholds, the disagreement will be more severe.

Several other cases, where the models are less successful, deserve to be singled out because the discrepancy with experiment may throw light on possible remaining problems in the theories. The worst performance of the theories is that of the KGHFP in the case of the three $^{68}Zn+p$ reactions studied. Below the (p,n) threshold, the (p,γ) and (p,α) cross sections, and above the threshold the (p,n) cross sections (Figures 23, 38, and 33, respectively) calculated by the KGHFP are too low by factors ranging from

1.5 to 3. This is perhaps because $^{68}Zn+p$ is near the proton size resonance at A = 70, and the neglect of the size resonances by the black nucleus strength functions of the KGHFP may result in a transmission function which is smaller than it should properly be. The competition effects are also predicted to be somewhat smaller than they are actually observed to be. This may result from the difficulty in choosing correct values for the neutron strength functions. Strength functions are listed in the compilation (Musgrove 1973) only for those cases for which experimental studies have been reported. But, for the (p,n) reactions we are interested in, the residual nuclei are radioactive; consequently the neutron strength functions have not been measured, and it is necessary to interpolate from those cases for which experimental studies have been reported. This is often difficult because of the sparseness of the strength function data and the fluctuations to which they are subject. This may also be the problem with the prediction of the size of the drops in cross section after the competition cusps in $^{62}Ni(\alpha,\gamma)^{66}Zn$ and $^{37}Cl(\alpha,\gamma)^{41}K$. For the latter reaction, in calculations performed with r = 0.1 for s- and p-wave neutrons (corresponding to $S(0) = S(1) = 0.25 \times 10^{-4}$ for the neutron strength functions as given by Musgrove), the fractional decrease is in agreement with the experimental data. Other sets of strength functions can also be found which will produce agreement. Although the strength functions which are interpolated from the compiled strength function data do not agree with the $^{37}Cl(\alpha,\gamma)^{41}K$ data, those which do agree with the $^{37}Cl(\alpha,\gamma)^{41}K$ data cannot be said to be inconsistent with the strength function data because of the impossibility of unambiguously interpolating the existing strength function data. In this connection, measurements of the $^{40}K+n$ strength

functions would be of great interest.

Finally, a word of warning must be added to the above considerations. A global model must be expected to be in error occasionally in predicting cross sections because it attempts to smooth over the fluctuations which occur in individual nuclei, especially for lighter nuclei where the statistical assumptions underlying the Hauser-Feshbach formula may be much less rigorously satisfied than for heavier species. It is only possible to be confident of conclusions which are based on a wide range of data. Such a situation is presented by the large and consistent discrepancy between the earlier Hauser-Feshbach calculations and the experimentally observed drops in cross sections resulting from competition; the greatly improved performance of the current models which have been altered to include width fluctuation corrections and, for the KGHFP, realistic neutron strength functions, clearly demonstrates the importance of including these effects in theoretical nuclear reaction models.

All in all, the performance of current global Hauser-Feshbach calculations represents a considerable advance over earlier theoretical calculations of reaction rates, as shown by the excellent agreement of the calculations with the data presented in this thesis.

APPENDIX A

A Cusp in the $^{54}Cr(p,\gamma)^{55}Mn$ Reaction

(Published in Nuclear Physics A301 (1978) 179)

2.A.1:
2.C

Nuclear Physics **A301** (1978) 179–188;

A CUSP IN THE $^{54}Cr(p, \gamma)^{55}Mn$ REACTION †

J. L. ZYSKIND††, J. M. DAVIDSON, M. T. ESAT, M. H. SHAPIRO††† and R. H. SPEAR‡

W. K. Kellogg Radiation Laboratory, California Institute of Technology, Pasadena, California 91125

Received 23 December 1977

Abstract: Absolute cross sections for the reactions $^{54}Cr(p, \gamma)^{55}Mn$ and $^{54}Cr(p, n)^{54}Mn$ are presented for effective bombarding energies E_p from 0.830 to 3.606 MeV. A substantial cusp is observed in the $^{54}Cr(p, \gamma)^{55}Mn$ excitation function. The data are compared with the predictions of global Hauser-Feshbach models in order to evaluate their applicability to nucleosynthesis calculations.

E NUCLEAR REACTIONS $^{54}Cr(p, \gamma)$, $^{54}Cr(p, n)$, $E = 0.83$ 3.61 MeV; measured $\sigma(E)$; Hauser-Feshbach calculation. Enriched target. Ge(Li) and BF_3 long counter.

1. Introduction

During explosive nucleosynthesis in supernovae, nuclei up to and beyond Fe are synthesized on a time scale too short for many of the nuclear reactions involved to attain statistical equilibrium; consequently the resulting elemental and isotopic abundances are determined by cross sections for over 500 reactions of importance [1]. Because of the impossibility of measuring all of these, some of which involve short-lived target nuclei or target nuclei in excited states, global Hauser-Feshbach codes have been developed by Woosley *et al.* [2] and Mann [3] to calculate the relevant cross sections. Such codes will also be useful in the prediction of radiation-damage effects in thermonuclear reactor design studies [4].

The energy averaged Wigner cusps [5–7] ‡‡ observed in some (p, γ) excitation functions on medium-mass nuclei provide an important test of the predictions of these codes. The cusps appear at the thresholds for neutron production where competition from neutron decay of the compound nucleus causes the excitation functions for γ-ray emission to drop sharply, giving them a cusp-like appearance. The ability to predict the size of this drop is crucial for the application of Hauser-Feshbach models to explosive nucleosynthesis. Not only does the magnitude of the cusp affect the absolute cross section of the reaction concerned, but it also provides a sensitive

† Supported in part by the National Science Foundation [PHY76-83685].
†† Fannie and John Hertz Foundation Fellow.
††† Permanent address: California State University, Fullerton, California 92634.
‡ On leave from Nuclear Physics Department, Australian National University, Canberra, Australia.
‡‡ Meyerhof [5] introduced the terminology "energy averaged Wigner cusps" in the reference cited. A. M. Lane has suggested privately that "level averaged" might be more appropriate. In what follows we use the single word "cusps".

test of the model's treatment of competition among the various channels and of other effects such as isospin mixing and level-width fluctuations.

The present paper describes a measurement of the excitation function of the reaction ^{54}Cr(p, γ)^{55}Mn in the region of the threshold for ^{54}Cr(p, n)^{54}Mn; this reaction is expected to display a substantial cusp [2].

2. Experimental procedures

Absolute cross sections for the reactions ^{54}Cr(p, γ)^{55}Mn and ^{54}Cr(p, n)^{54}Mn were measured in 50 keV steps for beam energies, E_b, from 0.9 to 3.7 MeV. A proton beam from the ONR-CIT tandem Van de Graaff accelerator was used to bombard a target of metallic Cr (enriched to 95.4% in ^{54}Cr)† mounted with its surface at an angle of 51° to the beam direction.

The target was prepared by heating a mixture of spectroscopically pure C and Cr_2O_3 in vacuum in a baffled Ta boat ††; the Cr_2O_3 was reduced and the Cr then evaporated onto a 254 μm thick W-backing. The target thickness was determined by weighing and by proton backscattering to be 1180 $\mu g \cdot cm^{-2}$, which corresponds to a beam energy loss of 130 keV at the (p, n) threshold for the target at 51°. Since the level density in ^{55}Mn at the excitation energies concerned is of the order of 2 keV^{-1}, this provides a statistical average over many resonances. The backscattering spectra showed that the target contained less than 3% by weight of oxygen. The target angle was determined by comparing the measured yields for three different γ-rays with their yields obtained with the target surface perpendicular to the beam direction. The target was mounted in an all-metal vacuum chamber pumped by an ion pump and isolated from the accelerator vacuum system by an in-line liquid-nitrogen cold trap [8]. The beam deposition of C was negligible. Secondary electron emission was suppressed by applying +300 V to the target, which was insulated from the chamber.

Gamma rays were detected using a 73 cm^3 Ge(Li) detector located at an angle of 55° to the beam direction, with its front face 2 cm from the target. The detector efficiency for γ-ray energies from 0.847 to 11.542 MeV was determined using the 2.046 and 1.800 MeV ^{27}Al(p, γ)^{28}Si resonances [9,10], a ^{56}Co source [9], and an absolutely calibrated ^{22}Na source placed at the reaction site. To check the accuracy of the γ-ray cross-section measurements, the absolute strength of the 2.046 MeV resonance in ^{27}Al(p, γ)^{28}Si was measured and found to be 22 ± 4 eV, in good agreement with other reported values [9].

Neutrons were detected with a BF_3 long counter located at a distance of 20 cm from the target at an angle of 30° to the beam direction. The counter efficiency was determined by comparing the number of neutrons counted from the reaction ^{48}Ca(p, n)^{48}Sc and the absolute intensity of 983 keV γ-rays (detected with a 100 cm^3 Ge(Li) detector) arising from the ^{48}Sc activity produced.

† Obtained from Separated Isotopes Division, Oak Ridge National Laboratory.

†† An SO-20 Silicon Monoxide Source obtained from R. D. Mathis Co. of Long Beach, California.

TABLE 1 181

^{55}Mn gamma rays employed in data analysis

E_x [a])	J^π [a])	Gamma-ray energy [a]) (keV)			
		excitation function		cross section	
		0	126	0	126
0	$\frac{5}{2}^-$				
126	$\frac{7}{2}^-$				
984	$(\frac{9}{2}^+)$		858		
1290	$(\frac{1}{2}^-)$				
1292	$(\frac{11}{2}^-)$			1290	1166
1293	$(\frac{5}{2}^-, \frac{9}{2}^+)$				
1529	$\frac{3}{2}^-$	1529			
1885	$(\frac{5}{2}^-, \frac{7}{2}^-)$	1885			
2199	$\frac{7}{2}^{(-)}$	2199			
2215	$(\frac{5}{2}^-, \frac{7}{2}^-)$			2215	
2253	$(\frac{1}{2}^-, \frac{3}{2}^-)$	2253			
2269	$(\frac{1}{2}^-, \frac{5}{2}^-)$	2269			
2312	$(\frac{1,3}{2}^-)$			2312	
2367	$\frac{5}{2}^-$	2367	2241		
2399	$(\frac{5}{2}^-, \frac{9}{2}^+)$				
2429	$\frac{1}{2}^+$			2429	
2565	$\frac{3}{2}^-$	2565			
2582				2589	2463 [b])
2727	$\frac{7}{2}^-$	2727			
2753	$(\frac{5}{2}^-, \frac{7}{2}^-)$			2753	2627
2823					
2825	$(\frac{5}{2}^-, \frac{9}{2}^+)$	2825			
2874				2874	
2952				2952	
2975		2975			
2990	$(\frac{3}{2}^-, \frac{5}{2}^-)^+$				
3004		3004			
3195				3195	
3351				3351	
3424					3298
3432				3432	
3528				3528	
3702				3702	
3860				3860	
3998	$(\frac{1}{2}^-, \frac{3}{2}^-)$			3998	
4293				4293	
4373				4373	
capture resonance				variable	variable

The first two columns identify by excitation energy, E_x, and spin and parity, J^π (when known), all confirmed states in ^{55}Mn with excitation energies less than 3 MeV, and higher states, the decays of which give rise to γ-rays employed in the data analysis. The third and fourth columns give γ-ray energies for decay to the ground state and 126 keV first excited state, respectively, for the thirteen γ-rays used to determine the excitation function. The fifth and sixth columns apply to other γ-rays used to determine the total cross sections as described in the text. Where no entry appears either no γ-ray was observed or it was not used in the analysis.

[a]) Ref. [11]).

[b]) Although their energies are inconsistent with those in ref. [11]), these two γ-rays were identified as arising from ^{55}Mn decay because of the 126 keV energy difference.

Dead-time corrections were negligible for the neutron system. For the γ-rays, they ranged from a few % below the neutron threshold to a maximum of about 20% at the highest bombarding energies.

3. Data analysis

3.1. GAMMA RAYS

The excitation functions for thirteen individual γ-rays from the residual nucleus ^{55}Mn were obtained using the full energy peak areas extracted from the γ-ray spectra by linear background subtraction. These γ-rays are identified in table 1 under the heading "excitation function".

Absolute cross sections were obtained for production of each γ-ray by assuming that the angular distributions are of the form $A_0 + A_2 P_2(\cos\theta)$. The two most prolific γ-rays were the 1529 and 2565 keV lines, the excitation functions of which

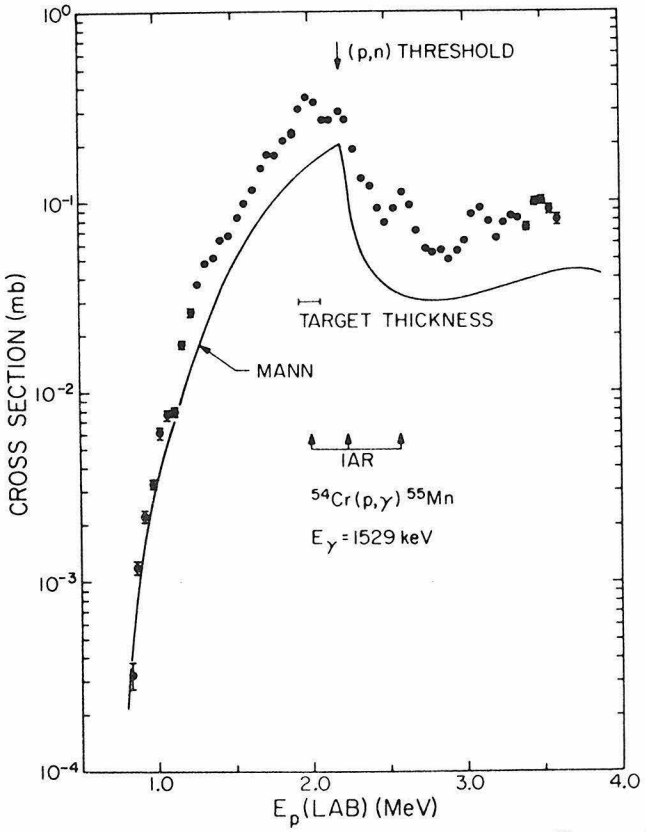

Fig. 1. Excitation function for production of 1529 keV γ-rays in the reaction ^{54}Cr(p, γ)^{55}Mn. Error bars shown are statistical only. The curve shows the results of a Hauser-Feshbach calculation performed using Mann's Code [3]). The arrows labelled IAR indicate proton energies for isobaric-analogue resonances which have been previously observed [20]).

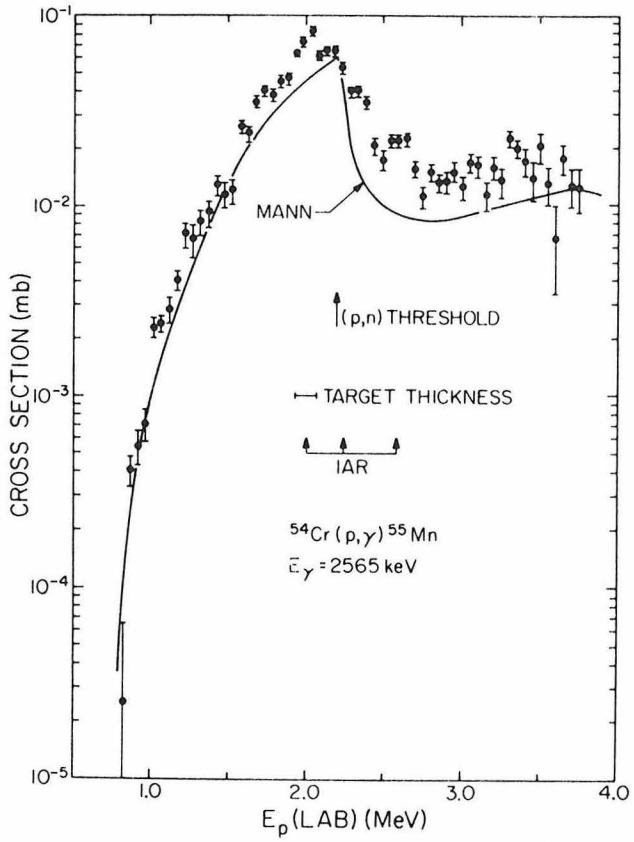

Fig. 2. Excitation function for production of 2565 keV γ-rays in the reaction $^{54}Cr(p, \gamma)^{55}Mn$. Error bars shown are statistical only. The curve shows the results of a Hauser-Feshbach calculation performed using Mann's code [3]). The arrows labelled IAR indicate proton energies for isobaric-analogue resonances which have been previously observed [20]).

are shown in figs. 1 and 2, respectively. Statistical errors are indicated wherever they are larger than the size of the data points. The reproducibility of the measurements was checked at many energies and found to be within statistics. It is estimated that systematic errors in the cross sections amount to about 20%; this is the quadratic sum of uncertainties in relative detector efficiency (5%), absolute efficiency due primarily to geometrical effects (10%), charge collection (2%), target thickness (10%), angular-distribution effects (10%) and target composition (3%).

To obtain the $^{54}Cr(p, \gamma)^{55}Mn$ cross section, we summed the cross sections for population of the twelve states, the decays of which give rise to the thirteen analyzed γ-rays. The cross sections for population of states with more than one decay mode were corrected, using published branching ratios [11]), for the decay modes not explicitly included in the above analysis. As the bombarding energy increased, it became more difficult to extract peak areas reliably because the spectra became more complex and the signal-to-noise ratio for the ^{55}Mn γ-ray lines deteriorated.

Consequently, for $E_p \geqq 3.2$ MeV, only the cross sections for populating the seven states of energies 1529, 1885, 2253, 2269, 2565, 2727 and 2975 keV were summed. This sum was then multiplied by a factor of 1.14 ± 0.01 to normalize to the sum of twelve cross sections. This factor was determined by taking the average of the ratios of the two sums for each of the spectra for proton energies from 2.646 to 3.152 MeV; the small standard deviation reflects the fact that the ratio remained relatively constant over this range; this is not surprising, since many decay modes are included in each sum and averages are taken over many resonances.

The cross section determination described above considers only decays which pass through the twelve states for which γ-decays are shown in table 1 under the heading "excitation function". Other decays may be treated in two groups: (i) decays proceeding via γ-transitions from the compound nucleus directly to the ground and first excited states, and (ii) other decays not passing through the twelve states. For group (i) decays only the primary γ-rays could be observed (the 126 keV decay of

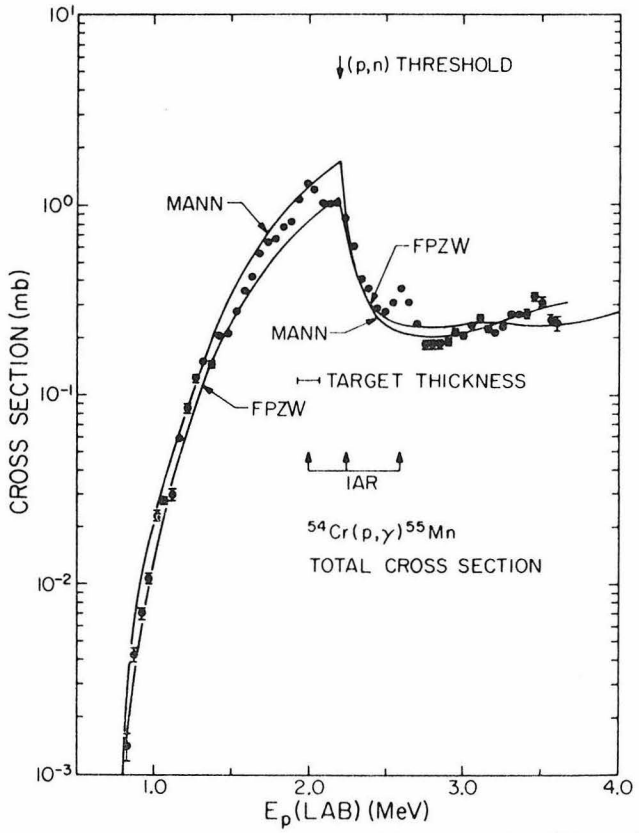

Fig. 3. Excitation function for all primary γ-rays emitted in the reaction $^{54}Cr(p, \gamma)^{55}Mn$. Error bars shown are statistical only. The curves show the results of Hauser-Feshbach calculations performed using the codes of Mann [3]) and Fowler *et al.* (FPZW) [18]). The arrows labelled IAR indicate proton energies for isobaric-analogue resonances which have been previously observed [20]).

the first excited state is swamped by Coulomb excitation and low energy tails from other γ-rays). Several spectra were obtained over the proton energy range from 1.4 to 2.8 MeV with sufficiently good statistics to permit the observation of primary transitions. From these we found that it was necessary to increase the cross section for the twelve states by $(10 \pm 4)\%$ to allow for group (i) decays.

The relative intensity of group (ii) transitions was determined by analyzing long runs and sums of runs. The major γ-rays observed in this manner are shown in table 1 in the columns headed "cross section". We increase the sum of twelve cross sections by $(18 \pm 4)\%$ to allow for group (ii) transitions. Thus, the overall normalization factor applied to the cross section in order to allow for transitions of groups (i) and (ii) is equal to 1.28 ± 0.06. Throughout this analysis care was taken to count each cascade once and only once. The total $^{54}Cr(p, \gamma)^{55}Mn$ cross section is plotted in fig. 3. It is estimated that the absolute accuracy of the total cross-section determination is about 25%.

The effective proton energies E_p shown in figs. 1–3 are target centered energies for $E_p \geqq 2.8$ MeV. For $E_p < 2.8$ MeV the cross section changes rapidly; therefore the shift of the effective energy from the target centered energy due to thick target effects was evaluated using the method described by Mak *et al.* [12]).

3.2. NEUTRONS

The $^{54}Cr(p, n)^{54}Mn$ excitation function is displayed in fig. 4. Absolute cross sections were determined by assuming that the neutron angular distributions are isotropic. Background corrections were estimated by extrapolating yields observed just below the threshold. These corrections amounted to 40% at 2.225 MeV, 9% at 2.253 MeV, 4% at 2.293 MeV, and rapidly decreased in importance thereafter.

For the first two runs above the (p, n) threshold, E_{th}, the amount by which the beam energy, E_b, exceeded E_{th} was less than the energy loss in the target, ΔE. Consequently, the target thickness used in computing the (p, n) cross sections for these runs was the measured target thickness multiplied by $(E_b - E_{th})/\Delta E$. The errors indicated for these two energies include the uncertainty in $(E_b - E_{th})/\Delta E$ as well as the statistical errors. For all other points the statistical errors are smaller than the data points.

A thick-target correction similar to that for the γ-ray data was applied to the bombarding energies for $E_p \leqq 2.444$ MeV. For $E_p > 2.444$ MeV target-centered energies were used.

We estimate that the uncertainty in the absolute cross sections is approximately 20%, the sources of error being similar to those described for the γ-ray data.

4. Discussion

The results of Hauser-Feshbach calculations performed using Mann's code Hauser 4 [ref. [3])] with a global optical-model parameter set are plotted in figs 1–4.

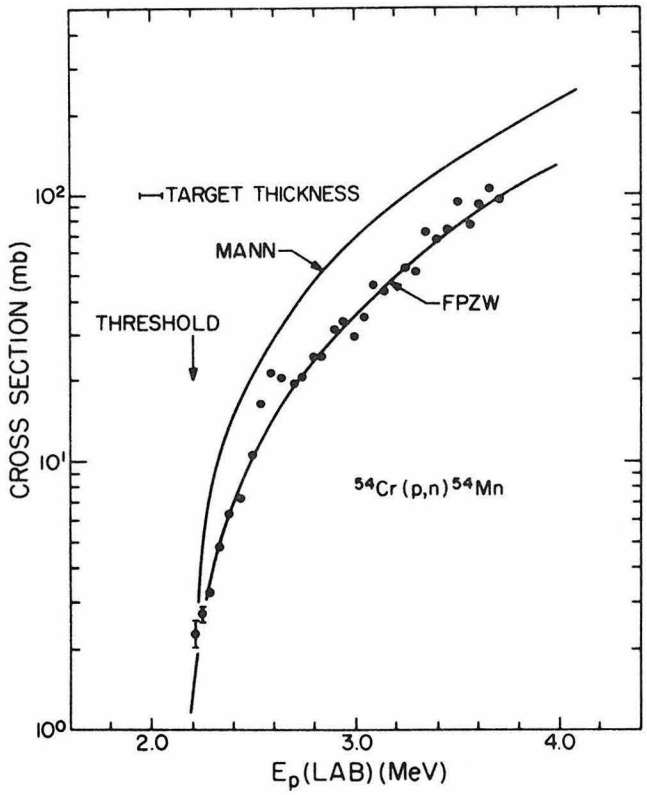

Fig. 4. Excitation function for the reaction ^{54}Cr(p, n)^{54}Mn. The error bars shown are discussed in the text. The curves show the results of Hauser-Feshbach calculations performed using the codes of Mann [3]) and of Fowler *et al.* (FPZW) [18]).

The neutron and proton transmission functions were calculated using optical-model parameters from Wilmore and Hodgson [13]) and from Bechetti and Greenlees [14]), respectively. The γ-ray transmission functions were calculated using a giant-dipole resonance form for the E1 strength function and a single-particle estimate for the M1 strength function [15]). Only dipole transitions were considered. The cross sections for production of 1529 and 2565 keV γ-rays were obtained using giant-dipole-resonance estimates (for E1) and single-particle estimates (for M1) to calculate the ratio of transitions populating the ground state and the excited state in question [16]). Width fluctuation corrections were included using the Tepel approximation [17]).

The results of Hauser-Feshbach calculations performed by Fowler *et al.* [18]) are plotted in figs. 3 and 4. An equivalent square-well representation of a Woods-Saxon potential was used to calculate the transmission functions as described in connection with earlier calculations in ref. [2]). The present calculations differ from those of ref. [2]) in two respects. Firstly, width fluctuation corrections are included using the Tepel approximation [17]). Secondly, the calculations of ref. [2]) used the average value of 2.7 for the equivalent square-well neutron reflection factor f, whereas the calcula-

tions of ref. [18]) allow for the effects of shape resonances by setting $f = 5$ for s-wave neutrons and $f = 0.25$ for p-wave neutrons, consistent with the low-energy neutron strength functions compiled by Musgrove [19]).

Four peaks are prominent in the experimental γ-ray excitation functions. These are at $E_p \approx 2.0$, 2.2, 2.6 and 3.1 MeV. The first three correspond fairly well to resonances which have been previously identified by Moses *et al.* [20]) as isobaric analogues of the ground, 242 and 565 keV states of ^{55}Cr. The resonance at $E_p = 3.1$ MeV has the correct energy to be the analogue of the 1135 keV state [11]). Both calculations considered in this paper ignore explicit isospin effects; they assume complete isospin mixing and equal strength functions in the $T^<$ and $T^>$ channels. Consequently, to compare the data with the calculations one should average out the excess cross section of the isobaric analogue resonances. This smoothing is unimportant for applications in which one must average the cross section over a broad Maxwell-Boltzmann distribution. It may be shown quantitatively [21]) that the strength of the 2.6 MeV resonance in the neutron data (fig. 4) compared with its strength in the γ-ray data (fig. 3) indicates that the isospin mixing is essentially complete. Qualitatively, this may be seen from the fact that only $T^<$ states of the compound nucleus ^{55}Mn may emit neutrons to the low-lying states of ^{54}Mn; hence, the observation of a strong resonance in the ^{54}Cr(p, n)^{54}Mn excitation function corresponding to a $T^>$ compound nucleus state indicates substantial mixing of $T^<$ states.

Both sets of calculations reproduce quite well the general features of the excitation functions, including the magnitude and shape of the drop at the cusp. It is important, however, that the calculations should also correctly predict absolute cross sections which are needed in astrophysical calculations and other applications.

Absolute cross sections calculated using Mann's code [3]) are in reasonable agreement with the data. The calculation for the total (p, γ) cross section (fig. 3) is high by about 50% at the peak of the cusp, while the cross sections for populating the 1529 and 2565 keV states (figs. 1 and 2) are underestimated by about 40% and 10%, respectively. This inconsistency may be due, at least in part, to uncertainties in the level scheme of ^{55}Mn. The calculated (p, n) cross section is about a factor of two higher than the data.

The calculations by Fowler *et al.* [18]) predict both the (p, n) and the total (p, γ) cross sections very accurately. No calculations for the 1529 and 2565 keV states using the Fowler *et al.* code are available.

On the whole, it may be said that current Hauser-Feshbach calculations are in encouraging agreement with the results presented in this paper. It seems likely that these calculations, or refinements thereof, will prove adequate for predicting reaction cross sections of significance for explosive nucleosynthesis. It is clear that further data are required to permit evaluation of the theory for a wide variety of reactions and to indicate where it may be improved; in this connection, the measurement of absolute cross sections is essential.

We thank William A. Fowler for stimulating our interest in the study of Wigner cusps. We acknowledge helpful conversations with C. A. Barnes. F. W. Mann has kindly assisted us in the use of the program "Hauser 4", and William A. Fowler, J. Powelson, B. A. Zimmerman and S. E. Woosley have graciously permitted us to use the results of their unpublished calculations. The participation of Dr. D. G. Sargood in the BF_3 long counter calibration has been most valuable.

References

1) W. A. Fowler, Proc. 4th Conf. on scientific and industrial applications of small accelerators, Denton, 1976, ed. J. L. Duggan and I. L. Morgan (IEEE, Piscataway, 1976) p. 11
2) S. E. Woosley, W. A. Fowler, J. A. Holmes and B. A. Zimmerman, Caltech preprint OAP-422 (1975), unpublished
3) F. M. Mann, Hanford Engineering Department Laboratory report HEDL-TME 76-80 (1976)
4) F. M. Mann and Z. E. Switkowski, Proc. Conf. on nuclear cross sections and technology, Washington, 1975, ed. R. A. Schrack and C. D. Bowman, NBS Special Publication 425 (NBS, Washington, 1975) p. 354
5) E. P. Wigner, Phys. Rev. **73** (1948) 1002; W. E. Meyerhof, Phys. Rev. **128** (1962) 2312; **129** (1963) 692
6) F. M. Mann, R. A. Dayras and Z. E. Switkowski, Phys. Lett. **58B** (1975) 420
7) J. L. Zyskind, R. Marrs, M. Shapiro, J. Davidson, C. A. Barnes and W. A. Fowler, Bull. Am. Phys. Soc. **22** (1977) 542
8) P. Dyer and C. A. Barnes, Nucl. Phys. **A233** (1974) 495
9) D. L. Kennedy, J. C. P. Heggie, P. J. Davies and H. H. Bolotin, Nucl. Instr. **140** (1977) 519
10) M. A. Meyer, I. Venter and D. Reitmann, Nucl. Phys. **A250** (1975) 235
11) D. C. Kocher, Nucl. Data Sheets **18** (1976) 463
12) H.-B. Mak, D. Ashery and C. A. Barnes, Nucl. Phys. **A226** (1974) 493
13) D. Wilmore and P. E. Hodgson, Nucl. Phys. **55** (1964) 673
14) F. D. Bechetti, Jr. and G. W. Greenlees, Phys. Rev. **182** (1969) 1190
15) J. A. Holmes, S. E. Woosley, W. A. Fowler and B. A. Zimmerman, Atomic and Nucl. Data Tables **18** (1976) 306
16) F. M. Mann and R. E. Schenter, Nucl. Sci. Eng. **63** (1977) 242
17) J. W. Tepel, H. M. Hofmann and H. A. Weidenmüller, Phys. Lett. **49B** (1974) 1
18) W. A. Fowler, J. Powelson, B. A. Zimmerman and S. E. Woosley, private communication
19) A. R. de L. Musgrove, Australian AEC report E277 (1973)
20) J. D. Moses, H. W. Newson, E. G. Bilpuch and G. E. Mitchell, Nucl. Phys. **A175** (1971) 556
21) W. A. Fowler, private communication

APPENDIX B

Cross Section Measurements and Thermonuclear Reaction Rates for $^{48}Ca(p,\gamma)^{49}Sc$ and $^{48}Ca(p,n)^{48}Sc$

(Published in Nuclear Physics A315 (1979) 430)

2.A.1 *Nuclear Physics* A315 (1979) 430–444;

CROSS SECTION MEASUREMENTS AND THERMONUCLEAR REACTION RATES FOR ^{48}Ca(p, γ)^{49}Sc AND ^{48}Ca(p, n)^{48}Sc †

J. L. ZYSKIND ††, J. M. DAVIDSON, M. T. ESAT, R. H. SPEAR †††, M. H. SHAPIRO ‡, WILLIAM A. FOWLER and C. A. BARNES

W.K.Kellogg Radiation Laboratory, California Institute of Technology, Pasadena, California 91125

Received 23 October 1978

Abstract: Absolute cross sections have been measured for the reaction ^{48}Ca(p, γ)^{49}Sc for 0.579 MeV $\leqq E_{p,\,lab} \leqq$ 2.670 MeV and for the reaction ^{48}Ca(p, n)^{48}Sc for 0.956 MeV $\leqq E_{p,\,lab} \leqq$ 2.670 MeV. Substantial competition effects in the cross section for ^{48}Ca(p, γ)^{49}Sc were observed at the thresholds for neutron emission to the 623 keV (3^+), 1143 keV (2^+) and 1402 keV (2^-) excited states of ^{48}Sc. Thermonuclear reaction rates were calculated from the measured cross sections for $0.1 \leqq T_9 \leqq 10.0$. The new rates differ considerably from those used in earlier calculations of the production of the rare, neutron-rich intermediate mass nuclides during explosive carbon burning. In particular, the new rates may change the predicted abundances for ^{48}Ca, ^{49,50}Ti and ^{50}V substantially. The good agreement between current global Hauser-Feshbach models and the experimental data indicates that Hauser-Feshbach calculations can provide sufficiently reliable rates for astrophysical calculations in cases where experimental data are non-existent.

E NUCLEAR REACTIONS ^{48}Ca(p, γ), ^{48}Ca(p, n), E = 0.58–2.67 MeV; measured $\sigma(E)$; deduced thermonuclear reaction rates as a function of temperature. Hauser-Feshbach calculations. Enriched target. Ge(Li) and BF_3 long counter.

1. Introduction

Explosive nucleosynthesis calculations explain the production, from the ashes left by earlier hydrostatic burning stages, of most of the intermediate mass nuclei with $A \leqq 62$ (ref. [1])). However, the abundances of the relatively rare, neutron-rich species such as ^{36}S, ^{40}K, ^{40}Ar, ^{43,46,48}Ca, ^{45}Sc, ^{47,49,50}Ti and ^{50}V resulting from these calculations are much too low. Howard *et al.*[2]) have proposed that these nuclei may be produced during explosive carbon burning by reactions of the free neutrons and protons with a small admixture of so-called seed nuclei assumed to be present at the time of the star's formation. In these calculations, all of these neutron-rich nuclei, as well as several heavier neutron-rich species arising from iron seed, were co-produced

† Supported in part by the National Science Foundation [PHY76-83685].
†† Fannie and John Hertz Foundation Fellow, September 1973–December 1977.
††† On leave from Department of Nuclear Physics, Australian National University, Canberra, Australia.
‡ Permanent address: Department of Physics, California State University, Fullerton, California 92634.

with ^{23}Na and ^{24}Mg in solar system abundance ratios to within a factor of 3 in most cases, and to within a factor of 8 in all cases. This level of agreement is encouraging in view of (i) the inexact treatment of the explosion, which was based on a parametrized adiabatic expansion of a single zone on the hydrodynamic time scale, and (ii) the severe uncertainties in the relevant reaction rates.

A more accurate treatment of the explosion should become possible as new results become available from supernova codes which can evolve stars from the pre-supernova stages through the supernova explosion (see, e.g., Weaver *et al.*[3]). The uncertainties in the nuclear reaction rates will then be the major obstacle to an improved understanding of the seed nucleosynthesis process.

The ^{48}Ca(p, γ)^{49}Sc and ^{48}Ca(p, n)^{48}Sc reactions are important in this context for two reasons. First, their rates are important in determining the abundances of ^{48}Ca, ^{49,50}Ti and ^{50}V (refs. [2,4]). These nuclei are of special interest in light of the recently discovered anomalous ^{48}Ca isotopic abundances in meteoritic inclusions [5]) which also show other anomalies of nuclear origin, possibly related to supernova nucleosynthesis. Second, these two reactions comprise an important test of relevant aspects of the recently developed global Hauser-Feshbach models, which must be used to calculate many of the needed reaction rates. The seed nucleosynthesis process resembles a mini r-process, and involves many reactions on β-unstable, neutron-rich targets. The most neutron-rich stable nuclide in the relevant mass range is ^{48}Ca. Because of the large neutron excesses of many of the nuclei involved in the seed nucleosynthesis, the neutron channels will be open at low energy and accurate treatment of their competititon with other channels is crucial. Substantial competition effects are expected in the proton-induced reactions on ^{48}Ca [ref. [6]) referred to as WFHZ]. Furthermore, the level density in ^{49}Sc is expected to be low ($\lesssim$ 0.07 levels/keV)[7]), and the application of models based on statistical concepts to an essentially doubly-magic target nucleus tests the models in rather extreme circumstances.

In previous studies of the ^{48}Ca(p, γ)^{49}Sc (refs. [7,8]) and ^{48}Ca(p, n)^{48}Sc (ref. [9])) reactions, the bombarding energy ranges were not sufficient to determine the reaction rates at temperatures of astrophysical interest ($T \approx 2 \times 10^9$ K), and absolute cross sections were not obtained at all in the case of the ^{48}Ca(p, γ)^{49}Sc reaction. In the present work we have measured absolute cross sections for the ^{48}Ca(p, γ)^{49}Sc reaction for laboratory bombarding energies from 0.579 MeV to 2.670 MeV, and for the ^{48}Ca(p, n)^{48}Sc reaction from 0.956 MeV to 2.670 MeV (ref. [10])). Thermonuclear reaction rates have been deduced from these data for both reactions, for the temperature range $0.1 \leqq T_9 \leqq 10.0$. The experimental cross sections are compared with the theoretical predictions of the Kellogg Global Hauser-Feshbach program (KGHFP)[6,11])† and with the predictions of F. M. Mann's program HAUSER*4 (ref. [13])).

† The version of the program used here, referred to as the Kellogg Global Hauser-Feshbach Program (KGHFP) was produced by B. A. Zimmerman in collaboration with W. A. Fowler, J. A. Holmes, J. Powelson and S. E. Woosley.

It has come to our attention that a similar study has been carried out recently at the University of Melbourne by Kennett *et al.* [14]).

2. Experimental procedure

Absolute cross sections for the reactions ^{48}Ca(p, γ)^{49}Sc and ^{48}Ca(p, n)^{48}Sc were measured over the energy ranges $0.579 < E_{p,lab} < 2.670$ MeV and $0.956 < E_{p,lab} < 2.670$ MeV, respectively, in steps of 30, 25 and 20 keV. A proton beam from the ONR-CIT tandem Van de Graaff accelerator was used to bombard a Ca target (enriched to 97.78% in ^{48}Ca †). The target was prepared by heating a mixture of Ta filings and $CaCO_3$ in vacuum in a baffled Ta boat ††. The $CaCO_3$ first dissociated into volatile CO and residual CaO; the CaO was then reduced by the Ta filings and metallic Ca was evaporated onto a 254 μm thick tungsten backing. The target thickness was determined to be 185 μg/cm^2 of ^{48}Ca by measuring the yield of 4.0 MeV α-particles elastically scattered at 160° from the calcium layer. At this angle the scattering was determined to be essentially Rutherford for energies less than 5.0 MeV. The target thickness was also measured at various times by weighing, and by observing the position of the scattering edge for α-particles scattered from the tungsten backing of our target relative to the position of the scattering edge for α-particles scattered from bare tungsten. These latter measurements include contributions from whatever oxygen and carbon is on the target as well as the calcium, and indicate that, in spite of storing and transporting the targets under argon, the calcium became oxidized and eventually turned to $CaCO_3$. The various thickness measurements indicated that it is a very good approximation to assume that the composition of the target was CaO during the experiment. Uncertainty in this assumption about the target composition introduces no uncertainty in the measured cross sections, and only a very small uncertainty in the effective bombarding energies. The target durability was excellent, as determined by the reproducibility of the data.

Gamma rays were detected with a 73 cm^3 Ge(Li) detector which was calibrated with standard radioactive sources and the ^{27}Al(p, γ)^{28}Si reaction. The details of the target assembly, and the γ-ray detector and its calibration were as described in another paper [15]), with the exceptions that in the present experiment the target was mounted with its surface normal to the beam direction and the face of the Ge(Li) detector was shielded by 3.2 mm of lead.

Neutrons were detected with a BF_3 "long counter" 25 cm from the target, at an angle of 90° with respect to the beam direction. The counter efficiency was determined by comparing the number of neutrons counted from the reactions ^{48}Ca(p, n)^{48}Sc, ^{51}V(p, n)^{51}Cr and ^{68}Zn(p, n)^{68}Ga with the absolute intensity of the 983 keV, 321 keV and 1077 keV γ-rays, arising from the ^{48}Sc, ^{51}Cr and ^{68}Ga activities, respectively.

† Obtained from Separated Isotopes Division, Oak Ridge National Laboratory.

†† An SO-20 Silicon Monoxide Source obtained from R. D. Mathis Co. of Long Beach, California.

All of these determinations of the neutron detector efficiency agreed well with one another.

Dead-time corrections were negligible for the neutron system. For the γ-rays, they ranged from less than 1 % for the runs below 1.950 MeV up to a maximum of 8 % at the highest energies. The measurements were not carried to still higher energies because of the rapidly increasing counting rates for the sum peaks at 2020, 2294 and 2348 keV, arising from the intense 983, 1037 and 1311 keV ^{48}Ti lines emitted in the ^{48}Sc decay, which interfered with the area determinations for the 2229 keV and 2372 keV lines used in the cross section determinations.

3. Data analysis and experimental results

3.1. GAMMA RAYS

The excitation functions for the 2229, 2372 and 3085 keV γ-rays arising from the decay of the first three excited states of ^{49}Sc (see fig. 1)[16]) were obtained from the full energy peak areas extracted from the γ-ray spectra with a linear background subtraction. Absolute cross sections were obtained for the production of each γ-ray by assuming that the angular distributions are of the form $w(\theta) = a_0 + a_2 P_2(\cos\theta)$. To obtain the ^{48}Ca(p, γ)^{49}Sc total cross section, the cross sections for production of these three γ-rays were added. Then by examining sums of the spectra for individual runs to obtain improved statistics, cross-over transitions from higher states (see fig. 1) too weak to be seen in the spectra for the individual runs were investigated. From the average intensity of these γ-rays relative to that of the 2229 keV line, it was determined that the cross sections should be increased by 14 % to include these cross-over transitions. From long runs at E_p = 1.075, 1.475, 1.845 and 1.985 MeV, the contribution of γ_0, the γ-transition from the capture energy to the ground state, was determined to be less than 1 %, except at the analogue resonance where it was about 5 %; γ_0 transitions were therefore not included in the analysis. The resulting cross sections are shown in fig. 2.

It is estimated that systematic uncertainties in the cross sections do not exceed 22 %; this is the sum in quadrature of uncertainties in relative detector efficiency (5 %), absolute efficiency arising primarily from geometrical effects (10 %), charge collection (2 %), target thickness (15 %), angular distribution effects (10 %), and the correction for cross-over transitions (5 %).

The effective laboratory proton energies, E_p, shown in fig. 2 are target-centered energies for $E_p \geqq 0.881$ MeV. For $E_p < 0.881$ MeV the cross section is a steep function of energy; therefore, the shift of the effective energy from the target-centered energy was evaluated using the e-folding technique of Mak *et al.* [17]). The error in the effective energies introduced by uncertainties in the target composition is less than 3 keV for all energies.

For comparison with the Hauser-Feshbach calculations the data were smoothed

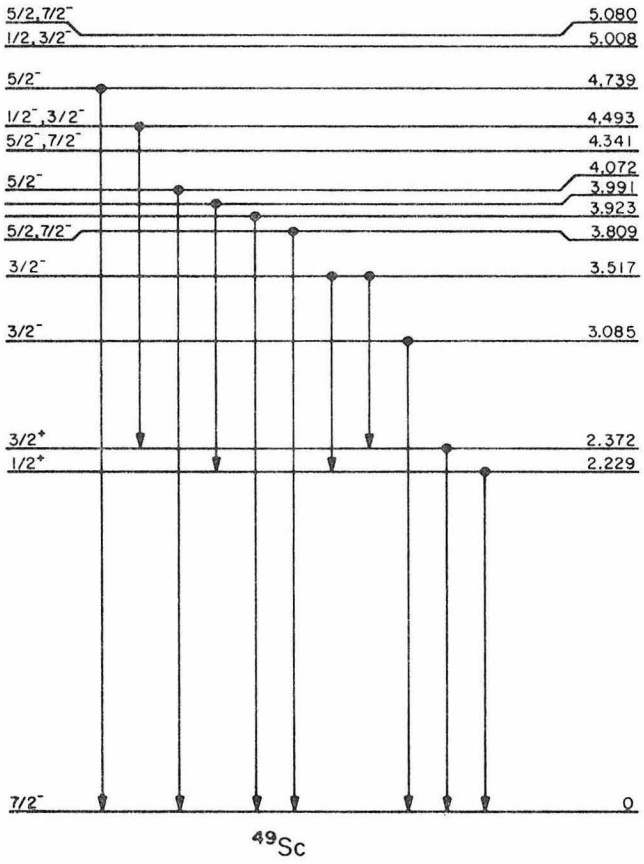

Fig. 1. The ^{49}Sc level scheme, showing the major known γ-decays, including all known cross-over transitions up to E_x = 5.090 MeV [ref. [16])].

over 100 to 120 keV intervals, corresponding usually to four or five data points. These partially smoothed ^{48}Ca(p, γ)^{49}Sc cross sections are shown in fig. 3. The energy assigned to each cross section is the center of the averaging interval for $E_p > 1$ MeV; for lower energies it was obtained using the e-folding technique [17]).

3.2. NEUTRONS

The measured ^{48}Ca(p, n)^{48}Sc excitation function is shown in fig. 4. Absolute cross sections were determined assuming isotropic angular distributions. All proton energies shown are target-centered. Below a bombarding energy of about 1 MeV contributions from contaminants, which produced a rather flat excitation function, became a very severe problem. The runs for $0.575 < E_p < 0.907$ MeV were used to determine an energy independent background correction. This background correction intro-

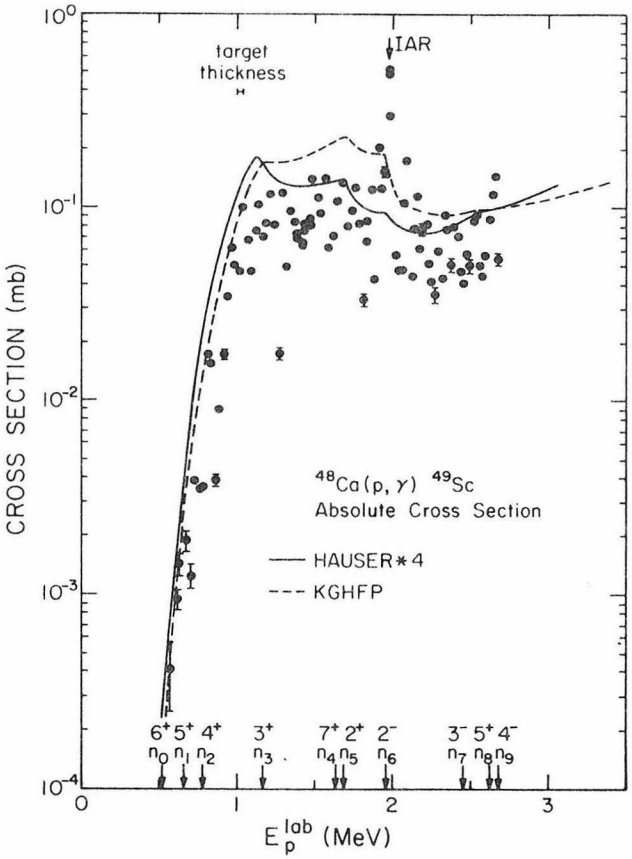

Fig. 2. Absolute cross sections for the reaction ^{48}Ca(p, γ)^{49}Sc. The error bars shown are statistical only. Where the error bars are not changing rapidly as a function of energy, they are shown for only a few typical points. For 0.95 MeV $\leqq E_p \leqq$ 1.95 MeV, the error bars are smaller than data points except where explicitly shown. The theoretical curves are described in the text. The arrow marked IAR indicates the position of the previously identified ^{49}Ca isobaric analogue resonance [8]).

duces considerable uncertainty in the cross sections for energies below 1.1 MeV. At E_p = 1.1 MeV the background comprises 40 % of the counting rate; at 1.183 MeV it comprises only 9 % and decreases rapidly in importance above this energy. The ^{48}Ca(p, n)^{48}Sc data were smoothed in a manner similar to the ^{48}Ca(p, γ)^{49}Sc data (fig. 5). Effective energies were obtained for $E_p \leqq$ 1.426 MeV using the e-folding technique [17]).

The systematic uncertainty in the absolute cross sections is approximately 20 %, the sources of error being similar to those described for the γ-ray data, except for the lowest energy points which suffer from additional uncertainties introduced by the contaminant background subtraction. We note that the cross sections reported in ref. [9]) are lower by a factor of approximately two than those measured in this work, for the energy range where the two data sets overlap.

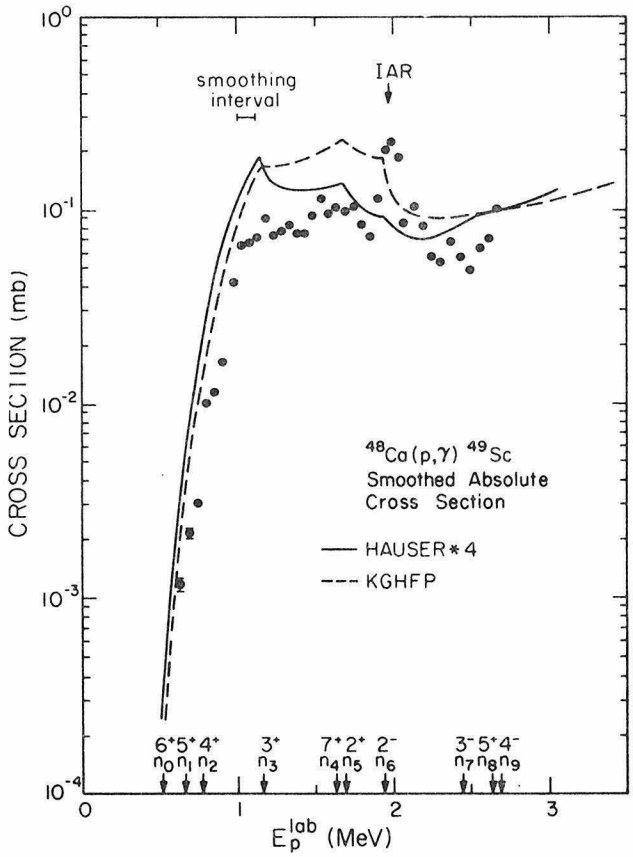

Fig. 3. The ^{48}Ca(p, γ)^{48}Sc data smoothed by averaging as described over four or five consecutive data points. The error bars are statistical only and are displayed wherever they are larger than the data points. The theoretical curves are described in the text.

4. Discussion

4.1. COMPARISON OF EXPERIMENTAL CROSS SECTIONS AND GLOBAL HAUSER-FESHBACH CALCULATIONS

The ^{48}Ca+p system has a relatively low density of resonances because of the doubly magic ^{48}Ca core. Our target, which is 37 keV thick for 1 MeV protons, spans an average of only about 7 compound states in this energy range [7]); consequently, our measured excitation functions show considerable fluctuations which are evident even after smoothing the data. In the ^{48}Ca(p, γ)^{49}Sc reaction the rise of the cross section, which is essentially determined by the Coulomb barrier, is abruptly halted at about 1.05 MeV, after which the average level of the cross section appears to remain constant or decrease slightly. The strong resonance in both the (p, γ) and

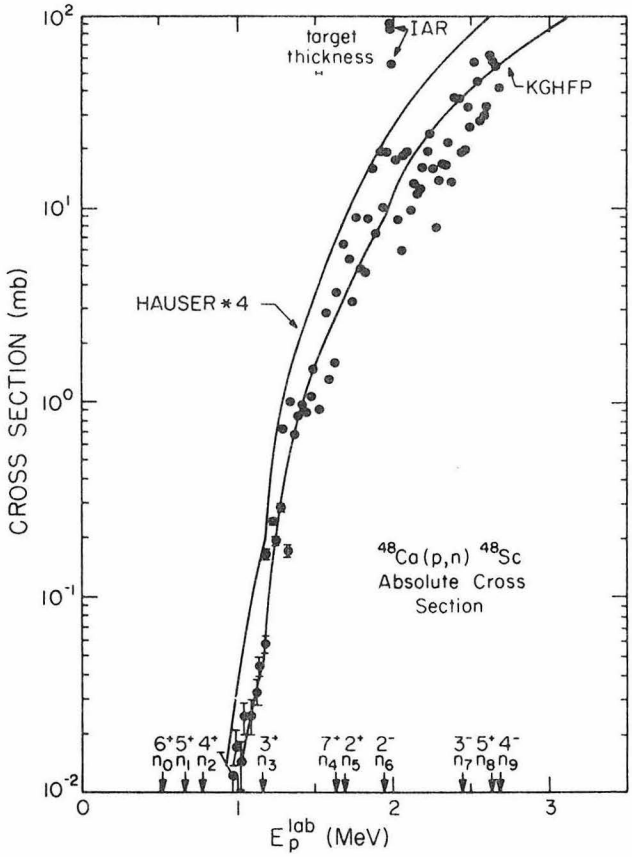

Fig. 4. Absolute cross sections for the reaction ^{48}Ca(p, n)^{48}Sc. The error bars are statistical only. The theoretical curves are described in the text.

(p, n) data at $E_p \approx 1.96$ MeV is attributed to the isobaric analogue of the ^{49}Ca ground state [8]).

The results of calculations performed using the Kellogg Global Hauser-Feshbach program (KGHFP)† and the program of Mann (HAUSER*4) [13]) are shown in figs. 2–5. In HAUSER*4, neutron and proton transmission functions are calculated by using the global optical-model parameter sets of Wilmore and Hodgson [18]), and Becchetti and Greenlees [19]), respectively. The γ-ray transmission functions are calculated using a giant dipole form for the E1 strength function and a single-particle estimate for the M1 strength function [11]). Width fluctuation corrections are included using the Tepel approximation [20]).

The KGHFP employs the so-called equivalent square well potential (equivalent to a Woods-Saxon potential) and black nucleus strength functions to calculate the

† See footnote at end of sect. 1.

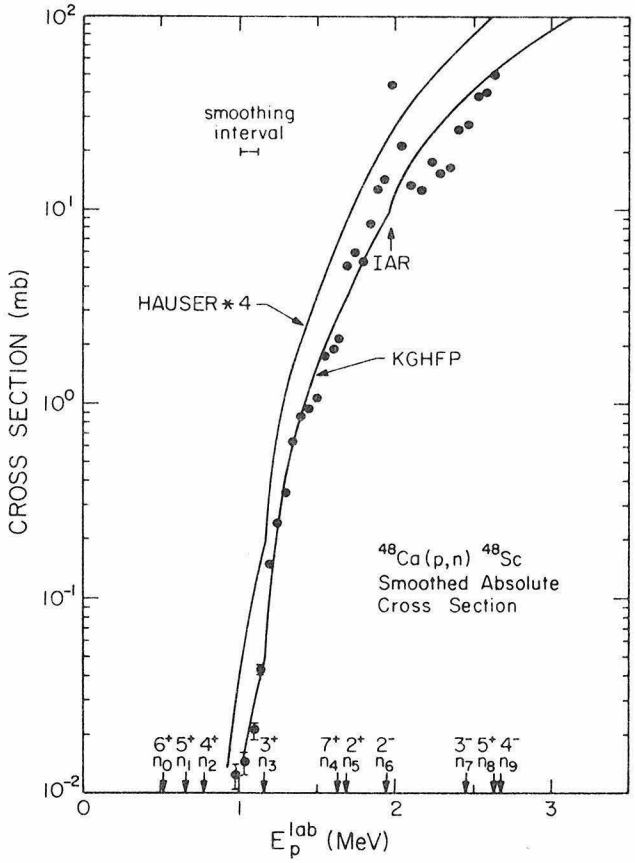

Fig. 5. The ^{48}Ca(p, n)^{48}Sc data smoothed by averaging over four or five consecutive data points. The error bars are statistical only. The theoretical curves are described in the text.

transmission functions, as did the earlier calculations of WFHZ[6]). The γ-ray transmission functions used in the KGHFP are similar to those for HAUSER*4. The KGHFP calculations differ from those of WFHZ in several respects. Width fluctuation corrections are now included using the Tepel approximation [20]). In the neutron channel the reflection factor of 2.7 is modified to $f = 3.0$ for even-l-wave neutrons and $f = 0.10$ for odd-l-wave neutrons, to include the effects of size resonances which are not included in the black nucleus strength functions. The choice of these values for f is based on the low energy neutron strength functions compiled by Musgrove [21]). Because we are effectively below the analogue threshold (there is only one analogue resonance in the region of interest) we have set the isospin mixing parameter μ to zero and used only the $T^<$ contribution to the cross section. The effects of these modifications are discussed at greater length in ref. [22]).

The Hauser-Feshbach calculations assume an average over many resonances and should be compared with the smoothed data. The KGHFP calculations of the

^{48}Ca(p, γ)^{49}Sc cross sections are approximately a factor of two higher than the experimental data, but accurately reproduce the shape of the excitation function except for the isobaric analogue resonance, which is outside the framework of the model. The HAUSER*4 calculations also reproduce the general features of the excitation function although they may not reproduce the shape of the cross section quite so well. The absolute cross sections predicted by HAUSER*4 are about a factor of three high below $E_p = 1$ MeV before competition effects are important.

The shape of the ^{48}Ca(p, n)^{48}Sc excitation function is reproduced fairly well by both calculations (see fig. 5). The absolute cross sections of the KGHFP calculations are in excellent agreement with the experimental data, while the HAUSER*4 calculations are about a factor of three too high. The good agreement of the KGHFP calculation with the (p, n) data indicates that the KGHFP proton transmission functions are quite acceptable. For the HAUSER*4 calculation, the discrepancy between theory and experiment is similar for the (p, n) and the low energy (p, γ) cross sections (below 1.1 MeV, before competititon effects become important) suggesting that the calculated proton transmission function is too large. This may reflect the insensitivity of the higher energy data analyzed by Becchetti and Greenlees [19]) to ingoing-channel penetration effects; the low energy proton transmission functions needed here will be strongly sensitive to these effects.

The data and current calculations do not show the deep competition cusp at about 900 keV predicted in earlier calculations [6]) to arise from a state reported at 388 keV in ^{48}Sc. The present data, as well as other experimental data indicate that no such state exists [23, 24]).

However, competition effects do play an important role which can be seen most clearly by reference to the Hauser-Feshbach formula for the reaction A(a, b)B of a projectile a incident on target A to form a compound nucleus which decays into b and the residual product B,

$$\sigma_{ab}(E_a) = \frac{\pi\lambda\!\!\!^{-2}_a}{(2s_a+1)(2s_A+1)} \sum_{J,\pi} (2J+1) \frac{T_a(J,\pi)T_b(J,\pi)}{\sum_c T_c(J,\pi)}.$$

In this expression, $\lambda\!\!\!^{-}_a$ is the c.m. reduced wavelength in the incident channel a; s_a and s_A are the projectile and target spins, respectively; c denotes the pair c+C and the sum runs over all open channels (including a and b); $T_a(J,\pi)$, $T_b(J,\pi)$ and $T_c(J,\pi)$ are transmission functions for decay of compound states of spin J and parity π into the channels a, b and c, respectively. These transmission functions are obtained from the optical model transmission functions, $T_a(j_a, l_a, s_a)$, where l_a is the relative orbital angular momentum in channel a, $\boldsymbol{s}_a$ is the projectile spin vector and $\boldsymbol{j}_a = \boldsymbol{l}_a + \boldsymbol{s}_a$, by summing over l_a and j_a:

$$T_a(J,\pi) = \sum_{l_a, j_a} T(j_a, l_a, s_a). \qquad (2)$$

The sum in eq. (2) runs over all combinations which can couple with s_A to make a compound state of spin J and parity π. Competition effects will be pronounced in a reaction A(a, b)B near the threshold for A(a, d)D if $T_d(J, \pi)$ increases rapidly and dominates $\sum_c T_c(J, \pi)$ for compound states of spin J and parity π which make a major contribution to σ_{ab}. At $E_p = 1.5$ MeV, where neutron decay to several ^{48}Sc states is already energetically allowed, the proton transmission functions for s-, p-, d- and f-waves (see fig. 6) are in the ratio 1.00 : 0.33 : 0.05 : 0.003, respectively. For $J \leqq \frac{9}{2}$ the γ-ray transmission functions do not vary strongly with compound spin and parity (see fig. 6). Therefore, referring to eq. (1) and taking into account the statistical weights, we see that the major contributions to the ^{48}Ca(p, γ)^{49}Sc cross section are expected for reactions proceeding through $\frac{1}{2}^+$ compound states formed by s-wave protons,

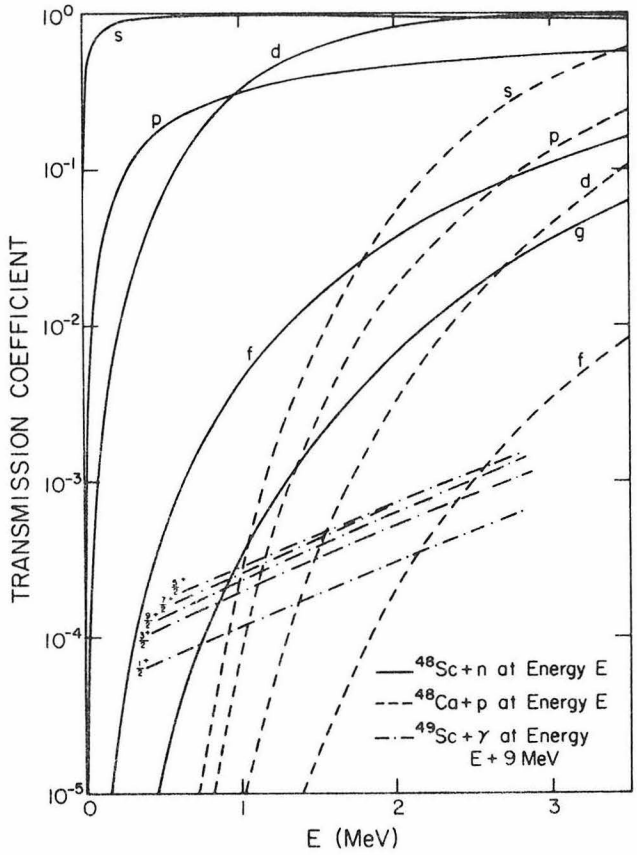

Fig. 6. Transmission functions calculated by the code HAUSER*4. For the particle channels, the labels indicate the partial wave orbital angular momentum, and the energies are center-of-mass channel energies. The transmission functions for γ-decay of positive parity compound states of spin $J \leqq \frac{9}{2}$ are also shown, and are given for $E_\gamma = E + 9$ MeV, to cover the relevant range of excitation energies ($Q = 9.62$ MeV). The transmission functions for the negative parity states behave similarly.

and $\frac{1}{2}^-$ and $\frac{3}{2}^-$ states formed by p-waves, together with significant though smaller contributions from $\frac{3}{2}^+$ and $\frac{5}{2}^+$ states formed by d-waves.

For s-wave neutrons, which have no angular momentum barrier, the neutron transmission functions rise sufficiently rapidly (see fig. 6) above newly open thresholds to cause competition cusps. For d-waves, this is not the case, although several hundred keV above a threshold the competition from both p- and d-wave neutron decay can seriously deplete the γ-ray decay.

Neither the data nor the calculations show competition effects at the n_0, n_1 and n_2 thresholds (see fig. 3) for decay to the 6^+ ground, 131 keV (5^+) and 252 keV (4^+) ^{48}Sc states, respectively. The compound states of lowest spin for which s-wave neutron emission to these three ^{48}Sc states is allowed are those with $J^\pi = \frac{11}{2}^+$, $\frac{9}{2}^+$ and $\frac{7}{2}^+$, respectively. For p-wave neutron emission, $\frac{9}{2}^-$, $\frac{7}{2}^-$ and $\frac{5}{2}^-$ compound states, respectively, are required. As shown above, such compound states do not play a significant part in the ^{48}Ca(p, γ)^{49}Sc reaction at low proton energies because of their small proton transmission functions.

The 623 keV (3^+) third excited state of ^{48}Sc, however, may be populated by s-wave neutron decay of $\frac{5}{2}^+$ compound states and p-wave neutron decay of $\frac{3}{2}^-$ states. The resulting competition effects are apparent in the abrupt halt of the cross section rise at this threshold, $E_p = 1.16$ MeV, both in the experimental data and in the theoretical calculations. The calculations show further competition effects at the thresholds for the 1143 keV (2^+) and 1402 keV (2^-) ^{48}Sc states. These occur because the 2^+ ^{48}Sc state may be formed by the s-wave decay of $\frac{3}{2}^+$ and $\frac{5}{2}^+$ compound states, and the 2^- state by s-wave decay of $\frac{3}{2}^-$ and $\frac{5}{2}^-$ compound states. Although the detailed structure of the data is obscured by cross section fluctuations and by the analog resonance, the effects of the thresholds for the 2^+ and 2^- ^{48}Sc states are shown by the excellent agreement of the calculations with the general trend of the experimental excitation function.

An accurate knowledge of the excited states in the (p, n) residual nucleus can be crucial in the treatment of competition effects. For example, the inclusion of a non-existent 2^+ state at 388 keV causes the ^{48}Ca(p, n) cross section to level out at a proton energy 250 keV lower than observed, and at a cross section which is only 25 % of its eventual value. Similarly, a drop of a factor of ten in cross section is predicted above the threshold of the 2^+, fifth excited state, if a standard level density formula is used in the calculation instead of actual discrete level information for $E_x > 1.402$ MeV in ^{48}Sc, because the ordinary level density formulae imply the existence of low spin states which do not actually exist in this excitation region in ^{48}Sc.

4.2. ASTROPHYSICAL REACTION RATES

For use in astrophysical nucleosynthesis calculations, the cross sections must be averaged over the Maxwell-Boltzmann energy distributions corresponding to the

appropriate temperatures to obtain the reaction rates as a function of temperature:

$$\langle \sigma v \rangle = \frac{(8/\pi)^{\frac{1}{2}}}{M^{\frac{1}{2}}(kT)^{\frac{3}{2}}} \int_0^{\infty} \sigma(E) E \exp(-E/kT) \mathrm{d}E. \tag{3}$$

E is the c.m. energy, M is the reduced mass in the incident channel, k is Boltzmann's constant and T is the temperature [12]). Table 1 gives the reaction rates deduced from the experimental cross section measurements by numerical integration. Where available, experimental cross sections were used in the integrand. The ^{48}Ca(p, γ)^{49}Sc cross sections were extrapolated for $E < 0.579$ MeV and $E > 2.670$ MeV by using the KGHFP calculation normalized to the experimental data. The ^{48}Ca(p, n)^{48}Sc cross sections for $E < 1.013$ MeV and $E > 2.670$ MeV were also extrapolated using the KGHFP calculation; no normalization was necessary for these cross sections, since the calculated and measured cross sections agreed so well. The contribution to the ^{48}Ca(p, γ)^{49}Sc reaction rate from the energy range for which we have experimental cross sections is 8 % at $T_9 = 0.3$, 84 % at $T_9 = 0.7$, 95 % at $T_9 = 1.0$, $\geqq$ 99 % for $1.5 \leqq T_9 \leqq 3.5$, 95 % at $T_9 = 5.0$, and 67 % at $T_9 = 10.0$. (T_9 is the temperature in degrees Kelvin divided by 10^9.) The contribution to the ^{48}Ca(p, n)^{48}Sc reaction rate from the energy range $1.011 < E_p < 2.670$ MeV for which experimental cross sections were available, is 7 % at $T_9 = 0.5$, 68 % at $T_9 = 0.9$, 96 % at $T_9 = 1.5$, 93 % at $T_9 = 2.5$, 66 % at $T_9 = 4.0$ and 13 % at $T_9 = 10.0$.

The "stellar reaction rates" in table 1 include the effects of the thermal population of excited target states [6]). They were determined by multiplying the "laboratory reaction rates" we have deduced by the ratio of the "stellar" and "laboratory" reaction rates given by WFHZ [6]). Because of the high excitation energy (3.83 MeV) of the first excited state of ^{48}Ca, these corrections have little effect on the reaction rates except at very high temperature.

Also shown in table 1 are the "stellar reaction rates" deduced from the KGHFP calculations, and the rates employed by Howard *et al.* [2]) at $T_9 = 2.0$ and 2.15.

The temperature dependence of the reaction rates deduced from the KGHFP calculations is very similar to the temperature dependence of the reaction rates deduced from the experimental data. The KGHFP rates are a factor of two high for ^{48}Ca(p, γ)^{49}Sc, and are in excellent agreement with the data for ^{48}Ca(p, n)^{48}Sc. Thus, it can be concluded that the competition between the two reactions is predicted to within a factor of two by the present global Hauser-Feshbach model.

The value employed by Howard *et al.* [2]) for the ^{48}Ca(p, γ)^{49}Sc reaction rate is a factor of six too high, perhaps because they omitted the ^{48}Ca(p, n)^{48}Sc reaction, for which the rate is a factor of six higher than the ^{48}Ca(p, γ)^{49}Sc rate. While their calculation of the rate of destruction of ^{48}Ca in the late proton-rich phase of explosive carbon burning may be roughly correct, the main product will be ^{48}Sc rather than ^{49}Sc. This may have a significant effect on the production of the nuclear species ^{49}Ti, ^{50}Ti and ^{50}V, much of which occurred via the reaction ^{48}Ca(p, γ)^{49}Sc in their calculations.

TABLE 1

Thermonuclear reaction rates [a]) for ^{48}Ca(p, γ)^{49}Sc and ^{48}Ca(p, n)^{48}Sc

	^{48}Ca(p, γ)^{49}Sc				^{48}Ca(p, n)^{48}Sc		
T_9 [b])	exp. [c]) lab [f])	exp. [c]) stellar [g])	KGHFP [d]) stellar [g])	Howard *et al.* [c])	exp. [c]) lab [f])	exp. [c]) stellar [g])	KGHFP [d]) stellar [g])
0.10	2.91E−14	2.91E−14	5.54E−14		3.40E−29	3.40E−29	3.40E−30
0.15	1.06E−10	1.06E−10	1.99E−10		3.80E−20	3.80E−20	3.80E−20
0.20	1.85E−08	1.85E−08	3.43E−08		4.39E−15	4.39E−15	4.39E−15
0.30	1.20E−05	1.20E−05	2.18E−05		1.90E−09	1.90E−09	1.90E−09
0.40	6.97E−04	6.79E−04	1.22E−03		1.85E−06	1.85E−06	1.86E−06
0.50	1.19E−02	1.19E−02	2.08E−02		1.44E−04	1.44E−04	1.43E−04
0.60	9.68E−02	9.68E−02	1.74E−01		3.16E−03	3.16E−03	3.08E−03
0.70	4.96E−01	4.96E−01	9.05E−01		3.41E−02	3.41E−02	3.26E−02
0.80	1.84E+00	1.84E+00	3.39E+00		2.34E−01	2.35E−01	2.21E−01
0.90	5.44E+00	5.44E+00	9.98E+00		1.17E+00	1.17E+00	1.09E+00
1.00	1.34E+01	1.34E+01	2.45E+01		4.58E+00	4.58E+00	4.26E+00
1.50	2.48E+02	2.48E+02	4.42E+02		4.51E+02	4.51E+02	4.05E+02
2.00	1.16E+03	1.16E+03	2.09E+03	6.6E+03	6.41E+03	6.41E+03	5.59E+03
2.15	1.61E+03	1.61E+03	2.90E+03	1.0E+04	1.16E+04	1.16E+04	1.01E+04
2.50	2.98E+03	2.98E+03	5.47E+03		3.65E+04	3.65E+04	3.23E+04
3.00	5.60E+03	5.60E+03	1.04E+04		1.27E+05	1.27E+05	1.16E+05
3.50	8.78E+03	8.78E+03	1.66E+04		3.27E+05	3.27E+05	3.08E+05
4.00	1.23E+04	1.23E+04	2.34E+04		6.95E+05	6.95E+05	6.72E+05
4.50	1.60E+04	1.60E+04	3.04E+04		1.29E+06	1.29E+06	1.27E+06
5.00	1.98E+04	1.97E+04	3.75E+04		2.18E+06	2.18E+06	2.17E+06
6.00	2.73E+04	2.68E+04	5.05E+04		5.05E+06	5.04E+06	5.06E+06
7.00	3.48E+04	3.23E+04	5.98E+04		9.61E+06	9.48E+06	9.57E+06
8.00	4.21E+04	3.38E+04	6.18E+04		1.60E+07	1.53E+07	1.55E+07
9.00	4.96E+04	3.11E+04	5.61E+04		2.43E+07	2.19E+07	2.22E+07
10.00	5.71E+04	2.60E+04	4.64E+04		3.42E+08	2.81E+07	2.85E+07

[a]) Thermonuclear reaction rates, $N_A\langle\sigma v\rangle$ where N_A is Avogadro's number and $\langle\sigma v\rangle$ is defined in eq. (3). Values are given in units of $cm^3 \cdot mole^{-1} \cdot sec^{-1}$.

[b]) Temperature divided by 10^9 K.

[c]) Deduced from the experimental data of this work and extrapolations as described in the text.

[d]) Deduced by numerical integration of cross sections calculated with the Kellogg Global Hauser-Feshbach Program.

[e]) Rates used in ref. [2]). This paper gives no rates for the ^{48}Ca(p, n)^{48}Sc reaction.

[f]) Based on the cross sections measured in the laboratory with the target in its ground state.

[g]) Reaction rates appropriate for the stellar situation deduced from the "lab reaction rates" as described in the text.

The success of the new calculations in predicting the cross sections and treating the competition effects indicates that they are capable of providing more reliable rates for the reactions participating in the seed nucleosynthesis process than were available at the time of the paper by Howard *et al.* [2]). From the present study and other recent studies [15, 22]), it seems reasonable to assume that reaction rates can now be calculated to within a factor of 2 in this mass range, even for neutron-rich nuclear species. It is still preferable, of course, to deduce the reaction rates from experimental

data where this is possible, as has been done in the present work for the reactions ^{48}Ca(p, γ)^{49}Sc and ^{48}Ca(p, n)^{48}Sc.

Because of the improved confidence with which reaction rates can now be calculated, and also because of the recent discovery of the ^{48}Ca isotopic anomalies in the Allende meteorite, it is to be hoped that new calculations will be made of the seed nucleosynthesis that may accompany explosive carbon burning.

It is a pleasure to acknowledge many helpful discussions with Dr. D. G. Sargood and his valuable participation in the calibration of the BF_3 "long counter" which was used in the present work for neutron detection.

References

1) V. Trimble, Rev. Mod. Phys. **47** (1975) 877
2) W. M. Howard, W. D. Arnett, D. D. Clayton and S. E. Woosley, Ap. J. **175** (1972) 201
3) T. A. Weaver, G. B. Zimmerman and S. E. Woosley, UCRL preprint 80460 (1977)
4) D. D. Clayton and S. E. Woosley, Rev. Mod. Phys. **46** (1974) 755
5) T. Lee, D. A. Papanastassiou and G. J. Wasserburg, Ap. J. **220** (1978) L21
6) S. E. Woosley, W. A. Fowler, J. A. Holmes and B. A. Zimmerman, Caltech preprint OAP-422 (1975), unpublished
7) J. Dubois, S. Maripuu and O. Almén, Ark. Fys. **31** (1965) 65
8) C. Chasman, K. W. Jones, R. A. Ristinen and J. T. Sample, Phys. Rev. Lett. **18** (1967) 219; G. B. Vingiani, G. Chilosi and W. Bruynesteyn, Phys. Lett. **26B** (1968) 285
9) T. J. de Waal, M. Peisach and R. Pretorius, J. Inorg. Nucl. Chem. **33** (1971) 2783
10) J. L. Zyskind, J. M. Davidson, M. T. Esat, M. H. Shapiro, R. H. Spear, W. A. Fowler and C. A. Barnes, Bull. Am. Phys. Soc. **23** (1978) 13
11) J. A. Holmes, S. E. Woosley, W. A. Fowler and B. A. Zimmerman, Atomic and Nucl. Data Tables **18** (1976) 305
12) W. A. Fowler, G. R. Caughlan and B. A. Zimmerman, Ann. Rev. Astron. Astrophys. **5** (1967) 525
13) F. M. Mann, Hanford Engineering Department Laboratory report HEDL-TME 76-80 (1976)
14) S. R. Kennett, Z. E. Switkowski, B. M. Paine and D. G. Sargood, J. of Phys. **G**, in press
15) J. L. Zyskind, J. M. Davidson, M. T. Esat, M. H. Shapiro and R. H. Spear, Nucl. Phys. **A301** (1978) 179
16) M. L. Halbert, Nucl. Data Sheets **24** (1978) 175
17) H.-B. Mak, D. Ashery and C. A. Barnes, Nucl. Phys. **A226** (1974) 493
18) D. Wilmore and P. E. Hodgson, Nucl. Phys. **55** (1964) 673
19) F. D. Becchetti, Jr. and G. W. Greenlees, Phys. Rev. **182** (1969) 1190
20) J. W. Tepel, H. M. Hoffmann and H. A. Weidenmüller, Phys. Lett. **49B** (1974) 1
21) A. R. de L. Musgrove, Australian AEC E277 (1973)
22) J. L. Zyskind, C. A. Barnes, J. M. Davidson, W. A. Fowler, R. E. Marrs and M. H. Shapiro, in preparation (1978)
23) S. R. Kennett, D. G. Sargood and Z. E. Switkowski, private communication (1977)
24) J. R. Beene, Nucl. Data Sheets **23** (1978) 1

REFERENCES

(Adachi 1973) M. Adachi and H. Taketani, J. Phys. Soc. Japan 35 (1973) 317

(Allen 1960) W. D. Allen in Fast Neutron Physics edited by J. B. Marion and J. L. Fowler (Interscience Publishers, Inc. New York, 1960) Pt. I, p. 3.

(Anderson 1979) M. R. Anderson, S. R. Kennett, Z. E. Switkowski, and D. G. Sargood, Nucl. Phys. (1979), in press.

(Auble 1978) R. L. Auble NDS 23 (1978) 163.

(Baz 1958) A. I. Baz, Soviet Phys. JETP 6(33) (1958) 709.

(Bechetti 1969) F. D. Bechetti, Jr. and G. W. Greenlees, Phys. Rev. 182 (1969) 1190.

(Beene 1978) J. R. Beene, NDS 23 (1978) 1.

(Bilpuch 1976) E. G. Bilpuch, A. M. Lane, G. E. Mitchell, and J. D. Moses, Phys. Reports 28C (1976) 145.

(Brown 1951) A. B. Brown, C. W. Snyder, W. A. Fowler, and C. C. Lauritsen, Phys. Rev. 82 (1951) 159.

(Chasman 1967) C. Chasman, K. W. Jones, R. A. Ristinen, and J. T. Sample, Phys. Rev. Lett. 18 (1967) 219.

(Chu 1978) W.-K. Chu, J. W. Mayer, and M.-A. Nicolet, Backscattering Spectrometry (Academic Press, New York, 1978), pp. 22 ff.

(Clayton 1974) D. D. Clayton and S. E. Woosley, Rev. Mod. Phys. 46 (1974) 755.

(Davidson 1977) J. M. Davidson, M. T. Esat, M. H. Shapiro, R. H. Spear, and J. L. Zyskind, BAPS 22 (1977) 1246.

(de Waal 1971) T. J. de Waal, M. Peisach, and R. Pretorius, J. Inorg. Nucl. Chem. 33 (1971) 2783.

(Dubois 1966) J. Dubois, S. Maripuu and O. Almén, Arkiv för Physik 31 (1966) 65.

(Dyer 1974) P. Dyer and C. A. Barnes, Nucl. Phys. A233 (1974) 495.

(Egan 1970) J. J. Egan, G. C. Dutt, M. McPherson, and F. Gabbard, Phys. Rev. C1 (1970) 176.

(Elwyn 1966) A. J. Elwyn, A. Marinov, and J. P. Schiffer, Phys. Rev. 145 (1966) 957.

(Endt 1973) P. M. Endt and C. Van der Leun, Nucl. Phys. A214 (1973) 1.

(Esat 1977) M. T. Esat, M. H. Shapiro, R. H. Spear, J. L. Zyskind, and J. M. Davidson, BAPS 22 (1977) 1246.

(Esat 1979) M. T. Esat, R. H. Spear, M. H. Shapiro, J. M. Davidson, and J. L. Zyskind (1979), in preparation.

(Faini 1973) G. J. Faini, R. L. Ezell, E. L. Wills, H. L. Scott, and W. G. Love, Nucl. Phys. A212 (1973) 541.

(Fowler 1975) W. A. Fowler, 14th International Cosmic Ray Conference Vol. 11 (Max-Planck-Institut für Extraterrestriche Physik, München, 1975), p. 3550.

(Fowler 1976) W. A. Fowler, Proc. 4th Conf. on Scientific and Industrial Applications of Small Accelerators, Denton, 1976, ed. by J. L. Duggan and I. L. Morgan (IEEE, Piscataway, 1976), p. 11.

(Grimes 1972) S. M. Grimes, J. D. Anderson, A. K. Kerman, and C. Wong, Phys. Rev. C5 (1972) 85.

(Harney 1977) H. L. Harney, H. A. Weidenmuller, A. Richter, Phys. Rev. C16 (1977) 1774.

(Hauser 1952) W. Hauser and H. Feshbach, Phys. Rev. 87 (1952) 366.

(Henry 1974) E. A. Henry NDS 11 (1974) 495.

(Hodgson 1971) P. E. Hodgson, Nuclear Reactions and Nuclear Structure (Clarendon Press, Oxford, England, 1971).

(Hoffmann 1975a) H. M. Hoffmann, J. Richert, J. W. Tepel, and H. A. Weidenmuller, Ann. Phys. 90 (1975) 403.

(Hoffmann 1975b) H. M. Hoffmann, J. Richert, and J. W. Tepel, Ann. Phys. 90 (1975) 391.

(Holmes 1976a) J. A. Holmes, S. E. Woosley, W. A. Fowler, and B. A. Zimmerman, Atomic Data and Nuclear Data Tables 18 (1976) 306.

(Holmes 1976b) J. A. Holmes, Ph.D. Thesis, California Institute of Technology (1976), unpublished.

(Howard 1972) W. M. Howard, W. D. Arnett, D. D. Clayton, and S. E. Woosley, Ap. J. 175 (1972) 201.

(Howard 1974) A. J. Howard, H. B. Jensen, M. Rios, W. A. Fowler, and B. A. Zimmerman, Ap. J. 188 (1974) 131.

(Kailas 1975) S. Kailas, S. K. Gupta, M. K. Mehta, S. S. Kerekatte, and L. V. Namjoshi, Phys. Rev. C12 (1975) 1789 .

(Kennedy 1977) D. L. Kennedy, J. C. P. Heggie, P. J. Davies, and H. H. Bolotin, NIM 140 (1977) 519.

(Kennett 1979) S. R. Kennett, Z. E. Switkowski, B. M. Paine, and D. G. Sargood, J. Phys. G (1979), in press.

(Lane 1978) A. M. Lane, Phys. Rev. C18 (1978) 1525.

(Lewis 1975) M. B. Lewis, NDS 14 (1975) 155.

(Lux 1977) C. R. Lux, N. T. Porile, and S. M. Grimes, Phys. Rev. C15 (1977) 1308.

(Mak 1974) H.-B. Mak, D. Ashery, and C. A. Barnes, Nucl. Phys. A226 (1974) 493.

(Mann 1975a) F. M. Mann and R. W. Kavanagh, Nucl. Phys. A255 (1975) 287.

(Mann 1975b) F. M. Mann, Ph.D. Thesis, Calif. Inst. of Technology (1975), unpublished.

(Mann 1975c) F. M. Mann, R. A. Dayras, and Z. E. Switkowski, Phys. Lett. 58B (1975) 420.

(Mann 1976) F. M. Mann, Hanford Engineering Dept. Laboratory Report HEDL-TME-76-80 (1976).

(McFadden 1966) L. McFadden and G. R. Satchler, Nucl. Phys. 84 (1966) 177.

(Mehta 1977) M. K. Mehta, S. Kailas, and K. K. Sekharan, Pramãna 9 (1977) 419.

(Mekjian 1973) A. Mekjian, in Advances in Nuclear Physics, ed. by M. Baranger and E. W. Vogt (Plenum Press, Inc., N.Y., 1973), Vol. 7, p. 1.

(Meyer 1975) M. A. Meyer, I. Venter, and D. Reitman, Nucl. Phys. A250 (1975) 235.

(Meyerhof 1962) W. E. Meyerhof, Phys. Rev. 128 (1962) 2312.

(Meyerhof 1963) W. E. Meyerhof, Phys. Rev. 129 (1963) 692.

(Michaud 1970a) G. Michaud, L. Scherk, and E. Vogt, Phys. Rev. C1 (1970) 864.

(Michaud 1970b) G. Michaud and W. A. Fowler, Phys. Rev. C2 (1970) 2041.

(Moldauer 1969) P. A. Moldauer, Phys. Rev. 177 (1969) 1841.

(Moldauer 1975) P. A. Moldauer, Phys. Rev. C11 (1975) 426.

(Moldauer 1976) P. A. Moldauer, Phys. Rev. C14 (1976) 764.

(Moses 1971a) J. D. Moses, J. C. Browne, H. W. Newson, E. G. Bilpuch, and G. E. Mitchell, Nucl. Phys. A168 (1971) 406.

(Moses 1971b) J. D. Moses, H. W. Newson, E. G. Bilpuch, and G. E. Mitchell, Nucl. Phys. A175 (1971) 556.

(Musgrove 1973) A. R. Musgrove, Australian AEC Report E277 (1973).

(Newton 1959) R. G. Newton, Phys. Rev. 114 (1959) 1611.

(Peters 1973) W. C. Peters, E. G. Bilpuch, and G. E. Mitchell, Nucl. Phys. A207 (1973) 626.

(Price 1972) H. G. Price, J. Phys. A 5 (1972) 1524.

(Roughton 1976) N. A. Roughton, M. J. Fritts, R. J. Peterson, C. S. Zaidins, and C. J. Hansen, Ap. J. 205 (1976) 302.

(Roy 1974) A. Roy, K.V.K. Iyengar, M. L. Jhingan, and S. K. Bhattacherjee, Pramãna 3 (1974) 186.

(Schiffer 1958) J. P. Schiffer and L. L. Lee, Jr., Phys. Rev. 109 (1958) 2098.

(Schmorak 1975) M. R. Schmorak, NDS 14 (1975) 586.

(Schmorak 1977) M. R. Schmorak NDS 22 (1977) 487.

(Snyder 1950) C. W. Snyder, S. Rubin, W. A. Fowler, and C. C. Lauritsen, Rev. Sci. Instr. 21 (1950) 852.

(Solomon 1978) S. B. Solomon and D. G. Sargood, Nucl. Phys. A312 (1978) 140.

(Struve 1973) H. Struve, H. C. Thomas, M. J. Bennett, and D. D. Armstrong, Phys. Rev. C 7 (1973) 1418.

(Switkowski 1978a) Z. E. Switkowski, J.C.P. Heggie, and F. M. Mann, Phys. Rev. C 17 (1978) 392.

(Switkowski 1978b) Z. E. Switkowski, J.C.P. Heggie, and F. M. Mann, Aust. J. Phys. 31 (1978) 253.

(Tepel 1974) J. W. Tepel, H. M. Hoffmann, and H. A. Weidenmuller, Phys. Lett. 49B (1974) 1.

(Teranishi 1966) E. Teranishi and B. Furubayashi, Phys. Lett. 20 (1966) 511.

(Toth 1977) K. S. Toth, NDS 21 (1977) 437.

(Trimble 1975) V. Trimble, Rev. Mod. Phys. 47 (1975) 877.

(Vingiani 1968) G. B. Vingiani, G. Chilosi, and W. Bruynesteyn, Phys. Lett. 26B (1968) 285.

(Vogt 1962) E. Vogt, Rev. Mod. Phys. 34 (1962) 723.

(Vogt 1968) E. W. Vogt in Advances in Nuclear Physics, ed. M. Baranger and E. W. Vogt (Plenum Press, Inc., New York, 1968), Vol. 7, p. 261.

(Vourvopoulos 1966) G. Vourvopoulos and J. D. Fox, Phys. Rev. 141 (1966) 1180.

(Wigner 1948) E. P. Wigner, Phys. Rev. 73 (1948) 1002.

(Wilkinson 1978) R. J. Wilkinson, S. R. Kennett, Z. E. Switkowski, D. G. Sargood, and F. M. Mann, private communication (1978), and to be published.

(Wilmore 1964) D. Wilmore and P. E. Hodgson, Nucl. Phys. 55 (1964) 673.

(Woosley 1975) S. E. Woosley, W. A. Fowler, J. A. Holmes, and B. A. Zimmerman, Caltech preprint OAP-422 (1975), unpublished.

(Woosley 1979) S. E. Woosley, W. A. Fowler, J. A. Holmes, and B. A. Zimmerman, Atomic Data and Nuclear Data Tables (1979), in press.

(Zimmerman 1977) The Kellogg Global Hauser-Feshbach program (KGHFP) was produced by B. A. Zimmerman in collaboration with W. A. Fowler, J. A. Holmes, J. Powelson, and S. E. Woosley, unpublished.

(Zyskind 1977) J. L. Zyskind, R. Marrs, M. H. Shapiro, J. Davidson, C. A. Barnes, and W. A. Fowler, BAPS 22 (1977) 542.

(Zyskind 1978) J. L. Zyskind, J. M. Davidson, M. T. Esat, M. H. Shapiro, and R. H. Spear, Nucl. Phys. A301 (1978) 179.

(Zyskind 1979a) J. L. Zyskind, J. M. Davidson, R. E. Marrs, M. H. Shapiro, C. A. Barnes, and W. A. Fowler, in preparation.

(Zyskind 1979b) J. L. Zyskind, J. M. Davidson, M. T. Esat, M. H. Shapiro, and R. H. Spear, in preparation.

(Zyskind 1979c) J. L. Zyskind, J. M. Davidson, M. T. Esat, R. H. Spear, M. H. Shapiro, W. A. Fowler, and C. A. Barnes, Nucl. Phys. A315 (1979) 430.

TABLES

Table 1

For each reaction studied the energy range covered and Q values are given. Also given are the lowest energy thresholds for neutron production for each projectile-plus-target pair.

Table 1

REACTIONS STUDIED

Reaction	Energy Range (MeV Lab)	$E_{th}^{(a)}$ (MeV Lab)	$Q^{(a)}$ (MeV)
$^{54}Cr(p,\gamma)^{55}Mn$	0.83 - 3.61		8.068
$^{54}Cr(p,n)^{54}Mn$	2.23 - 3.61	2.199	-2.159
$^{51}V(p,\gamma)^{52}Cr$	0.93 - 4.47		10.505
$^{51}V(p,n)^{51}Cr$	1.58 - 4.47	1.564	-1.534
$^{48}Ca(p,\gamma)^{49}Sc$	0.58 - 2.67		9.627
$^{48}Ca(p,n)^{48}Sc$	0.96 - 2.67	0.511	-0.501
$^{68}Zn(p,\gamma)^{69}Ga$	1.64 - 4.97		6.604
$^{68}Zn(p,n)^{68}Ga$	3.77 - 5.03	3.758	3.704
$^{68}Zn(p,\alpha)^{65}Cu$	3.36 - 5.48		2.119
$^{37}Cl(\alpha,\gamma)^{41}K$	2.90 - 5.23		6.223
$^{37}Cl(\alpha,n)^{40}K$	- -	4.292	3.873
$^{62}Ni(\alpha,\gamma)^{66}Zn$	5.07 - 8.64		4.578
$^{62}Ni(\alpha,n)^{65}Zn$	6.95 - 8.76	6.901	-6.482
$^{64}Ni(\alpha,\gamma)^{68}Zn$	4.50 - 7.45		5.333
$^{64}Ni(\alpha,n)^{67}Zn$	5.29 - 7.42	5.169	-4.865

(a) A, H. Wapstra and K. Bos, Atomic Data and Nuclear Data Tables 18 (1976) 306.

Table 2

Information concerning targets is given. The thickness is that which the target presented to the beam in the orientation in which it was mounted. The target angle is noted when the target surface was not normal to the beam. In the column headed Method, the technique by which the target thickness was determined is given: weighing (weigh), shift of the backscattering edge (BSS) or relative yields from Rutherford scattering from the target layer and backing (BSR). For the backscattering measurements the type of beam (p or α) and energy are indicated. See Section IIC for details.

Table 2

Reaction	Comments	Target Material	Isotopic Enrichment (%)	Thickness ($\mu gm/cm^2$)	Method
$^{54}Cr(p,\gamma)^{55}Mn$ $^{54}Cr(p,n)^{54}Mn$		Cr metal	95.4	1180†	BSS 3 MeV p
$^{51}V(p,\gamma)^{52}Cr$ $^{51}V(p,n)^{51}Cr$	(cross section check)	V metal	nat. (99.74%)	1200 (190)	Weigh (BSR 3.7 MeV α)
$^{48}Ca(p,\gamma)^{49}Sc$ $^{48}Ca(p,n)^{48}Sc$		Ca metal → Ca O	97.78	185	BSR 4 MeV α
$^{68}Zn(p,\gamma)^{69}Ga$ $^{68}Zn(p,n)^{68}Ga$		Zn metal	96.95	675††	BSS 3 MeV p
$^{68}Zn(p,\alpha)^{65}Cu$	transmission target	Zn metal	96.95	122	BSR 3.36 MeV p
$^{37}Cl(\alpha,\gamma)^{41}K$		$PbCl_2$	96.5	280††	Weigh
$^{62}Ni(\alpha,\gamma)^{66}Zn$ $^{62}Ni(\alpha,n)^{65}Zn$		Ni metal	97.94	280	BSS 4 MeV α
$^{64}Ni(\alpha,\gamma)^{68}Zn$ $^{64}Ni(\alpha,n)^{67}Zn$		Ni metal	98.02	315	BSS 4 MeV α

† for target at 51°

†† for target at 45°

Table 3

The distance from the target to the face of the Ge(Li) can is given. The face of the crystal is less than 0.5 cm from the wall of the can. The column headed Lead gives the thickness of Pb shielding placed over the Ge(Li) face to attenuate low energy γ-rays from Coulomb excitation of the backing. The angle between the beam direction and a line drawn from the target through the detector axis is given in the last column. See Section IID.

Table 3

Ge(Li) DETECTOR GEOMETRIES

Reaction	Comments	Distance (cm)	Lead (cm)	Angle
$^{54}Cr(p,\gamma)^{55}Mn$		2.2	0	55°
$^{51}V(p,\gamma)^{52}Cr$		9.2	0.32	125°
$^{51}V(p,\gamma)^{52}Cr$	cross section check	2.8	0	55°
$^{48}Ca(p,\gamma)^{49}Sc$		2.5	0.32	55°
$^{68}Zn(p,\gamma)^{69}Ga$		2.8	0.16	55°
$^{37}Cl(\alpha,\gamma)^{41}K$		4.5	0.32	55°
$^{62}Ni(\alpha,\gamma)^{66}Zn$		3.3	0	55°
$^{64}Ni(\alpha,\gamma)^{68}Zn$		3.3	0	55°

Table 4

Information is given concerning the sources used in the γ-ray calibration. Half-lives and absolute branching ratios are specified only where absolutely calibrated sources were used. The column headed Daughter gives the daughter nucleus in which the transition occurs which gives rise to the γ-ray in question. See Section IID.

Table 4

GAMMA-RAY CALIBRATION LINES

Source	Daughter	E_γ (keV)	γ's per decay	Relative intensity	Half-life	Reference
^{22}Na	^{22}Ne	1275	0.9994		2.602 yr	Endt (1973)
^{56}Co	^{56}Fe	847		1.0		Kennedy (1977)
		1038		0.137±0.006		
		1238		0.662±0.010		
		1772		0.159±0.003		
		2035		0.078±0.001		
		2599		0.173±0.004		
		3202		0.032±0.001		
		3254		0.082±0.004		
		3452		0.0100±0.0004		
$^{27}Al(p,\gamma)$ (2.046 MeV res.)	^{28}Si	1779		1.004±0.021		Kennedy (1977)
		2839		0.606±0.013		
		4613		0.0084±0.006		
		5110		0.333±0.014		
		6669		0.300±0.010		
		8940		0.505±0.016		
$^{27}Al(p,\gamma)$ (1.800 MeV res)	^{28}Si	1779		1.00		Meyer (1975)
		11542		0.98		
^{133}Ba	^{133}Cs	276	0.073		10.5 yr	Henry (1974)
		302	0.186			pp. 514,534
		356	0.623			
		382	0.088			
^{226}Ra	^{214}Bi	242		0.0759±0.0009		Toth (1977)
	^{214}Bi	295		0.195±0.003		
	^{214}Bi	352		0.377±0.004		
	^{214}Po	609		0.469		
	^{214}Po	1120		0.153±0.003		
	^{214}Po	1238		0.0602±0.0006		
	^{214}Po	1764		0.162±0.003		
^{182}Ta	^{182}W	179		0.090±0.003		Schmorak (1975)
		198		0.044±0.002		(see esp. p.586)
		222		0.216±0.006		
		229		0.104±0.003		

Table 4 (continued)

Source	Daughter	E_γ (keV)	γ's per decay	Relative intensity	Half-life	Reference
		264		0.104±0.003		
		1121		1.00		
		1189		0.470±0.005		
		1221		0.783±0.101		
		1231		0.331±0.004		
^{207}Bi	^{207}Pb	570		1.00		Schmorak (1977)
		1064		0.766±0.010		(see esp. p.523)
		1770		0.070±0.002		

Table 5

The first two columns identify by excitation energy, E_x, and spin and parity, J^π (when known), all confirmed states in ^{55}Mn with excitation energies less than 3 MeV, and higher states, the decays of which give rise to γ-rays employed in the data analysis. The third and fourth columns give γ-ray energies for decay to the ground state and 126-keV first excited state, respectively, for the 13 γ-rays used to determine the excitation function. The fifth and sixth columns apply to other γ-rays used to determine the total cross sections as described in the text. Where no entry appears either no γ-ray was observed or the γ-ray was not used in the analysis. See Section IID.

Table 5

E_x (a) (keV)	J^π (a)	Gamma-Ray Energy (a) (keV)			
		Excitation Function		Cross Section	
		0	126	0	126
0	$5/2^-$				
126	$7/2^-$				
984	$(9/2^-)$		858		
1290	$(1/2^-)$			1290	1166
1292	$(11/2^-)$				
1293	$(5/2 - 9/2)^{(-)}$				
1529	$3/2^-$	1529			
1885	$(5/2, 7/2)^-$	1885			
2199	$7/2^{(-)}$	2199			
2215	$(5/2^-, 7/2^-)$			2215	
2253	$(1/2, 3/2)^-$	2253			
2269	$(1/2 - 5/2)$	2269			
2312	$(13/2)$			2312	
2367	$5/2^-$	2367	2241		
2399	$(5/2 - 9/2)^-$				
2429	$1/2^+$			2429	
2565	$3/2^-$	2565			
2582				2589	2463 (b)
2727	$7/2$	2727			
2753	$(5/2, 7/2)^-$			2753	2627
2823					
2825	$(5/2, 9/2)$	2825			
2874				2874	
2952				2952	
2975		2975			
2990	$(3/2, 5/2)^+$				
3004		3004			
3195		3195			
3351		3351			

Table 5 (continued)

E_x (a) (keV)	J^π (a)	Gamma-Ray Energy (a) (keV) Excitation Function 0	Excitation Function 126	Cross Section 0	Cross Section 126
3424					3298
3432				3432	
3528				3528	
3702				3702	
3860				3860	
3998	$(1/2, 3/2)^-$			3998	
4293				4293	
4373				4373	
Capture resonance				Variable	Variable

(a) D. C. Kocher, Nucl. Data Sheets 18 (1976) 463.

(b) Although their energies are inconsistent with those in (Kocher 1976), these two γ-rays were identified as arising from ^{55}Mn decay by the 126 keV energy difference.

Table 6

For each reaction the second column (Energy range) gives the range of bombarding energies over which excitation functions were extracted for the γ-rays listed in the third column (γ-rays summed). These γ-rays were used to determine the "preliminary" cross sections, as described in Chapter II, Section B. For energy ranges for which peak areas could not be extracted for some of the γ-rays, the sum for the smaller set of γ-rays is normalized to that using the larger number of γ-rays with the factor given. The last three columns (Corrections) give the corrections to the "preliminary" cross sections for group (i) transitions (primaries), group (ii) transitions (secondaries), and the sum of the two (total). See Chapter II, Section E for a complete description of these cross section determinations.

Table 6

GAMMA-RAY ANALYSIS

Reaction	Energy Range (MeV)	γ-rays summed (E_γ in keV)	Normalization	Corrections: weak primaries %	Corrections: weak secondaries %	Corrections: total %
$^{54}Cr(p,\gamma)^{55}Mn$	$\leq$ 3.2	858 1529 1885 2199 2241 2253 2269 2367 2565 2727 2825 2975 3004	-	10	18	28
	$\geq$ 3.2	1529 1885 2253 2269 2565 2727 2975	1.14±0.01			
$^{51}V(p,\gamma)^{52}Cr$	all	1434	-			0($\lesssim$ 1%)
$^{48}Ca(p,\gamma)^{49}Sc$	all	2229 2372 3085		1%	14	14
$^{68}Zn(p,\gamma)^{69}Ga$	$\leq$ 4.0	318 574 872 1027 1107 1335 1487 1526 1573 1723 1972 2002 2022 2044		8-1	8	16-9

Reaction	Energy Range (MeV)	γ-rays summed (E_γ in keV)	Normalization	Corrections: primaries %	Corrections: weak secondaries %	Corrections: total %
	4.1-4.85	872 1107 1335 1487 1723 1972 2002 2022 2044	2.214±0.0004			
	4.91-4.97	872 1723 1972 2002 2022	4.763±0.191			
$^{37}Cl(\alpha,\gamma)^{41}K$		980 1294 1560 1677 1698	-	5	21	26
$^{62}Ni(\alpha,\gamma)^{66}Zn$		1039	-	∿4	3-3.8	7-8
$^{64}Ni(\alpha,\gamma)^{65}Zn$		1077	-	2.5	9.4	12

Table 7

Cross sections measured for the reaction $^{51}V(p,\gamma)^{52}Cr$. The first and second columns give the effective energies in the laboratory and center-of-mass systems, respectively. The fourth column gives the uncertainties arising only from the statistics of counting. The ratios of the cross sections calculated by Woosley et al. (1975) [from which were calculated the thermonuclear rates which are to be published (Woosley 1979)] to those measured are given in the fifth column for selected energies. See Section IIE for further details.

Table 7

Cross Sections for $^{51}V(p,\gamma)^{52}Cr$

E_{eff}^{lab} (MeV)	E_{eff}^{cm} (MeV)	$\sigma_{p\gamma}$ (mb)	$\Delta\sigma_{p\gamma}$ (mb)	$\frac{\sigma_{OAP-422}}{\sigma_{p\gamma}}$
0.925	0.907	1.07×10^{-2}	7.9×10^{-4}	
0.977	0.958	1.14×10^{-2}	8.1×10^{-4}	
1.029	1.009	1.61×10^{-2}	7.1×10^{-4}	1.5
1.080	1.059	2.41×10^{-2}	1.1×10^{-3}	
1.132	1.110	3.90×10^{-2}	1.4×10^{-3}	
1.182	1.159	6.21×10^{-2}	1.8×10^{-3}	
1.232	1.208	7.35×10^{-2}	1.9×10^{-3}	
1.284	1.259	9.41×10^{-2}	2.2×10^{-3}	
1.334	1.308	1.28×10^{-1}	2.5×10^{-3}	
1.386	1.359	1.68×10^{-1}	2.9×10^{-3}	
1.436	1.408	1.84×10^{-1}	3.0×10^{-3}	
1.488	1.459	2.52×10^{-1}	3.5×10^{-3}	
1.537	1.507	2.88×10^{-1}	3.8×10^{-3}	1.8
1.583	1.553	2.43×10^{-1}	3.5×10^{-3}	(threshold)
1.631	1.600	1.47×10^{-1}	2.7×10^{-3}	
1.686	1.654	1.12×10^{-1}	2.4×10^{-3}	
1.739	1.706	8.91×10^{-2}	2.2×10^{-3}	
1.789	1.755	1.07×10^{-1}	2.3×10^{-3}	
1.841	1.806	1.07×10^{-1}	1.8×10^{-3}	
1.892	1.856	1.23×10^{-1}	5.9×10^{-3}	
1.943	1.906	1.04×10^{-1}	4.0×10^{-3}	
1.995	1.957	1.20×10^{-1}	6.1×10^{-3}	
2.045	2.006	1.47×10^{-1}	7.1×10^{-3}	0.35
2.096	2.056	1.64×10^{-1}	1.1×10^{-2}	
2.147	2.106	1.51×10^{-1}	7.0×10^{-3}	
2.197	2.155	1.61×10^{-1}	7.3×10^{-3}	
2.248	2.205	1.35×10^{-1}	6.2×10^{-3}	

Table 7 (continued)

E_{eff}^{lab} (MeV)	E_{eff}^{cm} (MeV)	$\sigma_{p\gamma}$ (mb)	$\Delta\sigma_{p\gamma}$ (mb)	$\frac{\sigma_{OAP-422}}{\sigma_{p\gamma}}$
2.299	2.255	2.05×10^{-1}	1.08×10^{-2}	
2.350	2.305	1.70×10^{-1}	7.5×10^{-3}	
2.400	2.354	1.27×10^{-1}	5.8×10^{-3}	
2.451	2.404	1.54×10^{-1}	3.5×10^{-3}	
2.502	2.454	2.38×10^{-1}	1.2×10^{-2}	
2.552	2.503	2.04×10^{-1}	1.03×10^{2}	0.5
2.603	2.553	2.09×10^{-1}	1.15×10^{-2}	
2.654	2.603	2.33×10^{-1}	1.5×10^{-2}	
2.704	2.652	1.89×10^{-1}	9.3×10^{-3}	
2.755	2.702	2.19×10^{-1}	1.08×10^{-2}	
2.799	2.744	2.20×10^{-1}	4.8×10^{-3}	
2.848	2.793	2.60×10^{-1}	5.1×10^{-3}	
2.900	2.844	2.25×10^{-1}	5.0×10^{-3}	
2.950	2.893	2.67×10^{-1}	5.7×10^{-3}	
3.001	2.943	2.44×10^{-1}	5.7×10^{-3}	
3.052	2.993	2.27×10^{-1}	6.5×10^{-3}	0.8
3.102	3.042	2.33×10^{-1}	7.0×10^{-3}	
3.153	3.092	1.85×10^{-1}	7.5×10^{-3}	
3.204	3.142	2.08×10^{-1}	7.7×10^{-3}	
3.255	3.192	1.95×10^{-1}	9.2×10^{-3}	
3.305	3.241	2.39×10^{-1}	1.09×10^{-2}	
3.355	3.290	2.09×10^{-1}	1.06×10^{-2}	
3.404	3.339	1.62×10^{-1}	1.03×10^{-2}	
3.456	3.390	1.75×10^{-1}	1.16×10^{-2}	
3.513	3.445	1.85×10^{-1}	1.7×10^{-2}	
3.563	3.494	2.06×10^{-1}	2.1×10^{-2}	1.4
3.612	3.543	2.20×10^{-1}	2.5×10^{-2}	
3.662	3.592	2.86×10^{-1}	2.9×10^{-2}	
3.713	3.642	2.08×10^{-1}	3.0×10^{-2}	

Table 7 (continued)

E_{eff}^{lab} (MeV)	E_{eff}^{cm} (MeV)	$\sigma_{p\gamma}$ (mb)	$\Delta\sigma_{p\gamma}$ (mb)	$\frac{\sigma_{OAP-422}}{\sigma_{p\gamma}}$
3.763	3.691	2.46×10^{-1}	2.7×10^{-2}	
3.814	3.741	2.31×10^{-1}	3.3×10^{-2}	
3.864	3.790	2.05×10^{-1}	2.7×10^{-2}	
3.914	3.839	2.34×10^{-1}	3.1×10^{-2}	
3.964	3.888	2.45×10^{-1}	3.5×10^{-2}	1.5
4.015	3.938	2.74×10^{-1}	3.1×10^{-2}	
4.065	3.987	2.29×10^{-1}	3.2×10^{-2}	
4.116	4.037	2.53×10^{-1}	3.5×10^{-2}	
4.166	4.086	2.34×10^{-1}	3.5×10^{-2}	
4.216	4.135	2.33×10^{-1}	3.3×10^{-2}	
4.266	4.184	3.19×10^{-1}	3.6×10^{-2}	
4.316	4.233	2.60×10^{-1}	3.4×10^{-2}	
4.367	4.283	2.57×10^{-1}	4.0×10^{-2}	
4.417	4.332	3.06×10^{-1}	4.0×10^{-2}	
4.467	4.381	3.29×10^{-1}	3.7×10^{-2}	

Table 8

Cross sections measured for the reaction $^{54}Cr(p,\gamma)^{55}Mn$. The first and second columns give the effective energies in the laboratory and center-of-mass systems, respectively. The fourth column gives the uncertainties arising only from the statistics of counting. The ratios of the cross sections calculated by Woosley et al. (1975) [from which were calculated the thermonuclear rates which are to be published (Woosley 1979)] to those measured are given in the fifth column for selected energies. See Section IIE for further details.

Table 8

Cross Sections for $^{54}Cr(p,\gamma)^{55}Mn$

E_{eff}^{lab} (MeV)	E_{eff}^{cm} (MeV)	$\sigma_{p\gamma}$ (mb)	$\Delta\sigma_{p\gamma}$ (mb)	$\frac{\sigma_{OAP-422}}{\sigma_{p\gamma}}$
0.796	0.782	1.41×10^{-3}	2.4×10^{-4}	
0.849	0.834	4.21×10^{-3}	6.8×10^{-4}	
0.901	0.885	7.01×10^{-3}	5.6×10^{-4}	
0.954	0.937	1.08×10^{-2}	6.8×10^{-4}	
1.007	0.989	2.30×10^{-2}	1.4×10^{-3}	0.9
1.059	1.040	2.78×10^{-2}	1.2×10^{-3}	
1.111	1.091	2.99×10^{-2}	2.2×10^{-3}	
1.163	1.142	5.93×10^{-2}	2.1×10^{-3}	
1.215	1.193	8.57×10^{-2}	4.9×10^{-3}	
1.267	1.244	1.22×10^{-1}	5.8×10^{-3}	
1.318	1.294	1.52×10^{-1}	6.3×10^{-3}	
1.370	1.345	1.46×10^{-1}	7.0×10^{-3}	
1.422	1.396	2.07×10^{-1}	7.9×10^{-3}	
1.473	1.446	2.12×10^{-1}	8.1×10^{-3}	
1.525	1.497	2.77×10^{-1}	9.0×10^{-3}	1.1
1.576	1.547	3.53×10^{-1}	1.0×10^{-2}	
1.628	1.598	4.20×10^{-1}	1.1×10^{-2}	
1.679	1.648	5.57×10^{-1}	1.3×10^{-2}	
1.730	1.699	6.44×10^{-1}	1.4×10^{-2}	
1.781	1.749	6.66×10^{-1}	1.5×10^{-2}	
1.832	1.799	7.68×10^{-1}	1.6×10^{-2}	
1.883	1.849	8.18×10^{-1}	1.6×10^{-2}	
1.934	1.899	1.06	8.2×10^{-3}	
1.985	1.949	1.27	2.0×10^{-2}	
2.036	1.999	1.20	2.0×10^{-2}	0.8
2.087	2.049	1.02	1.8×10^{-2}	
2.138	2.099	1.01	1.8×10^{-2}	

Table 8 (continued)

E_{eff}^{lab} (MeV)	E_{eff}^{cm} (MeV)	$\sigma_{p\gamma}$ (mb)	$\Delta\sigma_{p\gamma}$ (mb)	$\frac{\sigma_{OAP-422}}{\sigma_{p\gamma}}$
2.189	2.149	1.01	1.8×10^{-2}	
2.240	2.199	8.55×10^{-1}	1.7×10^{-2}	(threshold)
2.290	2.248	6.07×10^{-1}	1.4×10^{-2}	
2.341	2.298	4.10×10^{-1}	1.2×10^{-2}	
2.392	2.349	3.68×10^{-1}	1.1×10^{-2}	
2.443	2.399	2.84×10^{-1}	1.1×10^{-2}	
2.494	2.449	2.74×10^{-1}	1.1×10^{-2}	
2.544	2.498	3.09×10^{-1}	8.2×10^{-3}	0.08
2.595	2.548	3.66×10^{-1}	1.0×10^{-2}	
2.646	2.598	3.10×10^{-1}	8.9×10^{-3}	
2.696	2.647	2.37×10^{-1}	7.6×10^{-3}	
2.747	2.697	1.83×10^{-1}	7.3×10^{-3}	
2.798	2.747	1.83×10^{-1}	7.6×10^{-3}	
2.848	2.796	1.84×10^{-1}	7.6×10^{-3}	
2.899	2.846	1.91×10^{-1}	7.8×10^{-3}	
2.950	2.896	2.17×10^{-1}	8.0×10^{-3}	
3.000	2.945	2.06×10^{-1}	7.8×10^{-3}	
3.051	2.996	2.33×10^{-1}	8.5×10^{-3}	0.14
3.102	3.046	2.56×10^{-1}	9.4×10^{-3}	
3.152	3.095	2.24×10^{-1}	8.9×10^{-3}	
3.203	3.145	2.12×10^{-1}	8.5×10^{-3}	
3.253	3.194	2.28×10^{-1}	8.7×10^{-3}	
3.304	3.244	2.67×10^{-1}	8.9×10^{-3}	
3.354	3.293	2.66×10^{-1}	1.04×10^{-2}	
3.405	3.343	2.69×10^{-1}	1.4×10^{-2}	
3.455	3.392	3.31×10^{-1}	1.6×10^{-2}	
3.506	3.442	3.09×10^{-1}	1.9×10^{-2}	
3.556	3.491	2.48×10^{-1}	1.7×10^{-2}	0.19
3.606	3.540	2.39×10^{-1}	2.0×10^{-2}	

Table 9

Cross sections measured for the reaction $^{68}Zn(p,\gamma)^{69}Ga$. The first and second columns give the effective energies in the laboratory and center-of-mass systems, respectively. The fourth column gives the uncertainties arising only from the statistics of counting. The ratios of the cross sections calculated by Woosley et al. (1975) [from which were calculated the thermonuclear rates soon to be published (Woosley 1979)] to those measured are given in the fifth column for selected energies. See Section IIE for further details.

Table 9

Cross Sections for $^{68}Zn(p,\gamma)^{68}Ga$

E_{eff}^{lab} (MeV)	E_{eff}^{cm} (MeV)	$\sigma_{p\gamma}$ (mb)	$\Delta\sigma_{p\gamma}$ (mb)	$\frac{\sigma_{OAP\ 422}}{\sigma_{p\gamma}}$
1.669	1.645	1.06×10^{-1}	5.8×10^{-3}	
1.700	1.675	1.30×10^{-1}	6.6×10^{-3}	1.0
1.730	1.705	1.60×10^{-1}	7.1×10^{-3}	
1.760	1.734	2.34×10^{-1}	8.0×10^{-3}	
1.790	1.764	2.36×10^{-1}	8.3×10^{-3}	
1.820	1.794	2.36×10^{-1}	8.1×10^{-3}	
1.851	1.824	2.41×10^{-1}	8.4×10^{-3}	
1.881	1.854	3.23×10^{-1}	9.2×10^{-3}	
1.931	1.903	3.59×10^{-1}	9.8×10^{-3}	
1.981	1.952	3.83×10^{-1}	1.0×10^{-2}	
2.032	2.003	5.13×10^{-1}	1.2×10^{-2}	0.9
2.082	2.052	6.13×10^{-1}	1.3×10^{-2}	
2.132	2.101	7.79×10^{-1}	1.4×10^{-2}	
2.182	2.150	8.05×10^{-1}	1.5×10^{-2}	
2.233	2.201	9.58×10^{-1}	1.6×10^{-2}	
2.283	2.250	1.11×10^{0}	1.8×10^{-2}	
2.333	2.299	1.38×10^{0}	2.0×10^{-2}	
2.358	2.324	1.47×10^{0}	2.1×10^{-2}	
2.383	2.348	1.38×10^{0}	2.0×10^{-2}	
2.408	2.373	1.47×10^{0}	2.0×10^{-2}	
2.434	2.399	1.60×10^{0}	2.1×10^{-2}	
2.459	2.423	1.66×10^{0}	2.2×10^{-2}	
2.484	2.448	1.78×10^{0}	2.3×10^{-2}	
2.509	2.473	1.93×10^{0}	2.3×10^{-2}	
2.534	2.497	2.05×10^{0}	2.4×10^{-2}	1.0
2.559	2.522	2.07×10^{0}	2.5×10^{-2}	
2.584	2.547	2.25×10^{0}	2.6×10^{-2}	

Table 9 (continued)

E_{eff}^{lab} (MeV)	E_{eff}^{cm} (MeV)	$\sigma_{p\gamma}$ (mb)	$\Delta\sigma_{p\gamma}$ (mb)	$\frac{\sigma_{OAP\ 422}}{\sigma_{p\gamma}}$
2.609	2.571	2.32×10^{0}	2.6×10^{-2}	
2.634	2.596	2.40×10^{0}	2.7×10^{-2}	
2.659	2.620	2.45×10^{0}	2.7×10^{-2}	
2.684	2.645	2.58×10^{0}	2.8×10^{-2}	
2.710	2.671	2.72×10^{0}	2.8×10^{-2}	
2.735	2.695	2.90×10^{0}	3.0×10^{-2}	
2.760	2.720	2.88×10^{0}	2.9×10^{-2}	
2.785	2.745	2.87×10^{0}	1.5×10^{-2}	
2.810	2.769	3.08×10^{0}	3.1×10^{-2}	
2.835	2.794	3.20×10^{0}	< 1%	
2.860	2.819	3.38×10^{0}	"	
2.885	2.843	3.68×10^{0}	"	
2.910	2.868	3.45×10^{0}	"	
2.960	2.917	3.70×10^{0}	"	
2.986	2.943	4.24×10^{0}	"	
3.011	2.967	4.61×10^{0}	"	
3.036	2.992	4.22×10^{0}	"	
3.061	3.017	4.41×10^{0}	"	1.1
3.086	3.041	4.36×10^{0}	"	
3.111	3.066	4.41×10^{0}	"	
3.136	3.091	4.68×10^{0}	"	
3.161	3.115	4.80×10^{0}	"	
3.186	3.140	5.00×10^{0}	"	
3.211	3.164	5.12×10^{0}	"	
3.236	3.189	5.65×10^{0}	"	
3.261	3.214	5.79×10^{0}	"	
3.286	3.238	5.61×10^{0}	"	
3.311	3.263	5.64×10^{0}	"	
3.336	3.288	5.55×10^{0}	"	

Table 9 (continued)

E_{eff}^{lab} (MeV)	E_{eff}^{cm} (MeV)	$\sigma_{p\gamma}$ (mb)	$\Delta\sigma_{p\gamma}$ (mb)	$\frac{\sigma_{OAP\ 422}}{\sigma_{p\gamma}}$
3.361	3.312	5.76×10^{0}	< 1%	
3.387	3.338	6.00×10^{0}	"	
3.412	3.363	6.47×10^{0}	"	
3.437	3.387	6.48×10^{0}	"	
3.462	3.412	6.90×10^{0}	"	
3.487	3.436	6.83×10^{0}	"	
3.512	3.461	7.10×10^{0}	"	
3.537	3.486	7.25×10^{0}	"	
3.562	3.510	6.99×10^{0}	"	1.1
3.587	3.535	7.17×10^{0}	"	
3.612	3.560	7.75×10^{0}	"	
3.637	3.584	8.10×10^{0}	"	
3.662	3.609	7.37×10^{0}	"	
3.687	3.732	8.59×10^{0}	"	
3.712	3.658	9.20×10^{0}	"	
3.737	3.683	8.58×10^{0}	"	
3.762	3.707	7.66×10^{0}	"	(threshold)
3.787	3.732	7.42×10^{0}	"	
3.813	3.758	7.30×10^{0}	"	
3.838	3.782	7.53×10^{0}	"	
3.863	3.807	6.42×10^{0}	"	
3.888	3.832	6.66×10^{0}	"	
3.913	3.856	6.41×10^{0}	"	
3.938	3.881	5.57×10^{0}	"	
3.963	3.906	5.06×10^{0}	"	
3.988	3.930	4.68×10^{0}	"	
4.008	3.950	4.62×10^{0}	7.3×10^{-2}	
4.028	3.970	4.50×10^{0}	7.5×10^{-2}	
4.048	3.989	4.70×10^{0}	8.0×10^{-2}	

Table 9 (continued)

E_{eff}^{lab} (MeV)	E_{eff}^{cm} (MeV)	$\sigma_{p\gamma}$ (mb)	$\Delta\sigma_{p\gamma}$ (mb)	$\frac{\sigma_{OAP\ 422}}{\sigma_{p\gamma}}$
4.068	4.009	5.16×10^{0}	9.1×10^{-2}	0.4
4.088	4.029	5.38×10^{0}	9.0×10^{-2}	
4.108	4.048	5.15×10^{0}	8.5×10^{-2}	
4.128	4.068	3.82×10^{0}	7.6×10^{-2}	
4.148	4.088	2.84×10^{0}	6.7×10^{-2}	
4.168	4.108	2.36×10^{0}	6.2×10^{-2}	
4.188	4.127	2.17×10^{0}	6.1×10^{-2}	
4.208	4.147	1.83×10^{0}	6.2×10^{-2}	
4.228	4.167	1.86×10^{0}	6.4×10^{-2}	
4.248	4.186	1.91×10^{0}	7.0×10^{-2}	
4.268	4.206	2.10×10^{0}	6.9×10^{-2}	
4.288	4.226	1.82×10^{0}	6.2×10^{-2}	
4.308	4.246	1.78×10^{0}	6.4×10^{-2}	
4.328	4.265	1.95×10^{0}	6.4×10^{-2}	
4.348	4.285	1.68×10^{0}	6.4×10^{-2}	
4.369	4.306	1.43×10^{0}	6.4×10^{-2}	
4.389	4.325	1.66×10^{0}	6.7×10^{-2}	
4.409	4.345	1.52×10^{0}	6.8×10^{-2}	
4.429	4.365	1.48×10^{0}	6.8×10^{-2}	
4.449	4.385	1.31×10^{0}	7.0×10^{-2}	
4.469	4.404	1.47×10^{0}	7.3×10^{-2}	
4.489	4.424	1.47×10^{0}	7.5×10^{-2}	
4.509	4.444	1.53×10^{0}	7.5×10^{-2}	
4.529	4.463	1.38×10^{0}	1.3×10^{-2}	
4.549	4.483	1.30×10^{0}	1.3×10^{-2}	
4.569	4.503	1.055×10^{0}	1.2×10^{-1}	0.5
4.589	4.522	1.26×10^{0}	1.2×10^{-1}	
4.609	4.542	1.22×10^{0}	1.1×10^{-1}	
4.629	4.562	1.43×10^{0}	1.2×10^{-1}	
4.649	4.582	1.41×10^{0}	1.2×10^{-1}	

Table 9 (continued)

E_{eff}^{lab} (MeV)	E_{eff}^{cm} (MeV)	$\sigma_{p\gamma}$ (mb)	$\Delta\sigma_{p\gamma}$ (mb)	$\frac{\sigma_{OAP\ 422}}{\sigma_{p\gamma}}$
4.669	4.601	1.53×10^{0}	1.2×10^{-1}	
4.729	4.660	1.37×10^{0}	1.5×10^{-1}	
4.789	4.720	1.50×10^{0}	1.2×10^{-1}	
4.849	4.779	1.30×10^{0}	1.3×10^{-1}	
4.909	4.838	1.52×10^{0}	1.9×10^{-1}	
4.969	4.897	1.38×10^{0}	1.8×10^{-1}	0.3

Table 10

Cross sections measured for the reaction $^{48}Ca(p\gamma)^{49}Sc$. The first and second columns give the effective energies in the laboratory and center-of-mass systems, respectively. The fourth column gives the uncertainties arising only from the statistics of counting. The ratios of the cross sections calculated by Woosley et al. (1975) [from which were calculated the thermonuclear rates soon to be published (Woosley 1979)] to those measured are given in the fifth column for selected energies. See Section IIE and Appendix B for further details, and see Appendix B for a calculation of thermonuclear reaction rates from the measured cross sections.

Table 10

E_{eff}^{lab} (MeV)	E_{eff}^{cm} (MeV)	$\sigma_{p\gamma}$ (mb)	$\Delta\sigma_{p\gamma}$ (mb)	$\frac{\sigma_{OAP\ 422}^{*}}{\sigma_{p\gamma}}$
0.579	0.569	4.1×10^{-4}	1.6×10^{-4}	
0.609	0.597	9.5×10^{-4}	1.2×10^{-4}	
0.639	0.626	1.43×10^{-3}	2.0×10^{-4}	
0.670	0.656	1.90×10^{-3}	2.2×10^{-4}	
0.700	0.686	1.26×10^{-3}	1.8×10^{-4}	
0.731	0.716	3.86×10^{-3}	3.1×10^{-4}	
0.755	0.740	3.51×10^{-3}	3.1×10^{-4}	
0.781	0.765	3.59×10^{-3}	3.2×10^{-4}	
0.806	0.790	1.76×10^{-2}	6.7×10^{-4}	
0.831	0.814	1.56×10^{-2}	6.8×10^{-4}	
0.857	0.840	3.88×10^{-3}	3.1×10^{-4}	
0.881	0.863	9.03×10^{-3}	7.5×10^{-4}	
0.906	0.888	1.73×10^{-2}	9.0×10^{-4}	
0.931	0.912	3.46×10^{-2}	1.4×10^{-3}	
0.956	0.937	6.13×10^{-2}	1.7×10^{-3}	
0.982	0.962	5.01×10^{-2}	1.6×10^{-3}	
1.007	0.986	4.64×10^{-2}	1.6×10^{-3}	
1.032	1.011	1.00×10^{-1}	2.4×10^{-3}	
1.057	1.035	6.77×10^{-1}	2.0×10^{-3}	
1.082	1.060	4.20×10^{-2}	1.6×10^{-3}	
1.108	1.085	7.58×10^{-2}	2.0×10^{-3}	
1.133	1.110	1.013×10^{-1}	2.4×10^{-3}	
1.158	1.134	7.04×10^{-2}	2.0×10^{-3}	
1.183	1.159	8.26×10^{-2}	2.1×10^{-3}	
1.209	1.184	1.18×10^{-1}	2.5×10^{-3}	
1.234	1.209	8.02×10^{-2}	1.8×10^{-3}	
1.259	1.233	1.75×10^{-2}	1.4×10^{-3}	
1.284	1.258	1.19×10^{-1}	3.1×10^{-3}	

Table 10 (continued)

E_{eff}^{lab} (MeV)	E_{eff}^{cm} (MeV)	$\sigma_{p\gamma}$ (mb)	$\Delta\sigma_{p\gamma}$ (mb)	$\frac{\sigma_{OAP\ 422}*}{\sigma_{p\gamma}}$
1.309	1.282	4.94×10^{-2}	2.0×10^{-3}	
1.335	1.308	9.55×10^{-2}	2.9×10^{-3}	
1.360	1.332	8.38×10^{-2}	2.7×10^{-3}	
1.385	1.357	7.32×10^{-2}	2.4×10^{-3}	
1.410	1.381	6.32×10^{-2}	2.4×10^{-3}	
1.435	1.406	7.57×10^{-2}	2.5×10^{-3}	
1.460	1.430	8.06×10^{-2}	2.5×10^{-3}	
1.486	1.456	1.40×10^{-1}	3.3×10^{-3}	
1.516	1.485	1.10×10^{-1}	2.9×10^{-3}	
1.536	1.505	9.38×10^{-2}	2.8×10^{-3}	
1.566	1.534	1.40×10^{-2}	3.4×10^{-3}	
1.586	1.554	6.16×10^{-2}	2.3×10^{-3}	
1.611	1.578	7.10×10^{-2}	2.4×10^{-3}	
1.637	1.604	1.08×10^{-1}	3.0×10^{-3}	
1.682	1.648	1.33×10^{-1}	3.3×10^{-3}	
1.707	1.672	7.95×10^{-2}	2.7×10^{-3}	
1.732	1.697	9.61×10^{-2}	2.8×10^{-3}	
1.757	1.721	1.26×10^{-1}	3.4×10^{-3}	
1.782	1.746	8.18×10^{-2}	2.7×10^{-3}	
1.807	1.770	3.36×10^{-2}	2.4×10^{-3}	
1.833	1.796	8.44×10^{-2}	3.6×10^{-3}	
1.858	1.820	1.22×10^{-1}	4.2×10^{-3}	
1.883	1.845	4.24×10^{-2}	3.7×10^{-3}	
1.908	1.869	2.02×10^{-1}	7.5×10^{-3}	
1.933	1.894	1.25×10^{-1}	5.8×10^{-3}	
1.948	1.908	1.53×10^{-1}	7.3×10^{-3}	
1.973	1.933	4.86×10^{-1}	1.2×10^{-3}	
1.988	1.947	2.98×10^{-1}	8.3×10^{-3}	
2.008	1.967	5.63×10^{-2}	3.3×10^{-3}	

Table 10 (continued)

E_{eff}^{lab} (MeV)	E_{eff}^{cm} (MeV)	$\sigma_{p\gamma}$ (mb)	$\Delta\sigma_{p\gamma}$ (mb)	$\frac{\sigma_{OAP\ 422}*}{\sigma_{p\gamma}}$
2.028	1.987	4.71×10^{-2}	2.7×10^{-3}	
2.048	2.006	4.72×10^{-2}	3.7×10^{-3}	
2.069	2.027	1.046×10^{-1}	5.2×10^{-3}	
2.089	2.046	1.74×10^{-1}	6.2×10^{-3}	
2.109	2.066	4.40×10^{-2}	3.8×10^{-3}	
2.129	2.086	7.79×10^{-2}	5.4×10^{-3}	
2.149	2.105	1.13×10^{-1}	5.2×10^{-3}	
2.169	2.125	6.11×10^{-2}	4.3×10^{-3}	
2.189	2.144	7.68×10^{-2}	4.5×10^{-3}	
2.209	2.164	8.18×10^{-2}	4.9×10^{-3}	
2.229	2.184	5.12×10^{-2}	4.2×10^{-3}	
2.249	2.203	4.14×10^{-2}	3.5×10^{-3}	
2.269	2.223	3.52×10^{-2}	3.3×10^{-3}	
2.289	2.242	5.95×10^{-2}	4.2×10^{-3}	
2.309	2.262	4.31×10^{-2}	4.0×10^{-3}	
2.329	2.281	9.11×10^{-2}	4.8×10^{-3}	
2.349	2.301	7.68×10^{-2}	4.7×10^{-3}	
2.370	2.322	5.04×10^{-2}	4.2×10^{-3}	
2.390	2.341	7.95×10^{-2}	5.2×10^{-3}	
2.410	2.361	7.01×10^{-2}	5.3×10^{-3}	
2.430	2.380	4.70×10^{-2}	4.5×10^{-3}	
2.450	2.400	4.11×10^{-2}	4.3×10^{-3}	
2.470	2.420	5.76×10^{-2}	4.9×10^{-3}	
2.490	2.439	4.95×10^{-2}	4.4×10^{-3}	
2.510	2.459	8.50×10^{-2}	6.0×10^{-3}	
2.530	2.478	9.05×10^{-2}	6.0×10^{-3}	
2.550	2.498	4.95×10^{-2}	4.7×10^{-3}	
2.570	2.518	4.41×10^{-2}	4.8×10^{-3}	
2.590	2.537	5.64×10^{-2}	3.5×10^{-3}	
2.610	2.557	8.66×10^{-2}	4.6×10^{-3}	

Table 10 (continued)

E_{eff}^{lab} (MeV)	E_{eff}^{cm} (MeV)	$\sigma_{p\gamma}$ (mb)	$\Delta\sigma_{p\gamma}$ (mb)	$\frac{\sigma_{OAP\ 422}*}{\sigma_{p\gamma}}$
2.630	2.576	1.18×10^{-1}	6.2×10^{-3}	
2.650	2.596	1.46×10^{-1}	4.8×10^{-3}	
2.670	2.616	5.39×10^{-2}	3.9×10^{-3}	

*No values are given. Because of the inclusion of a nonexistent 2^+ state at E_x = 388 keV in ^{48}Sc, the calculated cross sections are severely in error in almost the whole energy range studied.

Table 11

Cross sections measured for the reaction $^{37}Cl(\alpha,\gamma)^{41}K$. The first and second columns give the effective energies in the laboratory and center-of-mass systems, respectively. The fourth column gives the uncertainties arising only from the statistics of counting. The ratios of the cross sections calculated by Woosley et al. (1975) [from which were calculated the thermonuclear rates soon to be published (Woosley 1979)] to those measured are given in the fifth column for selected energies. See Section IIE for further details.

Table 11

Cross Sections for $^{37}Cl(\alpha,\gamma)^{41}K$

E_{eff}^{lab} (MeV)	E_{eff}^{cm} (MeV)	$\sigma_{\alpha\gamma}$ (mb)	$\Delta\sigma_{\alpha\gamma}$ (mb)	$\frac{\sigma_{OAP\ 422}}{\sigma_{\alpha\gamma}}$
2.942	2.655	4.78×10^{-3}	2.8×10^{-3}	
3.043	2.746	9.59×10^{-3}	3.9×10^{-3}	
3.144	2.837	1.63×10^{-2}	4.3×10^{-3}	
3.244	2.928	2.17×10^{-2}	6.2×10^{-3}	
3.345	3.019	2.82×10^{-2}	6.2×10^{-3}	1.0
3.446	3.110	4.28×10^{-2}	5.3×10^{-3}	
3.547	3.210	4.89×10^{-2}	5.8×10^{-3}	
3.647	3.291	7.81×10^{-2}	4.6×10^{-3}	
3.748	3.382	7.94×10^{-2}	7.1×10^{-3}	
3.849	3.473	9.73×10^{-2}	8.8×10^{-3}	1.1
3.949	3.564	1.16×10^{-1}	1.1×10^{-2}	
4.050	3.655	1.43×10^{-1}	1.1×10^{-2}	
4.100	3.700	1.43×10^{-1}	1.1×10^{-2}	
4.150	3.745	1.58×10^{-1}	1.2×10^{-2}	
4.200	3.790	2.11×10^{-1}	1.1×10^{-2}	
4.250	3.835	2.30×10^{-1}	6.9×10^{-3}	
4.301	3.881	1.94×10^{-1}	1.03×10^{-2}	(threshold)
4.351	3.927	1.25×10^{-1}	9.3×10^{-3}	
4.401	3.972	8.67×10^{-2}	7.3×10^{-3}	
4.451	4.017	9.02×10^{-2}	4.3×10^{-3}	0.2
4.501	4.062	7.49×10^{-2}	5.1×10^{-3}	
4.552	4.108	8.16×10^{-2}	4.4×10^{-3}	
4.602	4.153	6.69×10^{-2}	3.0×10^{-3}	
4.652	4.198	5.86×10^{-2}	5.6×10^{-3}	
4.702	4.243	7.37×10^{-2}	5.7×10^{-3}	
4.752	4.288	7.02×10^{-2}	4.8×10^{-3}	
4.803	4.334	7.83×10^{-2}	5.9×10^{-3}	

Table 11 (continued)

E_{eff}^{lab} (MeV)	E_{eff}^{cm} (MeV)	$\sigma_{\alpha\gamma}$ (mb)	$\Delta\sigma_{\alpha\gamma}$ (mb)	$\frac{\sigma_{OAP\ 422}}{\sigma_{\alpha\gamma}}$
4.853	4.380	7.27×10^{-2}	6.5×10^{-3}	
4.903	4.425	7.92×10^{-2}	8.4×10^{-3}	
4.953	4.470	8.68×10^{-2}	8.4×10^{-3}	
5.003	4.515	8.41×10^{-2}	7.6×10^{-3}	0.2
5.053	4.560	1.03×10^{-1}	1.07×10^{-2}	
5.104	4.606	1.06×10^{-1}	1.1×10^{-2}	
5.154	4.651	7.86×10^{-1}	1.1×10^{-2}	
5.204	4.696	9.06×10^{-1}	1.3×10^{-2}	
5.254	4.741	8.88×10^{-1}	1.3×10^{-2}	

Table 12

Cross sections measured for the reaction $^{62}Ni(\alpha,\gamma)^{66}Zn$. The first and second columns give the effective energies in the laboratory and center-of-mass systems, respectively. The fourth column gives the uncertainties arising only from the statistics of counting. The ratios of the cross sections calculated by Woosley et al. (1975) [from which were calculated the thermonuclear rates soon to be published (Woosley 1979)] to those measured are given in the fifth column for selected energies. See Section IIE for further details.

Table 12

Cross Sections for $^{62}Ni(\alpha,\gamma)^{66}Zn$

E_{eff}^{lab} (MeV)	E_{eff}^{cm} (MeV)	$\sigma_{\alpha\gamma}$ (mb)	$\Delta\sigma_{\alpha\gamma}$ (mb)	$\frac{\sigma_{OAP\ 422}}{\sigma_{\alpha\gamma}}$
5.070	4.763	4.7×10^{-3}	1.0×10^{-3}	
5.145	4.833	7.9×10^{-3}	1.2×10^{-3}	
5.221	4.905	1.07×10^{-2}	1.4×10^{-3}	
5.296	4.975	1.39×10^{-2}	1.5×10^{-3}	
5.344	5.020	2.02×10^{-2}	1.7×10^{-3}	0.7
5.371	5.045	1.55×10^{-2}	1.9×10^{-3}	
5.497	5.164	2.66×10^{-2}	2.1×10^{-3}	
5.572	5.234	2.90×10^{-2}	2.2×10^{-3}	
5.647	5.305	4.33×10^{-2}	2.5×10^{-3}	
5.723	5.376	6.37×10^{-2}	2.8×10^{-3}	
5.798	5.447	7.23×10^{-2}	3.0×10^{-3}	
5.874	5.518	8.72×10^{-2}	3.0×10^{-3}	0.7
5.949	5.588	1.078×10^{-1}	3.2×10^{-3}	
5.973	5.611	1.17×10^{-1}	3.3×10^{-3}	
6.049	5.682	1.37×10^{-1}	3.2×10^{-3}	
6.124	5.753	1.67×10^{-1}	3.9×10^{-3}	
6.200	5.824	1.96×10^{-1}	5.1×10^{-3}	
6.280	5.899	2.46×10^{-1}	5.5×10^{-3}	
6.350	5.965	2.91×10^{-1}	6.2×10^{-3}	
6.426	6.037	3.50×10^{-1}	6.4×10^{-3}	0.6
6.503	6.109	3.80×10^{-1}	6.5×10^{-3}	
6.576	6.177	4.25×10^{-1}	7.2×10^{-3}	
6.651	6.248	4.85×10^{-1}	7.4×10^{-3}	
6.726	6.318	5.34×10^{-1}	8.0×10^{-3}	
6.802	6.390	5.69×10^{-1}	4.4×10^{-3}	
6.877	6.460	6.10×10^{-1}	4.9×10^{-3}	

Table 12 (continued)

E_{eff}^{lab} (MeV)	E_{eff}^{cm} (MeV)	$\sigma_{\alpha\gamma}$ (mb)	$\Delta\sigma_{\alpha\gamma}$ (mb)	$\frac{\sigma_{OAP\ 422}}{\sigma_{\alpha\gamma}}$
6.951	6.530	4.07×10^{-1}	7.4×10^{-3}	0.2 (threshold)
7.026	6.600	2.93×10^{-1}	6.8×10^{-3}	
7.101	6.671	2.57×10^{-1}	6.7×10^{-3}	
7.177	6.742	2.13×10^{-1}	9.4×10^{-3}	
7.252	6.812	2.21×10^{-1}	9.5×10^{-3}	
7.325	6.884	2.60×10^{-1}	9.9×10^{-3}	
7.404	6.955	2.31×10^{-1}	1.4×10^{-2}	
7.479	7.026	2.13×10^{-1}	1.0×10^{-2}	0.4
7.554	7.096	2.67×10^{-1}	3.8×10^{-3}	
7.630	7.168	2.87×10^{-1}	1.1×10^{-2}	
7.705	7.238	3.06×10^{-1}	1.1×10^{-2}	
7.735	7.266	2.89×10^{-1}	8.8×10^{-3}	
7.780	7.308	2.90×10^{-1}	1.2×10^{-2}	
7.795	7.323	2.59×10^{-1}	8.7×10^{-3}	
7.855	7.379	2.78×10^{-1}	1.1×10^{-2}	
7.915	7.435	2.85×10^{-1}	9.5×10^{-3}	
7.976	7.493	2.47×10^{-1}	9.5×10^{-3}	0.5
8.036	7.549	2.57×10^{-1}	8.9×10^{-3}	
8.096	7.605	2.43×10^{-1}	9.2×10^{-3}	
8.156	7.662	2.53×10^{-1}	9.8×10^{-3}	
8.217	7.719	2.26×10^{-1}	1.1×10^{-2}	
8.277	7.775	2.56×10^{-1}	1.0×10^{-2}	
8.337	7.832	2.46×10^{-1}	9.3×10^{-3}	
8.397	7.888	2.45×10^{-1}	1.1×10^{-2}	
8.457	7.944	2.30×10^{-1}	1.0×10^{-2}	
8.517	8.001	2.94×10^{-1}	1.4×10^{-3}	0.3
8.578	8.058	2.98×10^{-1}	1.6×10^{-2}	
8.638	8.114	2.09×10^{-1}	2.6×10^{-3}	

Table 13

Cross section measured for the reaction $^{64}Ni(\alpha,\gamma)^{68}Zn$. The first and second columns give the effective energies in the laboratory and center-of-mass systems, respectively. The fourth column gives the uncertainties arising only from the statistics of counting. The ratios of the cross sections calculated by Woosley et al. (1975) [from which were calculated the thermonuclear rates soon to be published (Woosley 1979)] to those measured are given in the fifth column for selected energies. See Section IIE for further details.

Table 13

Cross Sections for $^{64}Ni(\alpha,\gamma)^{68}Zn$

E_{eff}^{lab} (MeV)	E_{eff}^{cm} (MeV)	$\sigma_{\alpha\gamma}$ (mb)	$\Delta\sigma_{\alpha\gamma}$ (mb)	$\frac{\sigma_{OAP\ 422}}{\sigma_{\alpha\gamma}}$
4.498	4.233	6.38×10^{-4}	2.9×10^{-4}	
4.598	4.328	9.52×10^{-4}	3.4×10^{-4}	
4.699	4.423	1.21×10^{-3}	3.5×10^{-4}	
4.799	4.517	3.05×10^{-3}	4.5×10^{-4}	0.6
4.899	4.611	3.65×10^{-3}	6.3×10^{-4}	
5.001	4.707	7.40×10^{-3}	8.2×10^{-4}	
5.096	4.796	8.33×10^{-3}	5.7×10^{-4}	
5.150	4.847	8.51×10^{-3}	8.7×10^{-4}	
5.200	4.894	7.01×10^{-3}	9.6×10^{-4}	(threshold)
5.298	4.986	4.92×10^{-3}	8.7×10^{-4}	0.16
5.401	5.083	1.83×10^{-3}	5.6×10^{-4}	
5.501	5.177	2.14×10^{-3}	3.6×10^{-4}	
5.602	5.272	2.73×10^{-3}	4.7×10^{-4}	
5.702	5.367	3.67×10^{-3}	8.7×10^{-4}	
5.803	5.462	2.07×10^{-3}	6.5×10^{-4}	0.3
5.903	5.556	1.57×10^{-3}	6.4×10^{-4}	
6.004	5.651	3.04×10^{-3}	1.4×10^{-3}	
6.104	5.745	3.39×10^{-3}	8.6×10^{-4}	
6.204	5.839	2.36×10^{-3}	8.4×10^{-4}	
6.305	5.934	3.05×10^{-3}	1.02×10^{-3}	0.25
6.607	6.218	5.20×10^{-3}	1.7×10^{-3}	
6.949	6.540	1.27×10^{-2}	2.1×10^{-3}	0.11
7.149	6.728	1.86×10^{-2}	3.5×10^{-3}	

Table 14

Long Counter Efficiency

d (cm)	ε	Reaction	E_γ (keV)	B_γ	$t_{1/2}$	λ_d sec^{-1}	Ref.
19.3	1.69_{-4}	$^{48}Ca(p,n)^{48}Sc$	984	1.00	43.7 hr	4.41_{-6}	†
19.3	1.60_{-4}	$^{51}V(p,n)^{51}Cr$	320	0.098	27.7 d	2.90_{-7}	*
26.8	1.16_{-4}	$^{48}Ca(p,n)^{48}Sc$					
26.8	1.12_{-4}	$^{68}Zn(p,n)^{68}Ga$	1077	0.033	68.3 min	1.69_{-4}	**
37.3	5.68_{-5}	$^{48}Ca(p,n)^{48}Sc$					
85.8	1.25_{-5}	$^{48}Ca(p,n)^{48}Sc$					
19.3	1.18_{-4}	Am-Be source					
26.8	7.78_{-5}	"					
37.3	4.88_{-5}	"					

† Beene (1978)

* Auble (1978)

** Lewis (1975)

Measurements of long counter efficiency, ε, as a function of distance, d, by the activation technique (see Section IIF). The energy, E_γ, of the γ-ray detected from the residual activity, the number of γ-rays produced per decay, B_γ, the half-life, $t_{1/2}$, and decay rate, λ_d, of the residual activity are also given.

Table 15

Long Counter Geometries

Reaction	distance* (cm)	angle**	Comments
$^{51}V(p,n)^{51}Cr$	92.8	90°	
	26.4	90°	Cross section check
$^{54}Cr(p,n)^{54}Mn$	23.4	30°	
$^{48}Ca(p,n)^{48}Sc$	31.0	80°	
$^{68}Zn(p,n)^{68}Ga$	55.6	29°	
$^{62}Ni(\alpha,n)^{65}Zn$	29.3	90°	
$^{64}Ni(\alpha,n)^{67}Zn$	15.5	90°	

*Distance is measured from target to surface of the long counter paraffin.

**Angle between the beam direction and a line drawn from the target through the long counter axis.

Table 16

Cross sections measured for the reaction $^{51}V(p,n)^{51}Cr$. The first and second columns give the effective energies in the laboratory and center-of-mass systems, respectively. The fourth column gives the uncertainties arising from the statistics of counting and, for the $E_{eff}^{lab} = 1.583$ MeV point, from the determination of the target thickness the beam traverses before energy loss reduces its energy below the threshold, 1.564 MeV. The ratios of the cross sections calculated by Woosley et al. (1975) [from which were calculated the thermonuclear rates which are soon to be published (Woosley 1979)] to those measured are given in the fifth column for selected energies. See Section IIG for further details.

Table 16

Cross Sections for $^{51}V(p,n)^{51}Cr$

E_{eff}^{lab} (MeV)	E_{eff}^{cm} (MeV)	σ_{pn} (mb)	$\Delta\sigma_{pn}$ (mb)	$\frac{\sigma_{OAP\ 422}}{\sigma_{pn}}$
1.583	1.553	1.62×10^{-1}	1.8×10^{-2}	
1.611	1.580	5.60×10^{-1}	3.4×10^{-2}	
1.642	1.610	7.30×10^{-1}	3.4×10^{-2}	1.8
1.691	1.658	9.00×10^{-1}	4.3×10^{-2}	
1.743	1.709	1.42×10^{0}	5.4×10^{-2}	
1.793	1.759	1.81×10^{0}	6.1×10^{-2}	
1.844	1.809	2.17×10^{0}	4.9×10^{-2}	
1.895	1.859	2.37×10^{0}	< 5%	
1.946	1.909	2.98×10^{0}	"	
1.998	1.960	4.07×10^{0}	"	
2.048	2.009	4.78×10^{0}	"	1.7
2.099	2.059	5.04×10^{0}	"	
2.148	2.107	8.02×10^{0}	"	
2.248	2.205	9.47×10^{0}	"	
2.299	2.255	1.65×10^{1}	"	
2.350	2.305	1.24×10^{1}	"	
2.400	2.354	1.07×10^{1}	"	
2.451	2.404	1.13×10^{1}	"	
2.502	2.454	1.66×10^{1}	"	
2.552	2.503	2.12×10^{1}	"	1.4
2.603	2.553	2.14×10^{1}	"	
2.654	2.603	2.13×10^{1}	"	
2.704	2.652	2.11×10^{1}	"	
2.755	2.702	2.30×10^{1}	"	
2.805	2.751	2.65×10^{1}	"	
2.855	2.800	3.29×10^{1}	"	
2.907	2.851	3.10×10^{1}	"	

Table 16 (continued)

E_{eff}^{lab} (MeV)	E_{eff}^{cm} (MeV)	σ_{pn} (mb)	$\Delta\sigma_{pn}$ (mb)	$\frac{\sigma_{OAP\ 422}}{\sigma_{pn}}$
2.957	2.900	3.96×10^1	< 5%	
3.008	2.950	3.52×10^1	"	
3.059	3.000	4.27×10^1	"	1.6
3.109	3.049	4.52×10^1	"	
3.159	3.098	5.06×10^1	"	
3.204	3.142	5.32×10^1	"	
3.261	3.198	6.37×10^1	"	
3.311	3.247	7.22×10^1	"	
3.361	3.296	6.50×10^1	"	
3.411	3.345	7.26×10^1	"	
3.463	3.396	7.28×10^1	"	
3.513	3.445	8.06×10^1	"	
3.563	3.494	8.26×10^1	"	1.4
3.612	3.543	8.77×10^1	"	
3.662	3.592	9.68×10^1	"	
3.713	3.642	9.74×10^1	"	
3.763	3.691	1.046×10^2	"	
3.814	3.741	1.092×10^2	"	
3.864	3.790	1.057×10^2	"	
3.914	3.839	1.22×10^2	"	
3.964	3.888	1.39×10^2	"	
4.015	3.938	1.20×10^2	"	
4.065	3.987	1.28×10^2	"	1.4
4.116	4.037	1.44×10^2	"	
4.166	4.086	1.36×10^2	"	
4.216	4.135	1.52×10^2	"	
4.266	4.184	1.57×10^2	"	
4.316	4.233	1.53×10^2	"	
4.367	4.283	1.68×10^2	"	
4.417	4.332	1.74×10^2	"	
4.467	4.381	1.69×10^2	"	

Table 17

Cross sections measured for the reaction $^{54}Cr(p,n)^{54}Mn$. The first and second columns give the effective energies in the laboratory and center-of-mass systems, respectively. The fourth column gives the uncertainties arising from the statistics of counting and, for the $E_{eff}^{lab} = 2.225$ and $E_{eff}^{lab} = 2.253$ points, from the determination of the target thickness the beam traverses before energy loss reduces its energy below the threshold, 2.199 MeV. The ratios of the cross sections calculated by Woosley et al. (1975) [from which were calculated the thermonuclear rates which are soon to be published (Woosley 1979)] to those measured are given in the fifth column for selected energies. See Section IIG for further details.

Table 17

Cross Sections for $^{54}Cr(p,n)^{54}Mn$

E_{eff}^{lab} (MeV)	E_{eff}^{cm} (MeV)	σ_{pn} (mb)	$\Delta\sigma_{pn}$ (mb)	$\frac{\sigma_{OAP\ 422}}{\sigma_{pn}}$
2.225	2.185	2.29×10^{0}	2.7×10^{-1}	
2.253	2.212	2.70×10^{0}	2.0×10^{-1}	
2.293	2.251	3.23×10^{0}	6.4×10^{-2}	
2.344	2.301	4.79×10^{0}	< 2%	
2.394	2.350	6.29×10^{0}	"	
2.444	2.400	7.17×10^{0}	"	
2.494	2.449	1.005×10^{1}	"	
2.544	2.498	1.64×10^{1}	"	1.4
2.595	2.548	2.14×10^{1}	"	
2.646	2.598	2.05×10^{1}	"	
2.696	2.647	1.94×10^{1}	"	
2.747	2.697	2.04×10^{1}	"	
2.798	2.747	2.46×10^{1}	"	
2.848	2.796	2.45×10^{1}	"	
2.899	2.846	3.11×10^{1}	"	
2.950	2.896	3.37×10^{1}	"	
3.000	2.945	2.92×10^{1}	"	
3.051	2.996	3.44×10^{1}	"	1.7
3.102	3.046	4.60×10^{1}	"	
3.152	3.095	4.37×10^{1}	"	
3.203	3.145	4.68×10^{1}	"	
3.253	3.193	5.23×10^{1}	"	
3.304	3.244	5.08×10^{1}	"	
3.353	3.292	7.13×10^{1}	"	
3.405	3.343	6.76×10^{1}	"	
3.455	3.392	7.34×10^{1}	"	

Table 17 (continued)

E_{eff}^{lab} (MeV)	E_{eff}^{cm} (MeV)	σ_{pn} (mb)	$\Delta\sigma_{pn}$ (mb)	$\frac{\sigma_{OAP\ 422}}{\sigma_{pn}}$
3.506	3.442	9.25×10^{1}	< 2%	
3.556	3.491	7.65×10^{1}	"	1.4
3.606	3.540	9.18×10^{1}	"	
3.657	3.591	1.039×10^{2}	"	
3.707	3.640	9.46×10^{1}	"	

Table 18

Cross sections measured for the reaction $^{68}Zn(p,n)^{68}Ga$. The first and second columns give the effective energies in the laboratory and center-of-mass systems, respectively. The fourth column gives the uncertainties arising from the statistics of counting. The ratios of the cross sections calculated by Woosley et al. (1975) [from which were calculated the thermonuclear rates which are soon to be published (Woosley 1979)] to those measured are given in the fifth column for selected energies. See Section IIG for further details.

Table 18

Cross Sections for $^{68}Zn(p,n)^{68}Ga$

E^{lab}_{eff} (MeV)	E^{cm}_{eff} (MeV)	σ_{pn} (mb)	$\Delta\sigma_{pn}$ (mb)	$\frac{\sigma_{OAP\ 422}}{\sigma_{pn}}$
3.766	3.711	12.1	0.59	
3.783	3.728	15.2	0.35	
3.808	3.753	23.7	< 2%	
3.833	3.777	25.6	"	
3.833	3.777	22.5	"	
3.858	3.802	24.0	"	1.3
3.883	3.827	24.7	"	
3.908	3.851	28.9	"	
3.933	3.876	36.0	"	
3.958	3.901	41.2	"	
3.983	3.925	44.3	"	
4.003	3.945	52.4	"	
4.023	3.965	53.9	"	
4.043	3.984	63.6	"	
4.063	4.004	76.9	"	0.8
4.083	4.024	98.1	"	
4.104	4.045	97.6	"	
4.124	4.064	84.8	"	
4.144	4.084	76.2	"	
4.164	4.104	69.1	"	
4.184	4.123	78.6	"	
4.204	4.143	83.1	"	
4.224	4.163	88.0	"	
4.244	4.182	94.1	"	
4.264	4.202	104.2	"	
4.284	4.222	104.0	"	
4.304	4.242	112.	"	
4.324	4.261	125.	"	
4.344	4.281	135.	"	

Table 18 (continued)

E_{eff}^{lab} (MeV)	E_{eff}^{cm} (MeV)	σ_{pn} (mb)	$\Delta\sigma_{pn}$ (mb)	$\frac{\sigma_{OAP\ 422}}{\sigma_{pn}}$
4.364	4.301	142	< 2%	
4.384	4.320	154	"	
4.404	4.340	155	"	
4.424	4.360	157	"	
4.444	4.380	164	"	
4.464	4.399	173	"	
4.484	4.419	182	"	
4.504	4.439	191	"	
4.524	4.458	202	"	
4.544	4.478	189	"	
4.565	4.499	175	"	0.7
4.585	4.519	176	"	
4.605	4.538	188	"	
4.625	4.558	175	"	
4.645	4.578	172	"	
4.665	4.597	188	"	
4.725	4.657	185	"	
4.785	4.716	214	"	
4.845	4.775	270	"	
4.905	4.834	242	"	
4.966	4.894	197	"	
5.026	4.953	218	"	0.8

Table 19

Cross sections measured for the reaction $^{48}Ca(p,n)^{48}Sc$. The first and second columns give the effective energies in the laboratory and center-of-mass systems, respectively. The fourth column gives the uncertainties arising from the statistics of counting. Below $E_{eff}^{lab} \simeq 1.1$ MeV the background was significant and introduced considerable uncertainties (see Appendix B). See Section IIG for further details and Appendix B for the thermonuclear rates calculated from the measured cross sections.

Table 19

Cross Sections for $^{48}Ca(p,n)^{48}Sc$

E_{eff}^{lab} (MeV)	E_{eff}^{cm} (MeV)	σ_{pn} (mb)	$\Delta\sigma_{pn}$ (mb)
0.956	0.937	1.22×10^{-2}	4×10^{-3}
0.982	0.961	1.71×10^{-2}	4×10^{-3}
1.007	0.986	1.44×10^{-2}	4×10^{-3}
1.032	1.011	2.47×10^{-2}	5×10^{-3}
1.057	1.036	9.76×10^{-4}	3×10^{-3}
1.083	1.060	2.52×10^{-2}	5×10^{-3}
1.108	1.085	3.33×10^{-2}	5×10^{-3}
1.133	1.110	4.56×10^{-2}	6×10^{-3}
1.158	1.134	6.85×10^{-2}	6×10^{-3}
1.183	1.159	1.68×10^{-1}	1.1×10^{-2}
1.209	1.184	2.46×10^{-1}	1.1×10^{-2}
1.234	1.208	1.94×10^{-1}	9×10^{-3}
1.259	1.233	2.93×10^{-1}	1.5×10^{-2}
1.284	1.258	7.15×10^{-1}	2.2×10^{-2}
1.309	1.282	1.76×10^{-1}	1.2×10^{-2}
1.335	1.307	9.89×10^{-1}	2.6×10^{-2}
1.360	1.332	6.73×10^{-1}	< 3%
1.385	1.356	8.49×10^{-1}	"
1.410	1.381	1.016×10^{0}	"
1.435	1.406	9.12×10^{-1}	"
1.461	1.430	1.071×10^{0}	"
1.486	1.455	1.44×10^{0}	"
1.516	1.485	8.95×10^{-1}	"
1.566	1.534	2.85×10^{0}	"
1.586	1.554	1.28×10^{0}	"
1.611	1.578	1.56×10^{0}	"
1.637	1.603	3.61×10^{0}	"

Table 19 (continued)

E_{eff}^{lab} (MeV)	E_{eff}^{cm} (MeV)	σ_{pn} (mb)	$\Delta\sigma_{pn}$ (mb)
1.682	1.647	6.41×10^{0}	< 3%
1.707	1.672	5.33×10^{0}	"
1.732	1.697	3.23×10^{0}	"
1.757	1.721	8.74×10^{0}	"
1.782	1.746	4.74×10^{0}	"
1.808	1.770	4.51×10^{0}	"
1.838	1.795	8.67×10^{0}	"
1.858	1.819	1.56×10^{1}	"
1.883	1.844	7.26×10^{0}	"
1.908	1.869	1.98×10^{1}	"
1.933	1.893	9.81×10^{0}	"
1.948	1.908	1.94×10^{1}	"
1.973	1.933	8.83×10^{1}	"
1.988	1.947	5.57×10^{1}	"
2.008	1.967	1.73×10^{1}	"
2.029	1.987	8.52×10^{0}	"
2.049	2.006	5.89×10^{0}	"
2.069	2.026	1.83×10^{1}	"
2.089	2.046	1.88×10^{1}	"
2.109	2.065	9.57×10^{0}	"
2.129	2.085	1.31×10^{1}	"
2.149	2.105	1.16×10^{1}	"
2.169	2.124	1.22×10^{1}	"
2.189	2.144	1.59×10^{1}	"
2.209	2.163	1.96×10^{1}	"
2.229	2.183	2.41×10^{1}	"
2.249	2.203	1.55×10^{1}	"
2.269	2.222	7.73×10^{0}	"
2.289	2.241	1.36×10^{1}	"

Table 19 (continued)

E_{eff}^{lab} (MeV)	E_{eff}^{cm} (MeV)	σ_{pn} (mb)	$\Delta\sigma_{pn}$ (mb)
2.309	2.261	1.64×10^{1}	< 3%
2.329	2.281	1.61×10^{1}	"
2.348	2.300	2.19×10^{1}	"
2.368	2.320	1.32×10^{1}	"
2.388	2.339	3.71×10^{1}	"
2.408	2.359	3.69×10^{1}	"
2.428	2.378	1.92×10^{1}	"
2.448	2.398	1.99×10^{1}	"
2.470	2.419	3.33×10^{1}	"
2.490	2.439	2.62×10^{1}	"
2.510	2.458	5.65×10^{1}	"
2.530	2.478	4.56×10^{1}	"
2.550	2.498	2.83×10^{1}	"
2.570	2.517	3.00×10^{1}	"
2.590	2.537	3.35×10^{1}	"
2.610	2.556	6.23×10^{1}	"
2.630	2.576	5.78×10^{1}	"
2.650	2.596	5.54×10^{1}	"
2.670	2.615	4.16×10^{1}	"

Table 20

Cross sections measured for the reaction $^{62}Ni(\alpha,n)^{65}Zn$. The first and second columns give the effective energies in the laboratory and center-of-mass systems, respectively. The fourth column gives the uncertainties arising from the statistics of counting and, for the E_{eff}^{lab} = 6.954 MeV point, from the determination of the target thickness the beam traverses before energy loss reduces its energy below the threshold, 1.564 MeV. The ratios of the cross sections calculated by Woosley et al. (1975) [from which were calculated the thermonuclear rates which are soon to be published (Woosley 1979)] to those measured are given in the fifth column for selected energies. See Section IIG for further details.

Table 20

Cross Sections for $^{62}Ni(\alpha,n)^{65}Zn$

E_{eff}^{lab} (MeV)	E_{eff}^{cm} (MeV)	$\sigma_{\alpha n}$ (mb)	$\Delta\sigma_{\alpha n}$ (mb)	$\frac{\sigma_{OAP\ 422}}{\sigma_{\alpha n}}$
6.954	6.533	1.15×10^{0}	7.4×10^{-2}	
7.027	6.601	2.25×10^{0}	9.9×10^{-2}	
7.102	6.672	3.37×10^{0}	1.2×10^{-1}	
7.176	6.741	4.00×10^{0}	2.1×10^{-1}	0.6
7.250	6.811	5.13×10^{0}	2.3×10^{-1}	
7.326	6.882	6.13×10^{0}	2.5×10^{-1}	
7.400	6.952	7.44×10^{0}	2.6×10^{-1}	
7.476	7.023	8.17×10^{0}	2.7×10^{-1}	0.6
7.552	7.094	9.48×10^{0}	1.5×10^{-1}	
7.626	7.164	1.085×10^{1}	2.4×10^{-1}	
7.702	7.235	1.195×10^{1}	3.1×10^{-1}	
7.777	7.306	1.51×10^{1}	3.4×10^{-1}	
7.853	7.377	1.76×10^{1}	3.6×10^{-1}	
7.919	7.439	1.88×10^{1}	< 2%	
8.079	7.589	2.49×10^{1}	"	0.5
8.154	7.660	3.93×10^{1}	"	
8.229	7.730	3.12×10^{1}	"	
8.305	7.801	3.68×10^{1}	"	
8.380	7.872	4.27×10^{1}	"	
8.455	7.943	4.65×10^{1}	"	
8.515	7.999	4.85×10^{1}	"	0.5
8.576	8.056	5.00×10^{1}	"	
8.636	8.112	5.65×10^{1}	"	
8.696	8.169	6.08×10^{1}	"	
8.756	8.225	6.53×10^{1}	"	

Table 21

Cross sections measured for the $^{64}Ni(\alpha,n)^{65}Zn$ reaction. The first and second columns give the effective energies in the laboratory and center-of-mass systems, respectively. The fourth column gives the uncertainties arising from the statistics of counting. The ratios of the cross sections calculated by Woosley et al. (1975) [from which were calculated the thermonuclear rates which are soon to be published (Woosley 1979)] to those measured are given in the fifth column for selected energies. See Section IIG for further details.

Table 21

Cross Sections for $^{64}Ni(\alpha,n)^{67}Zn$

E_{eff}^{lab} (MeV)	E_{eff}^{cm} (MeV)	$\sigma_{\alpha n}$ (mb)	$\Delta\sigma_{\alpha n}$ (mb)	$\frac{\sigma_{OAP\ 422}}{\sigma_{\alpha n}}$
5.291	4.980	2.51×10^{-2}	4.4×10^{-3}	
5.350	5.035	3.19×10^{-2}	7.8×10^{-3}	
5.390	5.073	6.19×10^{-2}	6.2×10^{-3}	
5.490	5.167	7.43×10^{-2}	9.1×10^{-3}	
5.590	5.261	5.15×10^{-2}	6.7×10^{-3}	0.7
5.690	5.355	6.91×10^{-2}	8.1×10^{-3}	
5.790	5.449	1.35×10^{-1}	9.7×10^{-3}	
5.890	5.544	1.71×10^{-1}	1.03×10^{-2}	0.6
5.991	5.639	2.07×10^{-1}	3.4×10^{-2}	
6.091	5.733	2.69×10^{-1}	1.9×10^{-2}	
6.191	5.827	3.56×10^{-1}	2.2×10^{-2}	
6.293	5.923	4.43×10^{-1}	2.6×10^{-2}	0.7
6.593	6.205	1.13×10^{0}	4.8×10^{-2}	
6.935	6.527	2.48×10^{0}	8.1×10^{-2}	0.6
7.136	6.716	3.80×10^{0}	1.15×10^{-1}	
7.437	7.000	7.25×10^{0}	1.57×10^{-1}	0.7

Table 22

Cross sections measured for the reaction $^{68}Zn(p,\alpha)^{65}Cu$. The first and second columns give the effective energies in the laboratory and center-of-mass systems, respectively. The fourth column gives the uncertainties arising from the statistics of counting. The ratios of the cross sections calculated by Woosley et al. (1975) [from which were calculated the thermonuclear rates which are soon to be published (Woosley 1979)] to those measured are given in the fifth column for selected energies. See Section IIH for further details.

Table 22

Cross Sections for $^{68}Zn(p,\alpha)^{65}Cu$

E^{lab}_{eff} (MeV)	E^{cm}_{eff} (MeV)	$\sigma_{p\alpha}$ (mb)	$\Delta\sigma_{p\alpha}$ (mb)	$\frac{\sigma_{OAP\ 422}}{\sigma_{p\alpha}}$
3.360	3.311	1.58×10^{-1}	3×10^{-2}	
3.400	3.351	2.10×10^{-1}	2×10^{-2}	
3.440	3.390	2.87×10^{-1}	2×10^{-2}	
3.480	3.430	2.81×10^{-1}	2×10^{-2}	
3.520	3.469	3.27×10^{-1}	2×10^{-2}	
3.560	3.508	3.87×10^{-1}	2×10^{-2}	0.7
3.600	3.548	3.87×10^{-1}	2×10^{-2}	
3.640	3.587	4.97×10^{-1}	2×10^{-2}	
3.680	3.627	5.73×10^{-1}	2×10^{-2}	
3.700	3.646	6.20×10^{-1}	2×10^{-2}	
3.720	3.666	6.44×10^{-1}	2×10^{-2}	
3.760	3.706	6.32×10^{-1}	2×10^{-2}	(threshold)
3.800	3.745	6.84×10^{-1}	2×10^{-2}	0.5
3.820	3.765	6.44×10^{-1}	2×10^{-2}	
3.840	3.784	7.25×10^{-1}	2×10^{-2}	
3.860	3.804	7.48×10^{-1}	2×10^{-2}	
3.880	3.824	8.72×10^{-1}	2×10^{-2}	
3.900	3.843	8.07×10^{-1}	3×10^{-2}	
3.920	3.863	9.07×10^{-1}	4×10^{-2}	
3.940	3.883	9.07×10^{-1}	3×10^{-3}	
3.960	3.903	6.84×10^{-1}	3×10^{-2}	
3.980	3.922	7.48×10^{-1}	3×10^{-2}	
4.000	3.942	9.66×10^{-1}	2×10^{-2}	
4.020	3.962	6.96×10^{-1}	3×10^{-2}	
4.040	3.981	8.30×10^{-1}	3×10^{-2}	
4.060	4.001	1.076×10^{0}	4×10^{-2}	0.7
4.080	4.021	7.20×10^{-1}	2×10^{-2}	

Table 22 (continued)

E_{eff}^{lab} (MeV)	E_{eff}^{cm} (MeV)	$\sigma_{p\alpha}$ (mb)	$\Delta\sigma_{p\alpha}$ (mb)	$\frac{\sigma_{OAP\ 422}}{\sigma_{p\alpha}}$
4.100	4.041	1.32×10^{0}	5×10^{-2}	
4.120	4.060	8.48×10^{-1}	3×10^{-2}	
4.140	4.080	6.90×10^{-1}	3×10^{-2}	
4.160	4.100	5.73×10^{-1}	3×10^{-2}	
4.180	4.119	6.49×10^{-1}	3×10^{-2}	
4.200	4.139	6.66×10^{-1}	3×10^{-2}	
4.220	4.159	6.49×10^{-1}	3×10^{-2}	
4.240	4.179	6.90×10^{-1}	2×10^{-2}	
4.260	4.198	6.96×10^{-1}	2×10^{-2}	
4.280	4.218	5.91×10^{-1}	3×10^{-2}	
4.300	4.238	6.66×10^{-1}	2×10^{-2}	
4.320	4.257	6.20×10^{-1}	2×10^{-2}	0.2
4.360	4.297	5.79×10^{-1}	2×10^{-2}	
4.400	4.336	6.73×10^{-1}	2×10^{-2}	
4.440	4.376	6.49×10^{-1}	2×10^{-2}	
4.480	4.415	6.66×10^{-1}	2×10^{-2}	
4.520	4.454	6.79×10^{-1}	2×10^{-2}	
4.560	4.494	6.66×10^{-1}	2×10^{-2}	0.2
4.600	4.533	6.55×10^{-1}	2×10^{-2}	
4.640	4.573	6.20×10^{-1}	2×10^{-2}	
4.680	4.612	7.08×10^{-1}	2×10^{-2}	
4.720	4.652	9.53×10^{-1}	2×10^{-2}	
4.760	4.691	9.12×10^{-1}	2×10^{-2}	
4.800	4.730	9.89×10^{-1}	3×10^{-2}	
4.840	4.770	9.53×10^{-1}	2×10^{-2}	0.2
4.920	4.849	1.11×10^{0}	3×10^{-2}	
4.960	4.888	1.04×10^{0}	3×10^{-2}	
4.975	4.903	1.05×10^{0}	3×10^{-2}	
5.000	4.928	1.00×10^{0}	3×10^{-2}	

Table 22 (continued)

E_{eff}^{lab} (MeV)	E_{eff}^{cm} (MeV)	$\sigma_{p\alpha}$ (mb)	$\Delta\sigma_{p\alpha}$ (mb)	$\frac{\sigma_{OAP\ 422}}{\sigma_{p\alpha}}$
5.040	4.967	1.13×10^{0}	3×10^{-2}	
5.080	5.006	1.04×10^{0}	3×10^{-2}	0.3
5.120	5.046	1.36×10^{0}	4×10^{-2}	
5.160	5.085	1.62×10^{0}	4×10^{-2}	
5.200	5.125	1.43×10^{0}	3×10^{-2}	
5.240	5.164	1.65×10^{0}	4×10^{-2}	
5.280	5.203	1.58×10^{0}	4×10^{-2}	
5.320	5.243	1.50×10^{0}	4×10^{-2}	
5.360	5.282	1.86×10^{0}	4×10^{-2}	
5.400	5.322	1.82×10^{0}	4×10^{-2}	
5.440	5.361	1.70×10^{0}	4×10^{-2}	
5.480	5.401	2.13×10^{0}	5×10^{-2}	0.2

Table 23

Optical Model Parameters Used in HAUSER*4 Calculations*

Term	(Units)	neutron parameters	proton parameters	α-particle parameters
U	(MeV)	$47.01-0.267E$ $-0.0018E^2$	$54-0.32E + 24\frac{(N-Z)}{2}$ $+ 0.4\ Z/A^{1/3}$	185
W_v	(MeV)	0	-2.7+0.22E or 0, whichever is greater	25
W_s	(MeV)	9.52-0.53E	$11.8-0.25E + 12\frac{(N-Z)}{A}$	0
$R_u A^{-1/3}$	(fm)	$1.322-0.76A \times (1-0.005A)$	1.17	1.40
$R_v A^{-1/3}$	(fm)	-	1.26	1.40
$R_s A^{-1/3}$	(fm)	$1.266-0.0037 \times A(1-0.005A)$	1.26	-
a_u	(fm)	0.66	0.75	0.52
a_v	(fm)	-	0.58	0.52
a_s	(fm)	0.48	0.58	-

*See Chapter III, Subsection B(ii).

Table 24

Ratio of Strength Functions to Black Nucleus Values*

Reaction	r_n even ℓ	odd ℓ
$^{54}Cr(p,n)^{54}Mn$	1.85	0.09
$^{51}V(p,n)^{51}Cr$	1.85	0.09
$^{48}Ca(p,n)^{48}Sc$	1.11	0.04
$^{68}Zn(p,n)^{68}Ga$	0.67	0.04
$^{37}Cl(\alpha,n)^{40}K$	0.44	0.74
$^{62}Ni(\alpha,n)^{65}Zn$	0.70	0.04
$^{64}Ni(\alpha,n)^{67}Zn$	0.67	0.04

*See Chapter II, subsection B(iv).

Table 25

Isospin Mixing Coupling Coefficients

Channel	$\beta^<$	$\beta^>$
p	$\frac{2T_c + 1}{2T_c + 2}$	$\frac{1}{2T_c + 2}$
n	1	0
α	1	0
γ	$\frac{T_c}{T_c + 1}$	$\frac{1}{T_c + 1}$

T_c is the compound nucleus ground state isospin $T_c = |T_{3c}|$ where $T_{3c} = \frac{N-Z}{2}$. In compiling this table it is assumed that $T_{3c} > 0$.

Figure 1

Schematic representation of a competition cusp. For simplicity it is assumed that only (p,p) (not illustrated), (p,γ) and (above threshold) (p,n) reactions occur. The total cross section (assumed approximately equal to the (p,γ) cross section below the neutron threshold) rises smoothly with energy as the proton penetrability increases. At E_{th}, the neutron threshold, the (p,n) cross section rapidly rises and emission of neutrons quickly becomes favored over that of γ-rays. To conserve the flux of particles emitted from compound nucleus decay, there must be a compensating decrease in the (p,γ) cross section because the (p,γ) and (p,n) cross sections must continue to add up to the total compound nucleus cross section. See pp. 3 and 4 for more details.

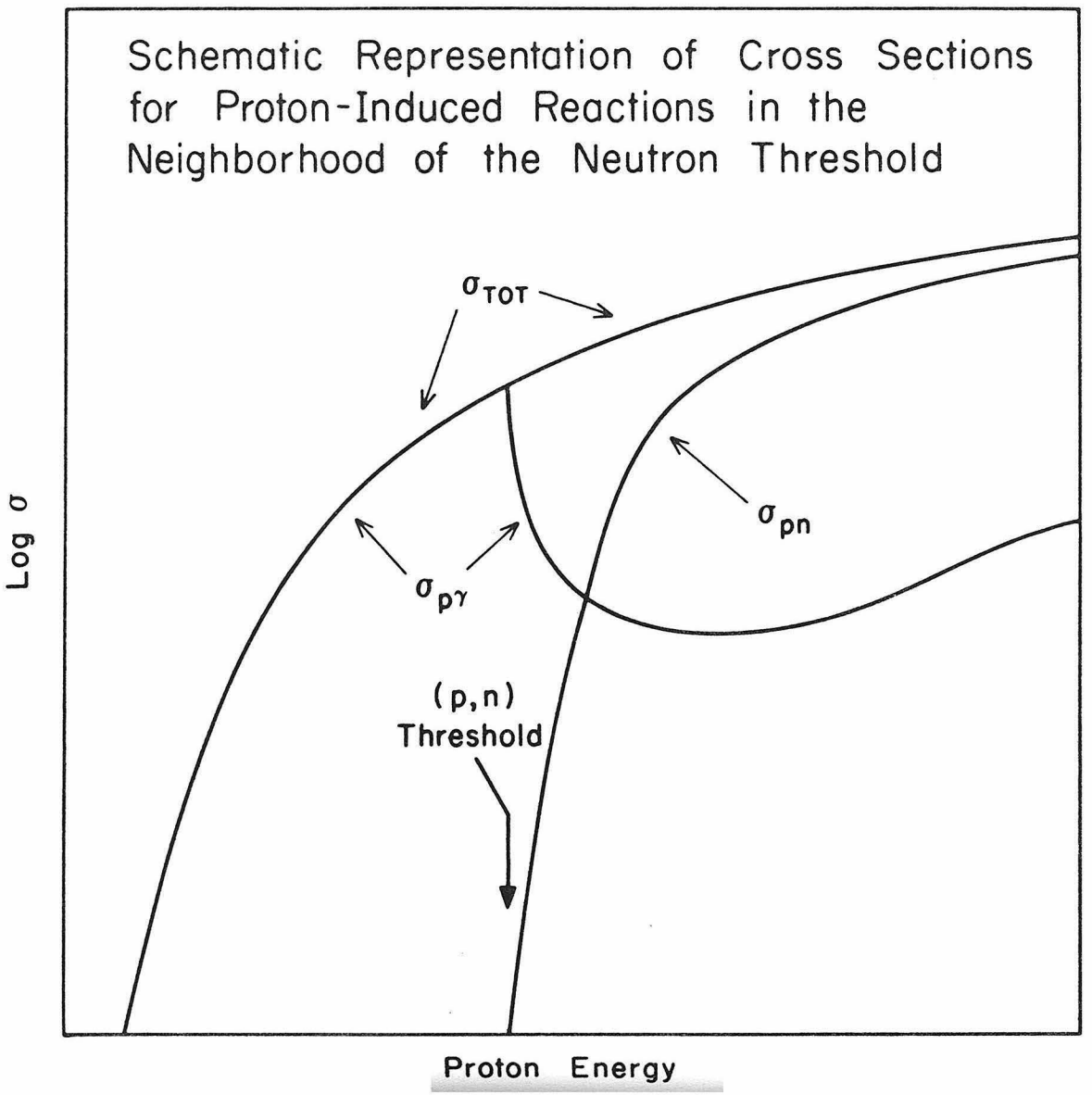
Schematic Representation of Cross Sections for Proton-Induced Reactions in the Neighborhood of the Neutron Threshold
σ_{TOT}
σ_{pn}
$\sigma_{p\gamma}$
(p,n) Threshold
Log σ
Proton Energy

Figure 2

All metal target chamber used in measurements of $^{54}Cr(p,\gamma)^{55}Mn$, $^{54}Cr(p,n)^{54}Mn$, $^{48}Ca(p,\gamma)^{49}Sc$, $^{48}Ca(p,n)^{48}Sc$, $^{62}Ni(\alpha,\gamma)^{66}Zn$, $^{62}Ni(\alpha,n)^{65}Zn$, $^{64}Ni(\alpha,\gamma)^{68}Zn$, and $^{64}Ni(\alpha,n)^{67}Zn$ cross sections and the normalization checks of the $^{51}V(p,\gamma)^{52}Cr$ and $^{51}V(p,n)^{51}Cr$ cross sections. See Section IIA for additional details.

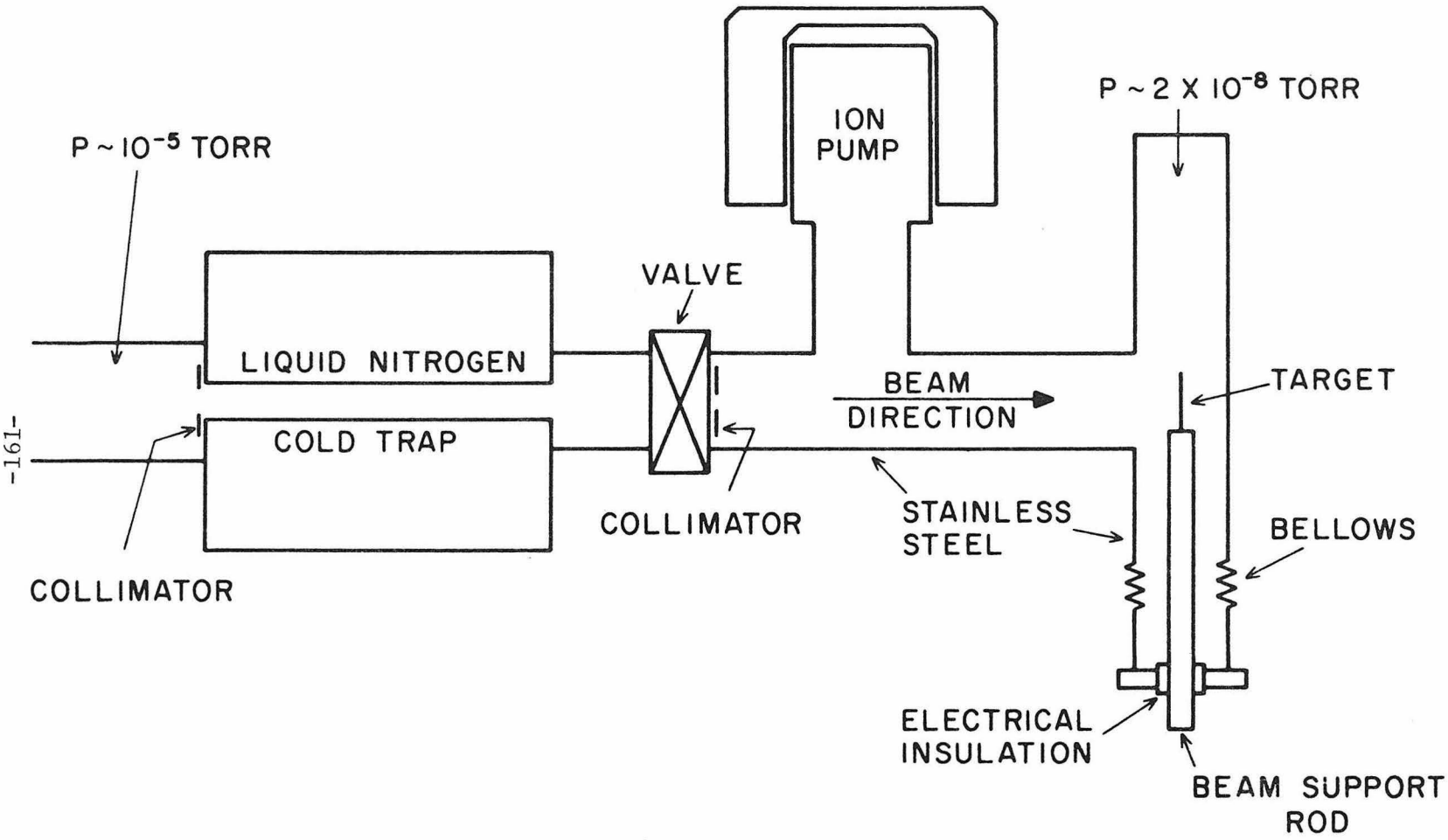

ALL METAL TARGET CHAMBER

Figure 3

Configuration of the scattering chamber for the $^{68}Zn(p,\alpha)^{65}Cu$ measurements. For backscattering measurements of target thickness the beam was stopped by the thick target backings, and charge was collected from the target rod which is insulated from the scattering chamber. See Sections IIA and IIH for additional details.

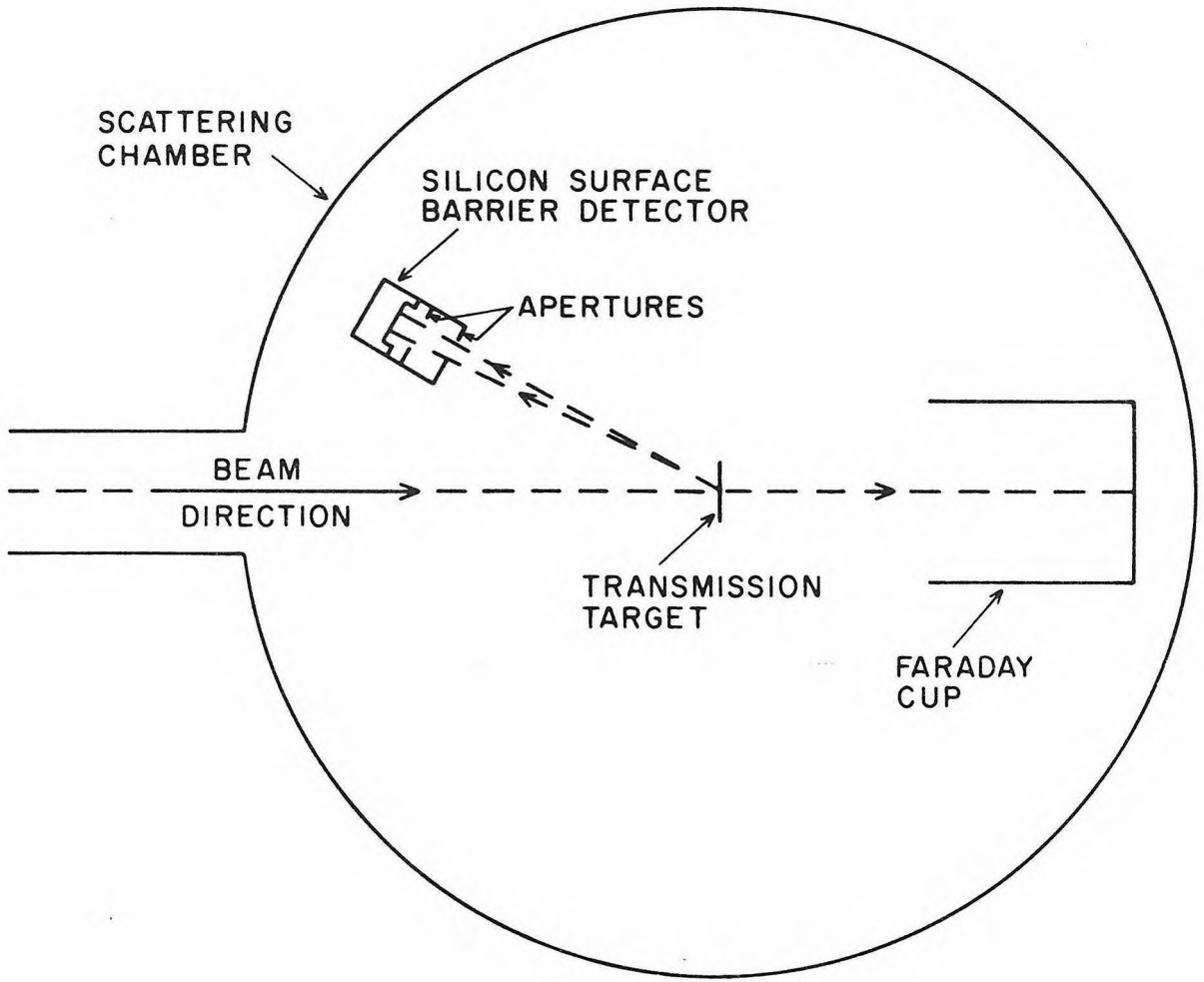

SCHEMATIC DIAGRAM OF CONFIGURATION FOR $^{68}Zn(p,\alpha)^{65}Cu$ MEASUREMENTS

Figure 4

Baffled, enclosed tantalum boat used in the fabrication of targets from oxides and carbonates of isotopically enriched metals. The boat is an SO-20 Silicon Monoxide Source obtained from R. D. Mathis Co. of Long Beach, California. See Section IIB for additional details.

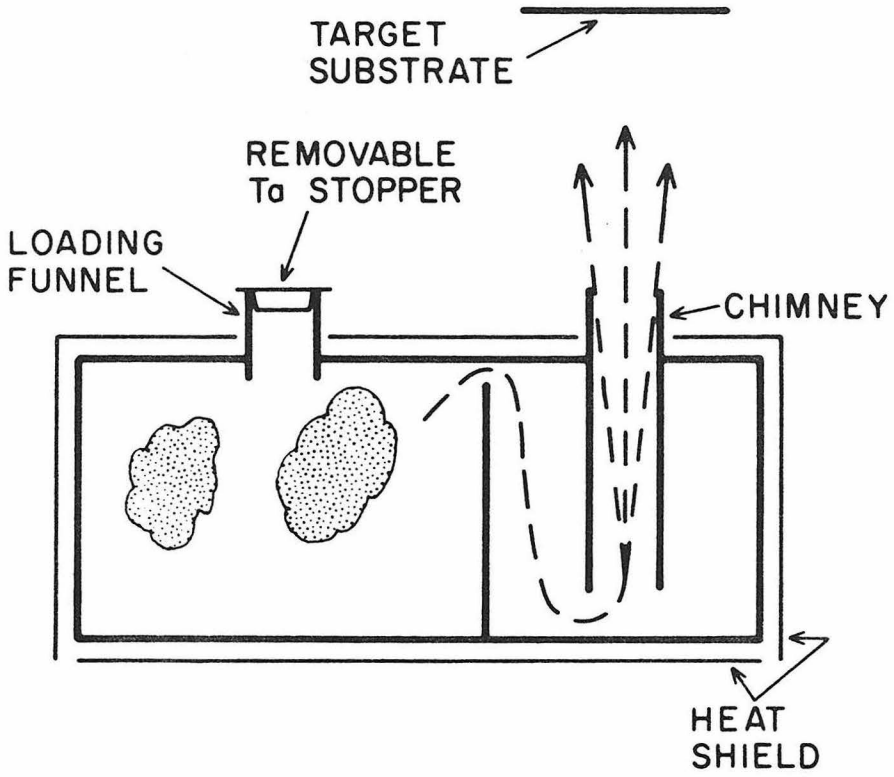

BAFFLED ENCLOSED TANTALUM BOAT

cut-away side view

Figure 5

Partial spectra of protons backscattered from a bare tungsten backing (top) and from a ^{54}Cr target layer and its tungsten backing (bottom). The portion of the spectrum shown includes the high energy edges corresponding to protons scattered from the surfaces of the tungsten backings and (in the bottom spectrum) the peak, representing protons scattered from the ^{54}Cr layer, which straddles the high energy edge as indicated. Notice the shift to lower energy of the high energy edge in the bottom figure caused by energy loss in the ^{54}Cr layer. The protons were detected with a silicon surface barrier detector at 160°. The proton bombarding energy was 3 MeV. Channels 1401 to 2300 are included so the relative channel numbers labelling the abscissas are 1400 less than the absolute channel numbers. See Figures 7a and 7b and Section IIC for additional details.

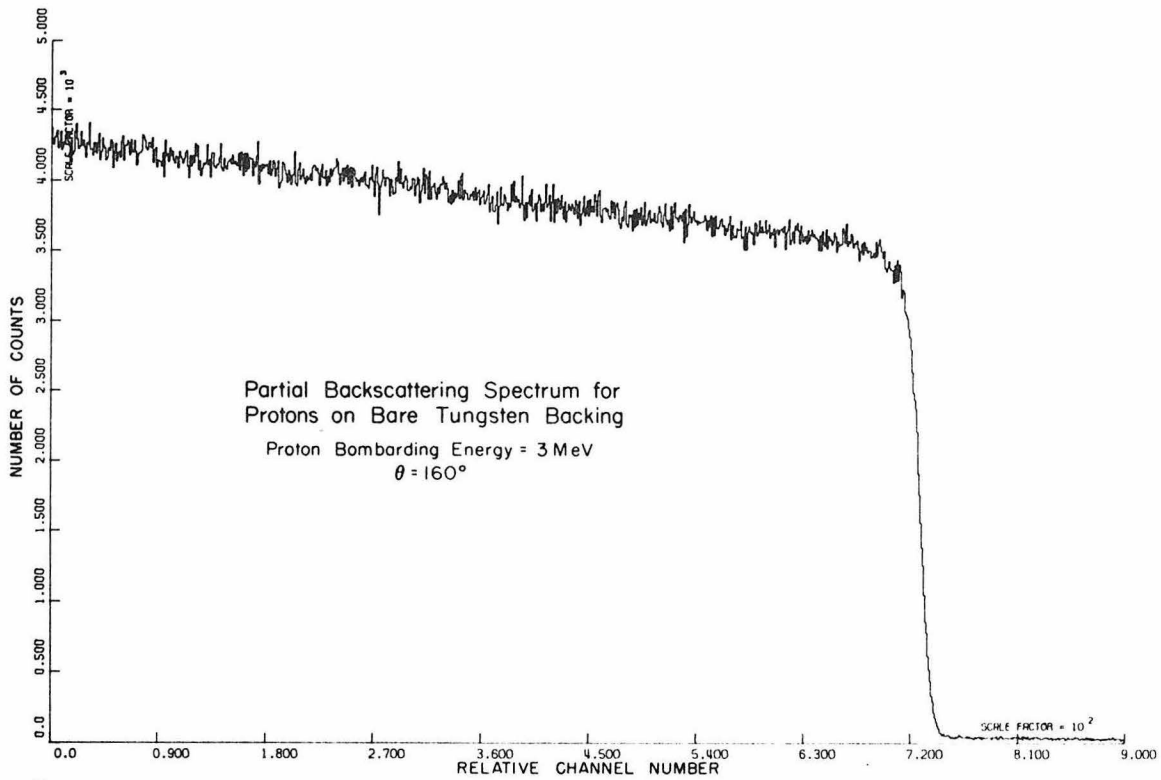
NUMBER OF COUNTS
SCALE FACTOR = 10³
Partial Backscattering Spectrum for
Protons on Bare Tungsten Backing
Proton Bombarding Energy = 3 MeV
θ = 160°
SCALE FACTOR = 10²
RELATIVE CHANNEL NUMBER

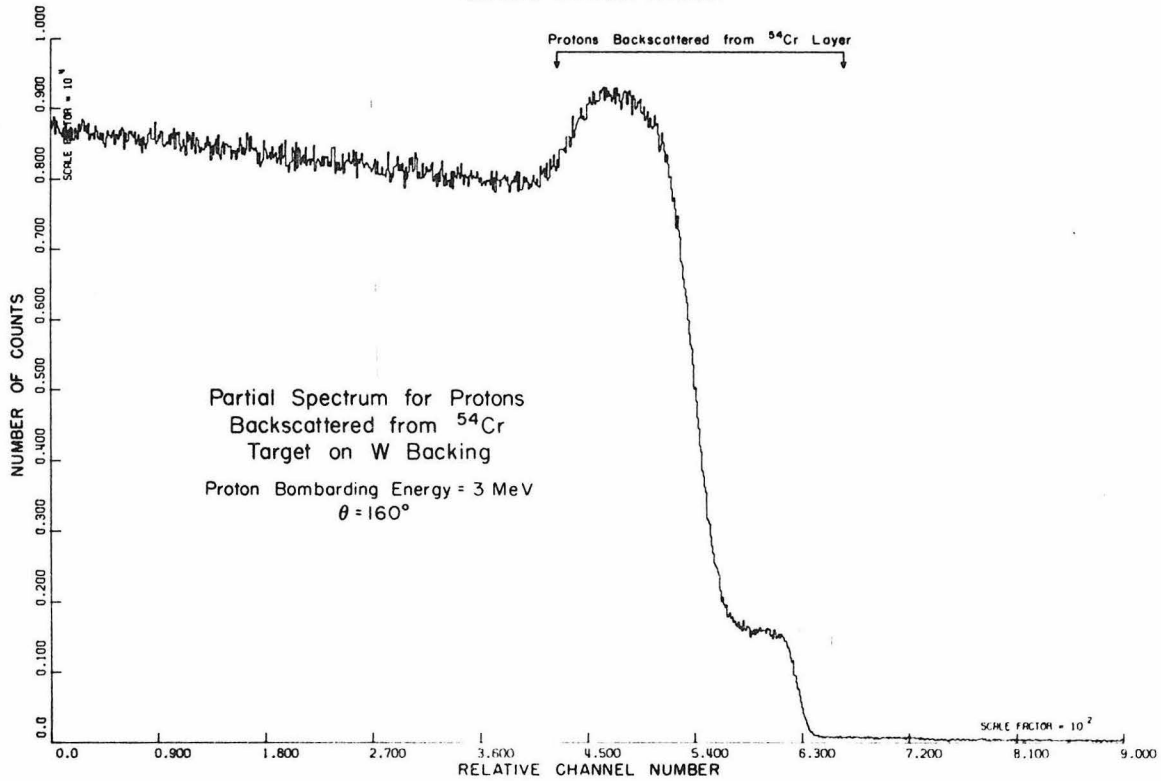
Protons Backscattered from ⁵⁴Cr Layer
NUMBER OF COUNTS
SCALE FACTOR = 10⁴
Partial Spectrum for Protons
Backscattered from ⁵⁴Cr
Target on W Backing
Proton Bombarding Energy = 3 MeV
θ = 160°
SCALE FACTOR = 10²
RELATIVE CHANNEL NUMBER

Figure 6

Spectrum of α-particles backscattered from a vanadium target layer deposited on a tungsten backing. The α-particle bombarding energy was 3.7 MeV. The scattered particles were detected using a silicon surface barrier detector at $\theta = 160°$. The thickness of the vanadium layer was determined to be 190 $\mu gm/cm^2$. The peak resulting from α-particles scattered from the vanadium surface layer is superposed on the thick target yield curve of particles scattered from the tungsten backing, as indicated. See Figure 7c and Section IIC for additional details.

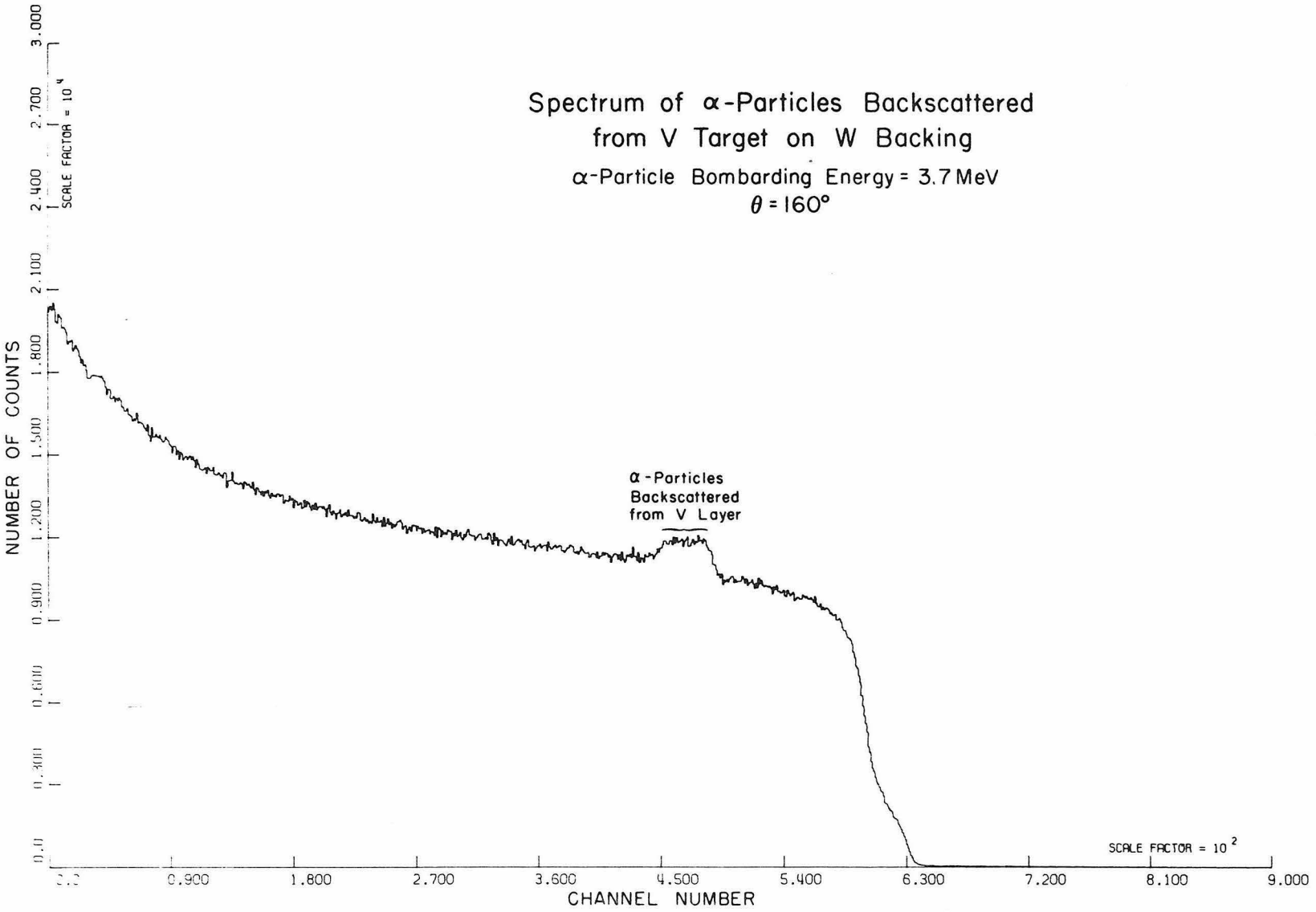
Spectrum of α-Particles Backscattered
from V Target on W Backing
α-Particle Bombarding Energy = 3.7 MeV
θ = 160°
NUMBER OF COUNTS
SCALE FACTOR = 10⁴
3.000
2.700
2.400
2.100
1.800
1.500
1.200
0.900
0.600
0.300
0.0
α-Particles
Backscattered
from V Layer
SCALE FACTOR = 10²
0.0
0.900
1.800
2.700
3.600
4.500
5.400
6.300
7.200
8.100
9.000
CHANNEL NUMBER

Figure 7

Schematic representation of backscattering techniques. (a) Backscattering from a bare backing. A detector placed at an angle of $\theta_s = \pi - (\theta_A + \theta_E)$ detects particles of energy kE_A scattered from the surface of the backing, where E_A is the bombarding energy and k is the scattering factor. The high energy edge of the thick target yield curve arising from particles scattered at different depths in the backing is located at kE_A.

(b) Backscattering from the surface of the backing of a target of thickness T_t. The energy E_E of the high energy edge of the thick target yield curve for scattering from the backing is given by

$$E_E = k\left(E_A - \int_A^C \frac{dE}{dx}\, dx\right) - \int_C^E \frac{dE}{dx}\, dx$$

$$= kE_C - \int_C^E \frac{dE}{dx}\, dx$$

The measured difference between E_E and kE_A provides a measure of the target thickness (see Section IIC).

(c) Backscattering from a layer of thickness ΔT_B at the surface of the target backing. The thickness of the backing surface layer, ΔT_B, is chosen so that the difference in detected energy between particles scattered from its surface and its back is dE/dn, the energy per channel in the spectrum. The height of the step at the high energy edge of the thick target yield curve corresponds to the area of the peak which would result from backscattering from a layer of backing material of thickness ΔT_B. See Section IIC for details.

(a) Backscattering from bare backing

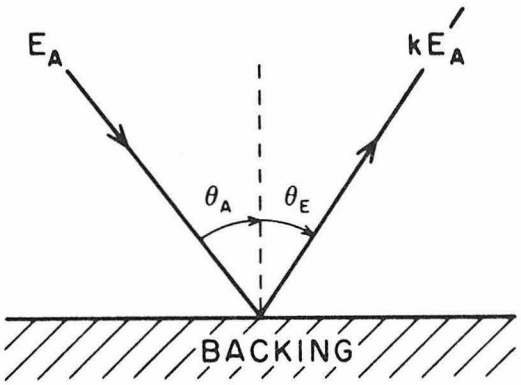

(b) Backscattering from backing of target of thickness T_t

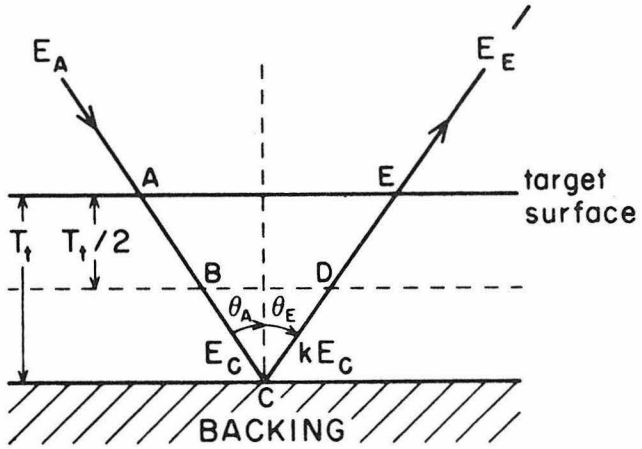

$$E_E = k\left(E_A - \int_A^C \frac{dE}{dx}\,dx\right) - \int_C^E \frac{dE}{dx}\,dx$$

(c) Backscattering from layer of thickness ΔT_B at surface of target backing

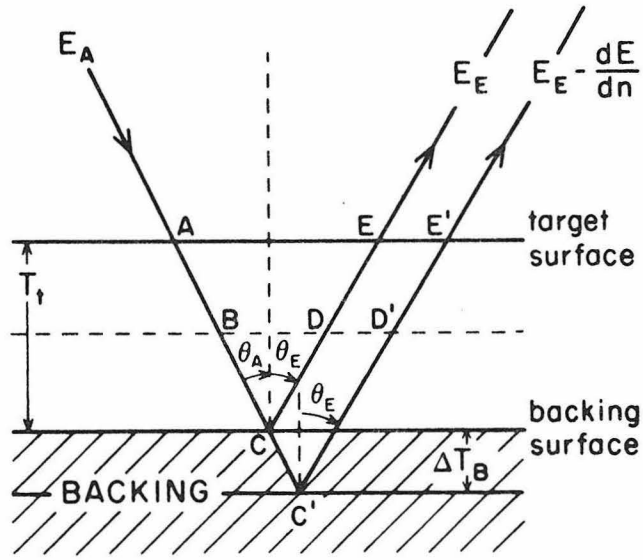

Figure 8

Absolute efficiency curve for low energy γ-rays for the 100 cc Ge(Li) detector. The source was located 10 cm from the detector. This configuration was used to detect the 320 keV ^{51}Cr γ-rays in the $^{51}V(p,n)^{51}Cr$ activation measurements of the BF_3 long counter efficiency (see Section IIF). The low energy Ge(Li) efficiency curve for the configuration used in the $^{68}Zn(p,\gamma)^{69}Ga$ measurement was similar, except that for E_γ = 574 keV the efficiency was 4% below the power law efficiency extrapolated from higher γ-ray energies, and for E_γ = 319 keV it was 16% below the power law. The efficiency curve began to bend over at low energies because of the greater thickness of absorber in this configuration. Gamma-ray detection is discussed in Section IID.

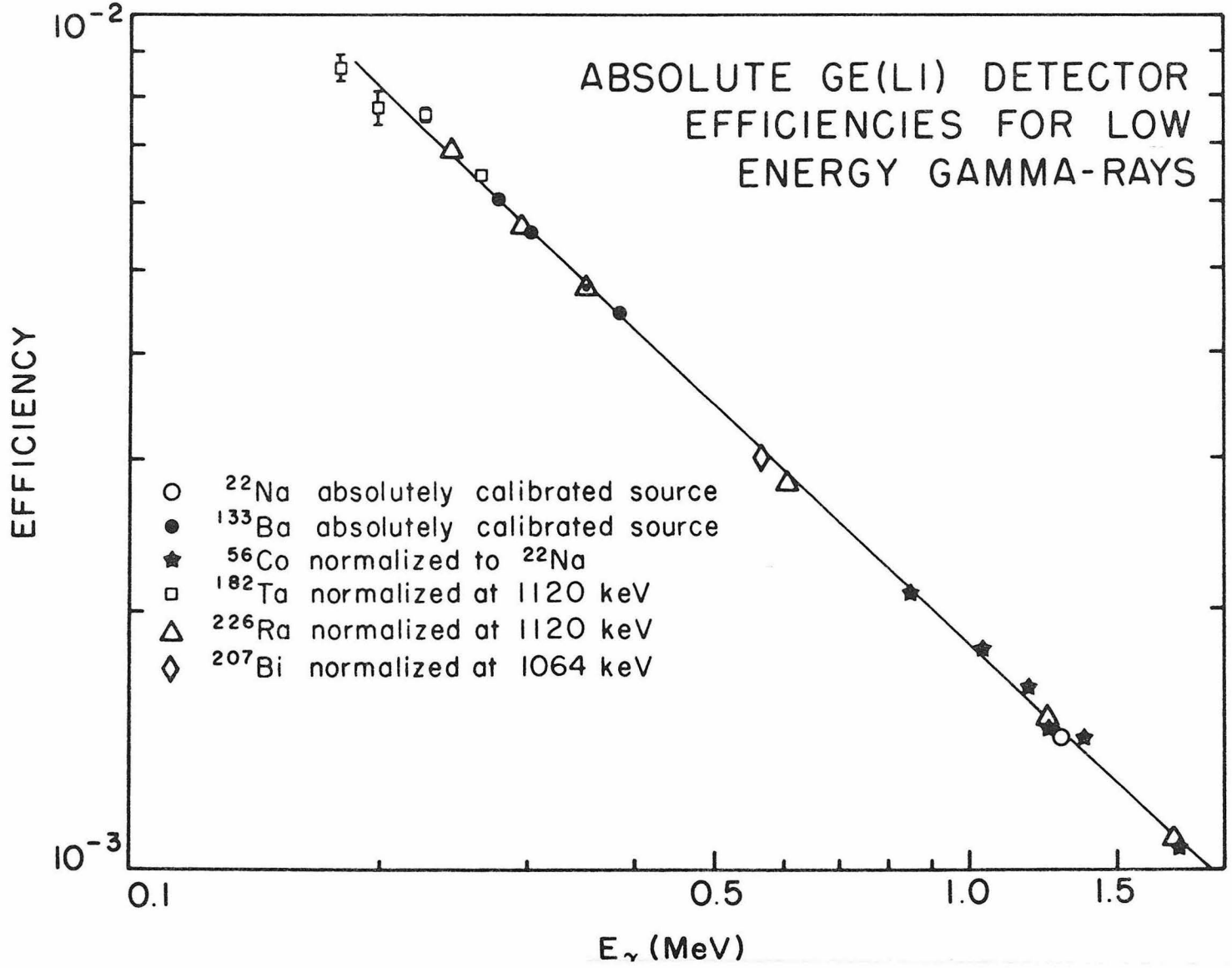
ABSOLUTE GE(LI) DETECTOR
EFFICIENCIES FOR LOW
ENERGY GAMMA-RAYS
EFFICIENCY
10^{-2}
10^{-3}
0.1
0.5
1.0
1.5
E_γ (MeV)
^{22}Na absolutely calibrated source
^{133}Ba absolutely calibrated source
^{56}Co normalized to ^{22}Na
^{182}Ta normalized at 1120 keV
^{226}Ra normalized at 1120 keV
^{207}Bi normalized at 1064 keV

Figure 9

Ge(Li) detector efficiencies determined for the 73 cc Ge(Li) detector in the geometry used for the measurement of high energy, primary γ-rays produced in the $^{54}Cr(p,\gamma)^{55}Mn$ reaction. The detector face was 3.3 cm from the reaction site. Gamma-ray detection is discussed in Section IID and the analysis of the γ-ray data is discussed in Section IIE.

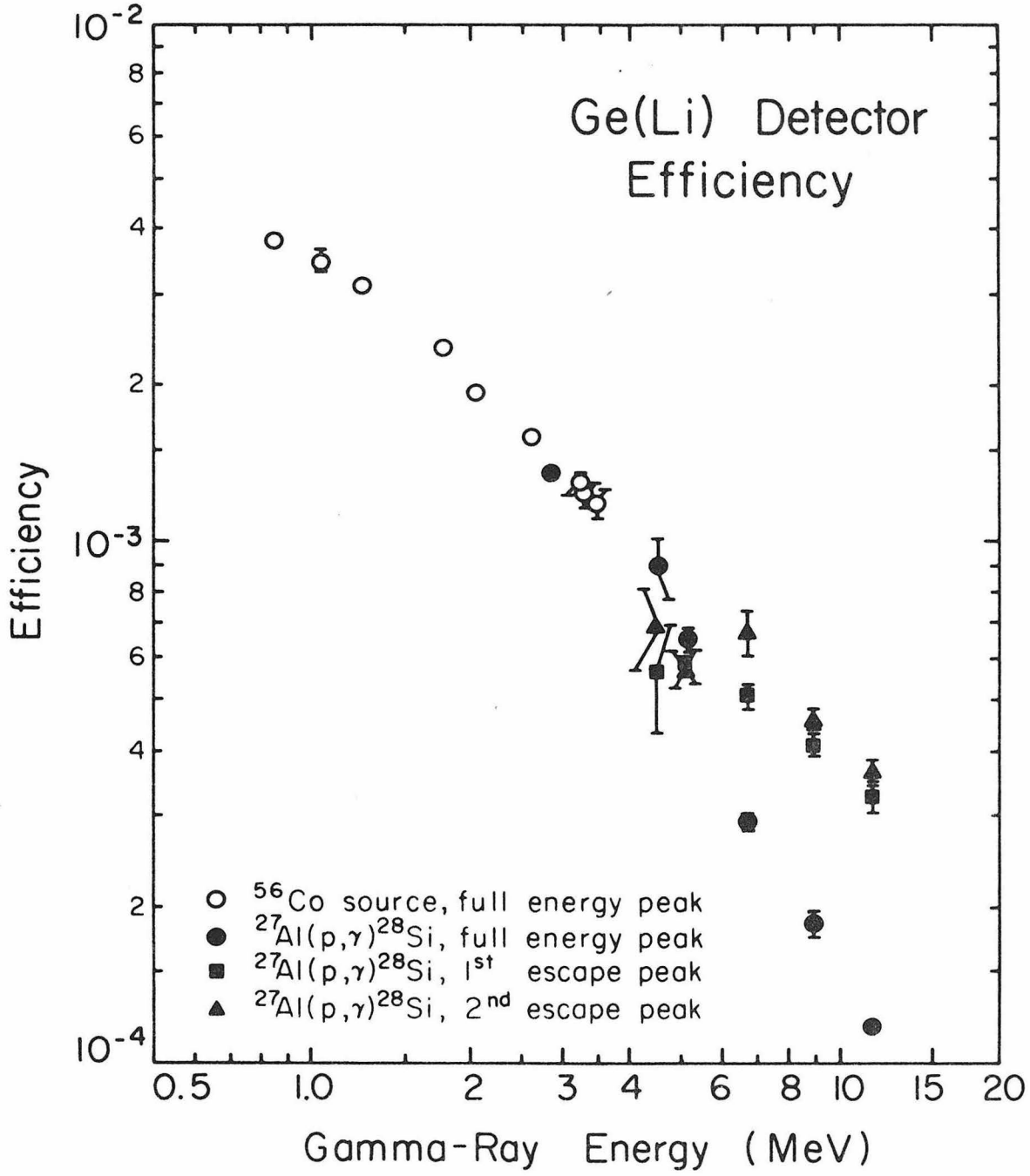
Ge(Li) Detector
Efficiency
Efficiency
Gamma-Ray Energy (MeV)
10^{-2}
8
6
4
2
10^{-3}
8
6
4
2
10^{-4}
0.5
1.0
2
3
4
6
8
10
15
20
^{56}Co source, full energy peak
^{27}Al(p,γ)^{28}Si, full energy peak
^{27}Al(p,γ)^{28}Si, 1st escape peak
^{27}Al(p,γ)^{28}Si, 2nd escape peak

Figure 10

Ge(Li) detector spectrum for γ-rays resulting from 1.9 MeV proton bombardment of the 1200 $\mu gm/cm^2$ vanadium target. Prominent peaks are identified by their energy (in MeV) and the nuclide from which they arise. Gamma-ray detection is discussed in Section IID.

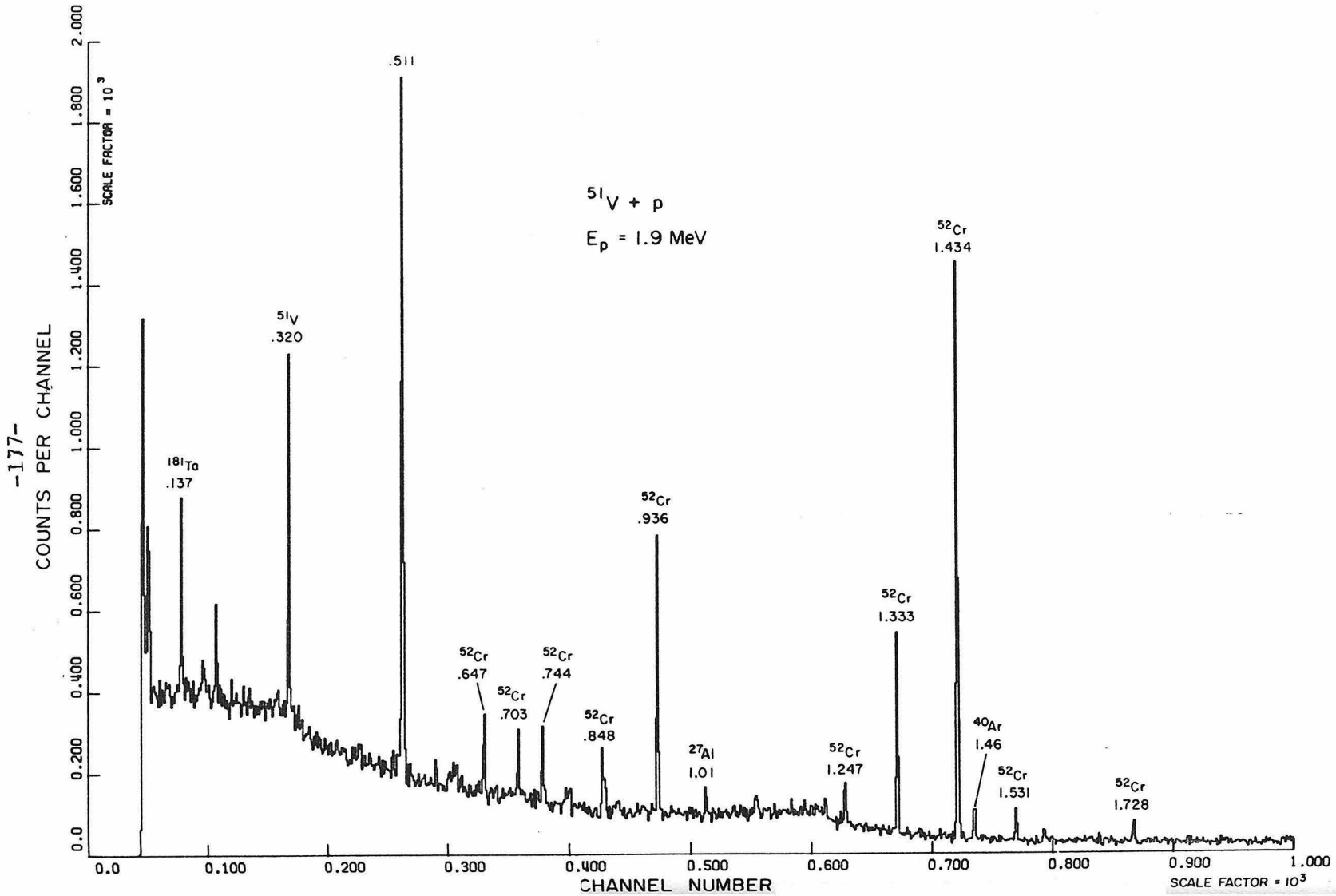
$^{51}V + p$
E_p = 1.9 MeV
.511
^{51}V .320
^{181}Ta .137
^{52}Cr .647
^{52}Cr .703
^{52}Cr .744
^{52}Cr .848
^{52}Cr .936
^{27}Al 1.01
^{52}Cr 1.247
^{52}Cr 1.333
^{52}Cr 1.434
^{40}Ar 1.46
^{52}Cr 1.531
^{52}Cr 1.728
SCALE FACTOR = 10^3
COUNTS PER CHANNEL
CHANNEL NUMBER
SCALE FACTOR = 10^3
0.0
0.100
0.200
0.300
0.400
0.500
0.600
0.700
0.800
0.900
1.000
0.0
0.200
0.400
0.600
0.800
1.000
1.200
1.400
1.600
1.800
2.000

Figure 11

Ge(Li) detector spectrum for γ-rays resulting from 3.75 MeV proton bombardment of the 1200 $\mu gm/cm^2$ vanadium target. Prominent peaks are identified by their energy (in MeV) and by the nuclide from which they arise. Gamma-ray detection is discussed in Section IID.

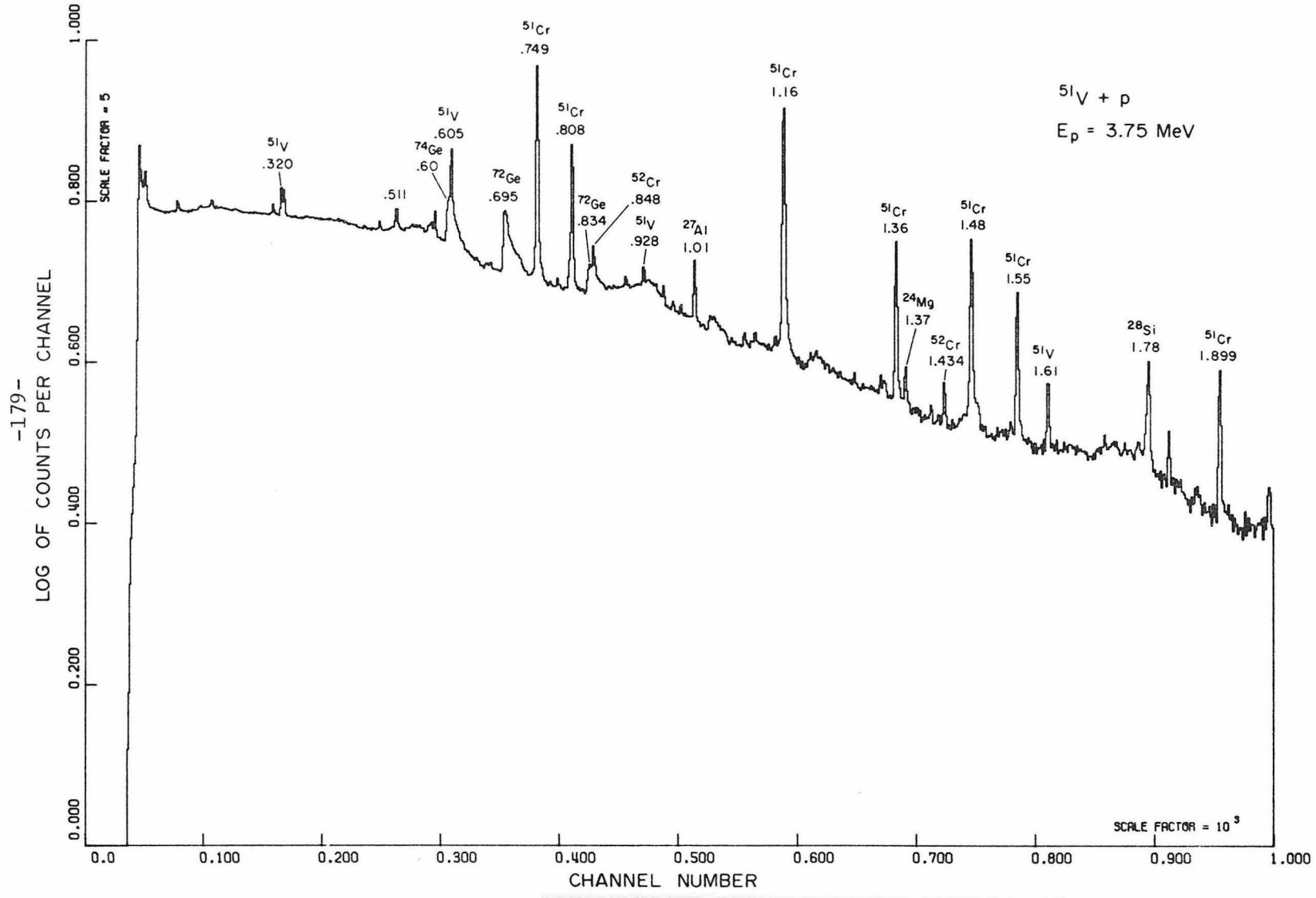
^{51}V + p
E_p = 3.75 MeV
SCALE FACTOR = 5
SCALE FACTOR = 10^3
^{51}V .320
.511
^{74}Ge .60
^{51}V .605
^{72}Ge .695
^{51}Cr .749
^{51}Cr .808
^{72}Ge .834
^{52}Cr .848
^{51}V .928
^{27}Al 1.01
^{51}Cr 1.16
^{51}Cr 1.36
^{24}Mg 1.37
^{52}Cr 1.434
^{51}Cr 1.48
^{51}Cr 1.55
^{51}V 1.61
^{28}Si 1.78
^{51}Cr 1.899
LOG OF COUNTS PER CHANNEL
CHANNEL NUMBER
0.000
0.200
0.400
0.600
0.800
1.000
0.0
0.100
0.200
0.300
0.400
0.500
0.600
0.700
0.800
0.900
1.000

Figure 12

Partial level scheme for ^{55}Mn showing known γ-rays from decays of states with $E_x \leq 3004$ keV. See Section IIE and Tables 5 and 6 for further details concerning the analysis of the ^{54}Cr(p,γ)^{55}Mn data.

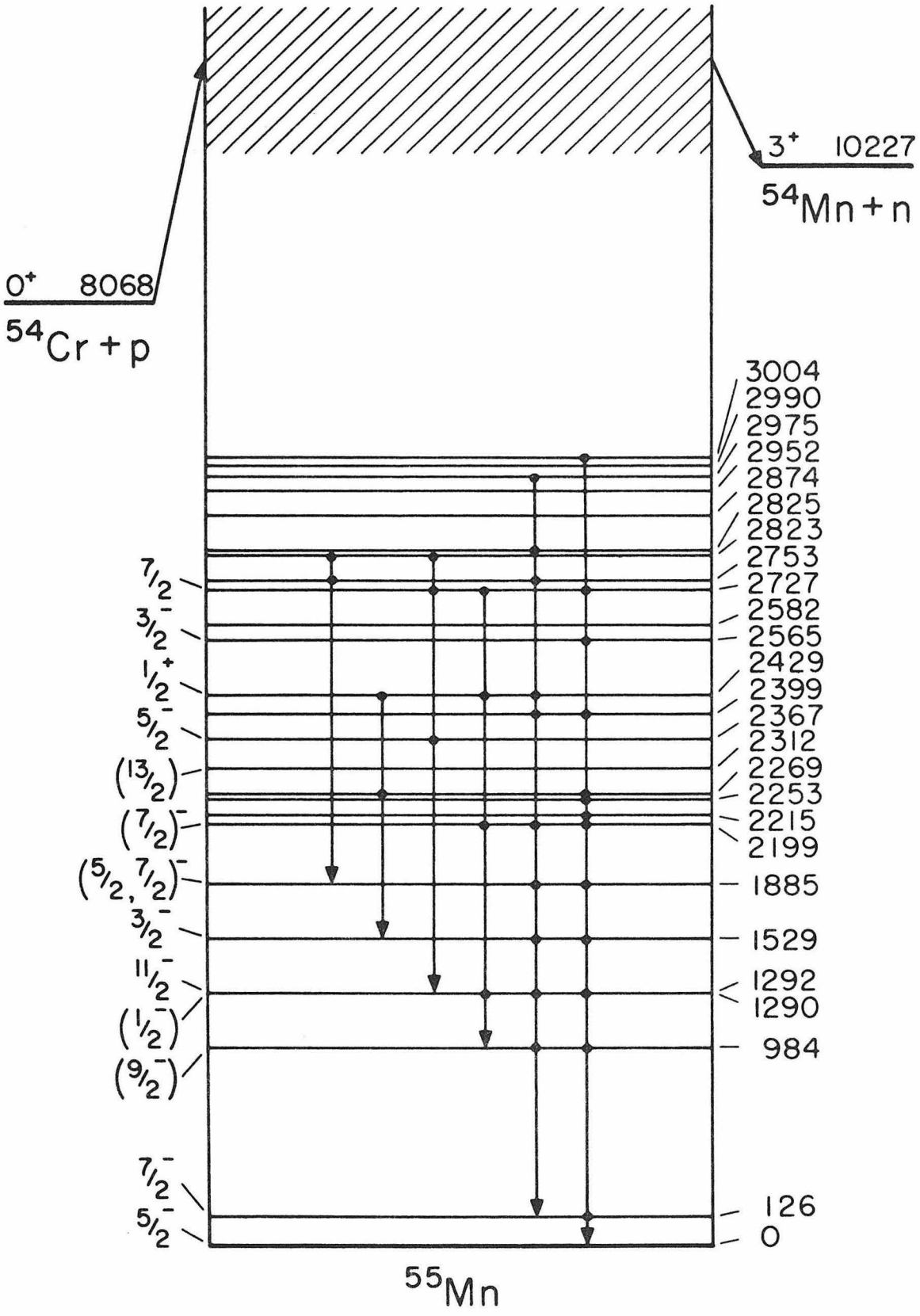
0+ 8068
54Cr + p
3+ 10227
54Mn + n
3004
2990
2975
2952
2874
2825
2823
2753
2727
2582
2565
2429
2399
2367
2312
2269
2253
2215
2199
1885
1529
1292
1290
984
126
0
7/2
3/2-
1/2+
5/2-
(13/2)
(7/2)-
(5/2, 7/2)-
3/2-
11/2-
(1/2-)
(9/2-)
7/2-
5/2-
55Mn

Figure 13

Partial level scheme for ^{52}Cr showing known γ-rays from decays of states with $E_x \leq 3900$ keV. See Section IIE and Table 6 for further details concerning the analysis of the $^{51}V(p,\gamma)^{52}Cr$ data.

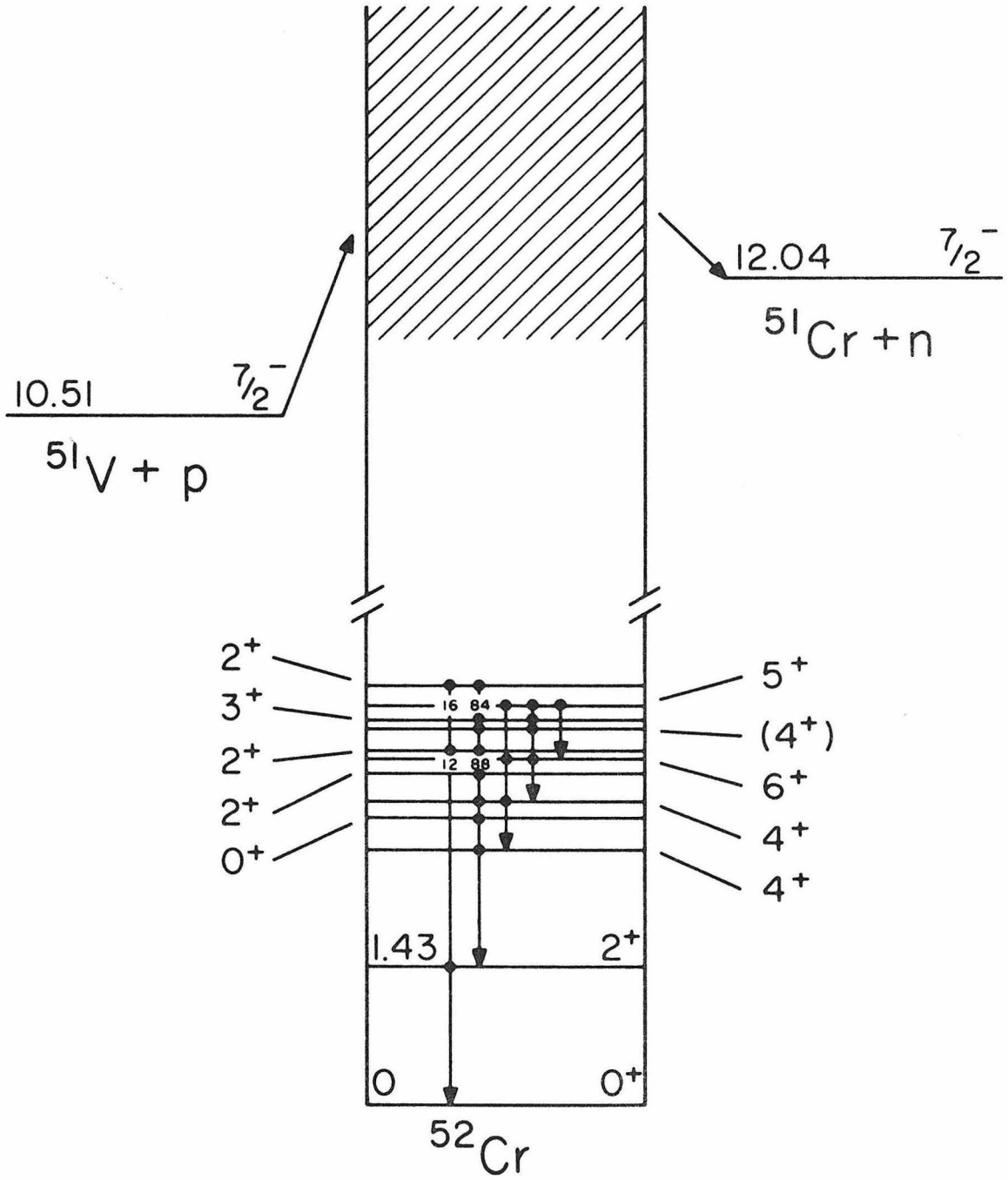
12.04
7/2⁻
51Cr + n
10.51
7/2⁻
51V + p
2+
3+
2+
2+
0+
16
84
12
88
5+
(4+)
6+
4+
4+
1.43
2+
0
0+
52Cr

Figure 14

Partial level scheme for ^{69}Ga showing known γ-rays from decays of states with $E_x \leq 2044$ keV. See Section IIE and Table 6 for further details concerning the analysis of the ^{68}Zn(p,γ)^{69}Ga data.

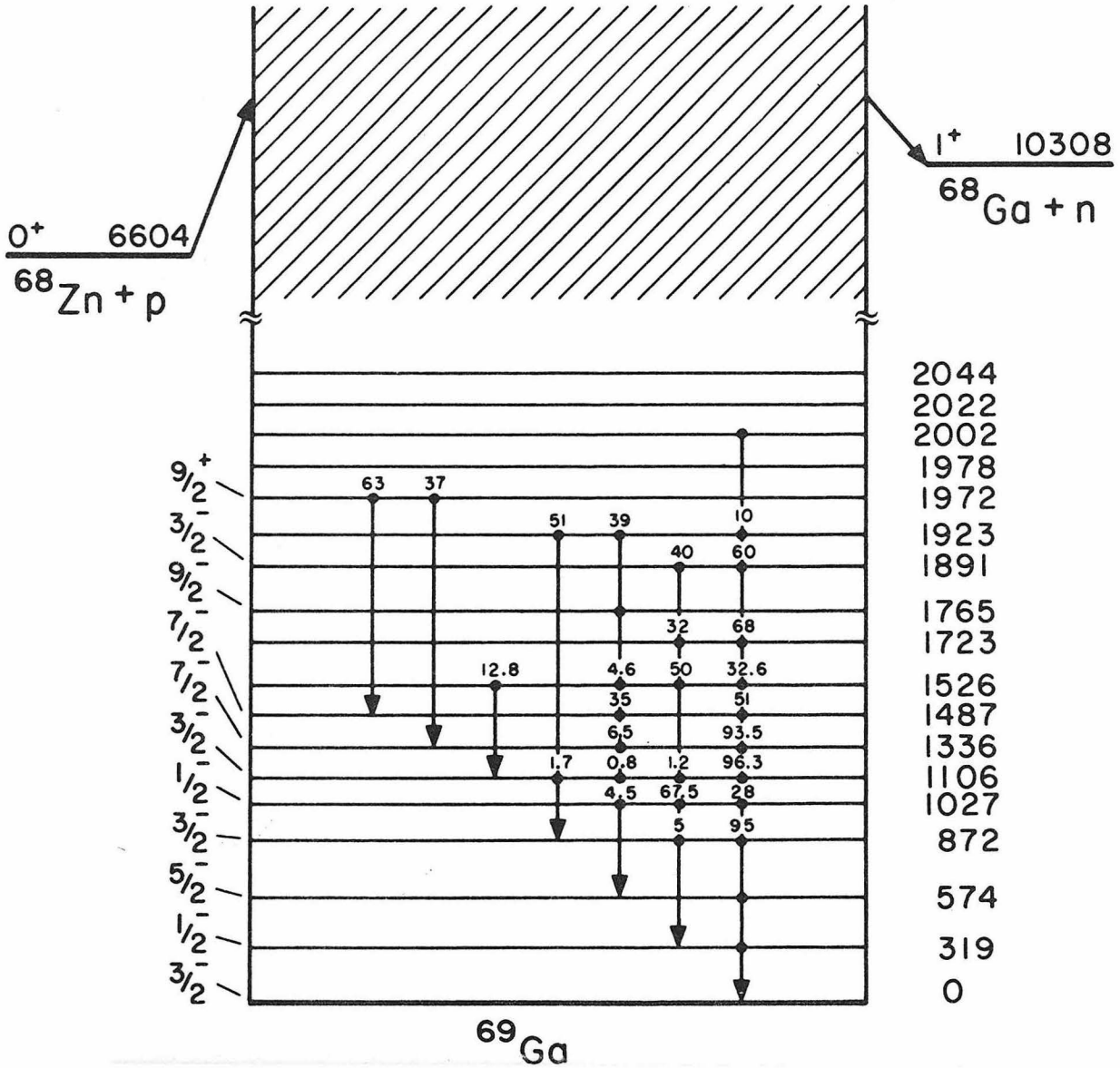
0+ 6604
68Zn + p
1+ 10308
68Ga + n
2044
2022
2002
1978
1972
1923
1891
1765
1723
1526
1487
1336
1106
1027
872
574
319
0
9/2+
3/2-
9/2-
7/2-
7/2-
3/2-
1/2-
3/2-
5/2-
1/2-
3/2-
63
37
51
39
10
40
60
32
68
12.8
4.6
50
32.6
35
51
6.5
93.5
1.7
0.8
1.2
96.3
4.5
67.5
28
5
95
69Ga

Figure 15

Partial level scheme for ^{49}Sc showing known γ-rays from decays of states with $E_x < 5080$ keV. See Section IIE and Table 6 for further details concerning the analysis of the $^{48}Ca(p,\gamma)^{49}Sc$ data.

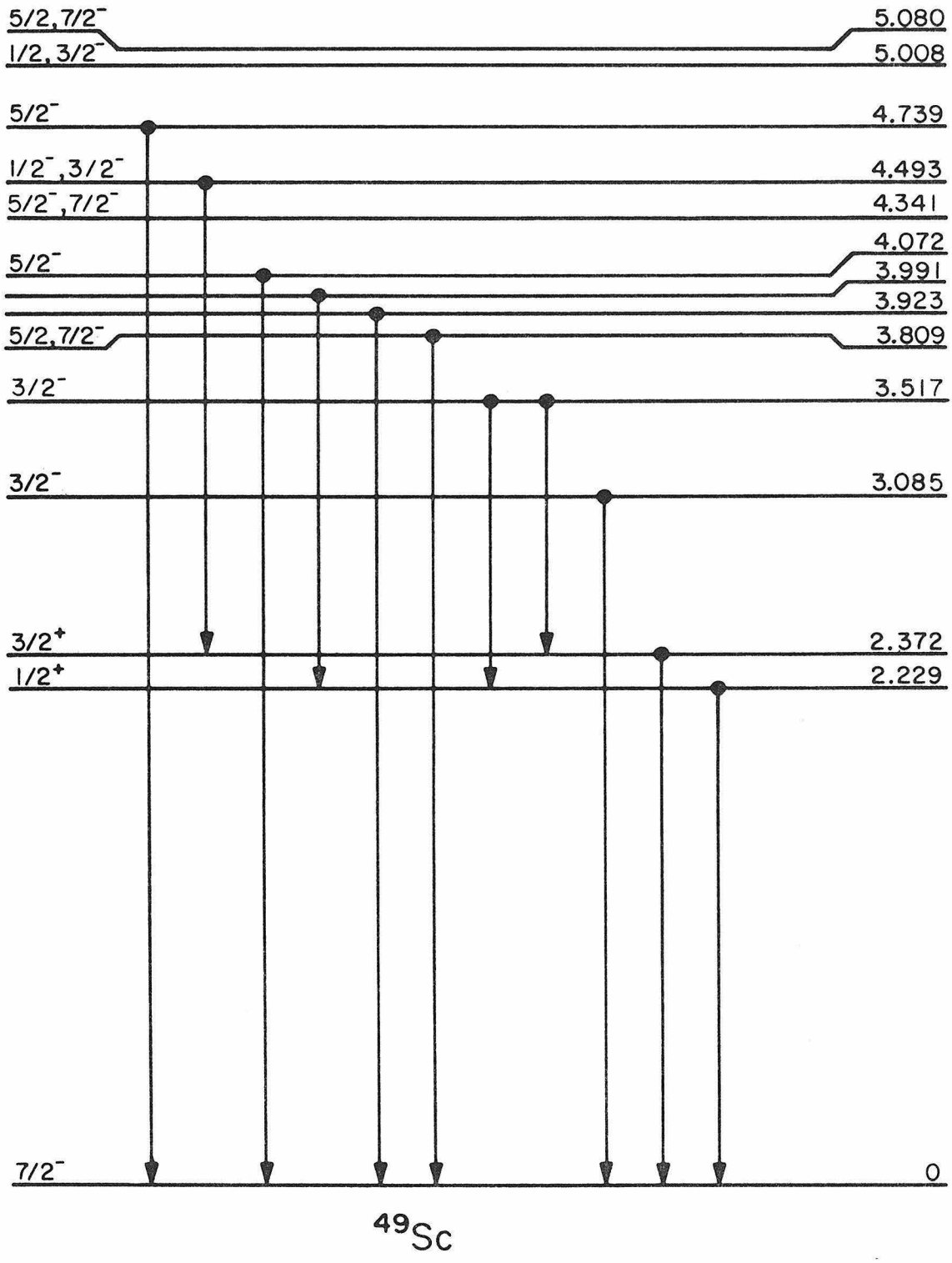
5/2,7/2⁻
5.080
1/2,3/2⁻
5.008
5/2⁻
4.739
1/2⁻,3/2⁻
4.493
5/2⁻,7/2⁻
4.341
4.072
5/2⁻
3.991
3.923
5/2,7/2⁻
3.809
3/2⁻
3.517
3/2⁻
3.085
3/2⁺
2.372
1/2⁺
2.229
7/2⁻
0

^{49}Sc

Figure 16

Partial level scheme for ^{41}K showing known γ-rays from decays of states with $E_x \leq 2770$ keV. The five transitions used in the determination of the "preliminary cross sections" for the $^{37}Cl(\alpha,\gamma)^{41}K$ reaction are denoted by bold arrows. See Section IIG and Table 6 for further details concerning the analysis of the $^{37}Cl(\alpha,\gamma)^{41}K$ data.

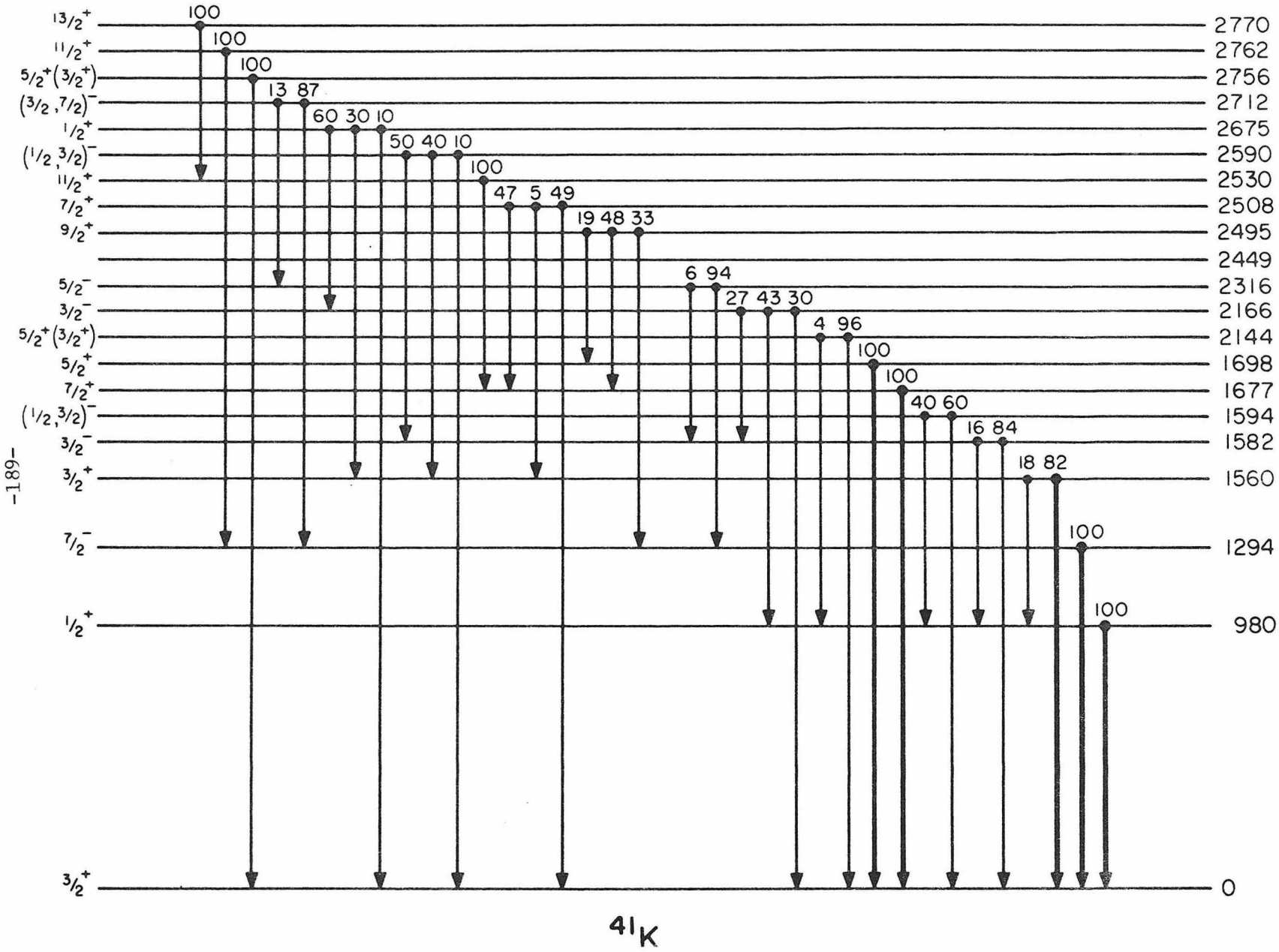
13/2+ 2770
11/2+ 2762
5/2+(3/2+) 2756
(3/2,7/2)− 2712
1/2+ 2675
(1/2,3/2)− 2590
11/2+ 2530
7/2+ 2508
9/2+ 2495
2449
5/2− 2316
3/2− 2166
5/2+(3/2+) 2144
5/2+ 1698
7/2+ 1677
(1/2,3/2)− 1594
3/2− 1582
3/2+ 1560
7/2− 1294
1/2+ 980
3/2+ 0
100
100
100
13 87
60 30 10
50 40 10
100
47 5 49
19 48 33
6 94
27 43 30
4 96
100
100
40 60
16 84
18 82
100
100
41K

Figure 17

Partial level scheme for ^{66}Zn showing known γ-rays from decays of states with $E_x \leq 3000$ keV. See Section IIG and Table 6 for further details concerning the analysis of the ^{62}Ni$(\alpha,\gamma)^{66}$Zn data.

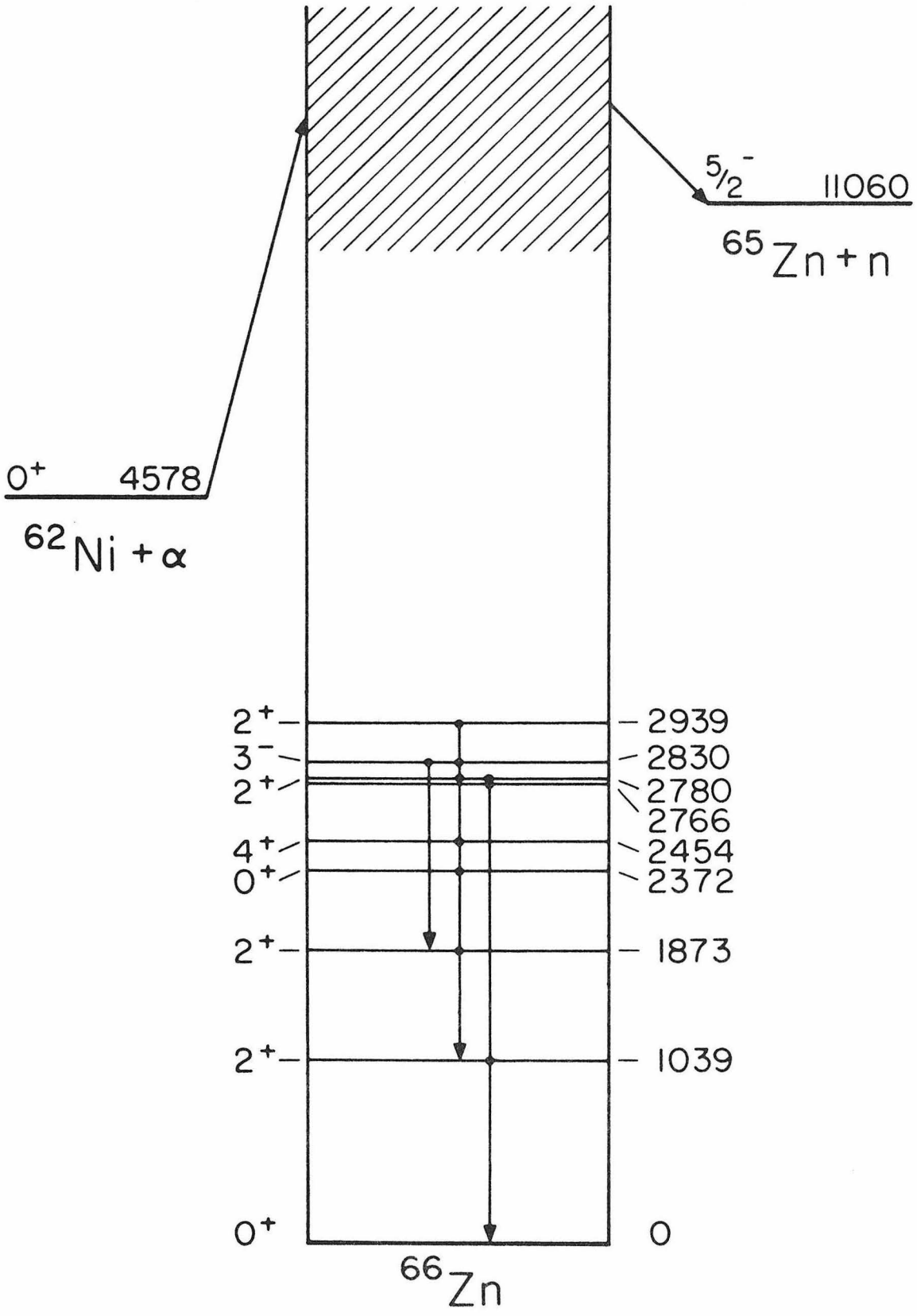
5/2⁻ 11060
65Zn + n
0⁺ 4578
62Ni + α
2⁺ 2939
3⁻ 2830
2⁺ 2780
2766
4⁺ 2454
0⁺ 2372
2⁺ 1873
2⁺ 1039
0⁺ 0
66Zn

Figure 18

Partial level scheme for ^{68}Zn showing known γ-rays from decays of states with $E_x \leq 3000$ keV. See Section IIG and Table 6 for further details concerning the analysis of the ^{64}Ni(α,γ)^{68}Zn data.

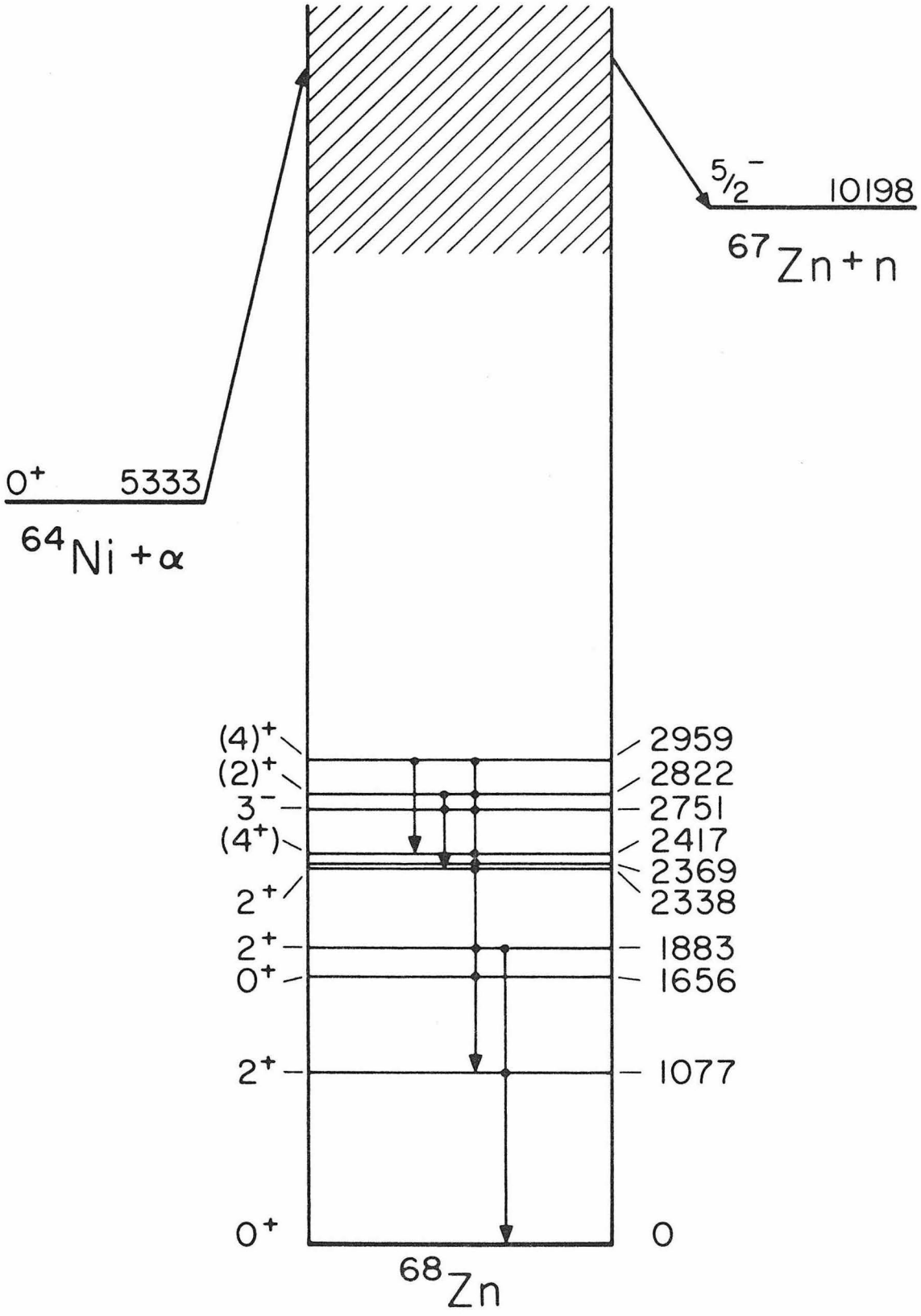
0+ 5333
64Ni + α
5/2− 10198
67Zn + n
(4)+ 2959
(2)+ 2822
3− 2751
(4+) 2417
2369
2+ 2338
2+ 1883
0+ 1656
2+ 1077
0+ 0
68Zn

Figure 19

Excitation function for production of 1529 keV γ-rays in the reaction $^{54}Cr(p,\gamma)^{55}Mn$. Error bars shown are statistical only. The curve shows the results of a Hauser-Feshbach calculation performed using Mann's code HAUSER*4 (Mann 1976), with γ-ray transmission functions for the population of the 1529 keV state calculated by the code TISO (Appendix A). The arrows labelled IAR indicate proton energies for isobaric analogue resonances which have been previously identified (Moses 1971b). See Section IIG for further details.

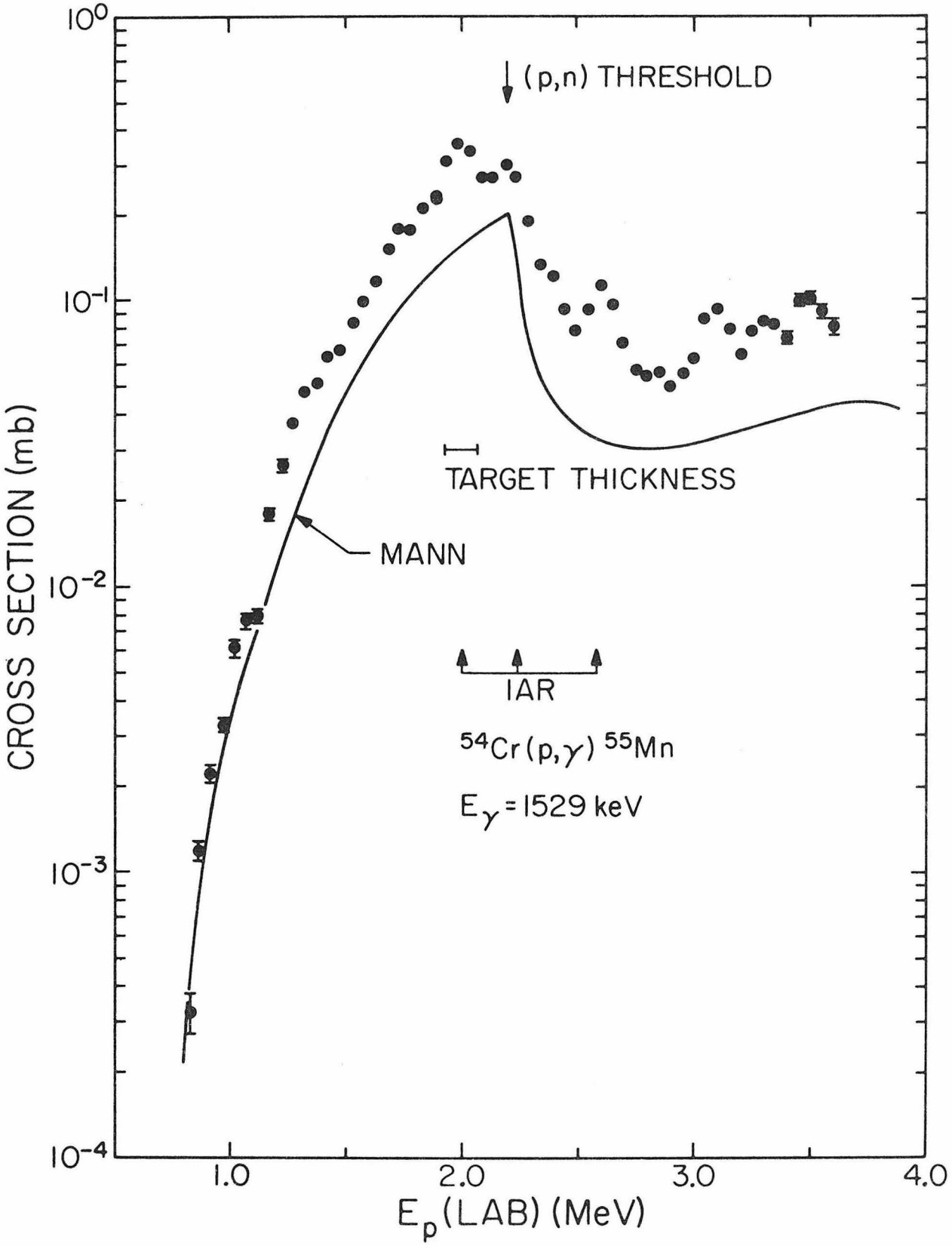
(p,n) THRESHOLD
TARGET THICKNESS
MANN
IAR
$^{54}Cr(p,\gamma)\,^{55}Mn$
$E_\gamma = 1529$ keV
CROSS SECTION (mb)
E_p(LAB) (MeV)
10^0
10^{-1}
10^{-2}
10^{-3}
10^{-4}
1.0
2.0
3.0
4.0

Figure 20

Excitation function for production of 2565 keV γ-rays in the reaction $^{54}Cr(p,\gamma)^{55}Mn$. Error bars are statistical only. The curve shows the results of a Hauser-Feshbach calculation performed using Mann's code HAUSER*4 (Mann 1976) with γ-ray transmission functions for the population of the 2565 keV state calculated using the code TISO (see Appendix A). The arrows indicate proton energies for isobaric analogue resonances which have been previously observed (Moses 1971b). See Section IIG for further details.

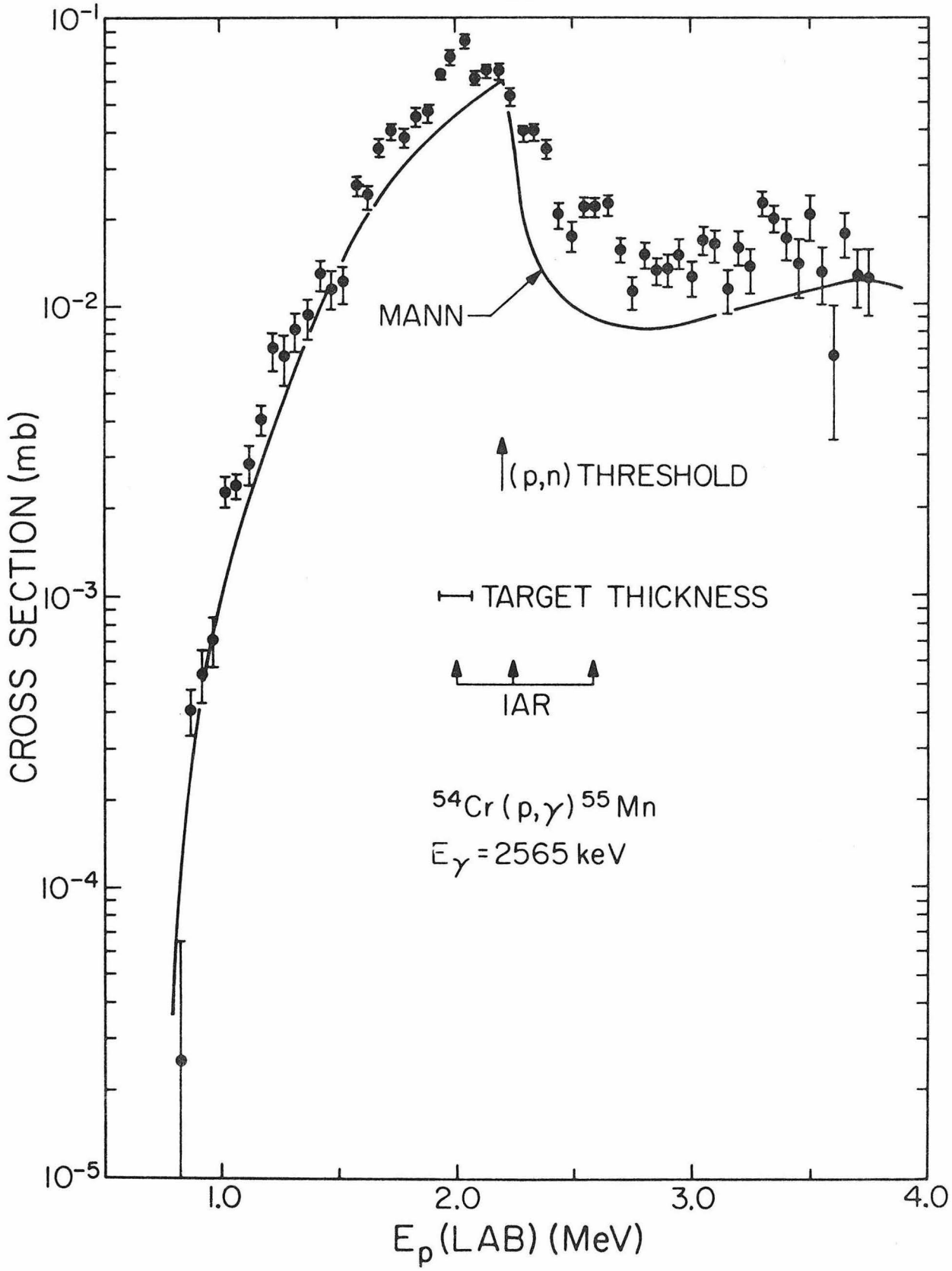
CROSS SECTION (mb)
10^{-1}
10^{-2}
10^{-3}
10^{-4}
10^{-5}
1.0
2.0
3.0
4.0
E_p (LAB) (MeV)
MANN
(p,n) THRESHOLD
TARGET THICKNESS
IAR
$^{54}Cr(p,\gamma)^{55}Mn$
E_γ = 2565 keV

Figure 21

Excitation function for all primary γ-rays emitted in the reaction $^{54}Cr(p,\gamma)^{55}Mn$. Error bars shown are statistical only. The curves show the results of Hauser-Feshbach calculations performed using the HAUSER*4 code of Mann, labelled "Mann," and the KGHFP, labelled "FPZW." (See Section IIIB for a discussion of the calculations.) Complete isospin mixing is assumed and width fluctuation corrections are included using the Tepel approximation (Tepel 1974). The neutron strength functions used in the KGHFP calculations are given in Table 24. The arrows labelled IAR indicate proton energies for isobaric analogue resonances which have been previously identified. See Section IIE for further details.

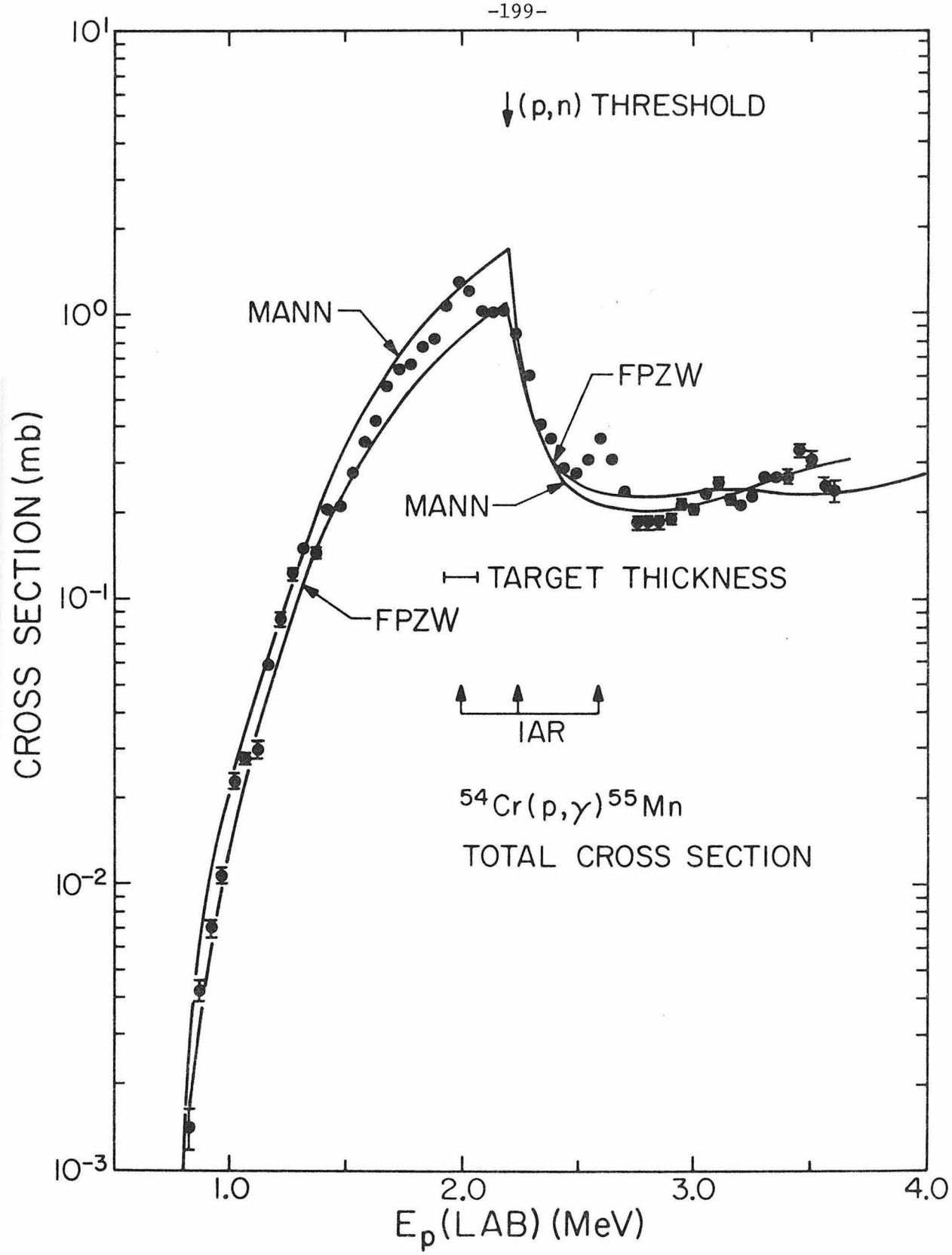
(p,n) THRESHOLD
MANN
FPZW
MANN
TARGET THICKNESS
FPZW
IAR
$^{54}Cr(p,\gamma)^{55}Mn$
TOTAL CROSS SECTION
CROSS SECTION (mb)
10^{1}
10^{0}
10^{-1}
10^{-2}
10^{-3}
1.0
2.0
3.0
4.0
E_p(LAB) (MeV)

Figure 22

Absolute cross sections for the $^{51}V(p,\gamma)^{52}Cr$ reaction. Error bars represent statistical errors only. The theoretical curves show the results of Hauser-Feshbach calculations using the KGHFP and Mann's program, HAUSER*4 (see Section IIIB). Complete isospin mixing is assumed and width fluctuation corrections are included using the Tepel approximation (Tepel 1974). The neutron strength functions used in the KGHFP calculations are given in Table 24. The theoretical calculations have been smoothed over an energy interval corresponding to the beam energy loss in the target as described on p. 34. Thresholds for $^{51}V(p,n)^{51}Cr$ are indicated by arrows, and the spins and parities of the ^{51}Cr states populated are given. See Section IIE for further details concerning the data analysis.

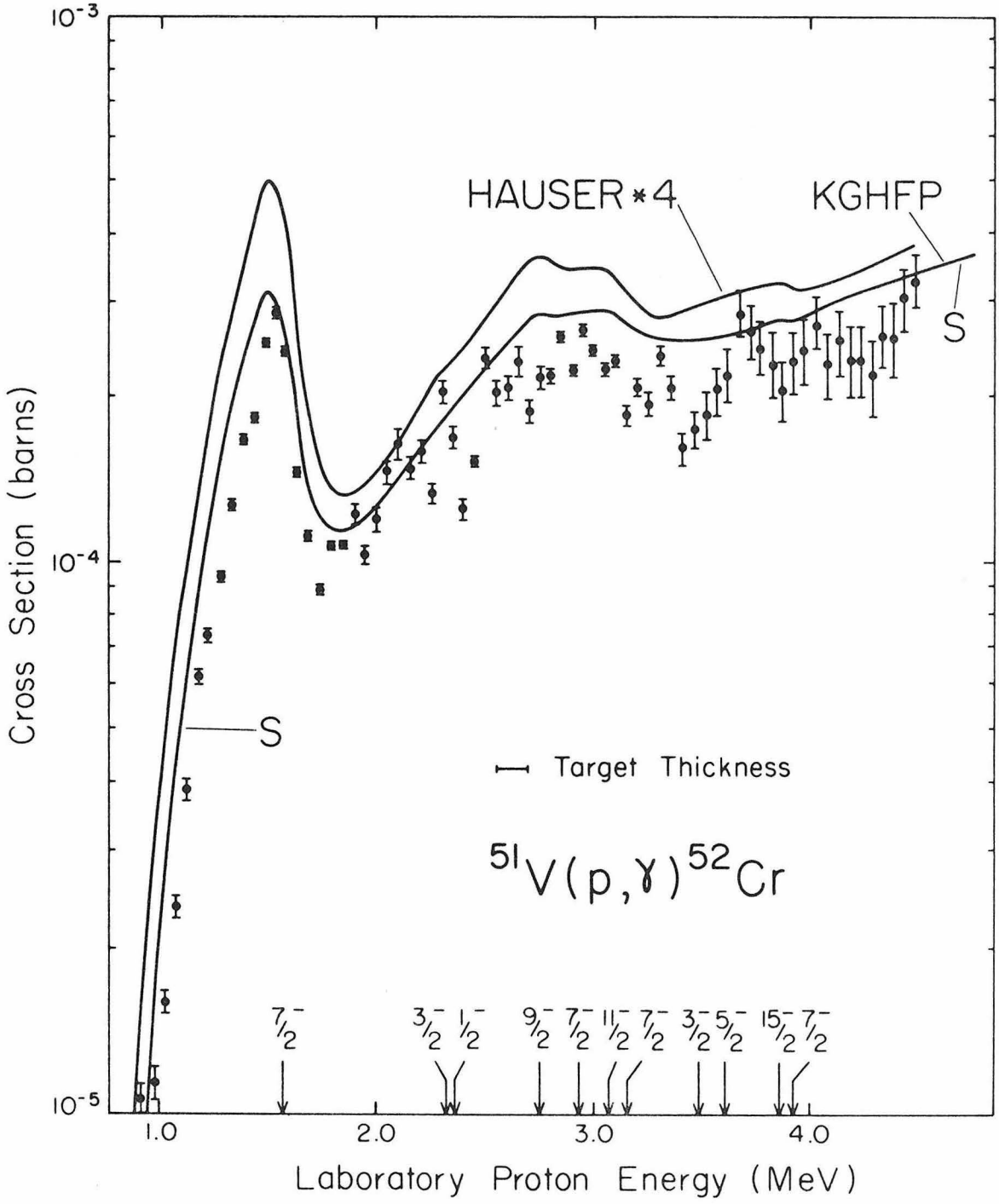
HAUSER*4
KGHFP
S
S
Target Thickness
$^{51}V(p,\gamma)^{52}Cr$
Cross Section (barns)
Laboratory Proton Energy (MeV)
10^{-3}
10^{-4}
10^{-5}
1.0
2.0
3.0
4.0
$7/2^-$
$3/2^-$ $1/2^-$
$9/2^-$ $7/2^-$ $11/2^-$ $7/2^-$
$3/2^-$ $5/2^-$
$15/2^-$ $7/2^-$

Figure 23

Absolute cross sections for $^{68}Zn(p,\gamma)^{69}Ga$. Error bars, representing statistical errors only, are shown where they are larger than the data points. Previously identified isobaric analogue resonances and neutron thresholds are indicated by arrows. The data are compared to results of global Hauser-Feshbach calculations performed using the KGHFP (Zimmerman 1977) and HAUSER*4 (Mann 1976). Complete isospin mixing and width fluctuation corrections are incorporated in the calculations. The neutron strength functions used in the KGHFP calculations are given in Table 24. The spins and parities for the ^{68}Ga states assumed in the calculations are indicated at the appropriate thresholds (only the first ten states are included in the KGHFP calculations). Many of these spins and parities are not known and are purely guesses. Thus there is considerable uncertainty in the calculation of the competition effects. See Section IIE for discussion of the data analysis, Section IIIB for discussion of the calculations, and Section IIIC for discussion of the results.

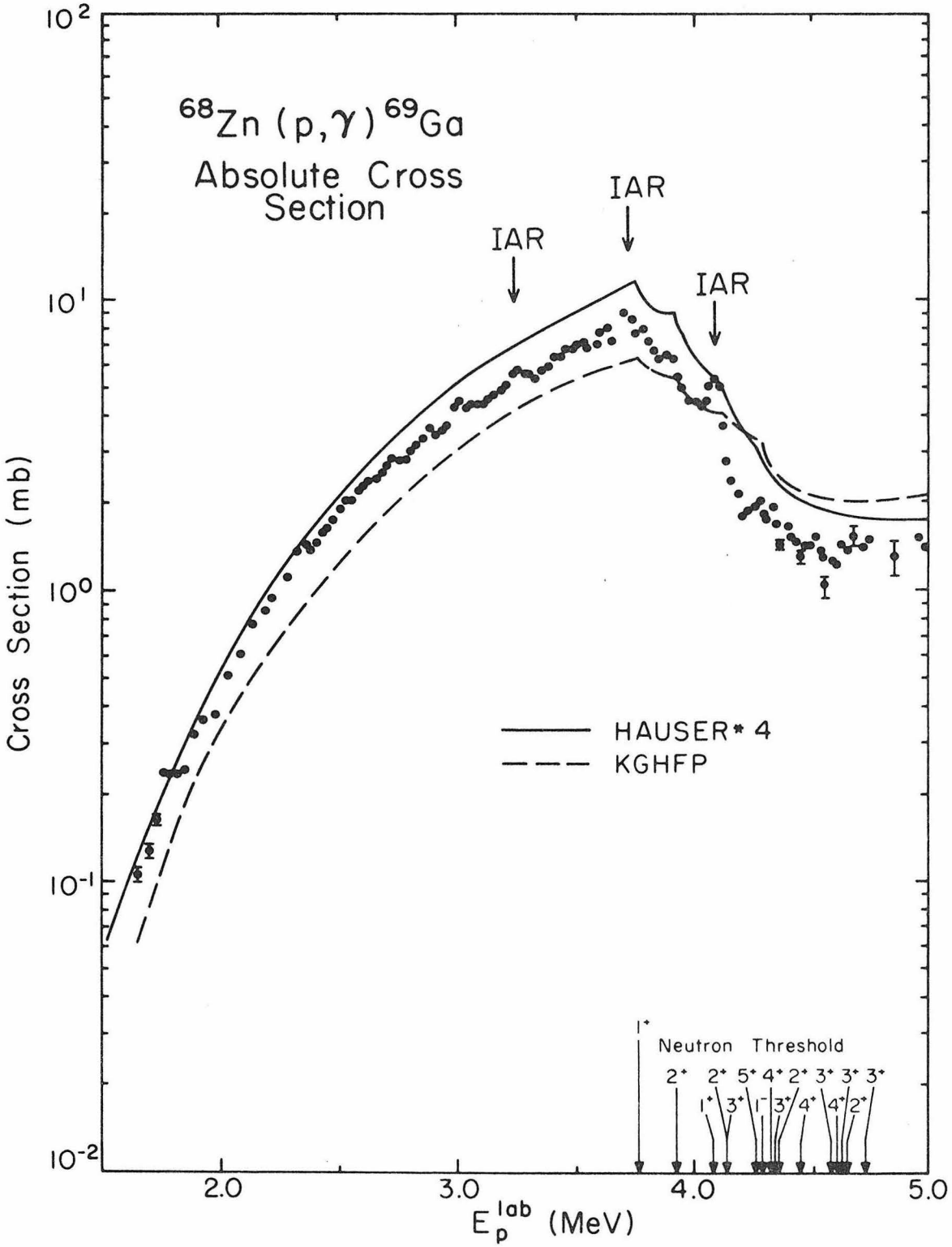
$^{68}Zn\,(p,\gamma)\,^{69}Ga$
Absolute Cross Section
IAR
IAR
IAR
HAUSER* 4
KGHFP
Neutron Threshold
Cross Section (mb)
E_p^{lab} (MeV)
10^2
10^1
10^0
10^{-1}
10^{-2}
2.0
3.0
4.0
5.0

Figure 24

Absolute cross sections for the reaction $^{48}Ca(p,\gamma)^{49}Sc$. The error bars shown are statistical only. Where the error bars are not changing rapidly as a function of energy, they are shown for only a few typical points. For 0.95 MeV $\leq E_p \leq$ 1.95 MeV, the error bars are smaller than the data points except where explicitly shown. The position of the previously identified isobaric analogue resonance is indicated. The energies of neutron thresholds and the spins and parities of the ^{48}Sc states populated are also indicated. Results of calculations performed with the KGHFP (Zimmerman 1977) and HAUSER*4 program (Mann 1976) are shown. Complete isospin mixing has been assumed and width fluctuations are included using the Tepel approximation (Tepel 1974). The neutron strength functions used in the KGHFP calculations are given in Table 24. See Section IIE for discussion of the data analysis, and Section IIIB for discussion of the calculations.

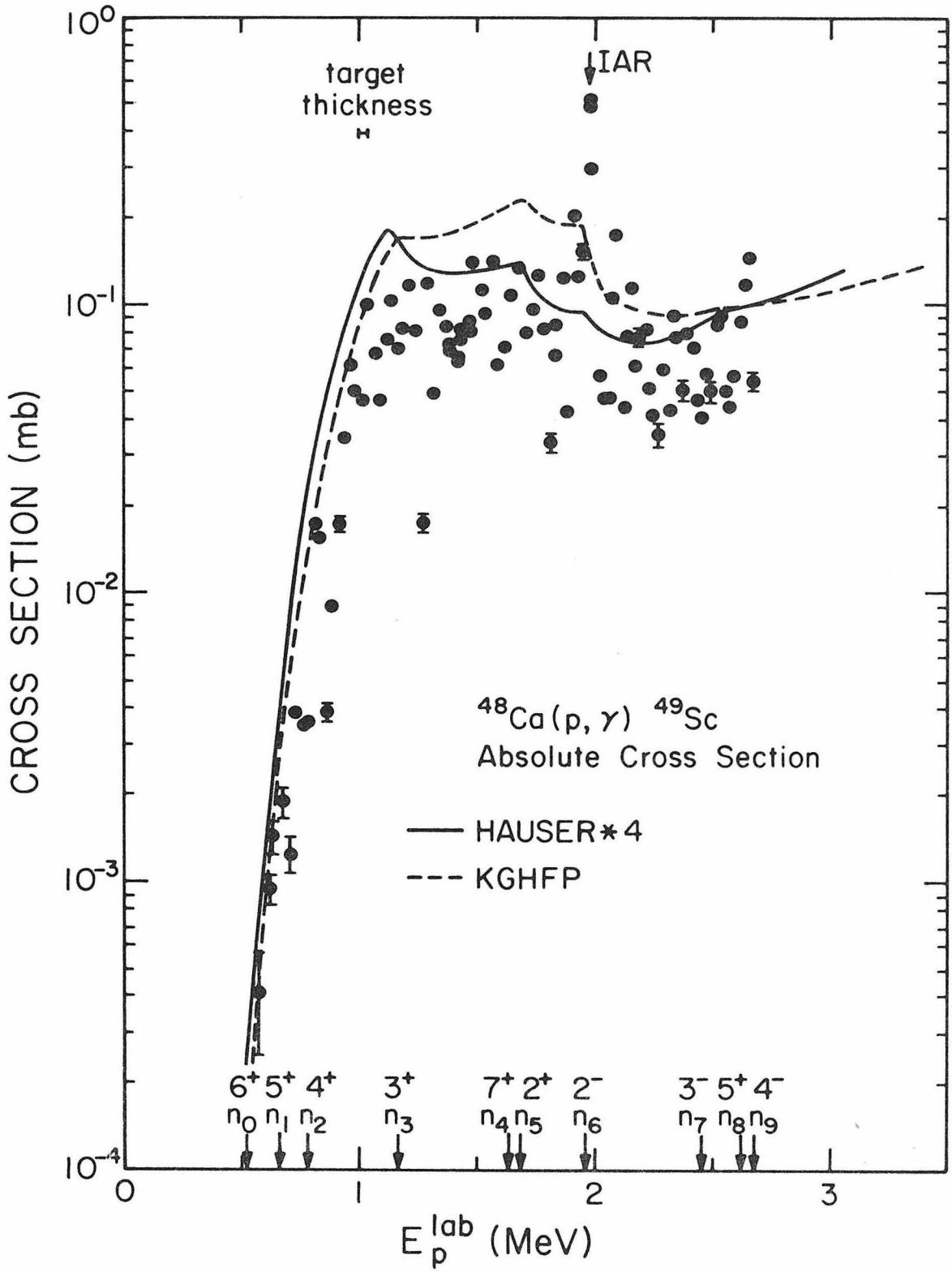
target thickness
IAR
$^{48}Ca(p,\gamma)\ ^{49}Sc$
Absolute Cross Section
HAUSER*4
KGHFP
CROSS SECTION (mb)
E_p^{lab} (MeV)
6^+ 5^+ 4^+ 3^+ 7^+ 2^+ 2^- 3^- 5^+ 4^-
n_0 n_1 n_2 n_3 n_4 n_5 n_6 n_7 n_8 n_9

Figure 25

Absolute cross sections for the $^{37}Cl(\alpha,\gamma)^{41}K$ reaction; error bars are statistical only. In global Hauser-Feshbach calculations performed with the KGHFP (Zimmerman 1977) and the HAUSER*4 program (Mann 1976), full isospin mixing has been assumed for all calculations. Where indicated, width fluctuation corrections have been included using the Tepel approximation (Tepel 1974). The neutron strength functions used in the KGHFP calculations are given in Table 24. The theoretical calculations have been smoothed over an energy interval corresponding to the beam energy loss in the target as described on p. 34. The data analysis is discussed in Section IIE, and the calculations in Section IIIB.

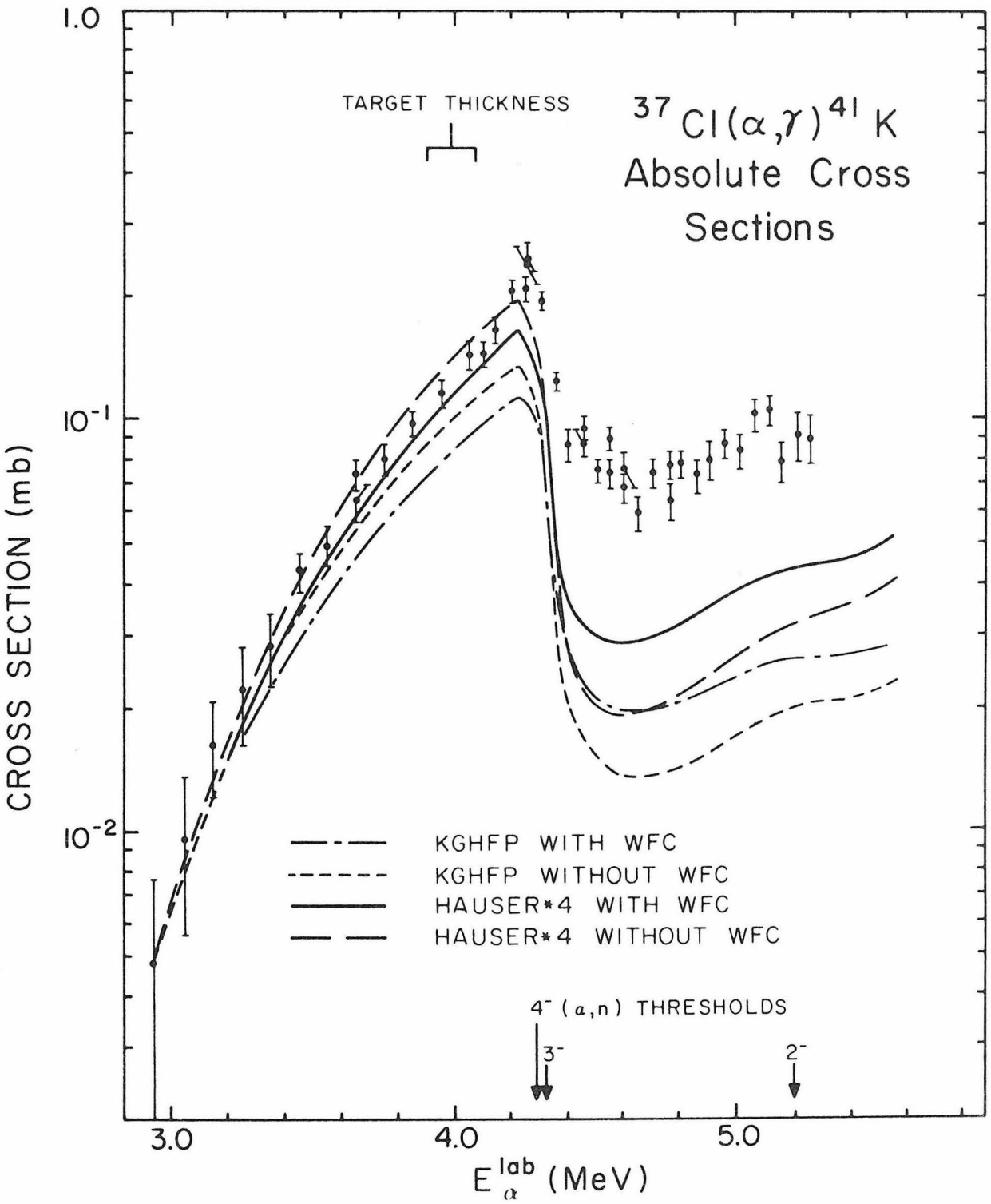
1.0
10^{-1}
10^{-2}
CROSS SECTION (mb)
TARGET THICKNESS
$^{37}Cl(\alpha,\gamma)^{41}K$
Absolute Cross Sections
KGHFP WITH WFC
KGHFP WITHOUT WFC
HAUSER*4 WITH WFC
HAUSER*4 WITHOUT WFC
4⁻ (α,n) THRESHOLDS
3⁻
2⁻
3.0
4.0
5.0
E_α^{lab} (MeV)

Figure 26

Absolute cross sections for the $^{62}Ni(\alpha,\gamma)^{66}Zn$ reaction; error bars are statistical only. In global Hauser-Feshbach calculations performed with the KGHFP (Zimmerman 1977) and the HAUSER*4 program (Mann 1976), full isospin mixing has been assumed for all calculations. Where indicated, width fluctuation corrections have been included using the Tepel approximation (Tepel 1974). The neutron strength functions used in the KGHFP calculations are given in Table 24. The theoretical calculations have been smoothed over an energy interval corresponding to the beam energy loss in the target as described on p. 34. The data analysis is discussed in Section IIE, and the calculations in Section IIIB.

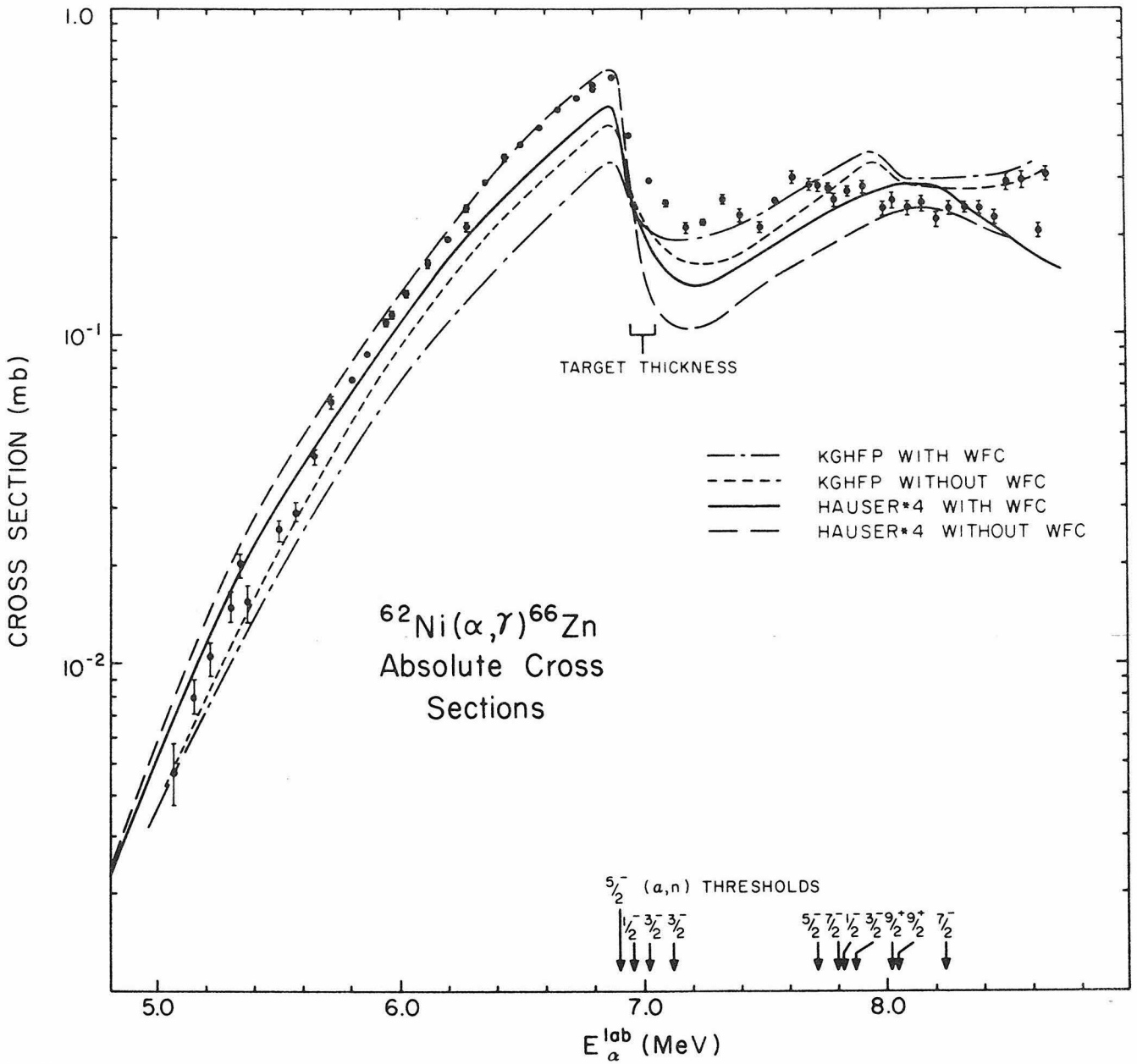
1.0
10^{-1}
10^{-2}
CROSS SECTION (mb)
TARGET THICKNESS
KGHFP WITH WFC
KGHFP WITHOUT WFC
HAUSER*4 WITH WFC
HAUSER*4 WITHOUT WFC
$^{62}Ni(\alpha,\gamma)^{66}Zn$
Absolute Cross
Sections
$5/2^-$ (a,n) THRESHOLDS
$1/2^-$ $3/2^-$ $3/2^-$
$5/2^-$ $7/2^-$ $1/2^-$ $3/2^-$ $9/2^+$ $9/2^+$ $7/2^-$
5.0
6.0
7.0
8.0
E_α^{lab} (MeV)

Figure 27

Absolute cross sections for the $^{64}Ni(\alpha,\gamma)^{68}Zn$ reaction; error bars are statistical only. In global Hauser-Feshbach calculations performed with the KGHFP (Zimmerman 1977) and the HAUSER*4 program (Mann 1976), full isospin mixing has been assumed for all calculations. Where indicated, width fluctuation corrections have been included.

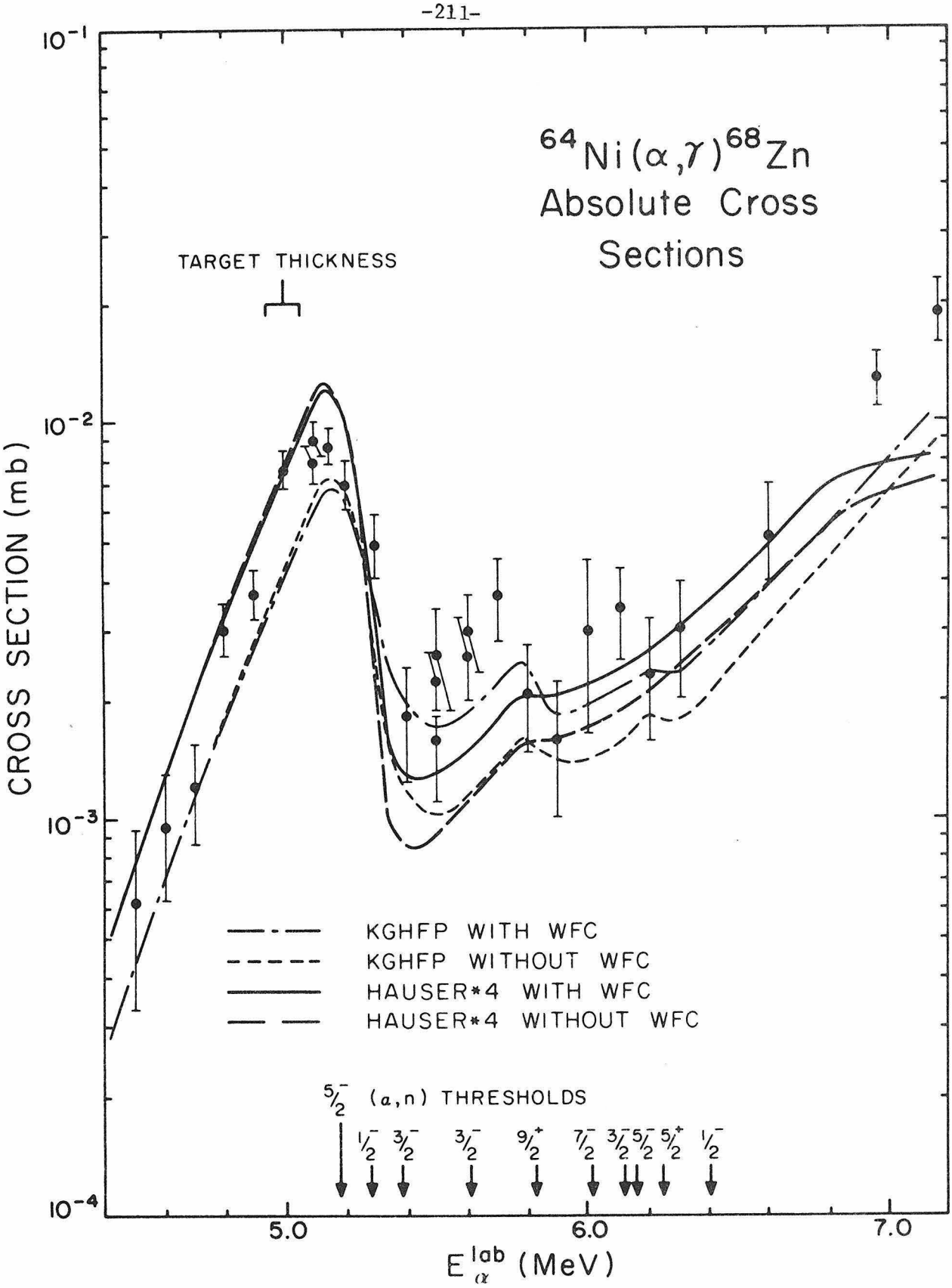
$^{64}Ni(\alpha,\gamma)^{68}Zn$
Absolute Cross Sections
TARGET THICKNESS
CROSS SECTION (mb)
10^{-1}
10^{-2}
10^{-3}
10^{-4}
KGHFP WITH WFC
KGHFP WITHOUT WFC
HAUSER*4 WITH WFC
HAUSER*4 WITHOUT WFC
$5/2^-$ (a,n) THRESHOLDS
$1/2^-$ $3/2^-$ $3/2^-$ $9/2^+$ $7/2^-$ $3/2^-$ $5/2^-$ $5/2^+$ $1/2^-$
5.0
6.0
7.0
E_α^{lab} (MeV)

Figure 28

Shielded BF_3 "long counter" used to count neutrons. The "long counter" is discussed in Section IIF.

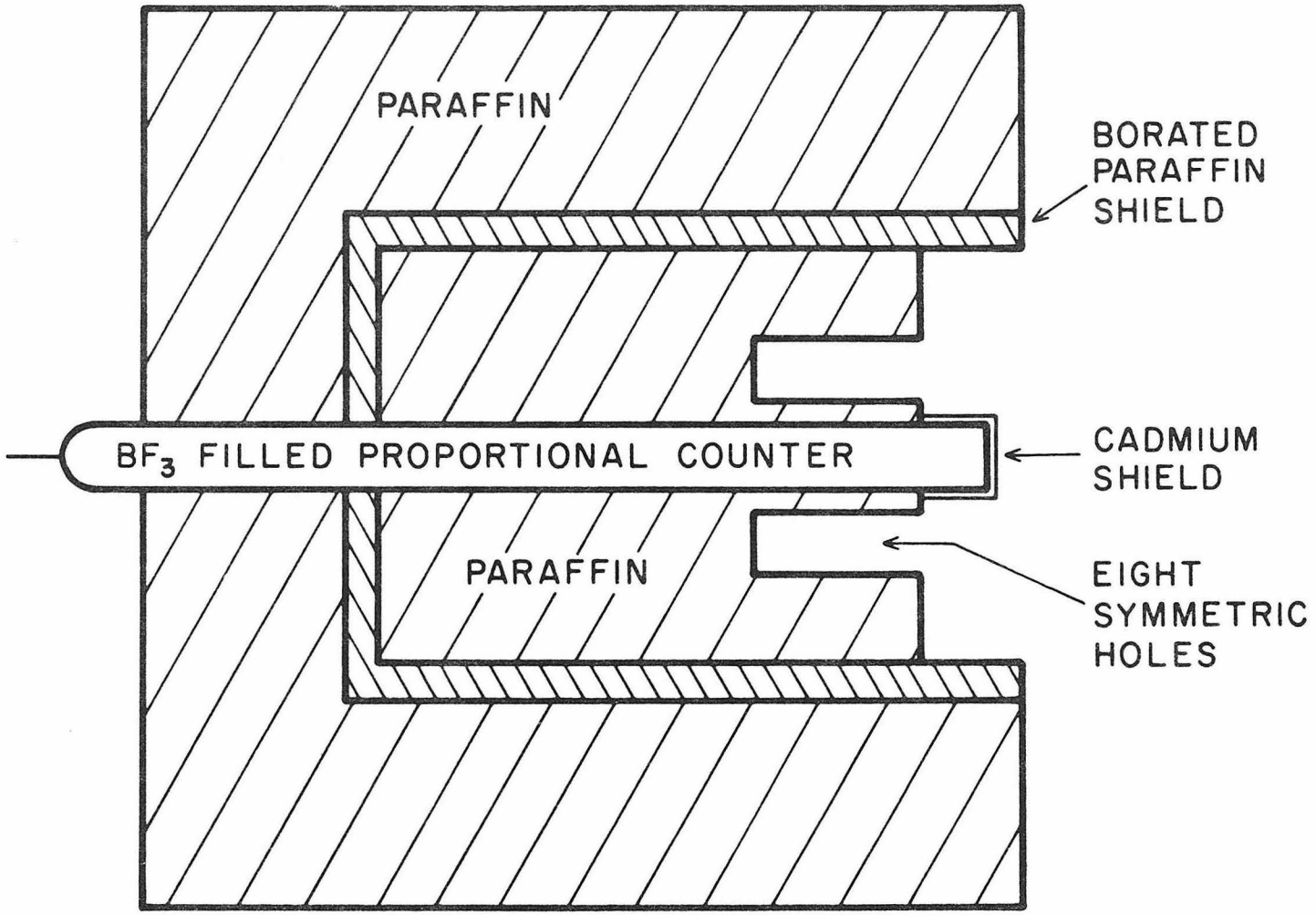

SHIELDED BF_3 LONG COUNTER

Figure 29

Sequence of operations in the measurements of the "long counter" efficiency described in Section IIF.

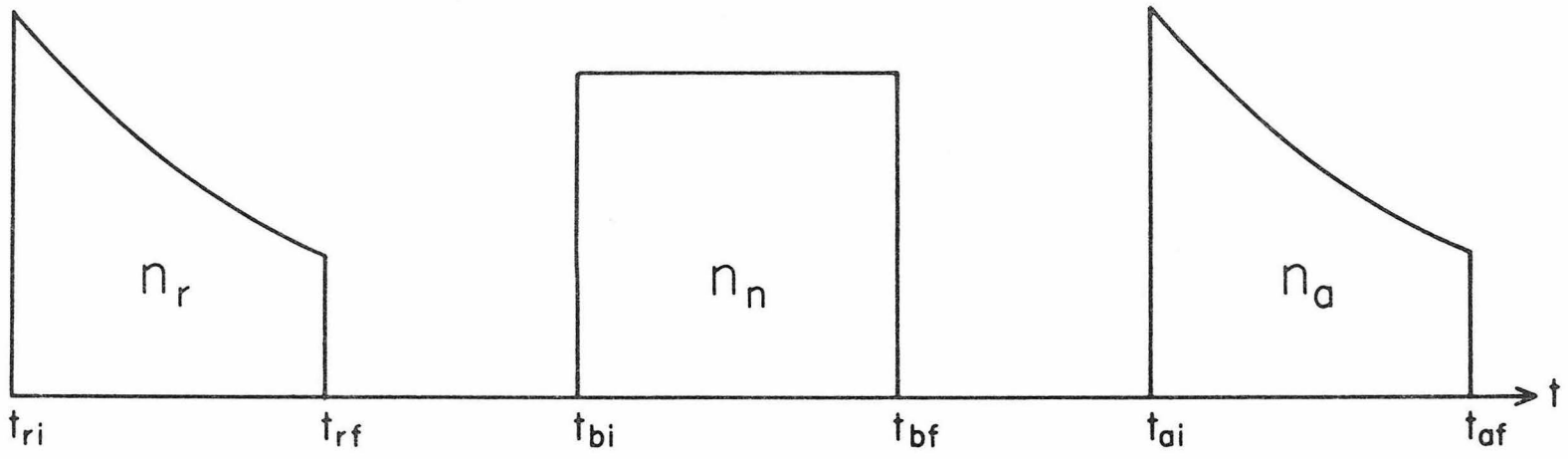

Beam off.
Ge(Li) detector
counts residual
activity

Beam on.
BF_3 long counter
counts neutrons

Beam off.
Ge(Li) detector
counts newly
produced and
residual activity

ACTIVATION TECHNIQUE FOR MEASUREMENT OF LONG COUNTER EFFICIENCY

Figure 30

BF_3 "long counter" efficiencies measured using the $^{48}Ca(p,n)^{48}Sc$ and $^{68}Zn(p,n)^{68}Ga$ reactions as described in Section IIF to test the flatness of the BF_3 "long counter" efficiency. The energy, $E_{cm} - E_{TH}$, is the center-of-mass energy in the proton channel at which the measurement was carried out, minus the center-of-mass thresholds for the $^{48}Ca(p,n_3)^{48}Sc^*(3^+)$ and $^{68}Zn(p,n_0)^{68}Ga$ reactions for the $^{48}Ca(p,n)^{48}Sc$ and $^{68}Zn(p,n)^{68}Ga$ measurements, respectively.

BF_3 LONG COUNTER EFFICIENCY

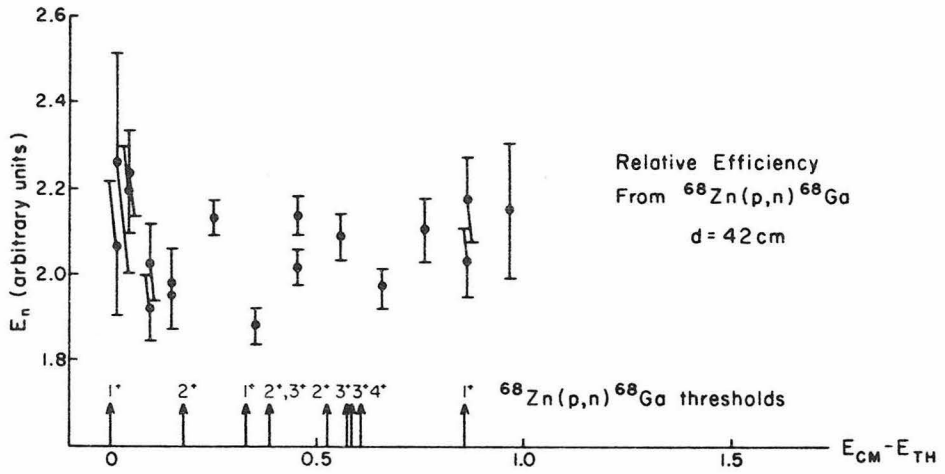

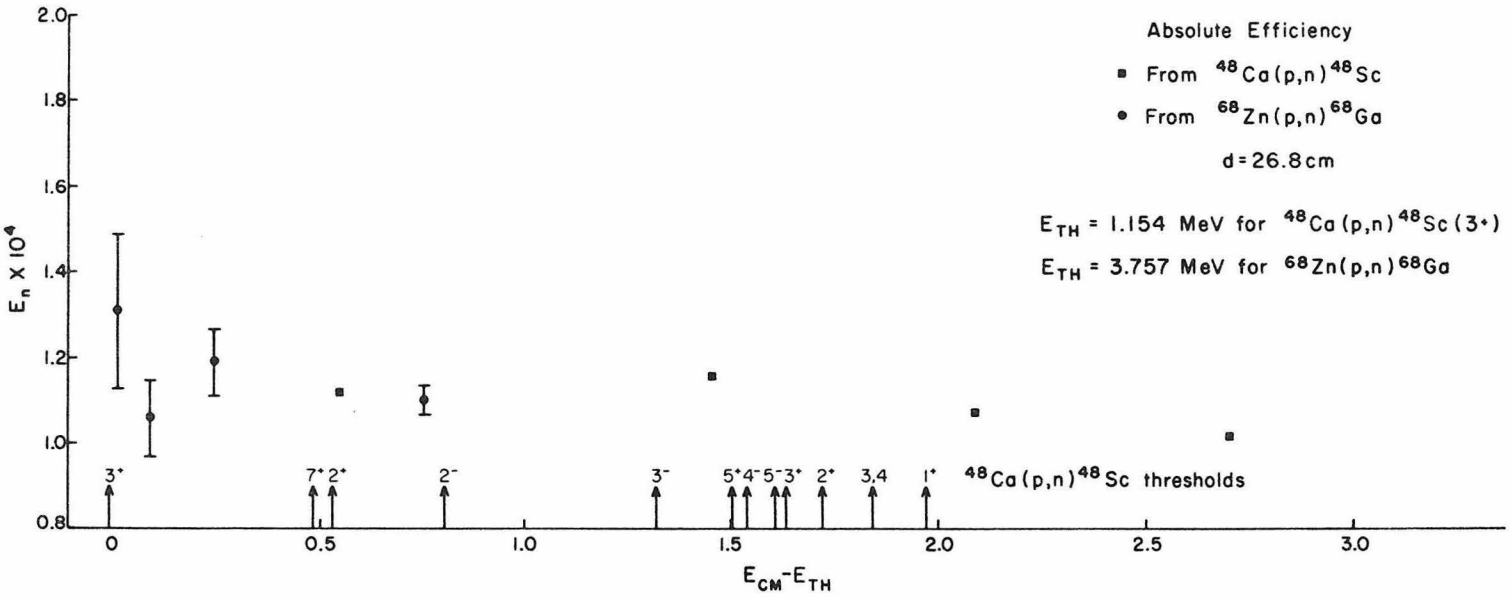

Figure 31

Absolute cross sections for the $^{51}V(p,n)^{51}Cr$ reaction. The experimental data are given in Table 26. The results of global Hauser-Feshbach calculations performed using the KGHFP (Zimmerman 1977) and the HAUSER*4 code (Mann 1976) are shown. Complete isospin mixing has been assumed and width fluctuation corrections are included in the Tepel approximation (Tepel 1974). The neutron strength functions used in the KGHFP calculation are given in Table 24. The data analysis is discussed in Section IIG and the calculations in Section IIIB.

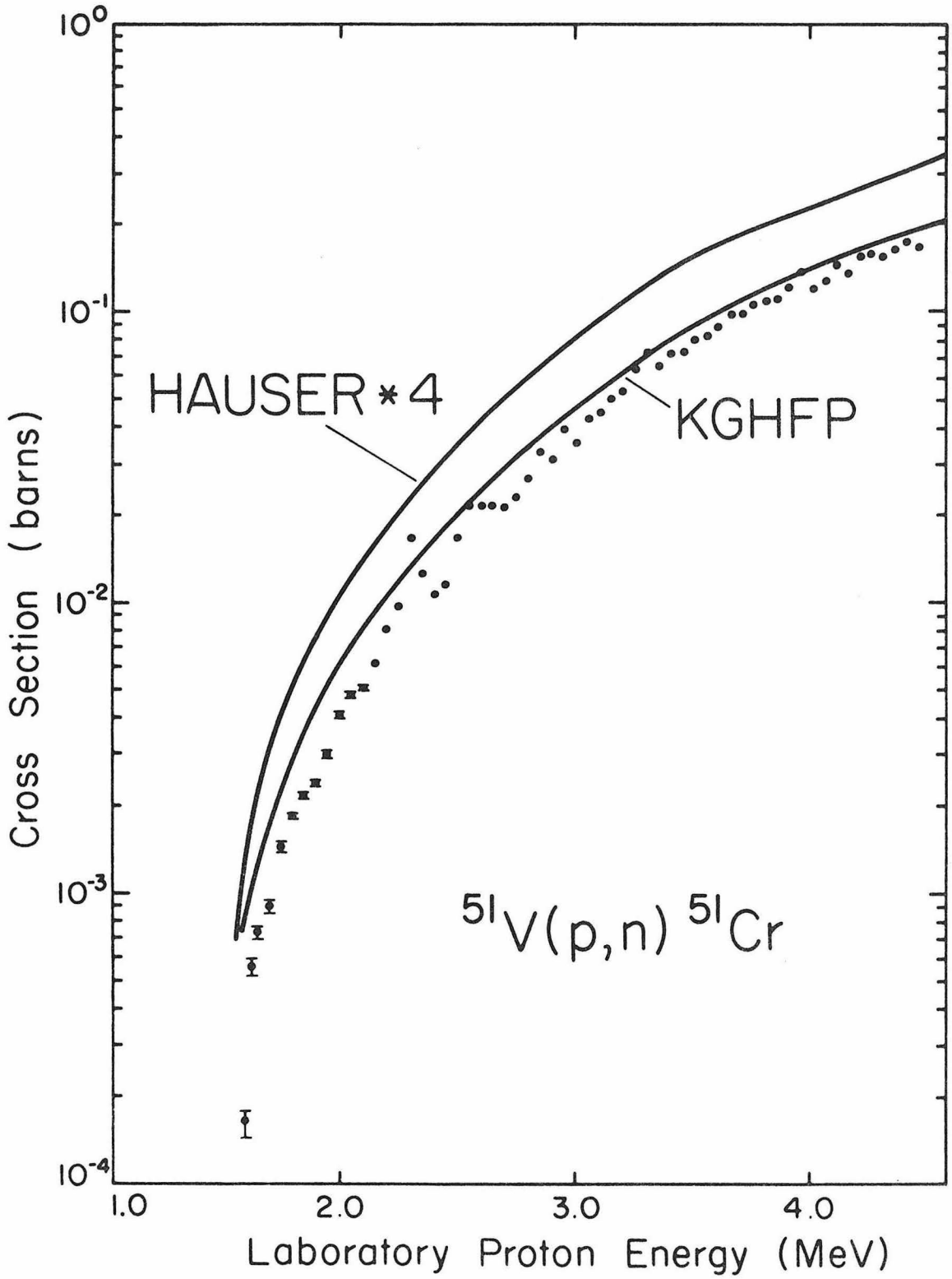
10^0
10^-1
10^-2
10^-3
10^-4
Cross Section (barns)
HAUSER*4
KGHFP
51V(p,n) 51Cr
1.0
2.0
3.0
4.0
Laboratory Proton Energy (MeV)

Figure 32

Absolute cross sections for the $^{54}Cr(p,n)^{54}Mn$ reaction. The experimental data are given in Table 17. The results of global Hauser-Feshbach calculations performed using the KGHFP (Zimmerman 1977) and the HAUSER*4 code (Mann 1976) are shown. Complete isospin mixing has been assumed and width fluctuation corrections are included in the Tepel approximation (Tepel 1974). The neutron strength functions used in the KGHFP calculation are given in Table 24. The data analysis is discussed in Section IIG and the calculations in Section IIIB.

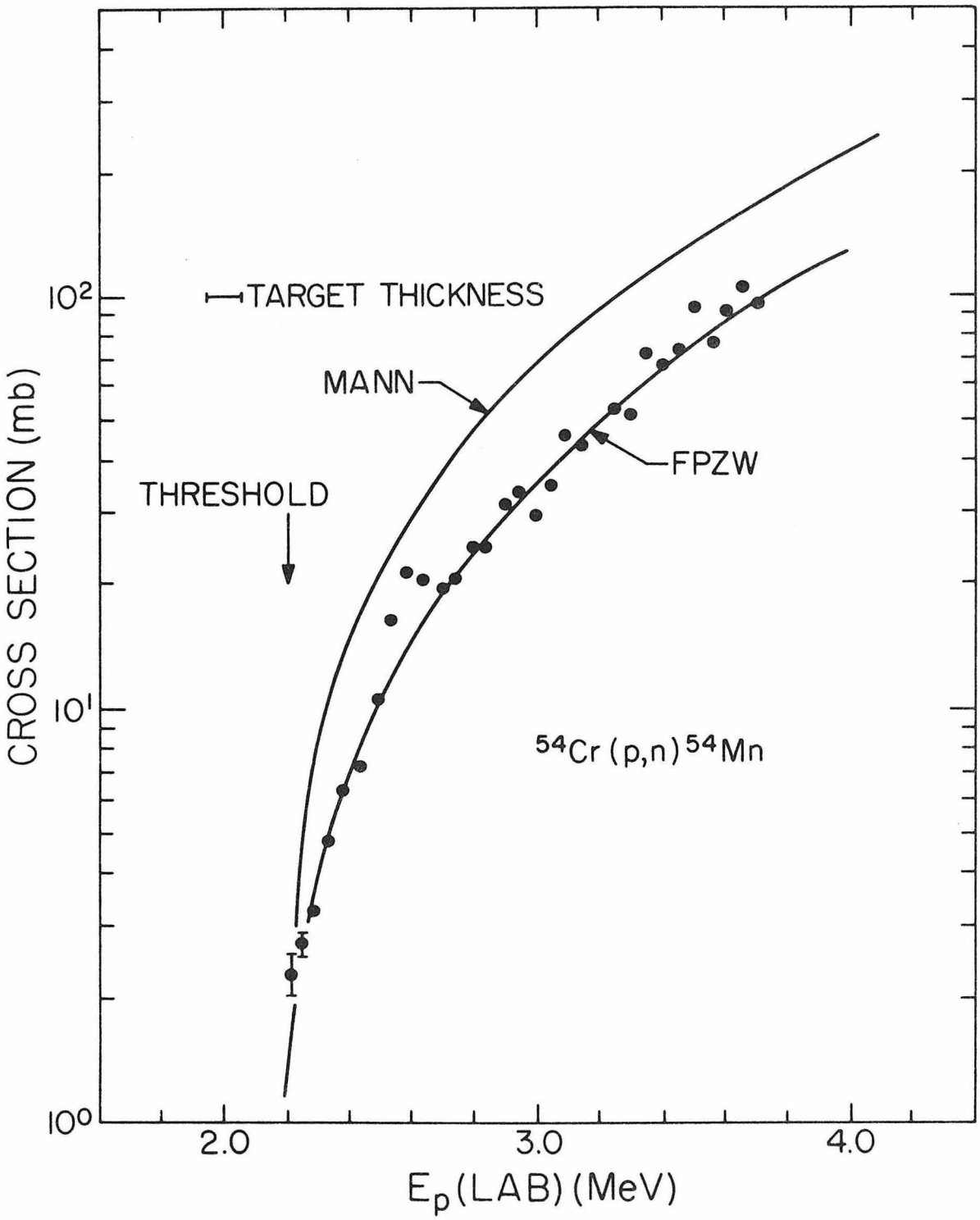
TARGET THICKNESS
MANN
FPZW
THRESHOLD
$^{54}Cr(p,n)^{54}Mn$
CROSS SECTION (mb)
10^2
10^1
10^0
2.0
3.0
4.0
E_p(LAB) (MeV)

Figure 33

Absolute cross sections for the $^{68}Zn(p,n)^{68}Ga$ reaction. The experimental data are given in Table 18. The results of global Hauser-Feshbach calculations performed using the KGHFP (Zimmerman 1977) and the HAUSER*4 code (Mann 1976) are shown. Complete isospin mixing has been assumed and width fluctuation corrections are included in the Tepel approximation (Tepel 1974). The neutron strength functions used in the KGHFP calculation are given in Table 24. The data analysis is discussed in Section IIG and the calculations in Section IIIB.

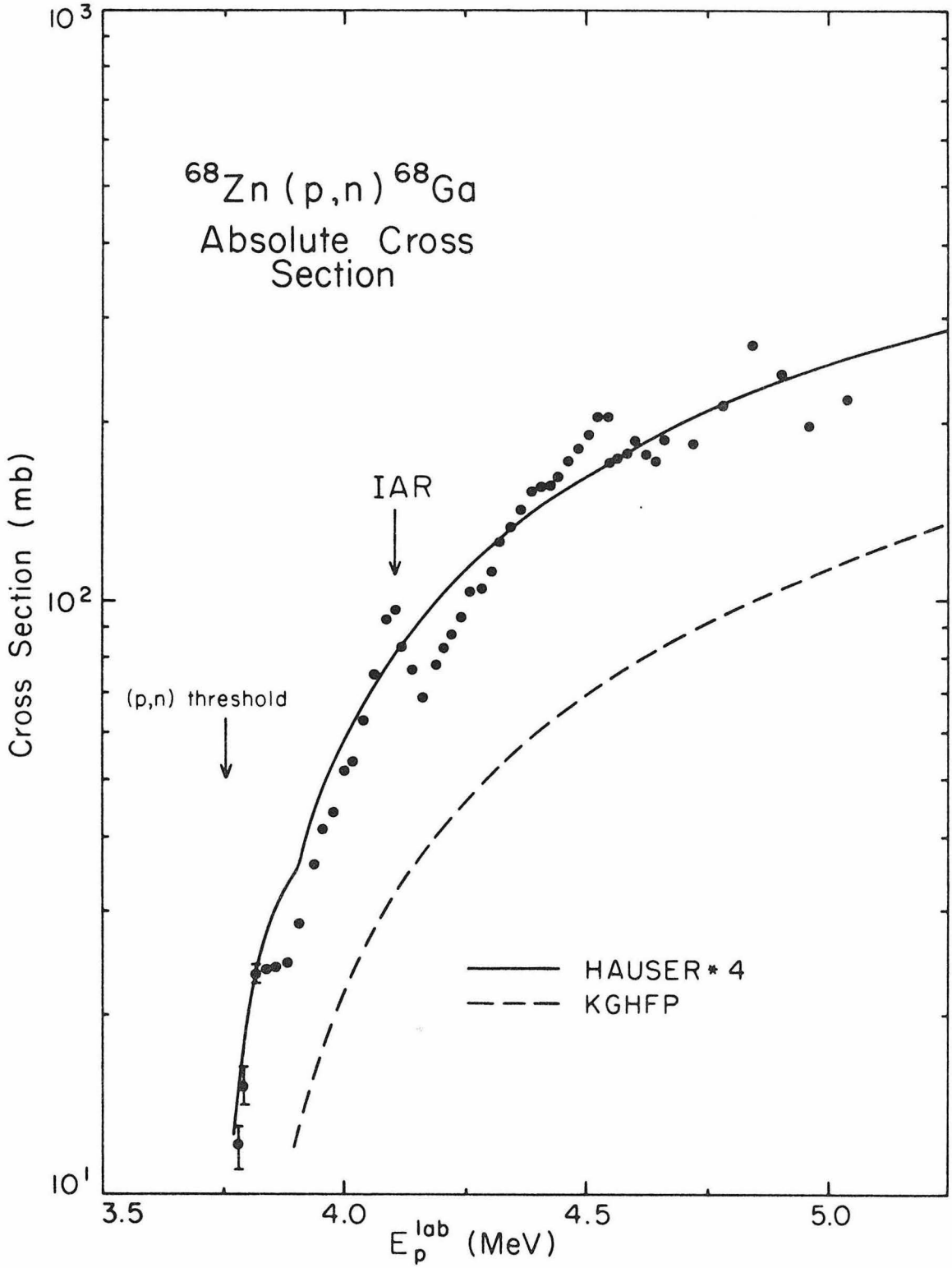
$^{68}Zn(p,n)^{68}Ga$
Absolute Cross Section
IAR
(p,n) threshold
HAUSER * 4
KGHFP
Cross Section (mb)
10^3
10^2
10^1
3.5
4.0
4.5
5.0
E_p^{lab} (MeV)

Figure 34

Absolute cross sections for the $^{48}Ca(p,n)^{48}Sc$ reaction. The experimental data are given in Table 19. The results of global Hauser-Feshbach calculations performed using the KGHFP (Zimmerman 1977) and the HAUSER*4 code (Mann 1976) are shown. Complete isospin mixing has been assumed and width fluctuation corrections are included in the Tepel approximation (Tepel 1974). The neutron strength functions used in the KGHFP calculation are given in Table 24. The data analysis is discussed in Section IIG and the calculations in Section IIIB.

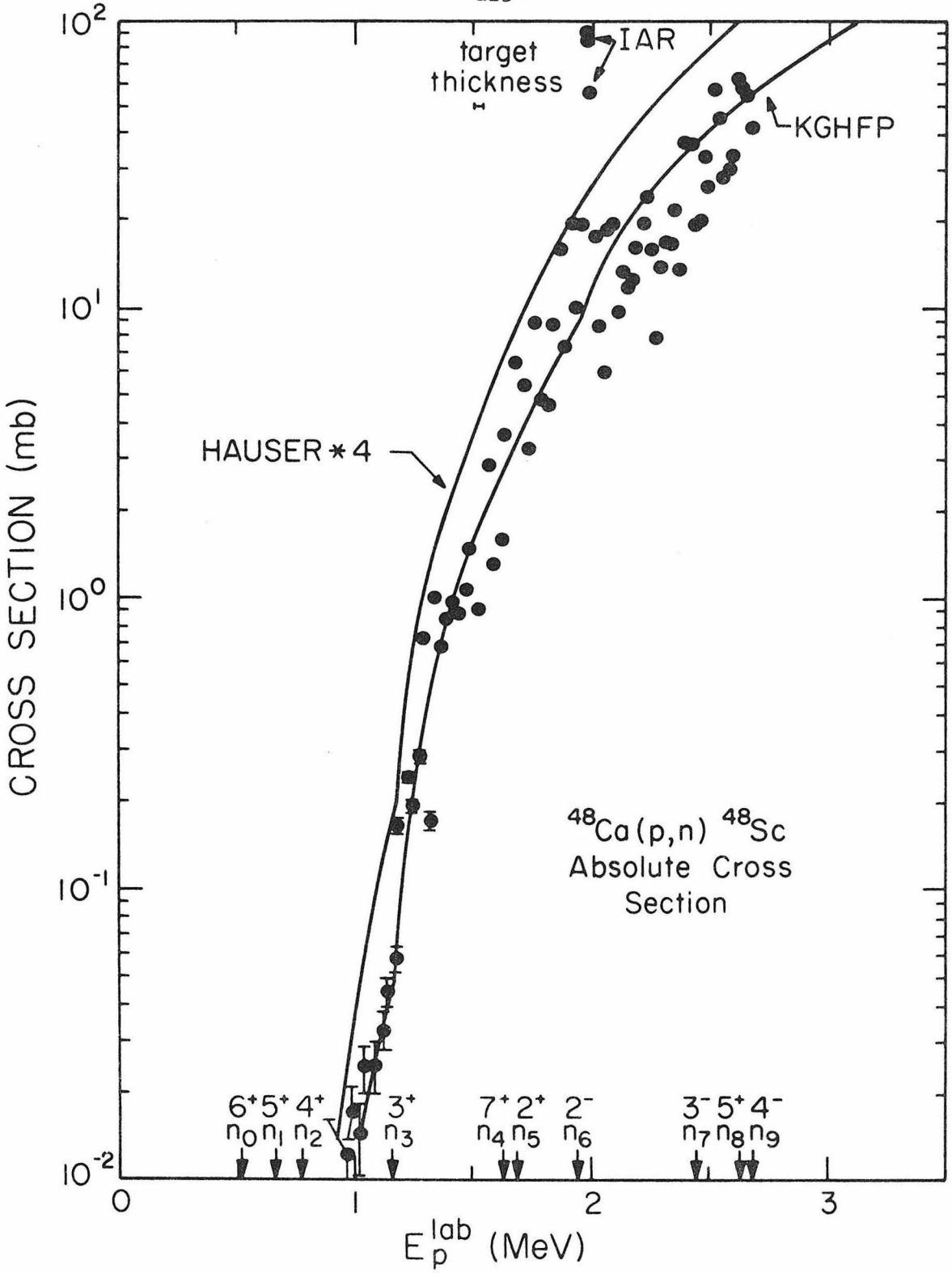
target thickness
IAR
KGHFP
HAUSER * 4
^{48}Ca(p,n) ^{48}Sc
Absolute Cross Section
CROSS SECTION (mb)
E_p^{lab} (MeV)
10^2
10^1
10^0
10^{-1}
10^{-2}
0
1
2
3
6^+ 5^+ 4^+ 3^+ 7^+ 2^+ 2^- 3^- 5^+ 4^-
n_0 n_1 n_2 n_3 n_4 n_5 n_6 n_7 n_8 n_9

Figure 35

Absolute cross sections for the $^{62}Ni(\alpha,n)^{65}Zn$ reaction. The experimental data are given in Table 20. The results of global Hauser-Feshbach calculations performed using the KGHFP (Zimmerman 1977) and the HAUSER*4 code (Mann 1976) are shown. Complete isospin mixing has been assumed and width fluctuation corrections are included in the Tepel approximation (Tepel 1974). The neutron strength functions used in the KGHFP calculation are given in Table 24. The data analysis is discussed in Section IIG and the calculations in Section IIIB.

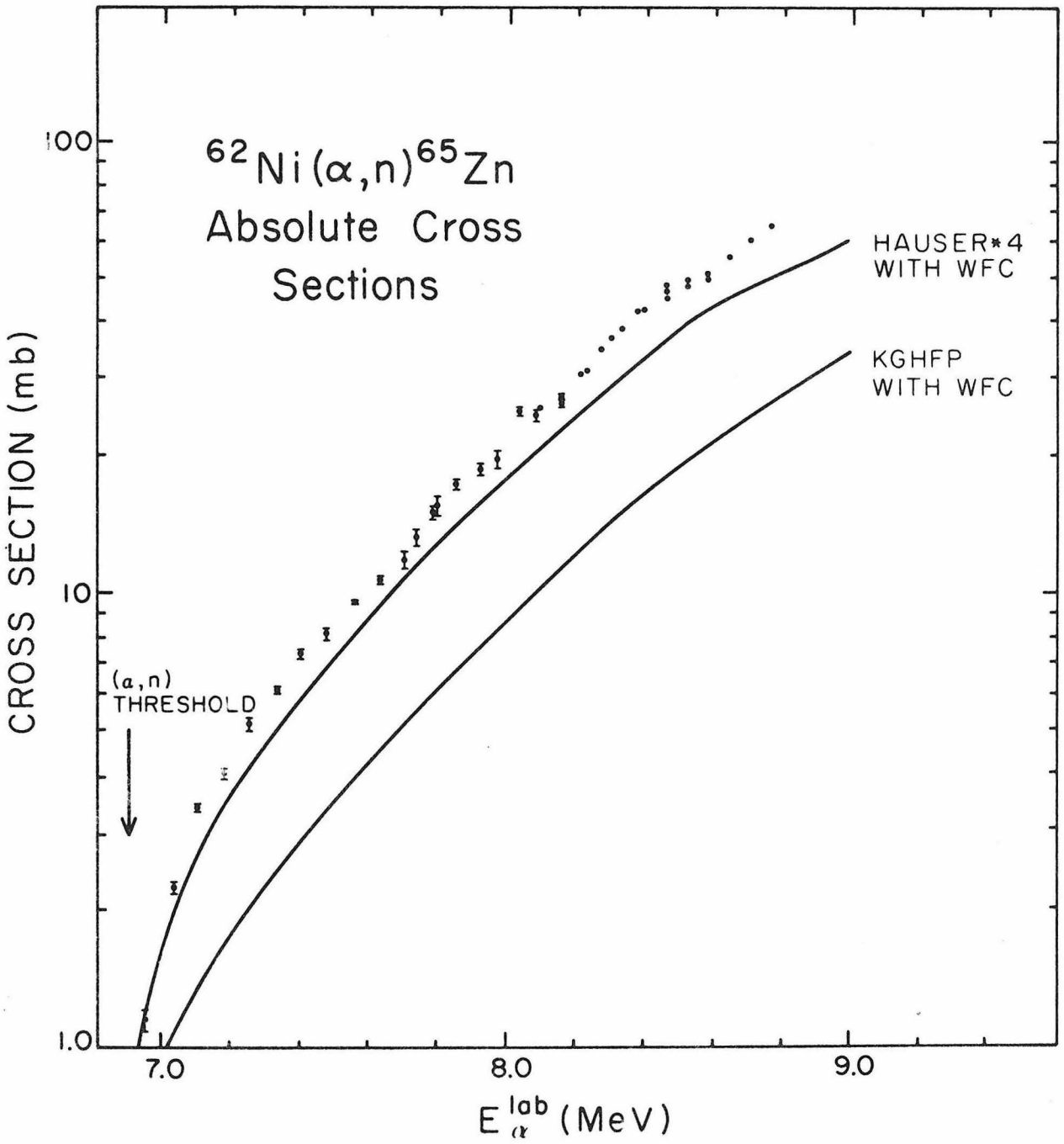
$^{62}Ni(\alpha,n)^{65}Zn$
Absolute Cross Sections
HAUSER*4 WITH WFC
KGHFP WITH WFC
(α,n) THRESHOLD
CROSS SECTION (mb)
100
10
1.0
7.0
8.0
9.0
E_α^{lab} (MeV)

Figure 36

Absolute cross sections for the $^{64}Ni(\alpha,n)^{68}Zn$ reaction. The experimental data are given in Table 21. The results of global Hauser-Feshbach calculations performed using the KGHFP (Zimmerman 1977) and the HAUSER*4 code (Mann 1976) are shown. Complete isospin mixing has been assumed and width fluctuation corrections are included in the Tepel approximation (Tepel 1974). The neutron strength functions used in the KGHFP calculations are given in Table 24. The data analysis is discussed in Section IIG and the calculations in Section IIIB.

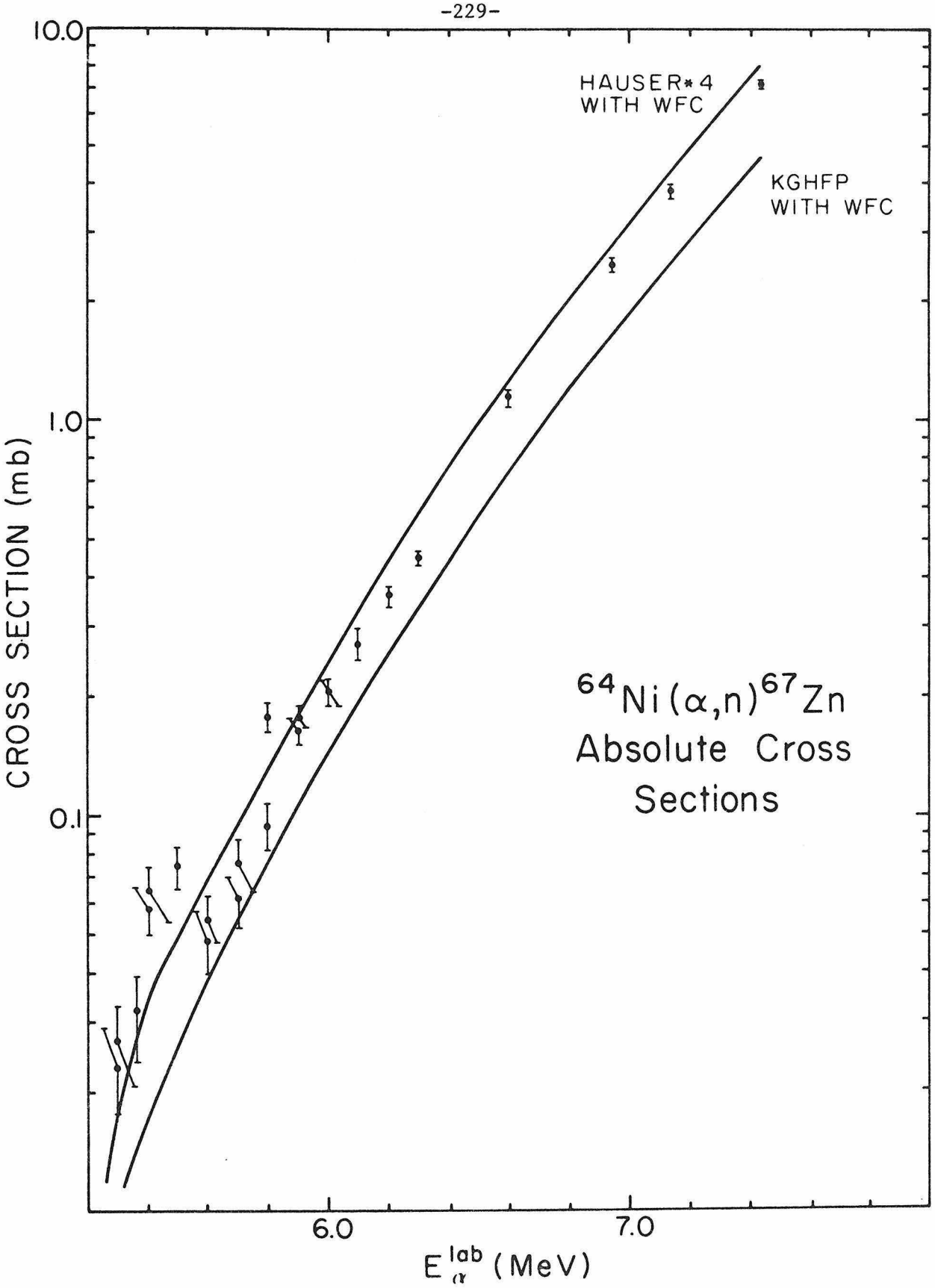
10.0
1.0
0.1
CROSS SECTION (mb)
HAUSER*4
WITH WFC
KGHFP
WITH WFC
$^{64}Ni(\alpha,n)^{67}Zn$
Absolute Cross
Sections
6.0
7.0
E_α^{lab} (MeV)

Figure 37

$^{68}Zn(p,\alpha)^{65}Cu$ spectrum for a proton bombarding energy of 3.92 MeV. The particles were detected with a silicon surface barrier detector at 160°. Protons elastically scattered from carbon, oxygen, and zinc, and α-particles produced in the $^{68}Zn(p,\alpha_0)^{65}Cu$ reaction were detected, and the corresponding peaks are identified in the figure. See Sections IIA and IIH for further details.

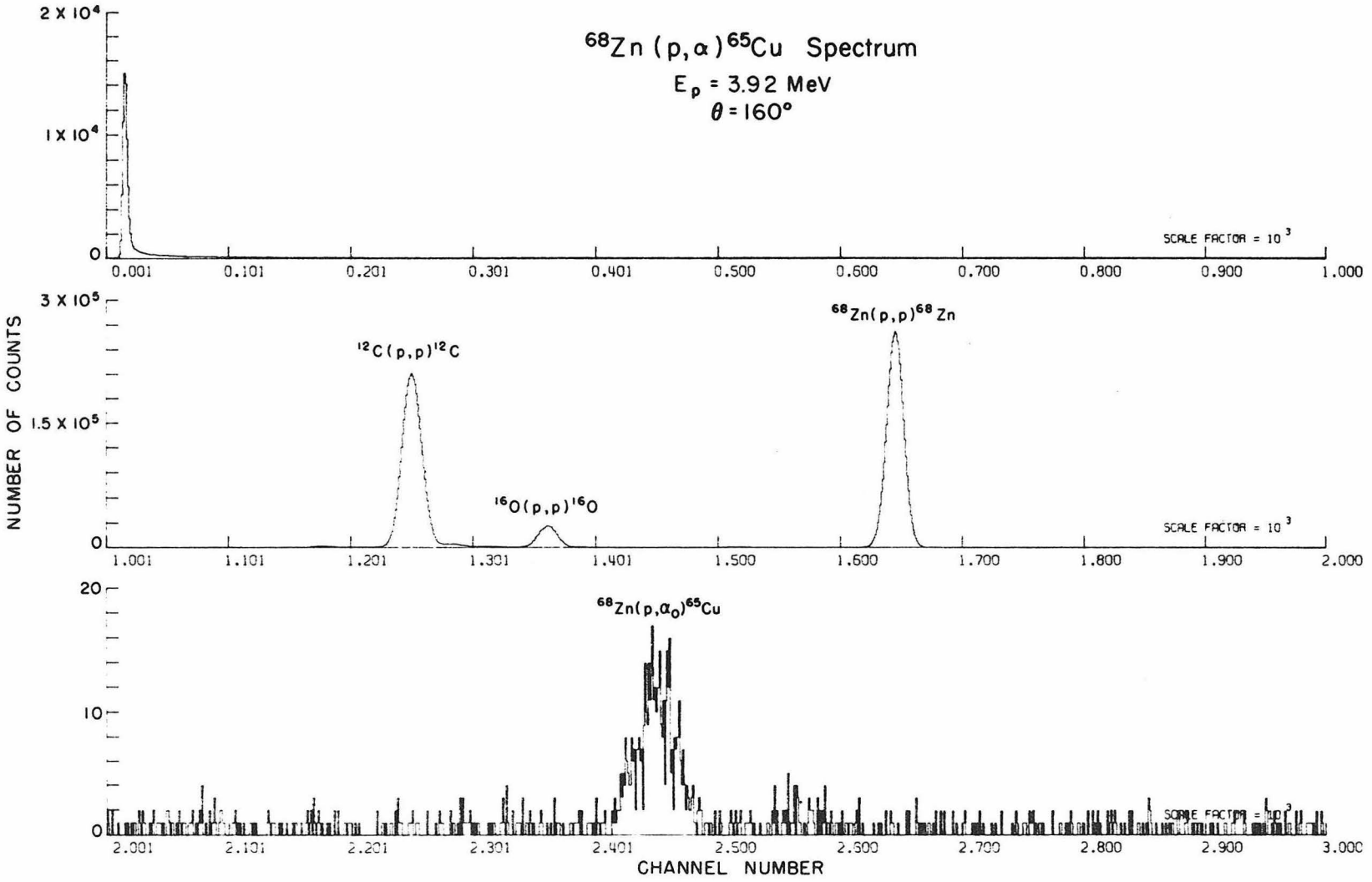
^{68}Zn (p,α)^{65}Cu Spectrum
E_p = 3.92 MeV
θ = 160°
NUMBER OF COUNTS
CHANNEL NUMBER
^{12}C(p,p)^{12}C
^{16}O(p,p)^{16}O
^{68}Zn(p,p)^{68}Zn
^{68}Zn(p,α$_0$)^{65}Cu
SCALE FACTOR = 10^3

Figure 38

Cross sections for the reaction $^{68}Zn(p,\alpha)^{65}Cu$. The experimental data are compared to results of global Hauser-Feshbach calculations performed using the KGHFP (Zimmerman 1977) and the HAUSER*4 code (Mann 1976). Complete isospin mixing and width fluctuation corrections are incorporated in the calculations. The neutron strength functions used in the KGHFP calculations are given in Table 24. The spins and parities are not known and are purely guesses. Thus there is considerable uncertainty in the calculation of the competition effects. See Sections IIA and IIH for discussion of experimental details and Section IIIC for discussion of the results.

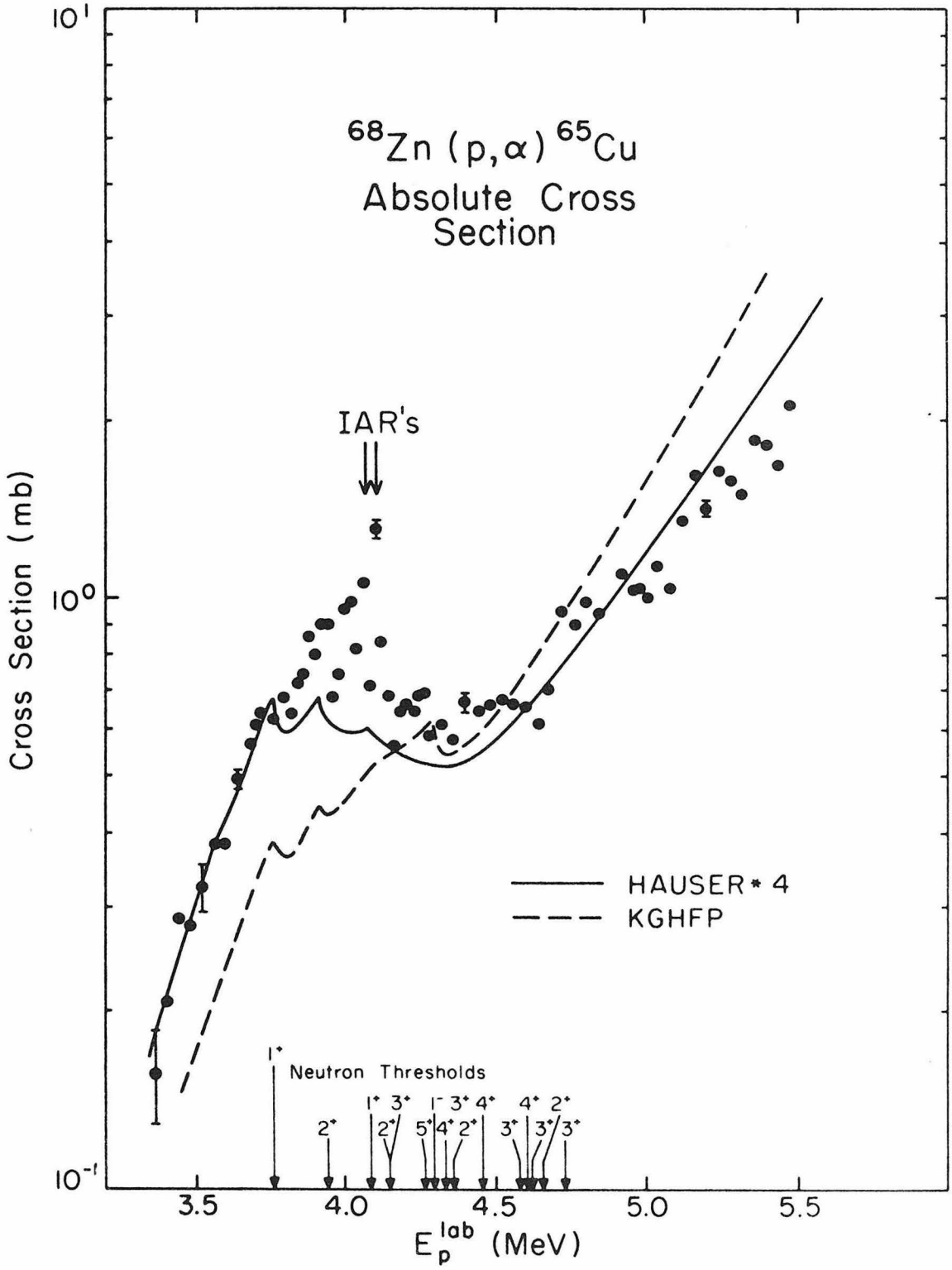
$^{68}Zn\,(p,\alpha)\,^{65}Cu$
Absolute Cross Section
IAR's
HAUSER * 4
KGHFP
Neutron Thresholds
1+
2+
1+ 3+
2+
1- 3+ 4+
5+ 4+ 2+
4+ 2+
3+ 3+ 3+
Cross Section (mb)
10^1
10^0
10^{-1}
3.5
4.0
4.5
5.0
5.5
E_p^{lab} (MeV)

Figure 39

The effects of width fluctuation corrections and realistic neutron strength functions on KGHFP calculations for the reaction $^{51}V(p,\gamma)^{52}Cr$. The inclusion of width fluctuation corrections (WFC, YES, curves S and C) decreases the neutron transmission functions to correct for the strong channel-channel correlations in the dominant neutron channel. The realistic p-wave neutron strength functions ($r_1 = 0.09$) are much smaller than the black nucleus strength functions ($r_1 = 1.0$) and result in lower p-wave neutron transmission functions. Doubling the s-wave strength function ($r_0 = 1.85$) has very little effect at energies more than a few keV above threshold because the s-wave neutron transmission functions dominate those for other channels, even for small channel energies, by much more than a factor of two (see Figure 6 in Appendix B). Thus, both width fluctuation corrections and realistic strength functions decrease the size of the drop in the $^{51}V(p,\gamma)^{52}Cr$ cross sections above the (p,n) threshold. The curves are smoothed as in Figure 22. The experimental data are the same as in Figure 22. Width fluctuation corrections and neutron strength functions are discussed in subsections (iii) and (iv) of Section IIIB.

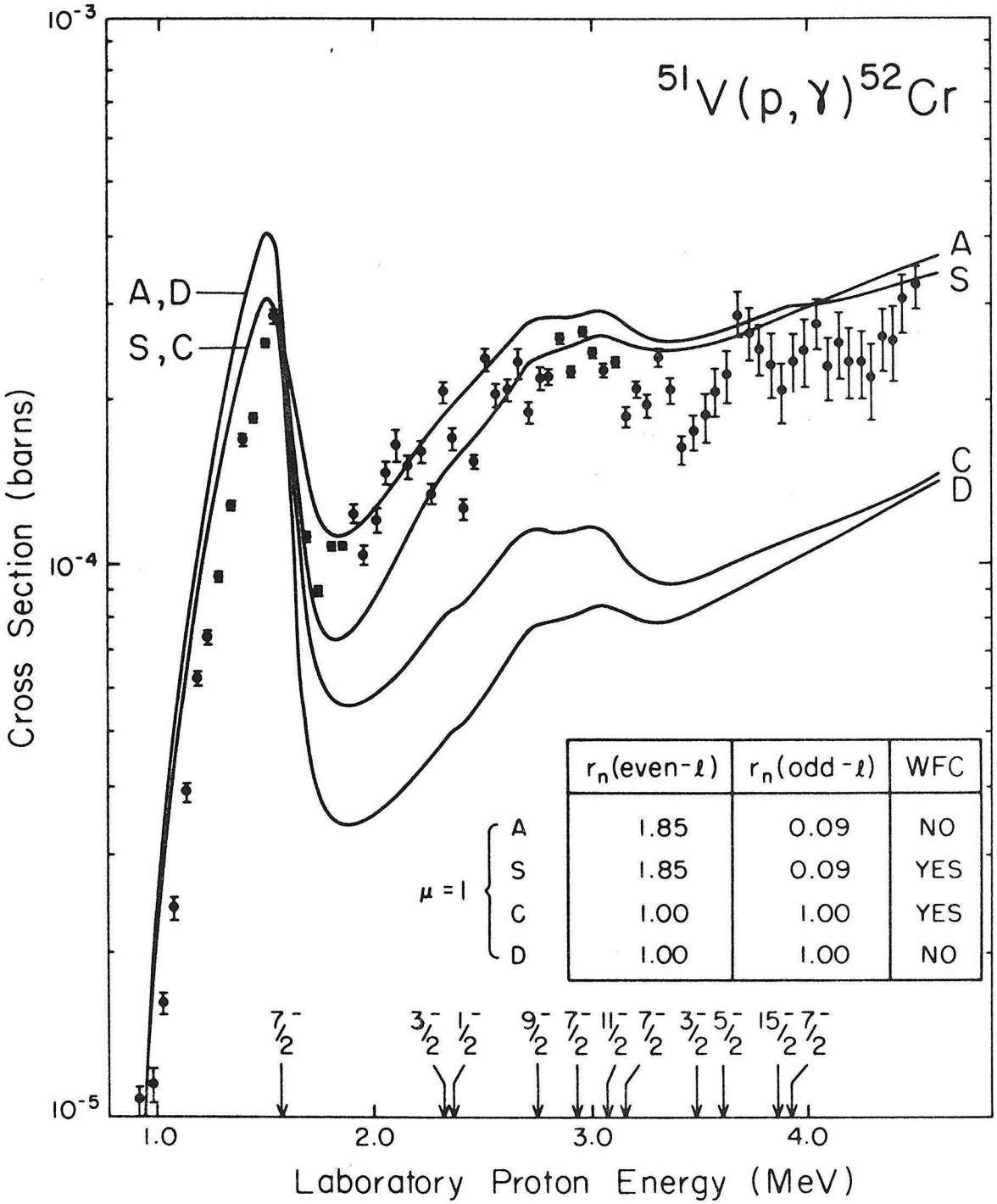

	r_n(even-ℓ)	r_n(odd-ℓ)	WFC
A	1.85	0.09	NO
S	1.85	0.09	YES
C	1.00	1.00	YES
D	1.00	1.00	NO

Figure 40

The effects of varying the proton strength functions in KGHFP calculations for $^{51}V(p,\gamma)^{52}Cr$. The black nucleus strength functions used in the standard calculation correspond to $r_p = 1$. For curve A (odd-protons only), γ-decay competes with odd-ℓ neutron partial waves below the (p,n_1) threshold, and the drop above the (p,n_0) threshold is smallest. For curve E (even-ℓ protons only), γ-decay competes with even-ℓ neutrons (including s-waves) and a large drop results. The curves are smoothed as in Figure 22 and the data are the same. Proton strength functions are discussed in subsection (iv) of Section IIIB.

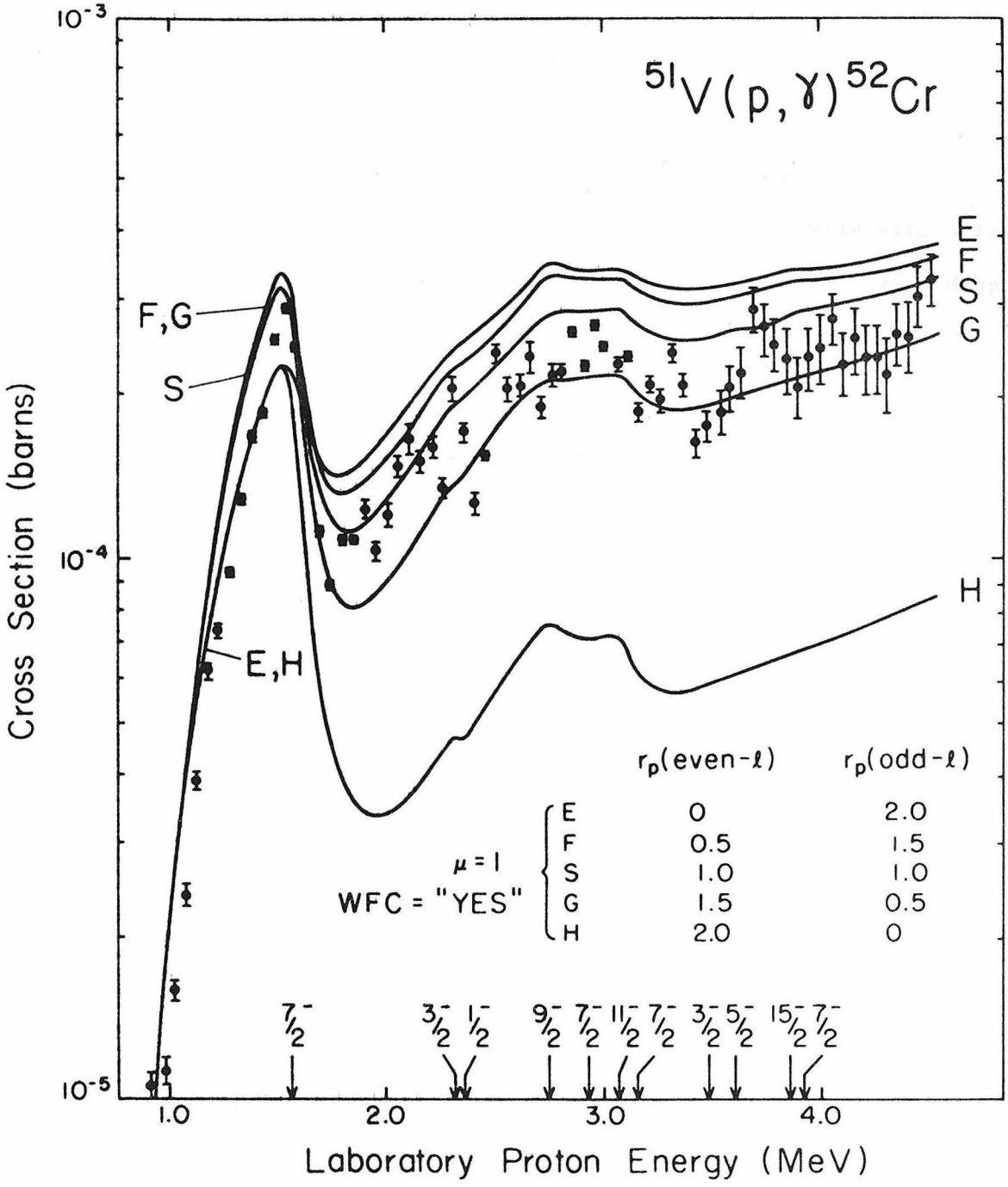
$^{51}V(p,\gamma)^{52}Cr$
Cross Section (barns)
Laboratory Proton Energy (MeV)
F,G
S
E,H
E
F
S
G
H
r_p(even-ℓ)
r_p(odd-ℓ)
μ = 1
WFC = "YES"
E 0 2.0
F 0.5 1.5
S 1.0 1.0
G 1.5 0.5
H 2.0 0
7⁻/2
3⁻/2 1⁻/2
9⁻/2 7⁻/2 11⁻/2 7⁻/2
3⁻/2 5⁻/2
15⁻/2 7⁻/2

Figure 41

Effect of isospin mixing on KGHFP calculations for the $^{51}V(p,\gamma)^{52}Cr$ reaction. Curves are shown for different values of the isospin mixing parameter, μ. When there is no mixing ($\mu = 0$), neutron emission competes with γ-ray emission only in the decay of $T^{>}$ states; when isospin is completely mixed ($\mu = 1$), neutron emission competes fully with γ-ray emission in the decay of both $T^{<}$ and $T^{>}$ states and causes a large drop in the $^{51}V(p,\gamma)^{52}Cr$ cross sections above the (p,n) threshold. The curves are smoothed as in Figure 22 and the data are the same. Isospin mixing is discussed in subsection (v) of Section IIIB.

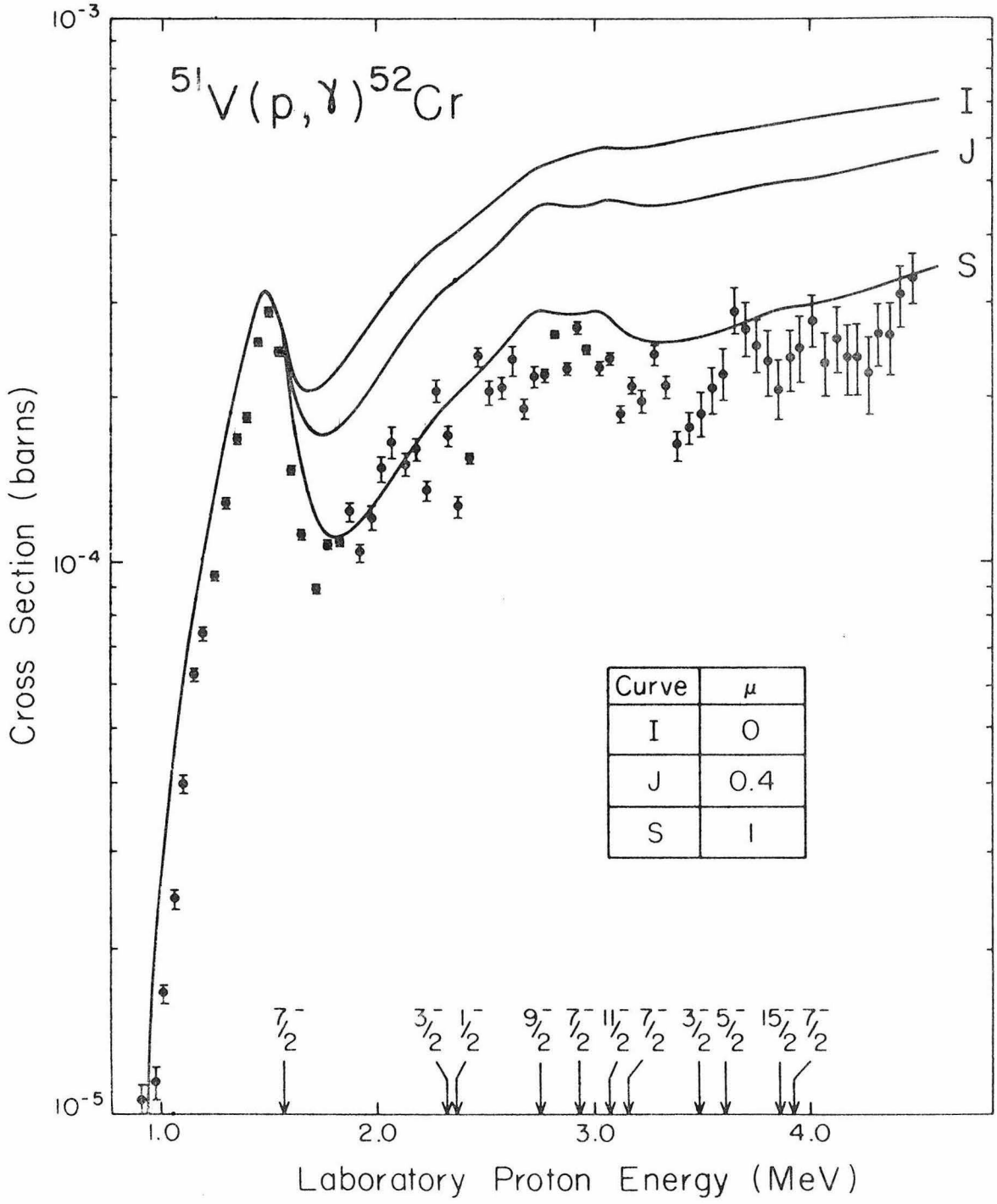
$^{51}V(p,\gamma)^{52}Cr$
I
J
S
Curve | μ
I | 0
J | 0.4
S | 1
10^{-3}
10^{-4}
10^{-5}
Cross Section (barns)
1.0
2.0
3.0
4.0
Laboratory Proton Energy (MeV)
$7/2^-$
$3/2^-$ $1/2^-$
$9/2^-$ $7/2^-$ $11/2^-$ $7/2^-$
$3/2^-$ $5/2^-$
$15/2^-$ $7/2^-$